MIXED BAROCLINIC-BAROTROPIC INSTABILITY WITH OCEANIC APPLICATIONS

by

DANIEL GORDON WRIGHT

B.Sc., Laurentian University, 1975

A THESIS SUBMITTED IN PARTIAL FULFILLMENT OF

THE REQUIREMENTS FOR THE DEGREE OF

DOCTOR OF PHILOSOPHY

in

THE FACULTY OF GRADUATE STUDIES

Department of Mathematics

Institute of Applied Mathematics and Statistics

Institute of Oceanography

We accept this thesis as conforming

to the required standard

THE UNIVERSITY OF BRITISH COLUMBIA

November, 1978

© Daniel Gordon Wright, 1978

In presenting this thesis in partial fulfilment of the requirements for an advanced degree at the University of British Columbia, I agree that the Library shall make it freely available for reference and study. I further agree that permission for extensive copying of this thesis for scholarly purposes may be granted by the Head of my Department or by his representatives. It is understood that copying or publication of this thesis for financial gain shall not be allowed without my written permission.

Department of Mathematics

The University of British Columbia
2075 Wesbrook Place
Vancouver, Canada
V6T 1W5

Date November 10, 1978

ABSTRACT

A brief introduction to the general subject of baroclinic-barotropic instability is given in chapter I followed by a discussion of the work done in the following chapters.

In chapter II a three-layer model is derived to study the stability of large-scale oceanic zonal flows over topography to quasi-geostrophic wave perturbations. The mean density profile employed has upper and lower layers of constant densities ρ_1^* and ρ_3^* respectively ($\rho_1^* < \rho_3^*$) and a middle layer whose density varies linearly from ρ_1^* to ρ_3^*. The model includes vertical and horizontal shear of the zonal flow in a channel as well as the effects of β (the variation with latitude of twice the local vertical component of the earth's rotation) and cross-channel variations in topography. In chapter II the effects of density stratification, vertical curvature in the mean velocity profile, β, constant slope topography and layer thicknesses H_i (i=1,2,3) are studied. The following general results with regard to the stability of the flow are found:

(1) curvature in the mean velocity profile has a very strong destabilizing influence

(2) density stratification stabilizes

(3) the β-effect stabilizes

(4) topography stabilizes one of two possible classes of instability (a bottom intensified instability) and

(5) increasing either H_1 or H_3 relative to H_2 stabilizes.

Finally, the model is compared with two-layer models and results clearly indicate the importance of having at least three layers when curvature of the mean velocity profile is present or when H_2 is significant.

In chapter III, mixed baroclinic-barotropic instability in a channel is studied using two- and three-layer models. The equations appropriate to the two-layer model used have been derived previously by Pedlosky (1964a). This model consists of two homogeneous layers of fluid with upper and lower layers of densities ρ_1^* and ρ_2^* respectively $(\rho_2^* > \rho_1^*)$ and the corresponding mean velocities are taken as $U_1 = U_0 \cdot (1-\cos \pi(y+1))$, $U_2 = \varepsilon U_1$(ε=constant). The choice of a cosine jet allows the possibility of barotropic instability (Pedlosky, 1964b) while the possibility of baroclinic instability is introduced by considering values of ε other than 1. In the study of the three-layer model, whose governing equations were derived in chapter II, the mean velocities are chosen in the form $U_1 = U_0(1-\cos \pi(y+1))$, $U_2 = \varepsilon U_1$ and $U_3 = 0$ and to simplify the interpretation of results, the effects of β and topography are neglected. Again the study of mixed baroclinic-barotropic instability is studied by varying ε.

The study of pure baroclinic or pure barotropic instability in either model is justified for the cases $(L/r_i)^2 \ll 1$ or $(L/r_i)^2 \gg 1$, respectively (L is the horizontal length scale of the mean currents and r_i is a typical internal (Rossby) radius of deformation for the system).

For the case $(L/r_i)^2 \sim 1$ it is found that the properties of the most unstable waves vary with the long-channel wavenumber. For each model, it is found that below the short wave cut-off for pure barotropic instability there are generally two types of instabilities: (1) a baroclinic instability which generally loses kinetic energy to the mean currents through the mechanism of barotropic instability and (2) a "barotropic instability" which in some cases extracts the majority of its energy from the available potential energy of the mean state. The latter type of instability is most apparent in the study of the three-layer model although it is also present in the two-layer case. It is a very interesting case since its structure is largely dictated by the mechanism of barotropic instability even when its energy source is that of a baroclinic instability. Beyond the short wave cut-off for pure barotropic instability, only the former of these two types of instabilities persists (i.e. the baroclinic instability).

Qualitative results for the three-layer model are also derived in chapter III (section 3). The energy equation is discussed, bounds on phase speeds and growth rates of unstable waves are derived and the condition for marginally stable waves with phase speed within the range of the mean currents is presented.

Chapter IV is concerned with oceanic applications. Low frequency motions ($\lesssim 0.25$ cpd) have recently been observed in Juan de Fuca Strait. The three-layer model developed in chapter II is used to show that at least part of this activity may be due to an instability (baroclinic)

of the mean current to low-frequency quasi-geostrophic disturbances.

Recent satellite infrared imagery and hydrographic maps show eddies in the deep ocean just beyond the continental shelf in the north-east Pacific. The wavelength of these patterns is about 100 km and the eddies are aligned in the north-south direction paralleling the continental slope region. A modification of the three-layer model derived in chapter II is used to study the stability of the current system in this area. It is found that for typical vertical and horizontal shears associated with this current system (which consists of a weak flow to the south at shallow depths, a stronger poleward flow at intermediate depths and a relatively quiescent region below), the most unstable waves have properties in agreement with observations.

TABLE OF CONTENTS

ABSTRACT ii

LIST OF TABLES viii

LIST OF FIGURES ix

ACKNOWLEDGEMENTS xix

I INTRODUCTION. 1

II BAROCLINIC INSTABILITY AND CONSTANT BOTTOM SLOPE. 14

1. Introduction. 15

2. Formulation 17

3. Linear Perturbation analysis. 30

4. Results of Independent Parameter Variations 40

5. Two-layer Models. 71

6. Conclusions 81

III MIXED BAROCLINIC-BAROTROPIC INSTABILITY IN TWO- AND THREE-LAYER MODELS. 86

1. Introduction. 87

2. The Two-layer Model 89

3. The Three-layer Model (Qualitative Results) 112

4. Baroclinic-barotropic Instability in the Three-layer Model (A numerical study) 124

5. Conclusions 141

IV OCEANIC APPLICATIONS. 150

1. Introduction. 151

2. Juan de Fuca Strait 153

3. The California Undercurrent off Vancouver Island. 169

4. Conclusions 193

V CONCLUDING DISCUSSION 195

REFERENCES CITED 205

APPENDIX (GLOSSARY OF SYMBOLS) 210

LIST OF TABLES

CHAPTER IV

Table 2.1: Properties of the most unstable wave found in the three-layer model of Juan de Fuca Strait 161

Table 3.1: Comparison of the instabilities found by Mysak (1977) and the corresponding instabilities found using the analogous three-layer model..... 181

Table 3.2: Properties of the most unstable wave corresponding to the system shown in figure 3.7 181

Table 3.3: Properties of the most unstable wave corresponding to the system shown in figure 3.8..... 188

Table 3.4: Properties of the most unstable waves found using two-layer models to study the stability of the upper layers of the California current system..... 192

LIST OF FIGURES

In this thesis, figure, table and equation numbers are local to each chapter. When a figure, table or equation is referred to which is found in a chapter other than the current one, the appropriate chapter is explicitly noted.

CHAPTER I

Figure 1.1: Different trajectories along which fluid elements are displaced in the discussion of baroclinic instability..... 6

Figure 1.2: The displacements of fluid elements through a velocity and vorticity distribution considered in the discussion of barotropic instability..... 9

CHAPTER II

Figure 2.1: A cross-section of the three-layer model studied here..... 18

Figure 4.1: Stability boundaries (a) for $H_1 = H_2 = H_3$, $\hat{T} = 0$, $\hat{\beta} = -6$ and first mode (m=1) dispersion curves corresponding to these parameter values with $F_2 = 1$ and $S_2 = -0.75$(b), 0.00(c), and 0.75(d)..... 45

Figure 4.2: Stability boundaries (a) for $H_1 = H_2 = H_3$, $\hat{T} = 0$, $\hat{\beta} = -3$ and first mode (m=1) dispersion curves corresponding to these parameter values with $F_2 = 1$ and $S_2 = -0.75$(b), 0.00(c), and 0.75(d). Statistics for positions of maximum growth rate (marked by plus signs in the figures) are given in the table. The signs of μ_{1_r} and μ_{3_r} are given in brackets following δ_1 and δ_3 respectively... 46

Figure 4.3: As in figure 4.2 with $\hat{\beta} = 0$. Also shown in part (a) is the corresponding result of Davey (1977). (broken curve).....47

Figure 4.4: As in figure 3 with $\hat{\beta} = 6$.....48

Figure 4.5: As in figure 3 with $\hat{\beta} = 12$.....49

Figure 4.6: Stability boundaries (a) for $H_1 = H_2 = H_3$, $\hat{T} = -30$, $\hat{\beta} = 0$ and first mode (m=1) dispersion curves corresponding to these parameter values with $F_2 = 1$ and $S_2 = -0.75$ (b), 0.00 (c), and 0.75 (d). Statistics for positions of maximum growth rate (marked by plus signs) are given in the table in order of increasing k.....51

Figure 4.7: As in figure 7 with $\hat{T} = -10$.....52

Figure 4.8: As in figure 7 with $\hat{T} = -5$.....53

Figure 4.9: As in figure 7 with $\hat{T} = 0$.....54

Figure 4.10: As in figure 7 with $\hat{T} = 5$.....55

Figure 4.11: As in figure 7 with $\hat{T} = 10$.....56

Figure 4.12: As in figure 7 with $\hat{T} = 30$.....57

Figure 4.13: Stability boundaries (a) for $H_1/H_2 = 0.5$, $H_3/H_2 = 1$, $\hat{T} = 0$, $\hat{\beta} = 0$ and first mode (m=1) dispersion curves corresponding to these parameter values with $F_2 = 1$ and $\delta_2 = -0.75$(b), 0.00(c), and 0.75(d). Statistics for positions of maximum growth rate (marked by plus signs) are given in the table.....61

Figure 4.14: As in figure 14 with $H_1/H_2 = 1$, $H_3/H_2 = 1$.....62

Figure 4.15: As in figure 14 $H_1/H_2 = 5$, $H_3/H_2 = 1$. Values are given in order of increasing k.....63

Figure 4.16: As in figure 14 with $H_1/H_2 = 1$, $H_3/H_2 = 0.5$. Values are given in order of increasing k.....64

Figure 4.17: As in figure 14 with $H_1/H_2 = 1$, $H_3/H_2 = 1$..... 65

Figure 4.18: As in figure 14 with $H_1/H_2 = 1$, $H_3/H_2 = 5$..... 66

Figure 5.1: A cross-section of the two-layer model obtained by letting $H_2 \to 0$..... 72

Figure 5.2: Dispersion curves for the first mode (m=1) for $S_1 = 1$, $f_o = 10^{-4}\ s^{-1}$, $\beta = 0$, T = -10, L = 10 km, $g' = 0.02\ m\ s^{-2}$, $H_T = 180$ m and $H_1 = H_3 = (H_T - H_2)/2$ for (a) $H_2 = 60$ m, (b) $H_2 = 6$m, and (c) $H_2 = 10^{-5}$ m..... 73

Figure 5.3: A cross-section of the two-layer model obtained by letting $H_1 \to 0$..... 76

Figure 5.4: Dispersion curves for the first mode (m=1) for $S_2 = 1$, $f_o = 10^{-4}\ s^{-1}$, $\beta = 0$, T = -10, L = 10 km, $g' = 0.02\ m\ s^{-2}$, H_T=180 m, and $H_2 = H_3 = (H_T - H_1)/2$ for (a) $H_1 = 60$ m, (b) $H_1 = 6$ m, and (c) $H_1 = 10^{-5}$ m..... 77

Figure 5.5: A cross-section of the two-layer model obtained by letting $H_3 \to 0$..... 80

Chapter III

Figure 2.1: (a) Mean potential vorticity gradients in the upper layer (solid line) and the lower layer (dashed line). (b) Complex amplitude for the stream function in the upper layer ($\phi_2 \simeq 0$).(c) Transfer of Available Potential Energy (T.A.P.E.). (d) Transfer of Kinetic Energy (T.K.E.) in the upper layer. Since $\phi_2 \simeq 0$, the transfer in the lower layer is very small. $f_o=10^{-4}$, $\beta=0$, L=57.735 km, g'=0.66 ms^{-2}, $H_1=H_2=$ 5 km ($F_1=F_2=0.01$), $U_1=$ 1-cos¶(y+1), $U_2=-U_1$..... 93

Figure 2.2: Stability boundary corresponding to the parameter values $f_o=10^{-4}s^{-1}$, $\beta=1.5$, L=1,000 km, g'=0.66 ms^{-2}, $H_1=H_2=5$ km ($F_1=F_2=3$), $U_1=U_0$(1-cos¶(y+1), $U_2=0$..... 96

Figure 2.3: Stability boundary corresponding to the parameter values $f_o=10^{-4}s^{-1}$, $\beta=0.0$, L=1,000 km, g'=0.66 ms^{-2}, $H_1=H_2=5$ km, ($F_1=F_2=3$), $U_1=U_2=U_0$(1-cos¶(y+1)..... 97

Figure 2.4: Approximate stability boundaries in ε vs. k space for the two-layer model with parameter values: $f_o=10^{-4}s^{-1}$, $\beta=0.0$, L=2,000 km, g'=0.66 ms^{-2}, $H_1=H_2=5$ km ($F_1=F_2=12$), $U_1=$1-cos¶(y+1), $U_2=\varepsilon U_1$. Also shown here is the stability boundary appropriate to $(L/r_i)^2 \ll 1$ (dashed line). Note: these boundaries are qualitative and details should not be taken seriously..... 99

Figure 2.5: (a) Mean potential vorticity gradients in the upper layer (solid line) and lower layer (dashed line). (b) Transfer of available potential energy. (c) Transfer of kinetic energy in the upper layer (≃transfer in the lower layer which is indicated by a dashed line in this and future figures). (d) Compex amplitude of the stream function in the upper layer. (e) Complex amplitude of the stream function in the lower

layer. Parameter values as in figure 2.4; ε=-1.0, k=1.5..... 101

Figure 2.6: As in figure 2.5 but ε=-0.5..... 102

Figure 2.7: As in figure 2.5 but ε=0.0..... 103

Figure 2.8: As in figure 2.7 - a second significant instability at the same position in parameter space..... 104

Figure 2.9: As in figure 2.9 but ε=0.5..... 106

Figure 2.10: As in figure 2.9 - a second significant instability at the same position in parameter space..... 107

Figure 2.11: (a) q_{1y} ($\equiv q_{2y}$) (b) T.K.E. (T.A.P.E.$\equiv$0) (c) ϕ_1($\equiv\phi_2$). Parameter values as in figure 2.4; ε=1.0, k=1.5..... 108

Figure 2.12: Parameter values as in figure 2.4; k=3.5, ε=0.0..... 110

Figure 2.13: Parameter values as in figure 2.4; k=3.5, ε=0.5..... 111

Figure 4.1: Approximate stability boundaries in ε vs. k space for the three layer model. $f_o=10^{-4}s^{-1}$, β=0.0, g'=1.0 ms^{-2}, $H_1=H_2=H_3$= 3333.33 m; L=57.735 km - approximately vertical line; L=1,000 km - dashed line; L=2,000 km -solid line..... 126

Figure 4.2: (a) The mean potential vorticity gradient in the upper layer (solid line); the middle layer (long dashes); the lower layer (short dashes). (b) Transfer of available potential energy due to shear between the upper layers (solid line) and that due to shear between the lower layers (dashed line). (c) The transfer of kinetic energy in the upper layer (solid line) and in the middle layer (dashed line). The transfer in the bottom layer is zero since $U_3\equiv$0. (d) The compex amplitude for the stream function in the upper layer.

(e) The compex amplitude for the stream function in the middle layer.

(f) The complex amplitude for the stream function in the bottom layer.

$f_o=10^{-4}s^{-1}$, $\beta=0.0$, L=1,000 km, $g'=1.00\ ms^{-2}$, $H_1=H_2=H_3=3333.33$ m ($F_1=F_2=F_3=3$), $U_1=1-\cos\pi(y+1)$, $U_2=\varepsilon U_1$; $\varepsilon=0.5$..... 129

Figure 4.3: As in figure 4.2 but L=2,000 km..... 130

Figure 4.4: As in figure 4.2 - the instability at larger k..... 131

Figure 4.5: As in figure 4.3 - the instability at larger k..... 132

Figure 4.6: As in figure 4.2 but $\varepsilon=0.75$..... 133

Figure 4.7: As in figure 4.2 but L=2,000 km, $\varepsilon=0.75$..... 135

Figure 4.8: As in figure 4.7..... 136

Figure 4.9: As in figure 4.6..... 138

Figure 4.10: As in figure 4.10 but L=2,000 km, $\varepsilon=1.0$..... 139

Chapter IV

Figure 2.1: (top) Juan de Fuca Strait and nearby geographical features. (bottom) Juan de Fuca Strait with positions at which Fissel's data (•) and one section of Cannon and Laird's data (x) were collected. (from Cannon and Laird, 1978) 154

Figure 2.2: The cross-section of Juan de Fuca Strait at which Fissel's data were collected. Numbers above each station are used to indicate the station considered in figure 2.5. Along-channel velocities are given in cm s^{-1}. The dashed line indicates the topography used in the model of the strait. (from Fissel, 1976) 155

Figure 2.3: The mean density profile on June 14-15, 1975 across the section at which Fissel's data was collected (from Fissel and Huggett, 1976)..... 156

Figure 2.4: Along-channel total-record average currents (cm/sec.) through the cross-section marked by x's in figure 2.1 (from Cannon and Laird, 1978) 157

Figure 2.5: The power spectral density of the residual currents for the current meter stations of Fissel (1976). Stations 130-136 are shown in figure 2.2 and station 137 is the additional station a few kilometers to the west of Sheringham Point seen in figure 2.1 (bottom). (from Fissel, 1976)..... 159

Figure 2.6: (a) Approximation to the mean currents used to model Juan de Fuca Strait; (b) the mean potential vorticity gradients corresponding to the three layers of our model: upper layer-solid line, middle layer-long dashes, lower layer-short dashes; (c) the eigenfunction corresponding to the most unstable wave in the model; (d) the transfer of available potential energy corresponding to this wave: the solid line corresponds to the transfer of energy due to the shear between the upper layers and the dashed line to that due to the shear between the lower layers; (e) the transfer of kinetic energy for this wave: solid line corresponds to the upper layer, long dashed line to the middle layer and the short dashed line to the bottom layer. 160

Figure 3.1: Enhanced infrared image of sea surface showing spatial structure of surface temperature on 10 September, 1975 off the west coast of British Columbia and Washington. The dark areas are warm water and the grey-white, cold water (after Gower and Tabata, 1976)..... 171

Figure 3.2: Geopotential topography (dyn m) of the 10, 150, 300 and 500 db surfaces (referred to 1000 db), 7-20 Septebmer, 1973. Open circles refer to time-series stations. The 100 and 500 fathom (1 fathom = 1.829m.) isobaths are also shown (from Reed and Halpern, 1976)..... 172

Figure 3.3: The two-layer model studied by Mysak (1977)..... 174

Figure 3.4: Temperature, salinity and σ_t profiles, 10 September, 1973, at 49°N, 127° 19'W (right-hand open circle in top line of time series stations shown in Fig. 3.2). (from Holbrook, 1975) 176

Figure 3.5: Isobaths (m) off Vancouver Island and Washington. Topographic cross-sections at lines A - E are plotted in figure 3.6. (from Mysak, 1977) 178

Figure 3.6: Topographic cross-sections at lines A - E shown in figure 3.4. (from Mysak, 1977). 179

Figure 3.7: The three-layer, channel model analogous to the two layer model of Mysak (1977)..... 180

Figure 3.8: The extension of the channel model to include effects of horizontal shear and reduce the influence of the artificially imposed western boundary. 182

Figure 3.9: Graph of c_r (non-dimensional phase speed) in the wave-number range $k = 0 - 5$ (wavelength = ∞ - 47.1 km) for the first two cross-channel modes. The unstable regions corresponding to those studied by Mysak (1977) are labelled as such. The position at which the most unstable wave is found is indicated by a plus sign..... 183

Figure 3.10: Transfer of available potential energy (in arbitrary units) corresponding to the most unstable 1st mode instability analogous to that considered by Mysak (1977). The position of this wave in figure 3.9 is marked by a circle. (The solid line corresponds to the transfer of energy due to the shear between the upper layers and the dashed line to that due to the shear between the lower layers) 185

Figure 3.11: Transfer of available potential energy corresponding to the most unstable wave found using the three-layer model (plus sign in Fig. 3.9) (The solid line corresponds to the energy transfer due to the shear between the upper layers and the dashed line to that due to the shear between the lower layers.) 185

Figure 3.12: (a) Approximation to the mean currents used to model the California undercurrent off Vancouver Island (see figure 3.8); (b) The mean potential vorticity gradients corresponding to the three layers of our model: upper layer-solid line, middle layer-long dashes, lower layer-short dashes; (c) The Eigenfunctions corresponding to the most unstable wave in our model; (d) the transfer of available potential energy corresponding to the above wave; (e) The transfer of kinetic energy in the three layers. (see figure 2.7 for the meaning of the different lines in (d) and (e).) 187

ACKNOWLEDGEMENTS

Although discussions with many people have contributed to the work presented in this thesis, I am particularly grateful to Dr. Lawrence Mysak for his efforts as my thesis supervisor. His encouragement, enthusiasm, interest, and good advice through every aspect of the preparation of this thesis have been practically unlimited and are greatly appreciated. I would also like to thank Drs. Paul LeBlond, Robert Miura, and Steve Pond for their helpful criticisms of a preliminary draft of this thesis.

The financial support of the National Research Council of Canada through a post-graduate scholarship, and that of the University of British Columbia through a teaching assistantship are also gratefully acknowledged. In particular it is a pleasure to express my gratitude to the Department of Mathematics for affording me the opportunity to proofread the book "Waves in the Ocean" by P.H. LeBlond and L.A. Mysak.

Finally, I would like to thank my wife, Donna, my good friend, Dan Frail, and my parents, Fred and Connie, for their encouragement, without which this work may never have been undertaken, let alone completed.

CHAPTER I

INTRODUCTION

Introduction

This chapter is designed to introduce the uninitiated to the processes of baroclinic and barotropic instability, and briefly outline the contributions made in this thesis. Our introduction will be brief and draws heavily on the references cited here.

The ocean basins are filled with a slightly compressible fluid subjected to the influences of the earth's rotation and gravity, as well as atmospheric forces. Of the many types of waves which exist in such a system (see LeBlond and Mysak, 1978) we are concerned with the free, low-frequency, quasi-geostrophic waves which exist due to an intrinsic instability in the system. Since the aspect ratio H/L, (H and L are vertical and horizontal scales for the motion) for such waves is generally much smaller than unity and the period is much longer than one day, it may be shown that vertical accelerations can be neglected relative to the acceleration due to the earth's gravity. The motions are thus in hydrostatic balance. Further since the length scale of density variations in the ocean is much larger than the vertical scale of motions, the continuity equation may be approximated by the incompressibility condition $\nabla \cdot \underline{u} = 0$. With exception of sound waves (which are filtered out under the assumption of incompressibility), this approximation is valid for most oceanic motions (see Phillips, 1969). Finally since the relative density variations are very small ($\sim 10^{-2}$ at most), their influence through the inertia and Coriolis accelerations are also small and can be neglected in these terms. These observations allow use of the Boussinesq approximation in which the actual density is replaced by a constant reference density exept when assoc-

iated with the gravity where a bouyancy force is introduced due to the density difference. This approximation may be shown to be valid if we have $N^2H/g \ll 1$ ($N^2=-(g/\rho_o)\partial\rho_o/\partial z$, where ρ_o is the potential density in the absence of motion), (see LeBlond and Mysak, 1978,p.15; and Pond and Pickard, 1978, chapter 5, for methods used to calculate N^2 in practice). LeBlond and Mysak have also given a detailed derivation of the β-plane equations in which the natural spherical coordinate system of the earth is approximated by a local cartesian coordinate system. It is readily seen from their derivation that these equations are valid for H/L << L/R << 1 (R is the radius of the earth). For the motions under consideration here, these conditions are satisfied. In particular, for Juan de Fuca Strait, $H \leq 200$m, $L \sim 20$km ($H/L \leq 1 \times 10^{-2}$, $L/R \sim 3 \times 10^{-3}$)† and for the California Undercurrent, $H \leq 3$km, $L \sim 50$km ($H/L \leq 5 \times 10^{-4}$, $L/R \sim 8 \times 10^{-3}$). Finally the influence of the horizontal component of the earth's rotation (which I shall neglect) on long period waves has been considered by Needler and LeBlond (1973). The neglect of this effect is justified for H/L << 1.

The effect of viscosity on these motions will be assumed negligible. This assumption will generally be true for the initial growth of the perturbations if the Ekman number (ν/f_oH^2; ν is the kinematic [eddy] viscosity and f_o is twice the local vertical component of the earth's rotation) is small in

---

† It must be noted here that the condition H/L << L/R arises as a condition under which the horizontal component of the earths rotation is negligible. The actual condition is $\frac{wR}{uy} \ll 1$. Scaling w with U H/L, y with L, and u with U, we get the condition H/L << L/R which is only weakly satisfied for Juan de Fuca Strait. However, we will find that for the motions considered here, w should be scaled with R_o U H/L so that this condition may be replaced by R_o H/L << L/R (note that we still need H/L << 1 and L/R << 1) which is strongly satisfied in our applications.

comparison to the square of the Rossby number. However, for finite amplitude motions, this approximation will not, in general, be valid (see Pedlosky, 1970).

Finally, we assume a simple equation of state of the form

$$\rho = \rho_* (1 - \alpha T + \beta S) \tag{1.1}$$

where ρ_*, α, β are constants and T and S are the temperature and salinity respectively. Restricting our attention to motions whose time scales are sufficiently short that the diffusion of heat and salt may be neglected, the equations for the conservation of internal energy and salt (neglecting external sources) reduce to the statement that density is conserved for individual fluid elements. i.e.,

$$\frac{D\rho}{Dt} = 0. \tag{1.2}$$

Under the approximations made above, the governing equations reduce to equations (2.2), chapter II. These equations will be taken as the starting point for our analysis.

We shall now turn our attention to the question of where the growing perturbations obtain their energy from. To answer this question we shall consider the special cases of baroclinic and barotropic instabilities seperately.

Baroclinic Instability

We begin with a discussion of the "wedge of instability". The basis of this argument was presented by Fjørtoft (1951) and has since been repeated in various forms by several authors. The discussion

given here is largely a reproduction of work presented by Pedlosky (1971b) and Orlanski and Cox (1973) and is given here solely for the readers convenience.

Let $p_o=p_o(z)$ and $\rho_o=\rho_o(z)$ be the pressure and density in the absence of motion and let δp and $\delta\rho$ be the deviations from these values due to a mean flow, U(z), in the x-direction. Then, as we shall show in chapter II, if the Rossby number ($=U/f_oL$) is small relative to unity, the mean state will be in hydrostatic and geostrophic balance. Thus, under the Boussinesq approximation we have:

$$\rho_* f_o U = -\delta p_y$$

$$\delta p_z = -\delta\rho \cdot g$$

where subscripts y, and z indicate partial differentiation.

Eliminating the pressure we obtain:

$$\delta\rho_y = \rho_* f_o U_z/g$$

Hence the isopycnals have a slope given by:

$$\left(\frac{\partial z}{\partial y}\right)_\rho = -\frac{\rho_y}{\rho_z} \simeq -\frac{\delta\rho_y}{\rho_{oz}} = \frac{\rho_* f_o U_z}{-g\rho_{oz}} = f_o U_z/N^2$$

where we have used $\delta\rho/\rho_o \ll 1$ in the second equality and $N^2 = -g\rho_{oz}/\rho_*$ is the square of the Brunt-Väisälä frequency. Such a tilt of the isopycnals supplies a possible source of potential energy for the growth

of perturbations. To examine the possibility of a wave extracting energy from this mean state, we consider the consequences of interchanging fluid elements constrained to move in a plane along the various trajectories indicated in figure 1.1.

A fluid element displaced from A to A′ will find itself in a region of lighter fluid and thus will experience a downward restoring force proportional to the density difference. This fluid element will thus return to its original position and no instability results. (Note that the fluid element will generally overshoot its original position and oscillate about this position until the motion is damped out by viscous effects. This type of motion is essentially an internal gravity wave).

Fluid elements displaced in the plane through BB′ experience no restoring force along BB′ since gravity acts perpendicular to this plane. No instability may result from this interchange either.

Similarly a fluid element displaced in the plane DD′ feels no restoring force since all fluid elements in this plane are of equal density.

Finally, consider the interchange of fluid elements originally positioned at C and C′. The particle displaced from C to C′ finds itself in a region of lighter fluid and thus the effect of gravity tends to accelerate the fluid element beyond C′. Similarly the fluid element displaced from C′ to C experiences a bouyancy force lifting it

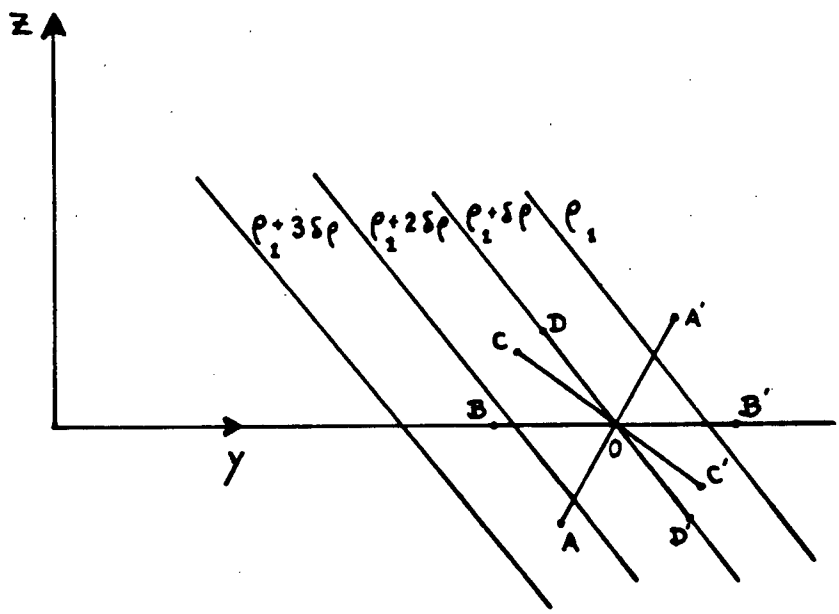

Figure 1.1: Different trajectories along which fluid elements are displaced in the discussion of baroclinic instability.

beyond C. Hence motions of this type (exchanging fluid between the wedges BOD and B′OD′) will be amplified. Note, however, that such an interchange of fluid elements results in a decrease in the potential energy of the system. This is the basic mechanism of baroclinic instability by which potential energy is released from the mean state to the perturbations. Further details of the nature of this type of instability may be found in Bretherton (1966b), Pedlosky (1971b), and Orlansky and Cox (1973).

Barotropic Instability

The basic mechanism of barotropic instability was described in 1945 by Lin. The presentation given here is simply a reproduction of part of Lin's paper and as in the previous section is given solely for the readers convenience. The argument is kept as simple as possible by considering wave perturbations to a horizontally sheared mean current in a homogeneous, inviscid fluid. Since the effect of the earth's rotation is not essential to the instability process, (This is not to say that the effects of rotation are negligible. Rather it is felt that the inclusion of rotation is not necessary to understand the nature of the instability.) we consider a two-dimensional parallel flow on a non-rotating plane.

Consider the interchange of fluid elements between lines L_1

and L_2, and lines L_3 and L_4 in figure 1.2. If one envisions the fluid as being full of vortex filaments, then when fluid elements are interchanged in an inviscid fluid, the fluid maintains its vorticity and the interchange of fluid elements implies the interchange of vortex filaments. Lin has shown that an element of fluid displaced in the y-direction (perpendicular to the direction of the mean flow) by the component v' of the perturbation velocity experiences an acceleration in the positive y-direction given by $\Gamma^{-1}\iint_{\text{fluid}} \left\{ v'(x\ y) \right\}^2 \zeta_o'(y)dxdy$, where $\zeta_o'(y)$ is the gradient of vorticity of the mean flow and $\Gamma = \iint_{\text{fluid}} \zeta'(\xi,\eta)\, d\xi d\eta$ is the strength of the superposed perturbation vortex (this restoring force is due to the distortion of the mean vorticity field). Now, consider the consequences of this acceleration on the fluid elements labelled a, b, c and d. The element a carries an excess of vorticity (relative to the surrounding fluid in its new position on L_1) with it so that $\Gamma > 0$. Since in this region $\zeta_o' < 0$, the fluid element experiences an acceleration in the negative y-direction thus restoring it to its original position. Similarly the fluid element b has $\Gamma < 0$ and $\zeta_o' < 0$ so this element experiences a positive acceleration and is also restored to its original position. Thus for the case in which fluid elements are <u>not</u> displaced across an extremum in the mean vorticity, the motion must be stable.

Now consider the forces acting on c after being displaced.

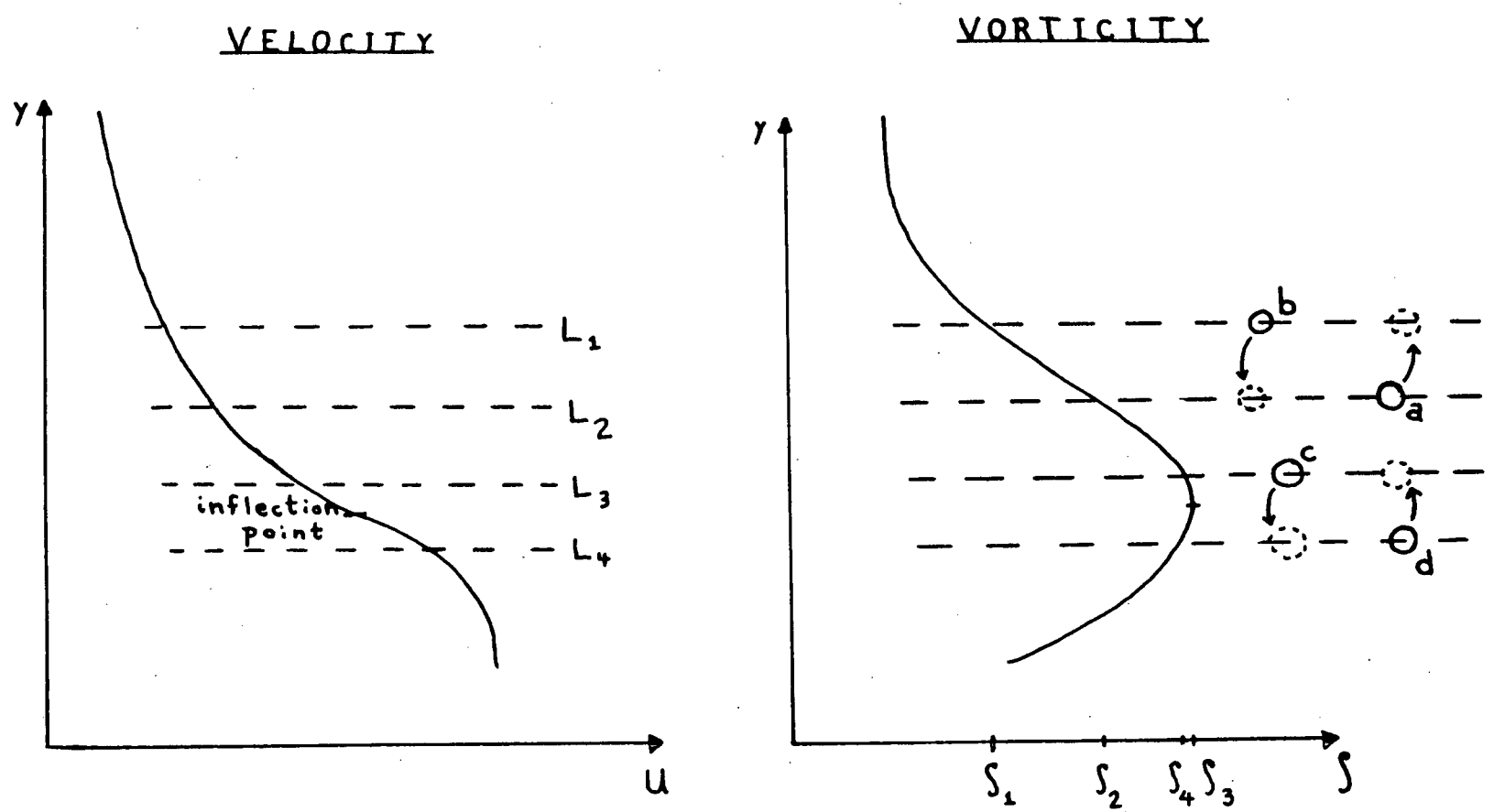

Figure 1.2: The displacements of fluid elements through a velocity and vorticity distribution considered in the discussion of barotropic instability.

Since ζ_o' changes sign between L_3 and L_4 the restoring force is clearly impaired by the presence of an inflection point in the mean velocity profile and if the integrated value of ζ_o' when weighted with v'^2 is of the opposite sign to Γ, the motion may actually be amplified. Thus, due to the conservation of vorticity following a fluid element a perturbation may under certain circumstances extract energy from the kinetic energy of the mean flow. This exchange of energy is, of course, only possible in the presence of a non-zero mean vorticity and, in particular, requires a local extremum in this quantity. The process by which this occurs is essentially the mechanism of barotropic instability. Further insight into this mechanism may be found in Lin (1945, Part II), Rossby (1949) and Brown (1972).

The physical arguments discussed here (for both baroclinic and barotropic instabilities) are unquestionably inadequate for a detailed investigation of the stability of a given system. A detailed study of the initial growth of wavelike disturbances to a given mean flow generally requires the solution of a singular non-separable partial differential equation (see Pedlosky 1964a, and chapter II).

In the literature several methods have evolved to study these equations. The earliest studies were made under the assumption that the mean state was either vertically or horizontally uniform. Under the assumption of vertical homogeneity the mechanism of baroclinic instability

is rendered inactive (see for example Kuo, 1949), and when the mean currents are assumed horizontally uniform, the mechanism of barotropic instability is rendered inactive (Charney, 1947; Eady, 1949; Fjørtoft, 1951). Probably the most natural extension of the study of pure baroclinic instability is the extension to include weak horizontal shears in which case the problem may be attacked using the WKB technique (Stone, 1969; Gent, 1974, 1975). Other important contributions have been made through the numerical integration of the governing equations (see for example Brown, 1969, Gill, et al, 1974), integral methods involving the use of generalized Green's functions (McIntyre, 1970), integral equations (Miles 1964a,b), and asymptotic methods (Miles, 1964 a,b,c,; Killworth, 1978). However, the most widely used method to study mixed baroclinic-barotropic instability is probably via the introduction of layered models in which the non-separable partial differential equation mentioned above is replaced by a system of n (where n is the number of layers) coupled, singular, ordinary differential equations. The study of layered models was initiated by Phillips (1951) who considered a two-layer model. This model has since been extensively studied, most notably by Pedlosky (1963, 1964 a,b,c; 1970, 1971a,b; 1972, 1974, 1975, 1976).

This thesis is mainly concerned with a model in which the density stratification is approximated by three layers. Davey (1977)

has studied pure baroclinic instability in a three-layer model similar to the two-layer model of Pedlosky. Here, on the other hand, we derive a three-layer model from the equations for a specialized continuously stratified fluid (see figure 1, chapter II). In deriving our equations from those appropriate to a continuously stratified fluid it is possible to circumvent one of the major difficulties in using layered models. That is, it is no longer necessary to "guess" (though an educated guess may be quite good) what the appropriate density differences between the layers should be. This choice is automatically built into the model when the actual density stratification is approximated by a simpler continuously stratified fluid.

The new three-layer model is then used to study the effects of density stratification, vertical curvature in the mean velocity profile, variation of the Coriolis parameter with latitude, bottom slopes and relative layer thicknesses, all in the absence of horizontal shear. A brief discussion of the limiting cases of two-layer models is then given. In chapter III a detailed study of mixed baroclinic-barotropic instability in two- and three-layer models is made, and in chapter IV, two case studies are considered. Further introductory comments on each of these studies may be found in an introductory section at the beginning of each chapter. Finally, some general concluding remarks are made in chapter V.

CHAPTER II

BAROCLINIC INSTABILITY AND CONSTANT BOTTOM SLOPE

1. Introduction

As discussed in the previous chapter, baroclinic instability is the process by which the kinetic energy of a quasi-geostrophic disturbance may increase with time by extracting energy from the available potential energy of the mean state, and barotropic instability is the process by which perturbations may extract energy from the kinetic energy made available by horizontal shear in the mean currents. One method of simplifying the study of baroclinic (or mixed baroclinic-barotropic) instability is to consider layered models. That is, one considers two or more layers of fluid, each of uniform but different densities, lying one above the other. In this way the essential dynamics of the baroclinic problem are retained while the possible modes of propagation are reduced to a small number. Most of the earlier work has been with two-layer models (see for example Pedlosky, 1963,1964a,b,c) but some work has recently been done on three-layer models. Holmboe (1967) has generalized Eady's baroclinic model of the atmosphere with constant entropy gradient to a vertically symmetric three-layer model with constant entropy gradient in each layer and Davey (1977) has generalized the two-layer model of Phillips (1951) to a three-layer model with each layer of uniform but different density.

By introducing density discontinuities, the usual layered models overemphasize the stabilizing influence of density stratification which must be compensated for by decreasing the density difference between successive layers in the model. By approximating a continuously stratified model with specialized density profile, this thesis attempts to make use of the simplifications of the layered approach without introducing discontinuities in density and velocity profiles.† The motivation for considering such a density profile is the desire to model situations in which the transition of density from its surface value to its value at depth occurs gradually. Such a situation occurs in Juan de Fuca Strait which is the subject of Chapter IV, Section 2 of this thesis.

The baroclinic problem for flows over constant slope topography is considered in this chapter. Later chapters are concerned with the combined case of mixed baroclinic-barotropic instability in the presence of more realistic topography.

† Following the completion of this thesis (October 30, 1978) it was brought to my attention that the choice of density stratification employed here had been considered earlier by Savithri Narayanan (1973). Her approach to the problem was, however, very different than that taken here. Emphasis is placed on the study of free waves and the study of pure baroclinic instability in the absence of vertical curvature in the middle layer (a case which we shall find to be rather more stable than the more general case including vertical curvature in this layer). No side walls are included so that the model is directly applicable to studies of the open ocean. For the case of no horizontal shear in the mean currents it is found that by transforming to density coordinates the continuously stratified problem is made analytically tractable and it is the resulting analytical solutions which are studied.

In section 2 of this chapter, the stability problem is formulated for a channel flow with mean velocities containing both horizontal and vertical shear under the assumption that the Rossby number is small. Section 3 is concerned with the study of small perturbations propagating on a steady mean flow. Necessary conditions for instability are discussed and an analytic solution is found for the strictly baroclinic problem in the presence of small, constant bottom slope. In section 4 some general results concerning parameter variations are discussed and in section 5 two-layer models are considered as limiting cases. Finally a brief summary of the results of this chapter is given in section 6.

2. Formulation

We will formulate the stability problem for quasi-geostrophic disturbances of oceanic channel flows containing both vertical and lateral shear. The beta effect is included but the fluid is assumed inviscid and non-diffusive. The basic state density stratification is modelled by three layers with upper and lower layers of constant densities ρ_1^* and ρ_3^* respectively ($\rho_1^*<\rho_3^*$) and a middle layer whose density varies linearly from ρ_1^* to ρ_3^* (Figure 2.1). This choice of density stratification is convenient as well as being a reasonable approximation to many real situations. The basic state density stratification is thus given by:

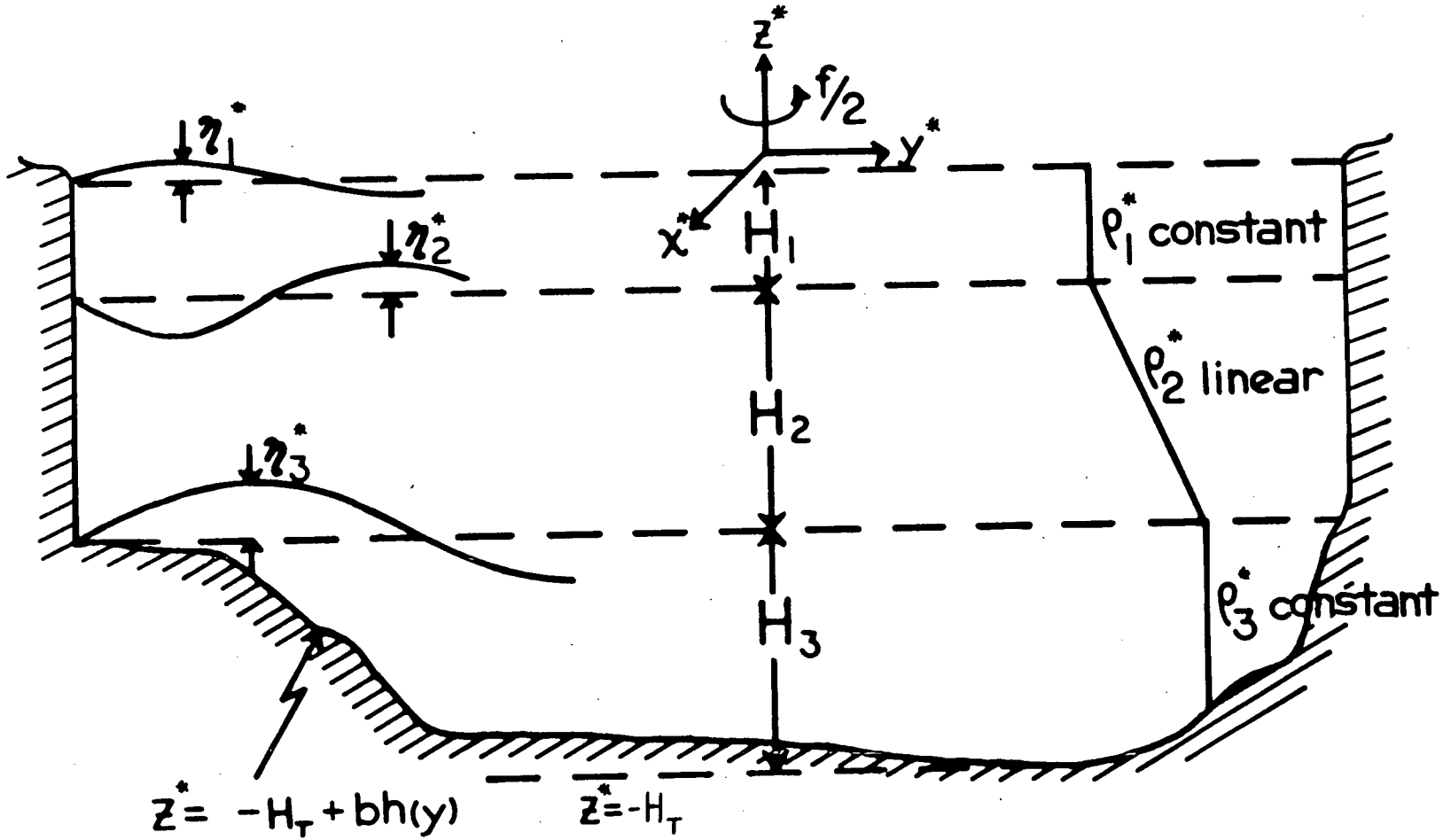

Figure 2.1: A cross-section of the three-layer model studied here.

$$\rho^* = \begin{cases} \rho_1^* & -H_1 < z^* \le 0 \\ \rho_2^* = \rho_1^* + \left(\dfrac{z^* + H_1}{H_2}\right)(\rho_1^* - \rho_3^*) & -H_1 - H_2 \le z^* \le -H_1 \\ \rho_3^* & -H_T + bh \le z^* < -H_1 - H_2 \end{cases} \tag{2.1}$$

H_1, H_2 and H_3 are the thicknesses of the upper, middle and lower layers in a state of no motion, $H_T = H_1 + H_2 + H_3$, and bh is the height of the bottom above $z^* = -H_T$ (b is a typical amplitude of the topographic variations). *'s are used to indicate dimensional variables.

We choose our coordinate system such that $y^* = 0$ is at the centre of the channel, with y^* increasing to the north, x^* points along the channel to the east and z^* is vertical with $z^* = 0$ as the position of the free surface in the absence of motion. If the effect of β is negligible the orientation of the x^*, y^* axis in the horizontal plane may, of course, be varied.

Under the hydrostatic approximation, the equations of motion for an inviscid, incompressible, non-diffusive fluid on the β-plane are:

$$\begin{aligned}
&\text{(a)} \quad u^*_{t^*} + u^*u^*_{x^*} + v^*u^*_{y^*} + w^*u^*_{z^*} = -p^*_{x^*}/\rho^* + fv^* \\
&\text{(b)} \quad v^*_{t^*} + u^*v^*_{x^*} + v^*v^*_{y^*} + w^*v^*_{z^*} = -p^*_{y^*}/\rho^* - fu^* \\
&\text{(c)} \quad p^*_{z^*} = -\rho^* g \\
&\text{(d)} \quad u^*_{x^*} + v^*_{y^*} + w^*_{z^*} = 0 \\
&\text{(e)} \quad \rho^*_{t^*} + u^*\rho^*_{x^*} + v^*\rho^*_{y^*} + w^*\rho^*_{z^*} = 0
\end{aligned} \tag{2.2}$$

Where (u^*, v^*, w^*) is the velocity of the fluid, p^* is the total pressure and ρ^* the density.

We now introduce the following nondimensional (unstarred) variables:

$$
\begin{aligned}
&\text{(a)} \quad (x^*,y^*) = L(x,y) \\
&\text{(b)} \quad z^* = Hz \\
&\text{(c)} \quad (u^*,v^*) = U(u,v) \\
&\text{(d)} \quad w^* = (UH/L)w \\
&\text{(e)} \quad t^* = (L/U)t \\
&\text{(f)} \quad f = f_o + \beta^* y^* = f_o(1+\beta R_o y) \; ; \quad \beta^* = \beta(U/L^2) \\
&\text{(g)} \quad p^* = p_o^*(z) + \rho_3^* U f_o L p \\
&\text{(h)} \quad \rho^* = \rho_o^*(z) + \rho_3^* R_o \left(\frac{f_o^2 L^2}{gH}\right)\rho
\end{aligned}
\tag{2.3}
$$

where $p_o^*(z)$ and $\rho_o^*(z)$ are the pressure and density in the state of no motion, U and L are typical horizontal velocity and length scales, H is a vertical scale ($= H_T$ say), and $R_o (= U/f_o L)$ is the Rossby number which we shall assume to be small.

Making these substitutions into (2.2), and invoking the Boussinesq approximation, we have:

$$
\begin{aligned}
&\text{(a)} \quad R_o(u_t+uu_x+vu_y+wu_z) = -p_x + v(1+R_o\beta y) \\
&\text{(b)} \quad R_o(v_t+uv_x+vv_y+wv_z) = -p_y - u(1+R_o\beta y) \\
&\text{(c)} \quad p_{oz}^* = -\rho_o^* gH \; , \quad p_z = -\rho \\
&\text{(d)} \quad u_x + v_y + w_z = 0 \\
&\text{(e)} \quad \rho_{oz}^* w = -\rho_3^* R_o \left(\frac{f_o^2 L^2}{gH}\right)[\rho_t+u\rho_x+v\rho_y]
\end{aligned}
\tag{2.4}
$$

Now expressing each of the dependent variables as a power series expansion in R_o, e.g. $p = \sum_{n=0}^{\infty} R_o^n p^{(n)}$, we find to lowest order in R_o:

$$\begin{aligned}
&(a)\quad v^{(0)} = p_x^{(0)} \\
&(b)\quad u^{(0)} = -p_y^{(0)} \\
&(c)\quad p_{oz}^* = -\rho_o^* gH \qquad p_z^{(0)} = -\rho^{(0)} \\
&(d)\quad w_z^{(0)} = 0
\end{aligned} \tag{2.5}$$

(Note that $p^{(0)}$ is a stream function for the zeroth order problem.) Now, since fluid elements on the surface (at $z^* = \eta_1^*$; see figure 2.1) remain there, we have:

$$\frac{D}{Dt^*}(z^* - \eta_1^*) = 0 \quad .$$

at the surface. We now scale η_1^* by:

$$\eta_1^* = H_1 R_o \frac{f^2 L^2}{g H_1} \eta_1 \quad .$$

This choice of scaling is consistent with (2.3g) and the hydrostatic approximation. Thus in terms of the non-dimensional variables we have:

$$w\Big|_{\text{surface}} = R_o \frac{f^2 L^2}{gH} \left[\left(\frac{\partial}{\partial t} + u^{(0)} \frac{\partial}{\partial x} + v^{(0)} \frac{\partial}{\partial y} \right) \eta_1^{(0)} \right] \Bigg|_{\text{surface}}$$

Expanding w in a power series in R_o and using $\frac{f^2 L^2}{gH} << 1$ (this condition states that the external Rossby radius of deformation is much greater than the channel width and is valid in many oceanic applications), we thus have:

$$w^{(0)} = w^{(1)} = 0$$

at the surface. Combined with (2.5d), $w^{(0)} = 0$ at the surface gives $w^{(0)} \equiv 0$, while $w^{(1)} = 0$ at the surface is the basis of the rigid lid approximation.

To the next order in R_o we have:

$$
\begin{aligned}
&\text{(a)} \quad u_t^{(0)} + u^{(0)}u_x^{(0)} + v^{(0)}u_y^{(0)} = -p_x^{(1)} + v^{(1)} + v^{(0)}\beta y \\
&\text{(b)} \quad v_t^{(0)} + u^{(0)}v_x^{(0)} + v^{(0)}v_y^{(0)} = p_y^{(1)} - u^{(1)} - u^{(0)}\beta y \\
&\text{(c)} \quad u_x^{(1)} + v_y^{(1)} + w_z^{(1)} = 0 \\
&\text{(d)} \quad \rho_{oz}^* w^{(1)} = -\rho_3^* \left(\frac{f_o^2 L^2}{gH}\right)\left[\rho_t^{(0)} + u^{(0)}\rho_x^{(0)} + v^{(0)}\rho_y^{(0)}\right]
\end{aligned}
\tag{2.6}
$$

Cross-differentiating (2.6 a,b) and using (2.6c) gives:

$$
\left(\frac{\partial}{\partial t} + u^{(0)}\frac{\partial}{\partial x} + v^{(0)}\frac{\partial}{\partial y}\right)\left[\overline{v_x^{(0)}} - \overline{u_y^{(0)}} + \overline{\beta y}\right] = w_z^{(1)} \tag{2.7}
$$

(2.1), (2.5), (2.6d) and (2.7) are the basic equation for the following analysis. These equations shall now be used to derive a consistent approximation to the continuously stratified flow which has three degrees

of freedom in the vertical. In the following work a subscript will be used to denote which of the three layers of fluid defined by (2.1) is being considered.

Since ρ^* is constant in the upper and lower layers, $\rho_1^{(0)} = \rho_3^{(0)} = 0$ and hence from (2.5) $u^{(0)}$ and $v^{(0)}$ are depth independent in these layers. Hence we may immediately integrate (2.7) over these layers. Using $w^{(1)} = 0$ at the surface and requiring the vertical velocity to be continuous across the interface between the layers, we have:

$$\left[\frac{\partial}{\partial t}+u_1^{(0)}\frac{\partial}{\partial x}+v_1^{(0)}\frac{\partial}{\partial y}\right][v_{1\,x}^{(0)}-u_{1\,y}^{(0)}+\beta y] = -\frac{H}{H_1}\,w_2^{(1)}\Big|_{z^*=-H_1+\eta_2^*} \tag{2.8}$$

where η_2^* is as shown in figure 2.1.

Using (2.6d) and (2.1) $w_2^{(1)}$ may be expressed as:

$$w_2^{(1)} = -\left(\frac{H_2}{H}\right)^2 F_2\left[\frac{\partial}{\partial t}+u_2^{(0)}\frac{\partial}{\partial x}+v_2^{(0)}\frac{\partial}{\partial y}\right]p_{2\,z}^{(0)} \tag{2.9}$$

where $F_2 = f_o^2L^2/g'H_2$, $g' = \left(\frac{\rho_3^*-\rho_1^*}{\rho_3^*}\right)g$.

Using this expression in (2.8) and using (2.5a,b) we have:

$$\left(\frac{\partial}{\partial t}-p_{1\,y}^{(0)}\frac{\partial}{\partial x}+p_{1\,x}^{(0)}\frac{\partial}{\partial y}\right)\left[\nabla_H^2 p_1^{(0)}+\beta y-\frac{H}{H_1}\left(\frac{H_2}{H}\right)^2 F_2 p_{2\,z}^{(0)}\Big|_{z^*=-H_1+\eta_2^*}\right] = 0 \tag{2.10}$$

From (2.7) and (2.9) the equation for the second layer is simply:

$$\left(\frac{\partial}{\partial t} - p_{2\,y}^{(0)}\frac{\partial}{\partial x} + p_{2\,x}^{(0)}\frac{\partial}{\partial y}\right)\left[\nabla_H^2 p_2 + \beta y + \left[\frac{H_2}{H}\right]^2 F_2 p_{2zz}^{(0)}\right] = 0 \qquad (2.11)$$

Finally integrating over the depth of the lower layer, using the fact that the vertical velocity is continuous across the upper surface of the layer and that particles on the bottom remain on the bottom (this gives $w_3^{(1)} = \left\{\frac{\partial}{\partial t} + u_3^{(0)}\frac{\partial}{\partial x} + v_3^{(0)}\frac{\partial}{\partial y}\right\}\frac{bh}{R_o H}$) we have:

$$\left(\frac{H_3 - bh}{H_3}\right)\left(\frac{\partial}{\partial t} - p_{3\,y}^{(0)}\frac{\partial}{\partial x} + p_{3\,x}^{(0)}\frac{\partial}{\partial y}\right)[\nabla_H^2 p_3^{(0)} + \beta y]$$

$$+ \left(\frac{\partial}{\partial t} - p_{3\,y}^{(0)}\frac{\partial}{\partial x} + p_{3\,x}^{(0)}\frac{\partial}{\partial y}\right)\left[\frac{\overline{b}}{R_o H_3}\, h + \frac{H_2}{H} F_3 p_{2\,z}^{(0)}\Big|_{z^* = -H_1 - H_2 + \eta_3^*}\right] = 0 \qquad (2.12)$$

Appropriate boundary conditions are that each of the stream functions $p_i^{(0)}$ (i=1,2,3) remain constant on the boundaries of the channel. Taking L to be the half channel width, the boundary conditions are:

$$\frac{\partial p_i^{(0)}}{\partial x} = 0 \quad \text{on} \quad y = \pm 1 \quad (i=1,2,3) \qquad (2.13)$$

We now expand $p_2^{(0)}$ in a power series about the middle of the second layer

$$p_2^{(0)} = \sum_{n=0}^{\infty} \gamma_n (z - z_m)^n \quad \text{with} \quad z_m = (-H_1 - \frac{H_2}{2})/H \qquad (2.14)$$

The procedure is now to assume that the first few terms in this series give a reasonable approximation to $p_2^{(0)}$. From the work done on

continuous models it appears that the most unstable waves have a relatively simple vertical structure (e.g. see Gill, et al; 1973, §6) and hence this approximation may be reasonable (provided, of course, that the mean currents also have a simple vertical structure). A second problem in using this approach is the neglect of possible critical layers. However as pointed out by Bretherton (1966a), it appears from the work of Green (1960) that the growth rates of unstable waves associated with critical layers (which are not found using the crude layered theory) are markedly smaller than those which are found using the layered model. Hence, provided the critical layers do not play a crucial role in the dynamics of the flow, the filtering out of critical layers should not cause significant errors.

Now, neglecting terms of order $\left(\frac{H_2}{2H}\right)^3$ in (2.10) and (2.12) and satisfying (2.11) exactly at the middle of the layer the following equations are derived.

$$\left(\frac{\partial}{\partial t} - \psi_{1y}\frac{\partial}{\partial x} + \psi_{1x}\frac{\partial}{\partial y}\right)\left[\nabla_H^2\psi_1 + \beta y - F_1(3\psi_1 - 4\psi_2 + \psi_3)\right] = 0$$

$$\left(\frac{\partial}{\partial t} - \psi_{2y}\frac{\partial}{\partial x} + \psi_{1x}\frac{\partial}{\partial y}\right)\left[\nabla_H^2\psi_2 + \beta y + 4F_2(\psi_1 - 2\psi_2 + \psi_3)\right] = 0 \qquad (2.15)$$

$$\left(\frac{H_3 - bh}{H_3}\right)\left(\frac{\partial}{\partial t} - \psi_{3y}\frac{\partial}{\partial x} + \psi_{3x}\frac{\partial}{\partial y}\right)\left[\nabla_H^2\psi_3 + \beta y\right]$$

$$+ \left(\frac{\partial}{\partial t} - \psi_{3y}\frac{\partial}{\partial x} + \psi_{3x}\frac{\partial}{\partial y}\right)\left[\frac{\overline{b}}{R_o H_3}\,h - F_3(\psi_1 - 4\psi_2 + 3\psi_3)\right] = 0$$

where $\psi_1 = p_1^{(0)} = p_2^{(0)}\Big|_{z=-H_1/H} = \gamma_o + \gamma_1\left[\frac{H_2}{2H}\right] + \gamma_2\left[\frac{H_2}{2H}\right]^2 + O\left[\left[\frac{H_2}{2H}\right]^3\right]$

$\psi_2 = p_2^{(0)}\Big|_{z=z_m} = \gamma_o$

$\psi_3 = p_3^{(0)} = p_2^{(0)}\Big|_{z=-(H_1+H_2)/H} = \gamma_o - \gamma_1\left[\frac{H_2}{2H}\right] + \gamma_2\left[\frac{H_2}{2H}\right]^2 + O\left[\left[\frac{H_2}{2H}\right]^3\right]$

and $F_i = f_o^2 L^2/g'H_i \qquad (i=1,2,3)$

Appropriate boundary conditions are:

$$\frac{\partial \psi_i}{\partial x} = 0 \quad \text{on} \quad y = \pm 1 \quad (i=1,2,3)$$

(Note that neglecting bh in $(H_3-bh)/H_3$ is valid if $bh \ll H_3$ since this causes only a negligible perturbation to the equations. However, if $bh \sim H_3$ then provided $u_3^{(0)}\cdot\nabla_H h \ll R_o$ is satisfied (so that (2.2) is valid), it is more accurate to retain this term. Since we will consider only variations in h across the channel, the condition $u_3^{(0)}\cdot\nabla_H h \ll R_o$ for $h \sim H_3$ is satisfied if $v_3^*/U \ll R_o$.)

The corresponding equations for a fluid with three layers of uniform densities ρ_1^*, ρ_2^* and ρ_3^* ($\rho_2^* = (\rho_1^*+\rho_3^*)/2$) have been given by Davey (1977). [When comparing this paper with Davey's it is important to note that where we have $\delta(=(\rho_3^*-\rho_1^*)/\rho_3^*)$ he has used $\delta/2$ $(=(\rho_2^*-\rho_1^*)/\rho^*)$ and whereas we have chosen L to be the half-channel width, he chose the full width]. When $(\psi_1-\psi_2) = (\psi_2-\psi_3)$ (corresponding to a linear velocity variation in the middle layer in our model and interpreted as a linear velocity variation through the total depth in Davey's model)

the two systems of equations are identical. When this equality is not satisfied the two systems may be quite different. In figure 4.3, we shall see that for the same mean velocities in each layer the model derived here gives an unstable range (in the total wavenumber squared) roughly twice as wide as that found by Davey using the model consisting of three layers of uniform density. This is not to be interpreted as an error in either model but rather as a reminder that when using a layered model care must be taken in fitting the model to the real continuous profile (see for example Phillips, 1951). The model derived here avoids this "fitting problem" for the density and velocity profiles considered here by consistently deriving the layered model from the equations for a continuously stratified fluid. On the other hand the usual layered models must be fitted by appropriate reduction of the density difference between the layers. Since both models are in agreement for the case $(\psi_1-\psi_2) = (\psi_2-\psi_3)$, some explanation is needed for the latter statement. From the form of the governing equations for the layered model of Davey (these equations are of the same general form as (2.11)) it is clear that decreasing the density difference between the layers has basically the same effect as increasing the vertical curvature of the. Hence the close relation between vertical curvature and density stratification is expected. Now, consider the approximations to the vertical curvature in the two models. In our model, the vertical curvature in the middle layer is approximated by:

$$U_{2zz} \simeq \left\{ \frac{U_{1o}-U_{2o}}{(H_2/2H)} - \frac{U_{2o}-U_{3o}}{(H_2/2H)} \right\} / (H_2/H)$$

$$= 2(H/H_2)^2 (U_{1o}-2U_{2o}+U_{3o}) \qquad (2.12)$$

whereas the corresponding approximation for the usual layered model is (for $H_1 = H_2 = H_3$):

$$U_{2zz} \simeq \left\{ \frac{U_{1o}-U_{2o}}{(H_2/H)} - \frac{U_{2o}-U_{3o}}{(H_2/H)} \right\} / (H_2/H) \qquad (2.13)$$

$$= (H/H_2)^2 (U_{1o}-2U_{2o}+U_{3o}).$$

Although we have written the approximation to U_{2zz} in terms of the values of the velocities at the middle of each layer, the layered models have the velocities in each layer indepentent of z and hence in these models, U_{2zz} is generally approximated by:

$$U_{2zz} = (H/H_2)^2 (U_1-2U_2+U_3) \qquad (2.14)$$

For an approximately linear velocity variation in each layer the difference between (2.13) and (2.14) is small. However, in the presence of large vertical curvature, the difference is significant. Even if we use (2.13) there is still a factor of two difference between it and (2.12). This difference arises due to the fact that in the usual layered model the velocity difference between the layers is essentially assumed to occur over a separation of $(H_1+H_2)/2$ (the distance from the middle of the upper layer to the middle of the second) while in our model, since the density is uniform in the upper and lower layers, the shear between the upper layer and the middle layer occurs over a distance of $H_2/2$ (the distance from the bottom of the upper layer to the middle of the second layer). Clearly the approximations of the vertical curvature in the two models are quite different and if both models are to be applied to the same situation, some fitting procedure is needed. The advantage of the model developed here is that the density stratification is chosen to closely approximate the actual density stratification whereas this is not the case for the usual layered model. If we want to use these

layered models it is clear that the density difference between successive layers must be reduced (The mean currents should not be tampered with as they also appear in the advective terms and thus changing them will change more than just the approximation to the vertical curvature of the mean currents. Note, however, that if one considers the case of large vertical curvature, U_1, U_2, and U_3 should be replaced by U_{1o}, U_{2o}, and U_{3o} in the layered models.). The fitting of the model by an appropriate choice of density structure is not all that surprising when one realizes that the differences in the approximations to the vertical curvature of the mean currents in the two models are originally due to the different choices of density stratification in the two models. Finally we note that if the actual density stratification is not well approximated by the model developed here, one might prefer to use the usual layered model (for which intuition through analogy with finite difference approximations is probably better) or derive a yet another layered model (either by the method described in this section or by some other method). The latter choice is certainly preferable but generally not as convenient.

3. Linear Perturbation Analysis

We now wish to consider the stability with respect to quasi-geostrophic disturbances of a steady mean flow which is uniform along the channel. Hence we take $\psi_i = \bar{\psi}_i + \xi_i$ $(i=1,2,3)$ where $\bar{\psi}_i = \bar{\psi}_i(y)$ is a zonally uniform time independent solution of (2.15) and ξ_i is a perturbation stream function which we take to be of the form appropriate to waves propagating along the channel (i.e. $\xi_i = \mathrm{Re}\{\phi_i(y)\exp[ik(x-ct)]\}$). The linearized equations to be satisfied by ϕ_1, ϕ_2 and ϕ_3 are:

$$(U_1-c)[\phi_{1yy}-k^2\phi_1-F_1(3\phi_1-4\phi_2+\phi_3)] + \phi_1[\beta-U_{1yy}+F_1(3U_1-4U_{2o}+U_3)] = 0$$

$$(U_{2o}-c)[\phi_{2yy}-k^2\phi_2+4F_2(\phi_1-2\phi_2+\phi_3)] + \phi_2[\beta-U_{2o_{yy}}-4F_2(U_1-2U_{2o}+U_3)] = 0$$

$$(U_3-c)\left[\left[\frac{H_3-bh}{H_3}\right](\phi_{3yy}-k^2\phi_3) - F_3(\phi_1-4\phi_2+3\phi_3)\right] + \phi_3\left[\left[\frac{H_3-bh}{H_3}\right](\beta-U_{3yy}) + F_3(U_1-4U_{2o}+3U_3) + \frac{b}{R_oH_3}h_y\right] = 0$$

where U_1 $(=-\bar{\psi}_{1y})$, $U_3(=-\bar{\psi}_{3y})$ are the time independent velocities in the upper and lower layers and U_{2o} $(=-\bar{\psi}_{2y})$ is the corresponding velocity at the middle of the second layer. It is convenient at this point to express U_{2o} in terms of the vertically averaged velocities in the three layers. In the preceeding analysis we have essentially approximated the velocity in the middle layer by:

$$U_2(z) = \sum_{n=0}^{2} U_{2n}(z-z_m)^n \quad \text{where} \quad z_m = -\left(\frac{2H_1+H_2}{2H}\right)$$

Requiring that $U_2(z=-H_1/H) = U_1$, $U_2(z=-(H_1+H_2)/H) = U_3$ and that $\frac{H}{H_2}\int_{-\frac{H_1+H_2}{H}}^{-\frac{H_1}{H}} U_2(z)dz = U_2$ (the vertically averaged mean velocity in the middle layer) it is easily shown that $U_{2_o} = (6U_2-U_1-U_3)/4$ (and $U_{2_1} = (H/H_2)\cdot(U_1-U_3)$, $U_{2_2} = 3(H/H_2)^2\cdot(U_1-2U_2+U_3)$: note that the local curvature in the middle layer is $U_{22}/2$) and hence that the equations for ϕ_1, ϕ_2, and ϕ_3 may be written as:

$$\begin{aligned}
&(U_1-c)[\phi_{1yy}-k^2\phi_1-F_1(3\phi_1-4\phi_2+\phi_3)] + \phi_1\frac{\partial q_1}{\partial y} = 0 \\
&(U_{2o}-c)[\phi_{2yy}-k^2\phi_2+4F_2(\phi_1-2\phi_2+\phi_3)] + \phi_2\frac{\partial q_2}{\partial y} = 0 \qquad (3.1) \\
&(U_3-c)\left[\left[\frac{H_3-bh}{H_3}\right](\phi_{3yy}-k^2\phi_3) - F_3(\phi_1-4\phi_2+3\phi_3)\right] + \phi_3\frac{\partial q_3}{\partial y} = 0
\end{aligned}$$

where $\frac{\partial q_1}{\partial y} = \beta - U_{1yy} + 2F_1(2U_1-3U_2+U_3)$

$$\frac{\partial q_2}{\partial y} = \beta - U_{2oyy} - 6F_2(U_1-2U_2+U_3)$$

$$\frac{\partial q_3}{\partial y} = \left(\frac{H_3-bh}{H_3}\right)(\beta-U_{3yy}) + 2F_3(U_1-3U_2+2U_3) + \frac{b}{R_o H_3} h_y$$

$$U_{2o} = (6U_2-U_1-U_3)/4$$

with boundary conditions $\phi_1 = \phi_2 = \phi_3 = 0$ on $y = \pm 1$.

Before discussing the solutions of (3.1) in particular cases, it is of interest to consider the possible mechanisms of energy transfer for this model. To derive an energy equation we begin with the real form of (3.1) for $bh << H_3$ (i.e. for topographic variations small compared to the depth of the lower layer).

$$\left(\frac{\partial}{\partial t} + U_1 \frac{\partial}{\partial x}\right)[\xi_{1xx}+\xi_{1yy}-F_1(3\xi_1-4\xi_2+\xi_3)] + \frac{\partial \xi_1}{\partial x}\frac{\partial q_1}{\partial y} = 0$$

$$\left(\frac{\partial}{\partial t} + U_{2o} \frac{\partial}{\partial x}\right)[\xi_{2xx}+\xi_{2yy}+4F_2(\xi_1-2\xi_2+\xi_3)] + \frac{\partial \xi_2}{\partial x}\frac{\partial q_2}{\partial y} = 0 \qquad (3.2)$$

$$\left(\frac{\partial}{\partial t} + U_3 \frac{\partial}{\partial x}\right)[\xi_{3xx}+\xi_{3yy}-F_3(\xi_1-4\xi_2+3\xi_3)] + \frac{\partial \xi_3}{\partial x}\frac{\partial q_3}{\partial y} = 0$$

$$\xi_1 = \xi_2 = \xi_3 = 0 \quad \text{on} \quad y = \pm 1$$

Multiplying the i^{th} equation by ξ_i/F_i and integrating from $y = -1$ to $y = +1$ and over one wavelength in the x direction (a region we shall refer to as R) and adding, the following energy equation is readily derived.

$$\frac{\partial}{\partial t}\left\{\iint_R \left[\frac{(\nabla_h \xi_1)^2}{2F_1} + \frac{(\nabla_h \xi_2)^2}{2F_2} + \frac{(\nabla_h \xi_3)^2}{2F_3} + (\xi_1-\xi_2)^2 + (\xi_2-\xi_3)^2 + \frac{1}{2}(\xi_1-2\xi_2+\xi_3)^2\right] dxdy\right\}$$

$$= \iint_R [U_{1y}\xi_{1x}\xi_{1y}/F_1 + U_{2oy}\xi_{2x}\xi_{2y}/F_2 + U_{3y}\xi_{3x}\xi_{3y}/F_3]dxdy \tag{3.3}$$

$$+ \iint_R [(4\xi_1\xi_{2x} + \xi_3\xi_{1x})(U_1-U_{2o}) + (4\xi_2\xi_{3x} + \xi_3\xi_{1x})(U_{2o}-U_3)]dxdy$$

The left hand side represents the rate of change of kinetic plus potential energy of the depth-averaged perturbations. The first energy transformation integral on the right hand side is an expression for the horizontal Reynolds stress conversion of kinetic energy in the three layers while the second integral expresses the conversion of the available potential energy of the mean flow. The i^{th} term of the first integral on the right hand side of (3.3) will thus be referred to as the transfer of kinetic energy (T.K.E.) in the i^{th} layer, and the two terms in the second integral will be referred to as the transfer of available potential energy (T.A.P.E.) due to the shear between the upper layers and lower layers respectively.

We note here that the terms involving the correlation between the upper and lower layers in the T.A.P.E. terms of (3.3) are absent in the usual layered models. These terms arise here as a direct consequence of the approximations to ξ_{1z} and ξ_{3z} at the upper and lower interfaces (see chapter V, p. 199-200).

Necessary Conditions for Instability

If the first and third equations of (3.1) are multiplied by $\phi_i^*/[(U_i-c)F_i]$ $(i=1,3)$ and the second equation by $\phi_2^*/[(U_{2o}-c)F_2]$ (this is justified if $Im(c)\neq 0$; a * indicates complex conjugation here), integrated from y=-1 to y=+1, and the three resulting equations added, the following equation is derived:

$$\int_{-1}^{1} \sum_{i=1}^{3} \frac{|\phi_{iy}|^2+k^2|\phi_i|^2}{F_i} + 2\left[|\phi_2-\phi_1|^2 + |\phi_3-\phi_2|^2 + \frac{1}{2}|\phi_1-2\phi_2+\phi_3|^2\right] dy$$

$$= \int_{-1}^{1} \sum_{i=1}^{3} \frac{|\phi_i|^2}{U_{io}-c} \frac{\partial q_i}{\partial y} \frac{1}{F_i} dy \qquad (3.4)$$

(Note that since the upper and lower layers are vertically uniform, the vertical mean value of the velocities (U_1 and U_3) and the value at the middle of these layers (U_{1o} and U_{3o}) are equivalent.)

Taking the imaginary part of this equation gives:

$$c_i \int_{-1}^{1} \sum_{i=1}^{3} \frac{|\phi_i|^2}{|U_{io}-c|^2} \frac{\partial q_i}{\partial y} \frac{1}{F_i} dy = 0 \qquad (3.5)$$

We see that the expected necessary condition for instability is found, i.e. the potential vorticity gradient must change sign either within a given layer or in going from one layer to another.

For $c_i\neq 0$, the real part of (3.4), after using (3.5) yields:

$$\int_{-1}^{1} \left\{ \sum_{i=1}^{3} \frac{|\phi_{iy}|^2+k^2|\phi_i|^2}{F_i} + 2\left[|\phi_2-\phi_1|^2 + |\phi_3-\phi_2|^2 + \frac{1}{2}|\phi_1-2\phi_2+\phi_3|^2\right] \right\} dy$$

$$= \int_{-1}^{1} \sum_{i=1}^{3} \frac{|\phi_i|^2}{|U_{io}-c|^2 U_{io}} \frac{\partial q_i}{\partial y} \frac{1}{F_i} dy \qquad (3.6)$$

Since the left hand side of (3.6) is positive, it is clear that the product of the mean velocity and potential vorticity gradient must be positive, at least somewhere in one of the layers. Thus a sufficient condition for stability in this case is that $U_{io}\frac{\partial q_i}{\partial y} < 0, (i = 1,2,3)$.

Analytic Solutions

For the remainder of this chapter we shall be concerned with the case in which the following conditions hold:

$$\begin{aligned} &U_i = \text{constant} \qquad (i = 1,2,3) \\ &bh << H_3 \\ &h_y = \text{constant} \end{aligned} \tag{3.7}$$

Under these conditions, solutions of (3.1) exist in the form $\phi_i = \mu_i \sin[\frac{m\pi}{2}(y+1)]$, $(i = 1,2,3)$ where the μ_i's are constants to be determined from the following eigenvalue problem (with the Doppler shifted phase speed, $C = c - U_{2o}$ as the eigenvalue).

$$\begin{aligned} (S_{1o}-C)[-K_m^2\mu_1 - F_1(3\mu_1-4\mu_2+\mu_3)] + \mu_1\frac{\partial q_1}{\partial y} = 0 \\ -C[-K_m^2\mu_2+4F_2(\mu_1-2\mu_2+\mu_3)] + \mu_2\frac{\partial q_2}{\partial y} = 0 \\ (-S_{2o}-C)[-K_m^2\mu_3-F_3(\mu_1-4\mu_2+3\mu_3)] + \mu_3\frac{\partial q_3}{\partial y} = 0 \end{aligned} \tag{3.8}$$

where $K_m^2 = k^2 + (\frac{m\pi}{2})^2$

$$\frac{\partial q_1}{\partial y} = \beta + 2F_1(2S_1 - S_2)$$

$$\frac{\partial q_2}{\partial y} = \beta - 6F_2(S_1 - S_2)$$

$$\frac{\partial q_3}{\partial y} = \beta + 2F_3(S_1 - 2S_2) + (b/R_o H_3)h_y$$

$$S_1 = U_1 - U_2$$

$$S_2 = U_2 - U_3$$

$$S_{1o} = U_1 - U_{2o} = (5S_1 - S_2)/4$$

$$S_{2o} = U_{2o} - U_3 = (5S_2 - S_1)/4$$

(Note that although I have expressed the equations in terms of $c-U_{2o}$, in the dispersion curves plotted in the following sections we have used $U_{2o}=U_2-(S_1-S_2)/4$ to plot the results in terms of $(c-U_2)\cdot k$.)

The condition for a nontrivial solution (the vanishing of the coefficient matrix of μ_1, μ_2, μ_3) gives the following dispersion relation:

$$\begin{vmatrix} -(3F_1+K_m^2)(S_{1o}-C) + \frac{\partial q_1}{\partial y} & 4F_1(S_{1o}-C) & -F_1(S_{1o}-C) \\ -4F_2C & (8F_2+K_m^2)C + \frac{\partial q_2}{\partial y} & -4F_2C \\ F_3(S_{2o}+C) & -4F_3(S_{2o}+C) & (3F_3+K_m^2)(S_{2o}+C) + \frac{\partial q_3}{\partial y} \end{vmatrix} = 0 \tag{3.9}$$

For our calculations we will want to consider many different values of K_m^2 for each set of parameters so that it is convenient to rearrange the dispersion relation into the form given in Appendix a, at the end of this chapter.

If we normalize with respect to the middle layer by setting $\mu_2 = 1$, then μ_1 and μ_3 are given by:

$$\begin{bmatrix} -(3F_1+K_m^2)(S_{1o}-C) + \frac{\partial q_1}{\partial y} & -F_1(S_{1o}-C) \\ F_3(S_{2o}+C) & (3F_3+K_m^2)(S_{2o}+C) + \frac{\partial q_3}{\partial y} \end{bmatrix} \begin{bmatrix} \mu_1 \\ \mu_3 \end{bmatrix} = \begin{bmatrix} -4F_1(S_{1o}-C) \\ 4F_3(S_{2o}+C) \end{bmatrix} \tag{3.10}$$

The perturbation velocity components are now readily computed by using the relations $u_n = -\xi_{ny}$ and $v_n = \xi_{nx}$; they take the forms

$$u_n = -\mathrm{sgn}(\mu_{n_r})|\mu_n| \ \frac{m\pi}{2} e^{\omega_i t} \cos(kx-\omega_r t+\delta_n) \cos[\tfrac{m\pi}{2}(y+1)]$$

$$v_n = -\mathrm{sgn}(\mu_{n_r})|\mu_n| \ k \, e^{\omega_i t} \sin(kx-\omega_r t+\delta_n) \sin[\tfrac{m\pi}{2}(y+1)] \tag{3.11}$$

$$(n = 1,2,3)$$

where $\omega = ck$, $\omega_r = \mathrm{Re}(\omega)$, $\omega_i = \mathrm{Im}(\omega)$, $\mu_{n_r} = \mathrm{Re}(\mu_n)$, and $\tan \delta_n = \mu_{n_i}/\mu_{n_r}$, $-\pi/2 \le \delta_n \le \pi/2$. sgn is the signum function which gives the sign of the argument.

Following Davey (1977) we now reduce the range of parameters to be studied. Defining $T = (\frac{b}{R_0 H_3})h_y$ it is clear from (3.8) that if the system $(S_1, S_2, \beta, T, H_1, H_2, H_3)$ has solution (C, μ_1, μ_2, μ_3) , then the system $(\alpha S_1, \alpha S_2, \alpha\beta, \alpha T, H_1, H_2, H_3)$ has solution $(\alpha C, \mu_1, \mu_2, \mu_3)$. Further, if the system $(S_1, S_2, \beta, 0, H_1, H_2, H_3)$ has solution (C, μ_1, μ_2, μ_3) , then $(-S_2, -S_1, \beta, 0, H_3, H_2, H_1)$ has

solution (C, μ_3, μ_2, μ_1) . The first of these relations corresponds to a simple rescaling while the second follows by virtue of the rigid lid approximation and corresponds to interchanging the top and bottom layers. From the first relation it is clear that we need only consider the case $S_1 = 1$. This corresponds to taking the horizontal velocity scale, U , equal to the shear between the upper layers. (Note that although U is taken to be a typical horizontal velocity for the preceding analysis, once the equations have been derived it factors out of each equation and hence we may choose it to be $S_1^* = U_1^* - U_2^*$ for convenience.) If $T = 0$, then using the above relations, one may show that the systems $(1, S_2, \beta, 0, H_1, H_2, H_3)$ and $(1, 1/S_2, -\beta/S_2, 0, H_3, H_2, H_1)$ have the same stability with respect to K_m^2 . Hence in this case, the behaviour of all systems with T=0 can be deduced from the subset $(S_1=1, -1\leq S_2\leq 1, \beta, 0, H_1, H_2, H_3)$. In fact, in every case considered we will take $S_1 = 1$ and consider $-2 \leq S_2 \leq 2$. In this manner, most cases of interest are covered simply by choosing $U = S_1^*$.

We may also reduce the range of β to be considered. From (3.5) we know that for instabilities to occur the following relation must be satisfied.

$$\int_{-1}^{1} \left\{ \sum_{i=1}^{3} \frac{|\phi_i|^2}{|U_{io}-c|^2} \frac{\partial q_i}{\partial y} \frac{1}{F_i} \right\} dy = 0$$

Hence, if all the basic state potential vorticity gradients are of one sign no instabilities will occur. This condition will thus give us

bounds on β for instabilities to occur. For $S_1=1, -1 \leq S_2 \leq 1$, and T=0, all the $\frac{\partial q_i}{\partial y}$ are positive for $\hat{\beta} \equiv \beta/F_2 > \max(12, 2\,H_2/H_3)$ and all are negative for $\hat{\beta} < -6\max(H_2/H_1, H_2/H_3)$. It is interesting to note further that the corresponding range of $\hat{\beta}$ found by Davey using a model with three layers of constant density and equal thicknesses is $-2 \leq \hat{\beta} \leq 4$. The range of $\hat{\beta}$ for which instabilities occurs is reduced by a factor of three due to the over estimation of the stabilizing effect of density statification (see the last paragraph in section 2).

It is important to note here that although it appears that waves with $\hat{\beta} < 0$ (corresponding to a relative westward flow in the surface layer) are more stable than those with $\hat{\beta} > 0$ (eastward flow in the surface layer), our results do not contradict the qualitative statement made by Gill et al (1973) that, "because of the effect of β on stability, the most favourable conditions for instability are found where the isopycnal slope upwards towards the equator ...". On the contrary, if we consider $S_1 = S_2$ (which is approximately satisfied in the studies mentioned above) we find that instabilities can only occur for

$$-2H_2/H_1 < \hat{\beta} < 2H_2/H_3$$

Since we generally have $H_1 \ll H_3$ we recover the result that for the open ocean (or anywhere that $S_2 \sim S_1$, and $H_1 \ll H_3$) it appears that flows with a relative westward flow in the surface layer are more favourable for instabilities than those with a relative eastward flow in the surface layer. It is, however, important to note that

this conclusion relies strongly on the condition $H_1 << H_3$.

4. Results of Independent Parameter Variations

For the purpose of considering the effect of parameter variations, it is useful to first divide each of the equations in (3.8) by F_2 . The resulting set of equations is:

$$\begin{aligned}(S_{1o}-C)[-(K_m^2/F_2)\phi_1 - (H_2/H_1)(3\phi_1-4\phi_2+\phi_3)] + \phi_1 \frac{\partial Q_1}{\partial y} &= 0 \\ - C[-(K_m^2/F_2)\phi_2 + 4(\phi_1-2\phi_2+\phi_3)] + \phi_2 \frac{\partial Q_2}{\partial y} &= 0 \\ (-S_{2o}-C)[-(K_m^2/F_2)\phi_3 - (H_2/H_3)(\phi_1-4\phi_2+3\phi_3)] + \phi_3 \frac{\partial Q_3}{\partial y} &= 0\end{aligned} \qquad (4.1)$$

where

$$\frac{\partial Q_1}{\partial y} = \hat{\beta} + 2(H_2/H_1)(2S_1-S_2)$$

$$\frac{\partial Q_2}{\partial y} = \hat{\beta} - 6(S_1-S_2)$$

$$\frac{\partial Q_3}{\partial y} = \hat{\beta} + 2(H_2/H_3)(S_1-2S_2) + \hat{T}$$

$$\hat{\beta} = \beta/F_2 = \beta^* L^2/F_2 U$$

$$\hat{T} = T/F_2 = (g'/fU)(H_2/H_3)bh_{y^*}$$

Note that if plotting is done against K_m^2/F_2 and if the velocity scale, U , is chosen to be equal to $S_1^* = U_1^* - U_2^*$ (so that $S_1 = 1$), then the parameters to be considered are S_2, H_1/H_2, H_3/H_2, $\hat{\beta}$ and $\hat{T}$. From the form of the equations above we may also make some general conclusions about the effect of density stratification. The effect of varying each of these parameters independently shall be

discussed in this section.

Before beginning a study of the effects of parameter variations, it is useful to give a qualitative discussion of the roots of (3.9). There are, of course, three roots for a given wavenumber, k. In all of the dispersion curves presented in this chapter, I have plotted $\omega_r - U_2 k$ $(=(c-U_2)k)$ vs. k for the first cross-channel mode (m=1). The non-dimensional phase speed is thus obtained by dividing the ordinate by the absissa in the graphs and then adding the appropriate value of U_2, and the non-dimensional group velocity is obtained by taking the slope of the dispersion curve and adding U_2. When two distinct real dispersion curves cross each other so that the phase speeds and wavelengths are identical,an interaction between the two waves (and the mean state) is possible and an instability may occur. Since we have neglected horizontal shear and considered only constant bottom slopes, any such instability must extract its energy from the potential energy of the mean state (i.e. we are considering only pure baroclinic instability here). Since vertical shear clearly plays a fundamental role in the mechanism of baroclinic instability (through its role in tilting the isopycnals), I have have chosen to classify the different waves in terms of the vertical shear of the mean current. To make this classification, we consider the case $\beta=T=0$, to eliminate all but the effects of the shears. In this case we note that if $S_1=S_2$ (no curvature in the middle layer-see the paragraph preceeding (3.1)) then the constant term in the dispersion relation (δ in appendix a) vanishes identically since $q_{2y} \equiv 0$ for this case. Thus for zero curvature, one of the roots of (3.9) is $C = 0$ (i.e. $c = U_{2o}$). (This is due to the fact that for $\beta = 0$ and $S_1 = S_2$, $q_{2y} \equiv 0$. Analogous results also hold for $q_{1y} \equiv 0$, and $q_{3y} \equiv 0$, i.e. $q_{iy} \equiv 0$ $\Rightarrow$ $c = U_{io}$ is one root of the dispersion relation, i=1,2,3). Since in the absence of β, the wave corresponding to this root depends on the curvature

of the mean currents to give it a non-zero phase speed relative to the mean flow in the middle layer, I shall refer to this wave as the curvature wave. In the dispersion curves presented in figures 4.1-4.18, this root generally lies near $\omega_r - U_2 k = 0$ at large k (note that at very large k, this root reduces to $c = U_{2o}$, i.e. $\omega_r - U_2 k = -k(S_1 - S_2)/4$ so if we went to large enough k this root would be better identified by its slope). For $S_1 \neq S_2$ this root plays a fundamental role in destabilizing the flow. A careful examination of figures 4.1 to 4.18 reveals that when this curve meets either of the others, the flow is generally destabilized. The other two waves do not generally interact in this way unless H_2 is relatively small. These other waves may be classified as an upper shear wave (S_1-wave) and a lower shear wave (S_2-wave). [Alternatively each of the roots may be classified by its dependence on the mean potential vorticity gradient - the S_1-wave depends critically on $\frac{\partial q_1}{\partial y}$, the curvature wave on $\frac{\partial q_2}{\partial y}$, and the S_2-wave on $\frac{\partial q_3}{\partial y}$.] The lower shear wave is indicated by a dashed curve in the figures and is clearly very sensitive to variations in S_2 as well as variations in topography and β. The upper shear wave is rather insensitive to variations in S_2 and rises up to the left showing relatively little variation throughout the figures in this section (figures 4.1-4.18). It is however strongly affected by variations in S_1 holding S_2 fixed. Finally we note that although these three types of waves are quite distinct at short wavelengths (where the layers tend to decouple), the distinction at long wavelengths (where the layers are strongly coupled) is not nearly as clear.

Also shown in figures 4.1 to 4.18 are stability boundaries (part(a) in each figure). The stability boundary for each set of parameters is a plot of S_2 vs. K_m^2/F_2 and shows the curve in parameter space on which the discriminant of the cubic given by (3.9)vanishes. This curve separates the region in

which waves grow with time (Im(c) $\neq$ 0) from the region of stable waves (Im(c) = 0) and hence is very useful in studying the stability of a given flow. The position of this curve was determined by numerical evaluation using the form of (3.9) given in Appendix a.

Let us now consider the effect of independently varying the parameters in the model.

Variation of the Coriolis Parameter with Latitude

The variation of the local normal component of the earth's rotation enters (4.1) through the term:

$$\hat{\beta} \equiv (g'/f_o S_1^*) \frac{H_2}{f_o} \beta^*$$

A negative value of $\hat{\beta}$ corresponds to $S_1^* < 0$, and we see that at a given latitude the effective β is increased by either an increase in density stratification or by a decrease in shear. (Note that if $S_1 = S_2 = 0$, the only non-zero terms in q_{iy} (i=1,2,3) are due to β and topography. In this case the only non-trivial roots of the dispersion relation correspond to Rossby waves. i.e. one of the planetary Rossby wave ($\beta \neq 0, T=0$), the topographic Rossby wave ($\beta=0, T\neq 0$),or the topographically modified planetary Rossby wave ($\beta\neq 0, T\neq 0$). The case $S_1 = S_2 = 0$, $\beta=0$, $T \neq 0$ is briefly considered in appendix a.

From figures 4.1 to 4.3 we see that decreasing $\hat{\beta}$ from zero stabilizes the flow and from figures 4.3 to 4.5 we see that increasing $\hat{\beta}$ from zero also stabilizes the flow. In each case the effect is very similar with the very long waves being quickly stabilized as expected. Further, we note that the instabilities near $S_1 = S_2 = 1$ are quickly stabilized by $\hat{\beta}$ (either positive or negative). This result is not very surprising as the unstable waves in

this region are long and strongly affected by β. Perhaps more surprising is the stabilizing effect of β on the short waves corresponding to the branch extending to the right in figure 4.3. However, the growth rates corresponding to these waves are very small even for $\beta = 0$.

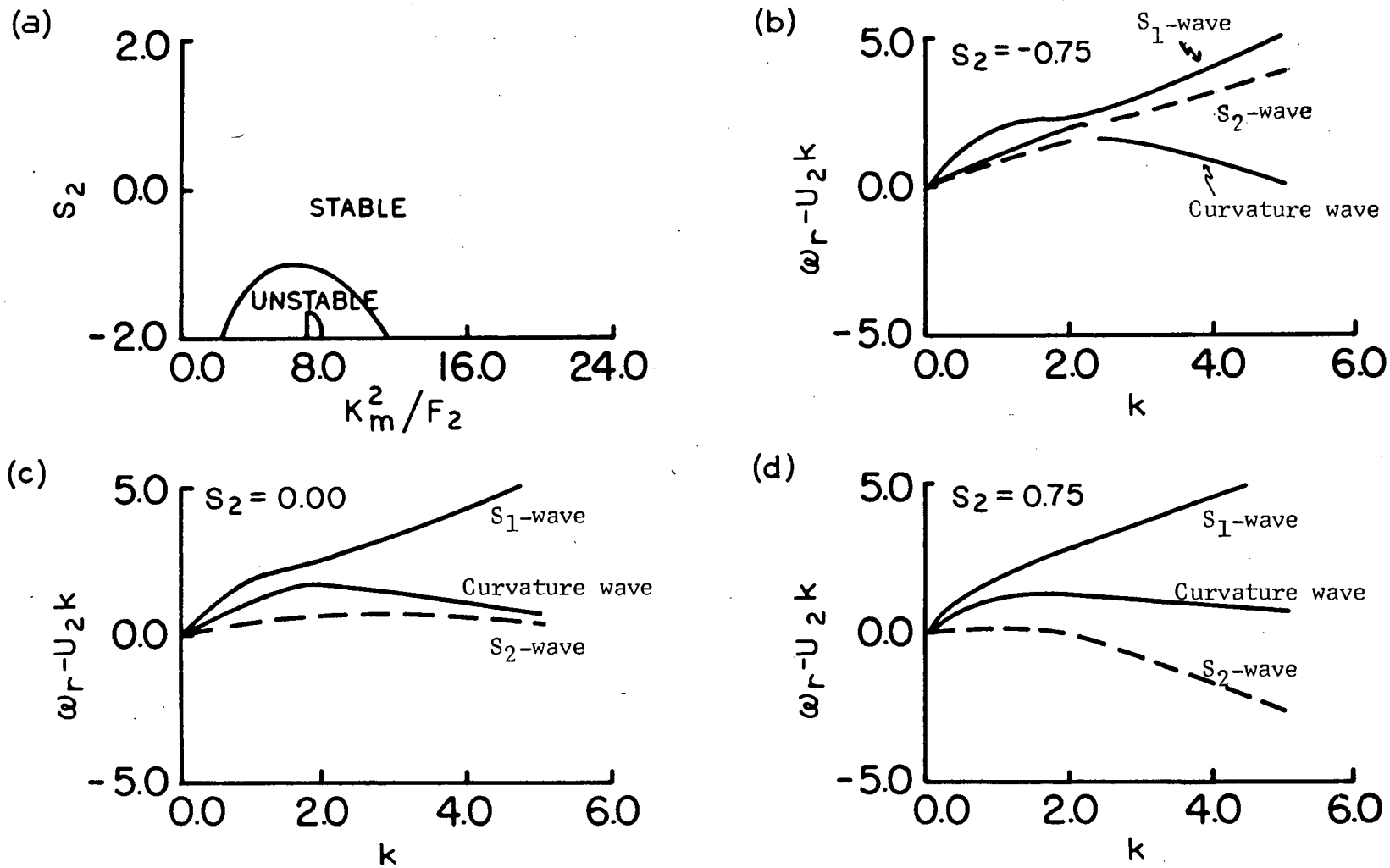

Figure 4.1: Stability boundaries (a) for $H_1 = H_2 = H_3$, $\hat{T} = 0$, $\hat{\beta} = -6$ and first mode (m=1) dispersion curves corresponding to these parameter values with $F_2 = 1$ and $S_2 = -0.75$(b), 0.00(c), and 0.75(d)

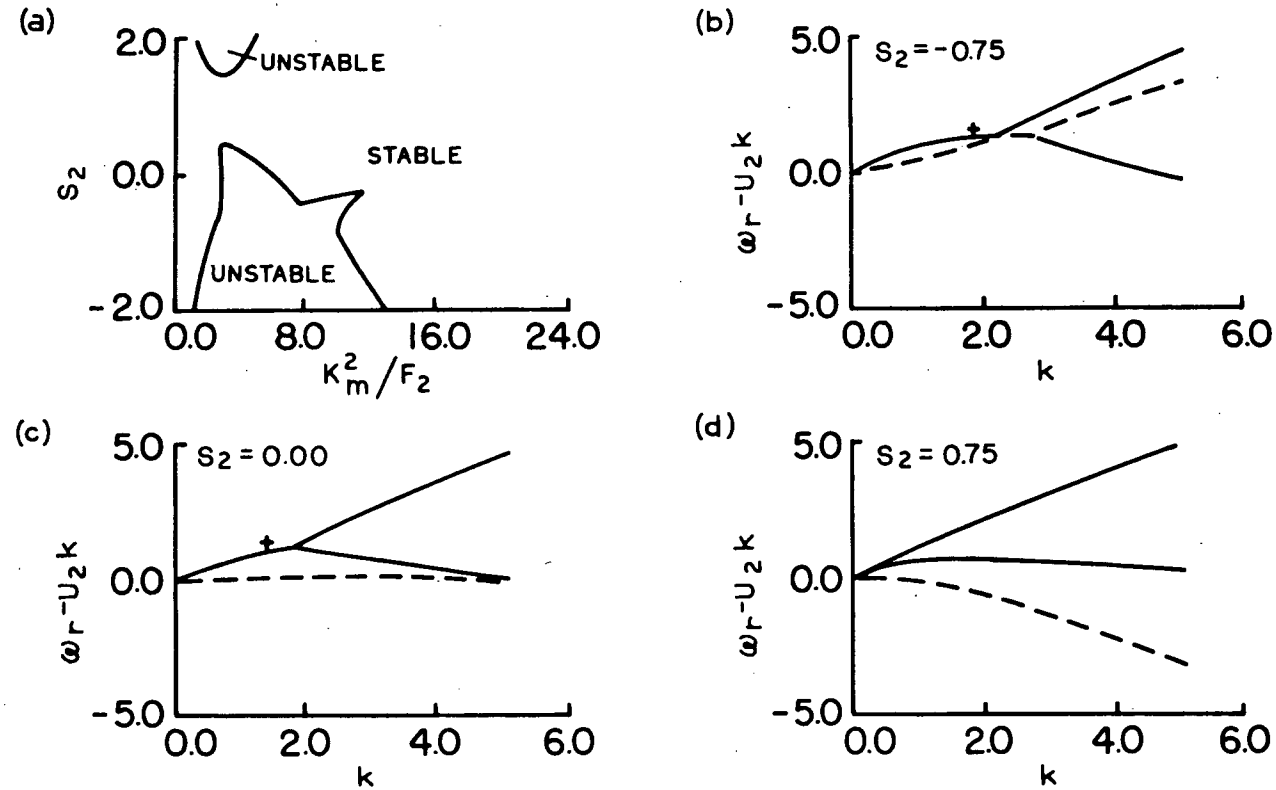

Figure 4.2:

S_2	Maximum Growth Rate	$\lvert\mu_1/\mu_2\rvert$	$\lvert\mu_3/\mu_2\rvert$	δ_1	δ_3
-0.75	0.48	0.61	0.33	46.32(+)	35.25(+)
0.00	0.23	0.65	0.56	36.14(+)	- 8.37(+)

Stability boundaries (a) for $H_1 = H_2 = H_3$, $\hat{T} = 0$, $\hat{\beta} = -3$ and first mode (m=1) dispersion curves corresponding to these parameter values with $F_2 = 1$ and $S_2 = -0.75$(b), 0.00(c), and 0.75(d). Statistics for positions of maximum growth rate (marked by plus signs in the figures) are given in the table. The signs of μ_{1_r} and μ_{3_r} are given in brackets following δ_1 and δ_3 respectively.

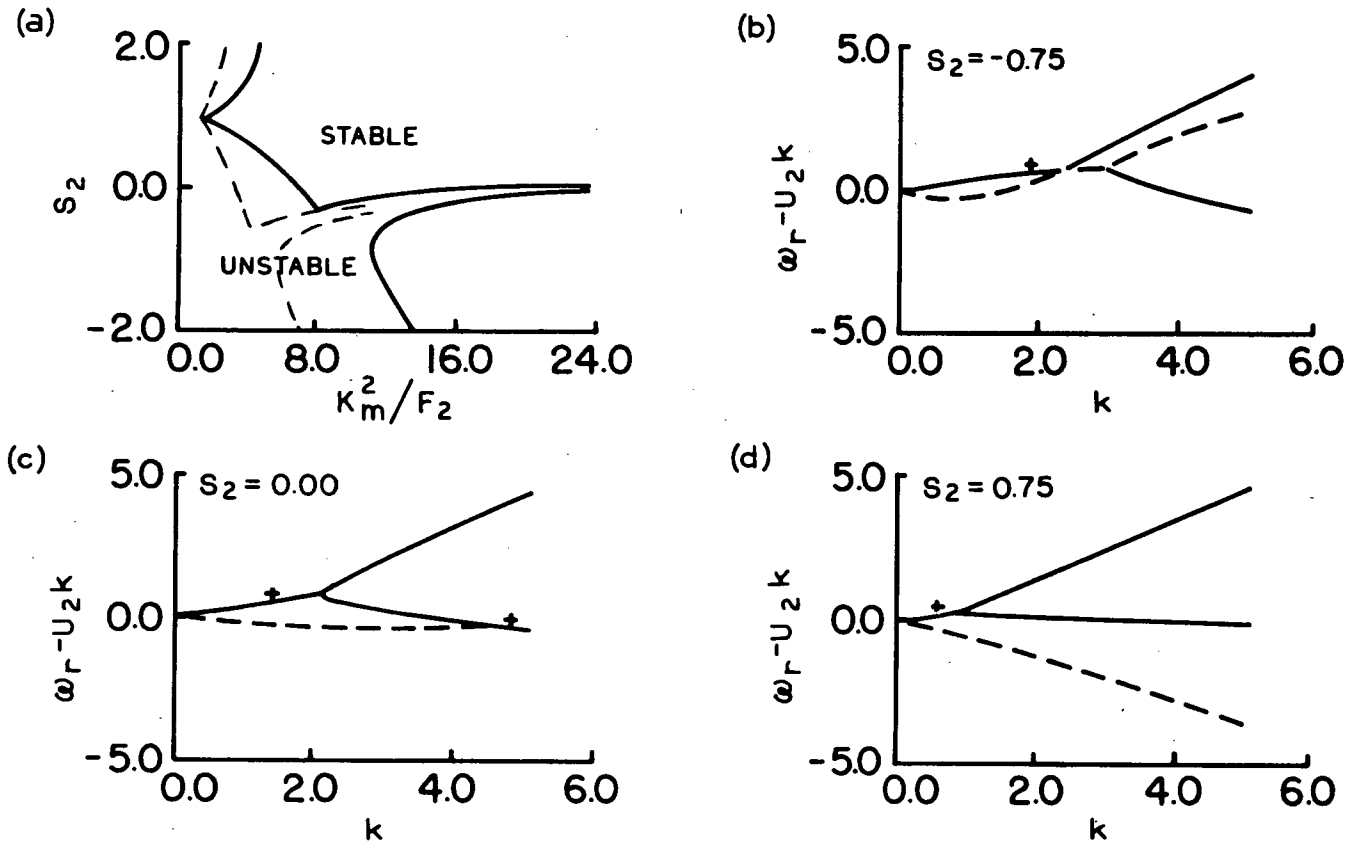

Figure 4.3:

S_2	Maximum Growth Rate	$\lvert\mu_1/\mu_2\rvert$	$\lvert\mu_3/\mu_2\rvert$	δ_1	δ_3
-0.75	0.64	0.88	0.51	54.87(+)	64.20(+)
0.00	0.38	1.19	0.30	48.70(+)	- 2.42(+)
0.00	0.07	0.16	0.66	- 9.28(+)	87.72(+)
0.75	0.09	1.38	0.56	19.79(+)	-11.40(+)

As in figure 4.2 with $\hat{\beta} = 0$. Also included in part (a) is the corresponding result of Davey (1977), (broken curve)

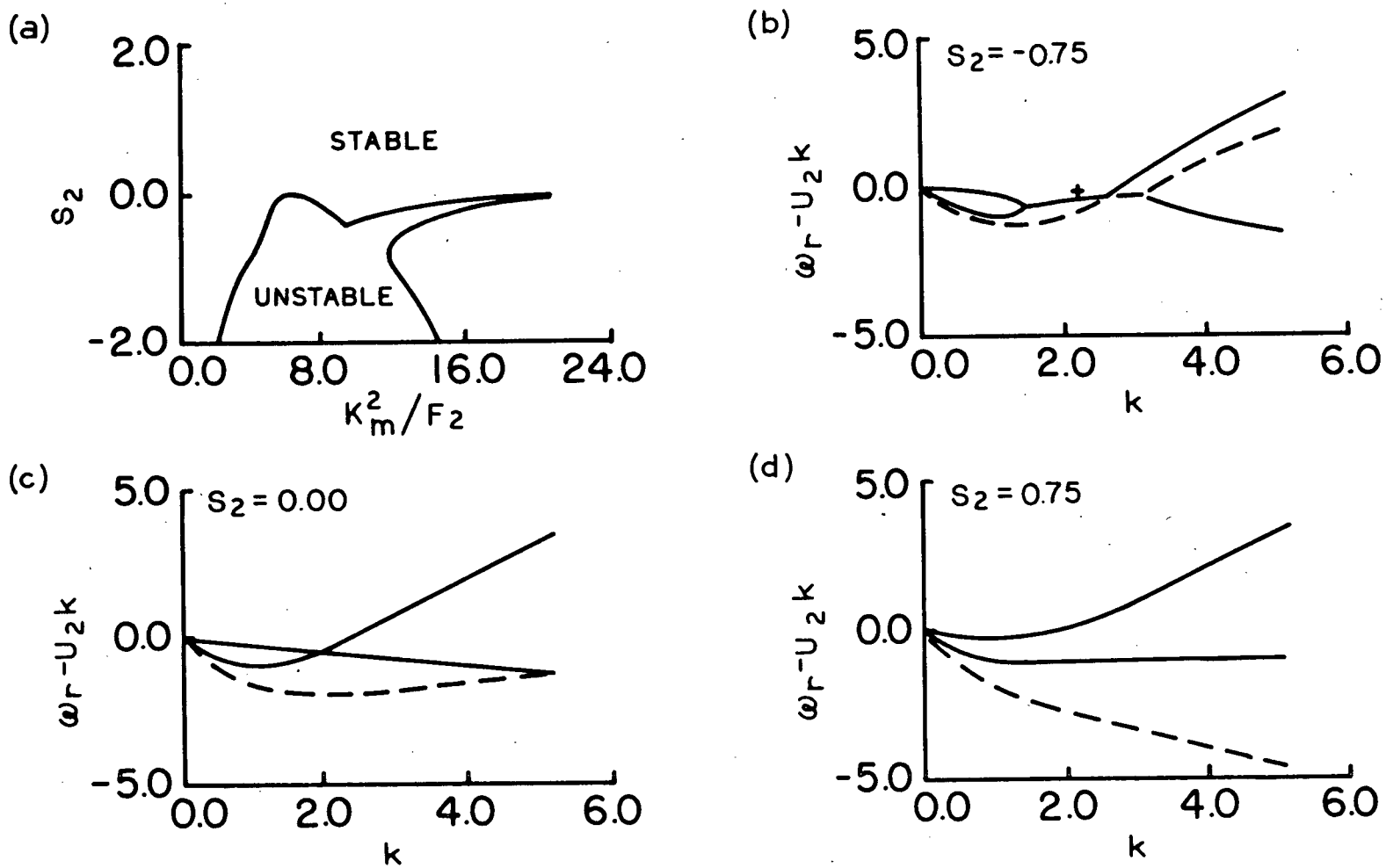

Figure 4.4:

S_2	Maximum Growth Rate	$\lvert\mu_1/\mu_2\rvert$	$\lvert\mu_3/\mu_2\rvert$	δ_1	δ_3
-0.75	0.53	1.81	1.05	45.36(+)	77.20(+)

As in figure 4.2 with $\hat{\beta} = 6$.

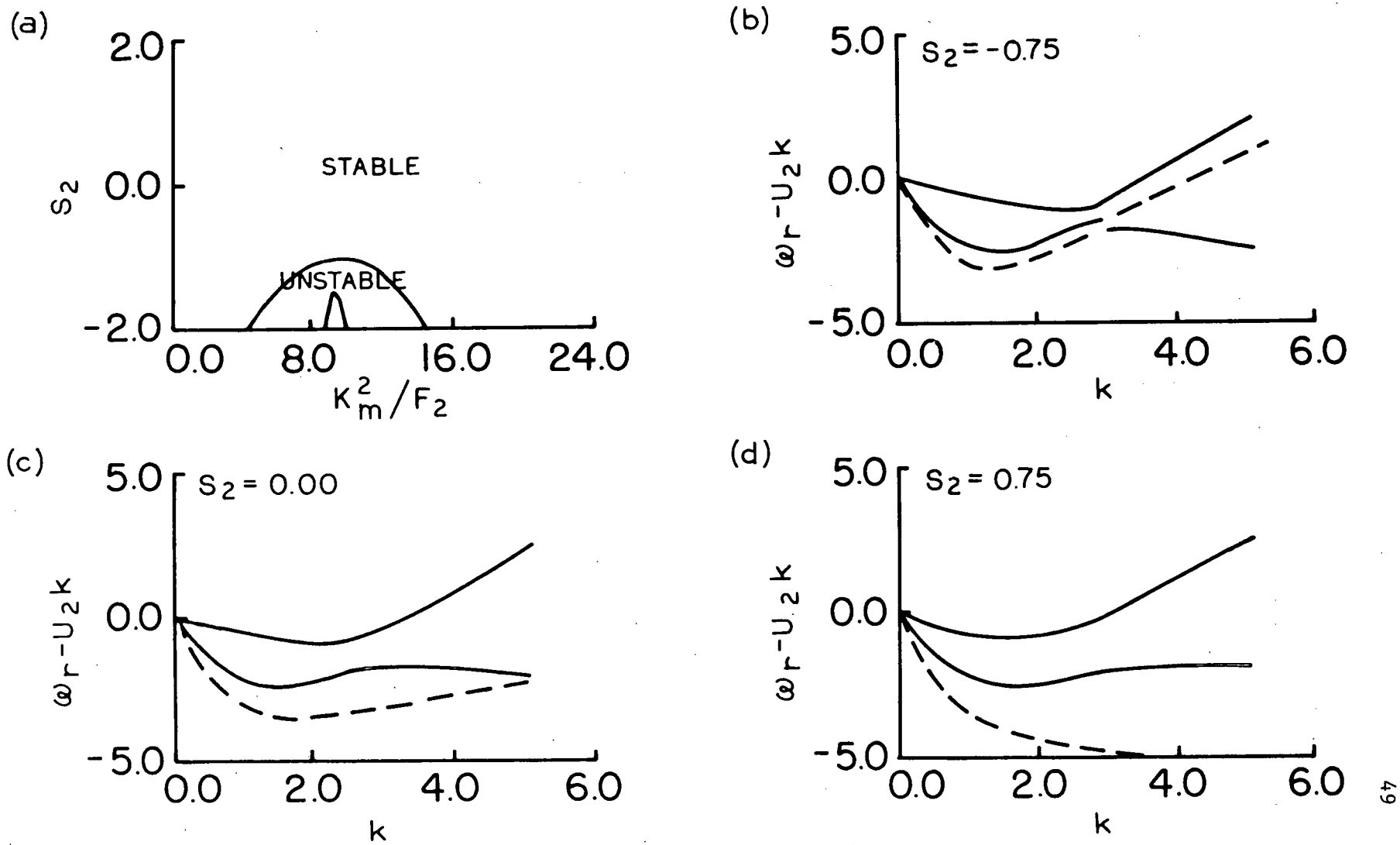

Figure 4.5: As in figure 4.2 with $\hat{\beta} = 12$.

Finally, we note here that whereas we have chosen to classify our waves in terms of shears, when $\hat{\beta}$ is significant a classification in terms of potential vorticity gradients, as mentioned earlier, is more appropriate. These comments also apply to the following section on topography, however we shall continue to classify our waves in terms of shears, due to the role of vertical shear in supplying an energy source for baroclinic instability.

Topography

The effect of topography in (4.1) is given by:

$$\hat{T} = \left(\frac{b}{R_0 H_3 F_2}\right) h_y$$

$$= \left(\frac{g'}{f_0 S_1^*}\right) (H_2/H_3)\, b h_{y*}$$

as in the case of β we see that an increase in stratification or a decrease in shear increases the effect of bottom topography. Bottom topography is, of course, also felt more strongly if the depth of the lower layer is decreased.

The qualitative difference in stability between the cases $\hat{T} < 0$ and $\hat{T} > 0$ is understood when one realizes that of the three roots of (3.9), only the S_2-wave is significantly affected by topography. (This is, of course, consistent with a classification in terms of potential vorticity gradients.) From figures 4.6 to 4.12 we see that as $\hat{T}$ increases

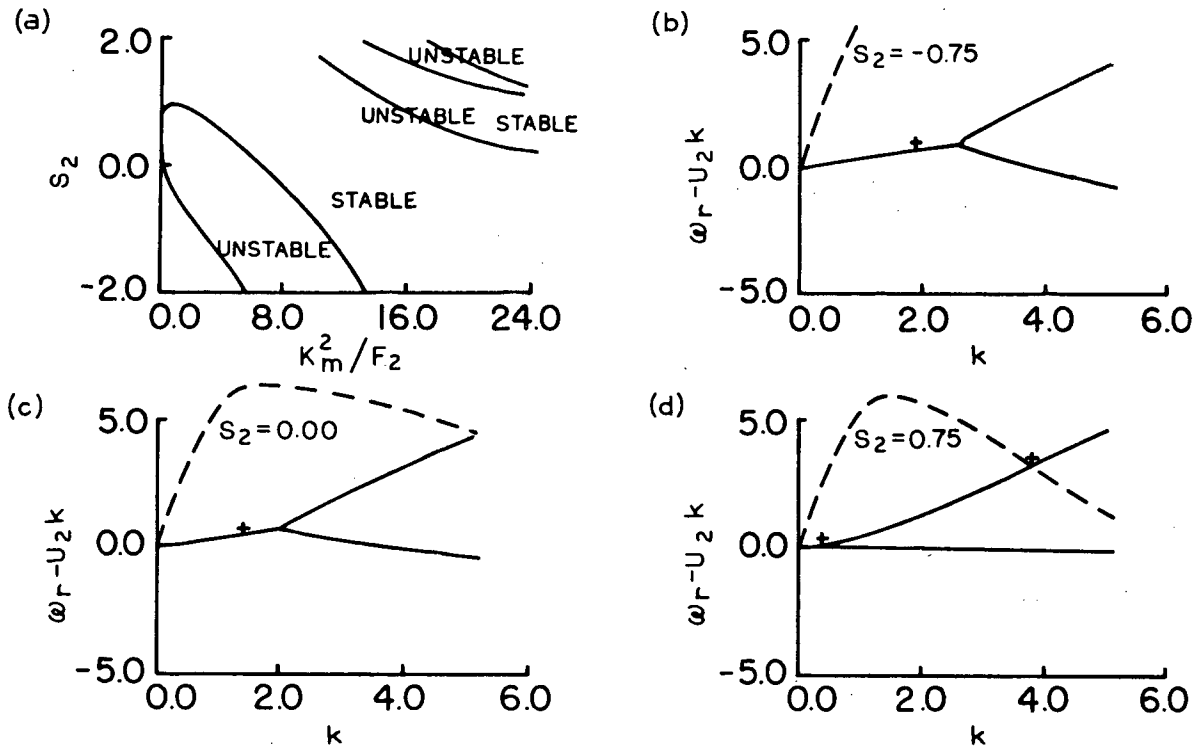

Figure 4.6:

S_2	Maximum Growth Rate	$\lvert\mu_1/\mu_2\rvert$	$\lvert\mu_3/\mu_2\rvert$	δ_1	δ_3
-0.75	0.50	1.14	0.06	66.47(+)	-47.18(+)
0.00	0.35	1.38	0.05	43.37(+)	23.44(-)
0.00	0.03	2.90	7.66	-71.94(+)	21.16(+)
0.75	0.04	1.73	0.09	11.38(+)	- 1.17(-)
0.75	0.03	0.90	6.51	77.16(+)	16.54(+)

Stability boundaries (a) for $H_1 = H_2 = H_3$, $\hat{T} = -30$, $\hat{\beta} = 0$ and first mode (m=1) dispersion curves corresponding to these parameter values with $F_2 = 1$ and $S_2 = -0.75$ (b), 0.00 (c), and 0.75 (d). Statistics for positions of maximum growth rate (marked by plus signs) are given in the table in order of increasing k.

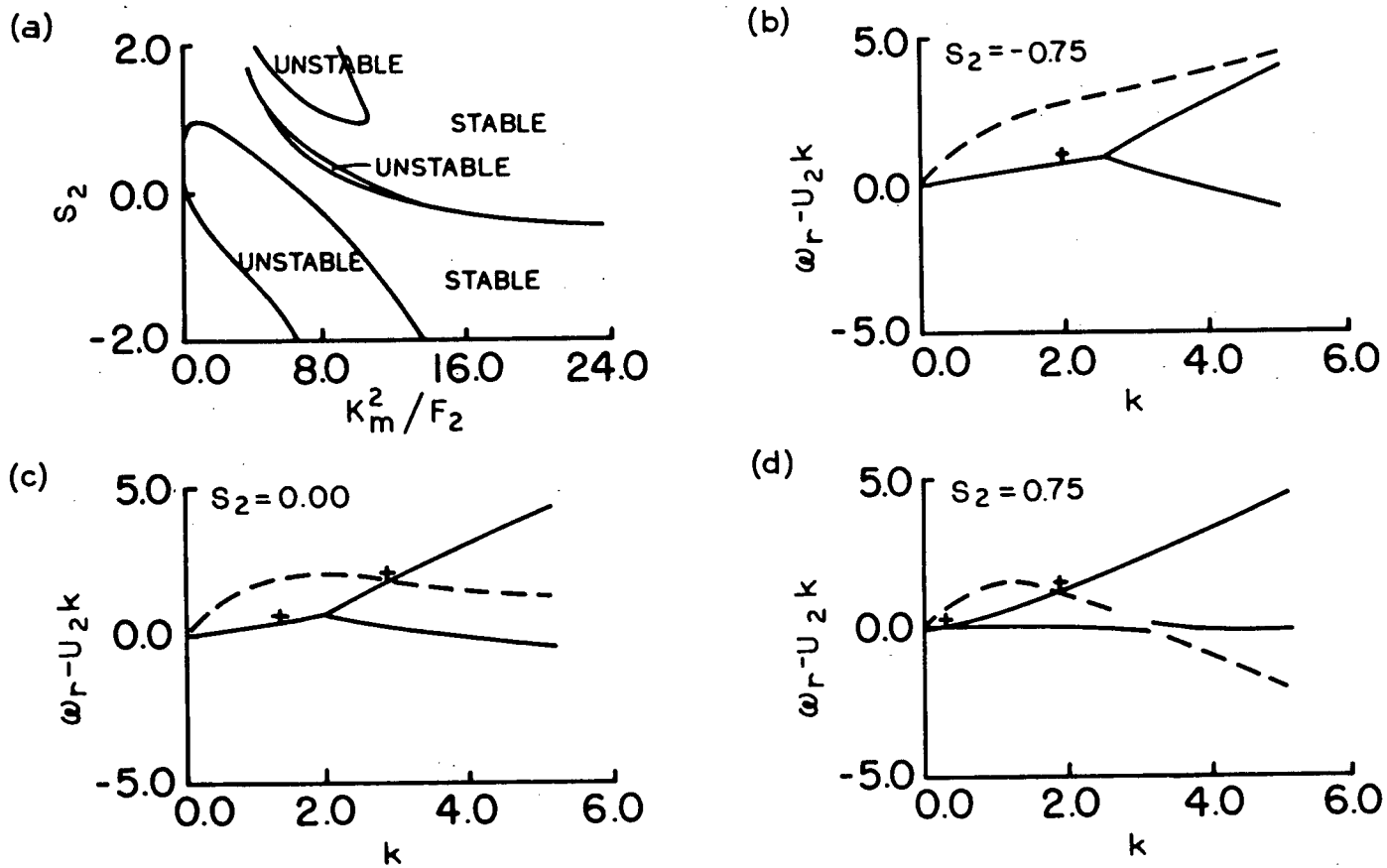

Figure 4.7:

S_2	Maximum Growth Rate	$\lvert\mu_1/\mu_2\rvert$	$\lvert\mu_3/\mu_2\rvert$	δ_1	δ_3
-0.75	0.48	1.10	0.18	61.61(+)	-33.85(+)
0.00	0.33	1.48	0.22	43.47(+)	33.81(+)
0.00	0.04	1.84	2.54	59.23(+)	-37.82(+)
0.75	0.02	1.91	0.04	5.81(+)	0.78(-)

As in figure 4.6 with $\hat{T} = -10$.

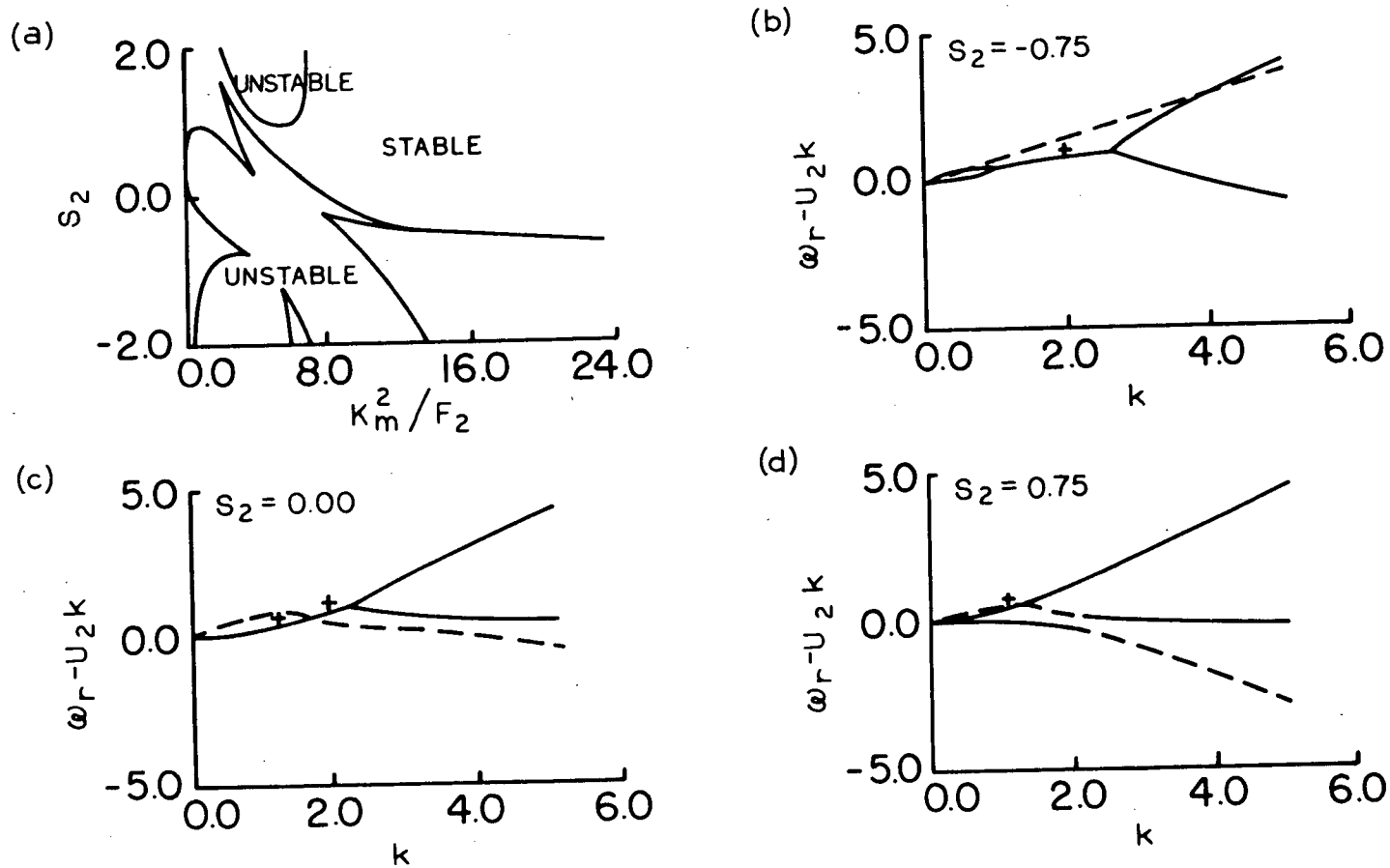

Figure 4.8:

S_2	Maximum Growth Rate	$\lvert\mu_1/\mu_2\rvert$	$\lvert\mu_3/\mu_2\rvert$	δ_1	δ_3
-0.75	0.49	0.99	0.39	67.38(+)	-14.24(+)
0.00	0.26	1.88	0.80	58.54(+)	69.16(-)
0.00	0.23	1.45	1.11	60.06(+)	-53.07(+)
0.75	0.12	1.32	1.94	62.36(+)	-32.63(+)

As in figure 4.6 with $\hat{T} = -5$.

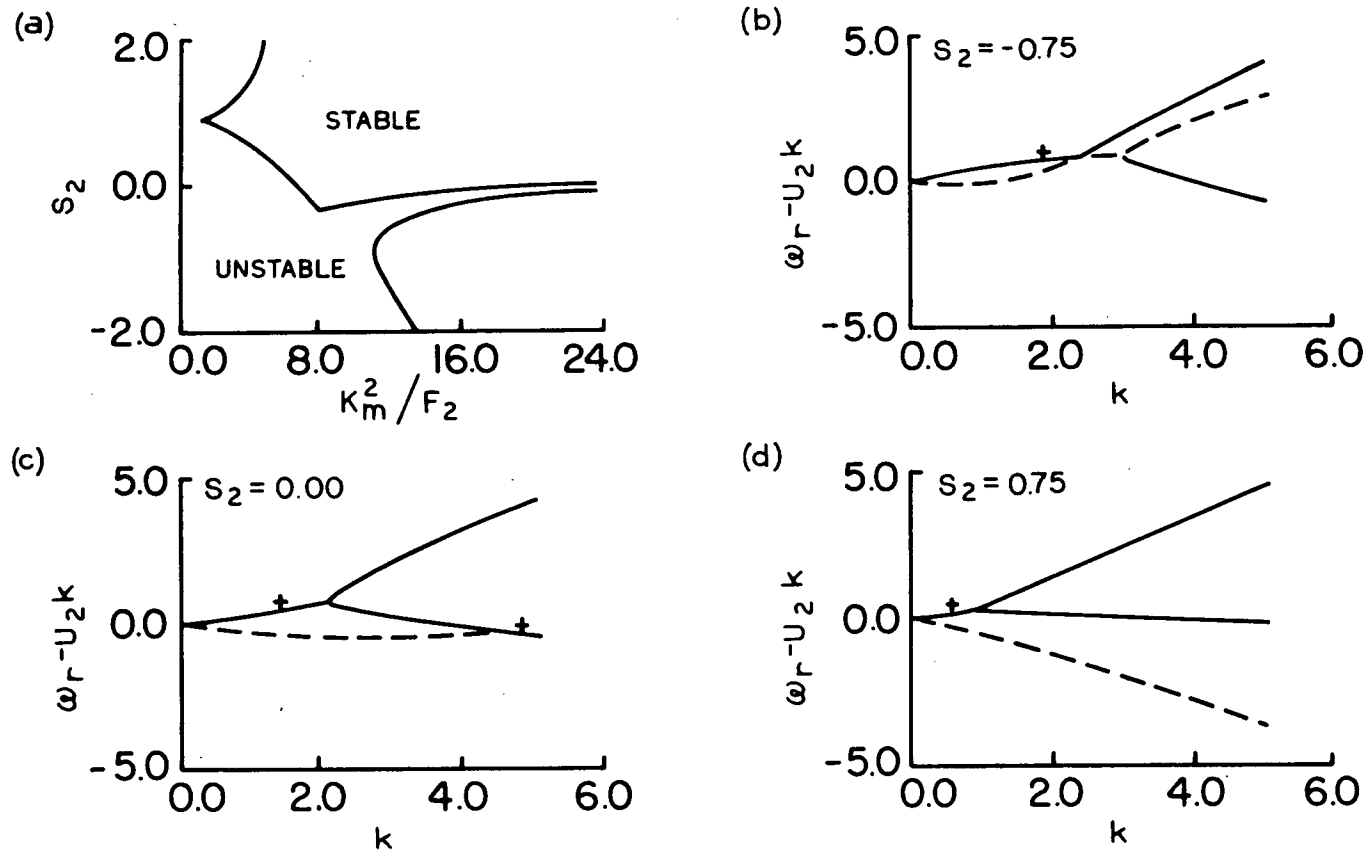

Figure 4.9:

S_2	Maximum Growth Rate	$\lvert\mu_1/\mu_2\rvert$	$\lvert\mu_3/\mu_2\rvert$	δ_1	δ_3
-0.75	0.64	0.88	0.51	54.87(+)	64.20(+)
0.00	0.38	1.19	0.30	48.70(+)	- 2.42(+)
0.00	0.07	0.16	0.66	- 9.28(+)	87.72(+)
0.75	0.09	1.38	0.56	19.79(+)	-11.40(+)

As in figure 4.6 with $\hat{T} = 0$.

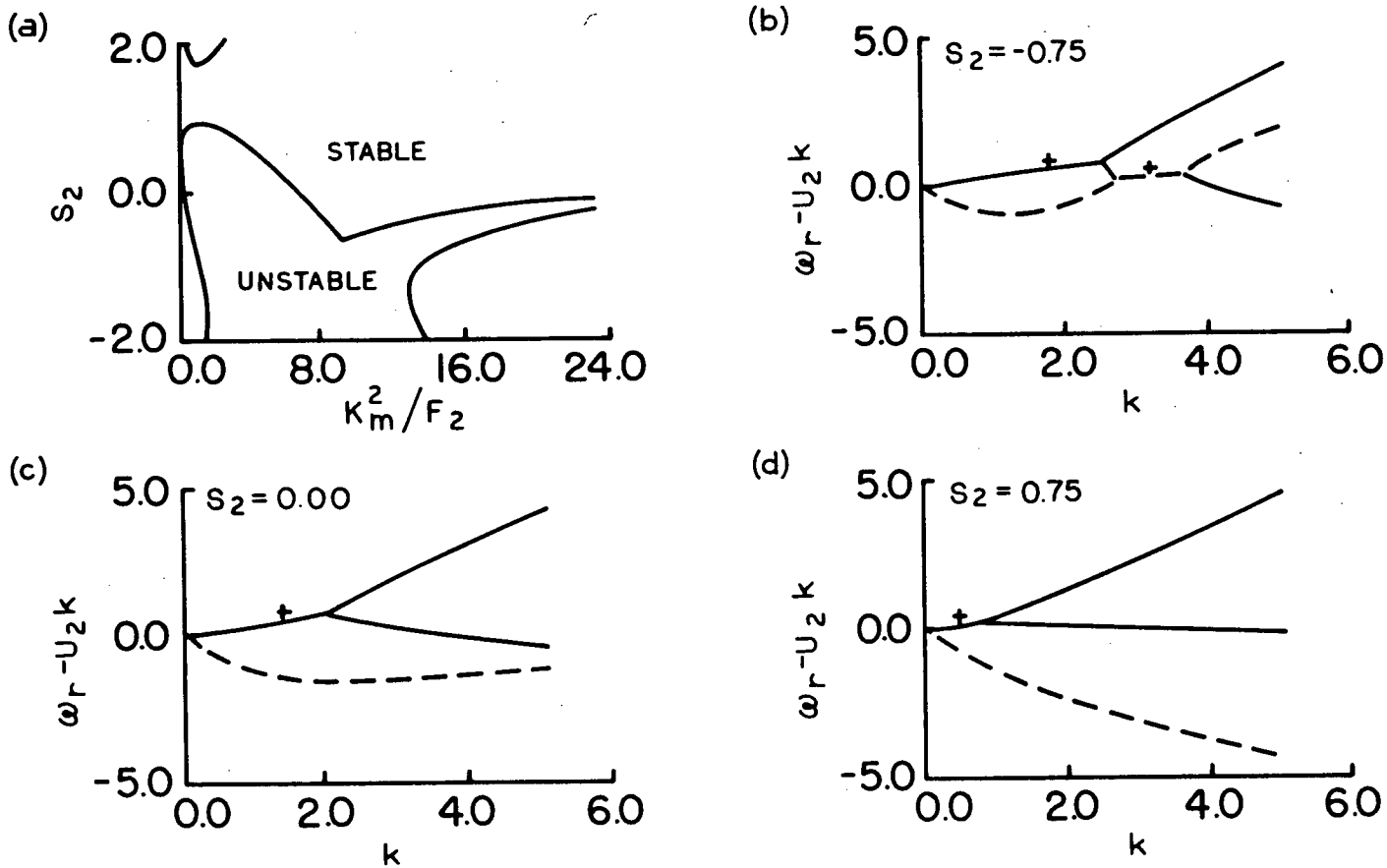

Figure 4.10:

S_2	Maximum Growth Rate	$\lvert\mu_1/\mu_2\rvert$	$\lvert\mu_3/\mu_2\rvert$	δ_1	δ_3
-0.75	0.56	1.09	0.26	56.68(+)	-75.27(-)
-0.75	0.41	0.41	1.17	-11.76(+)	78.50(+)
0.00	0.37	1.26	0.15	45.28(+)	9.36(+)
0.75	0.07	1.51	0.26	13.09(+)	- 5.21(+)

As in figure 4.6 with $\hat{T} = 5$.

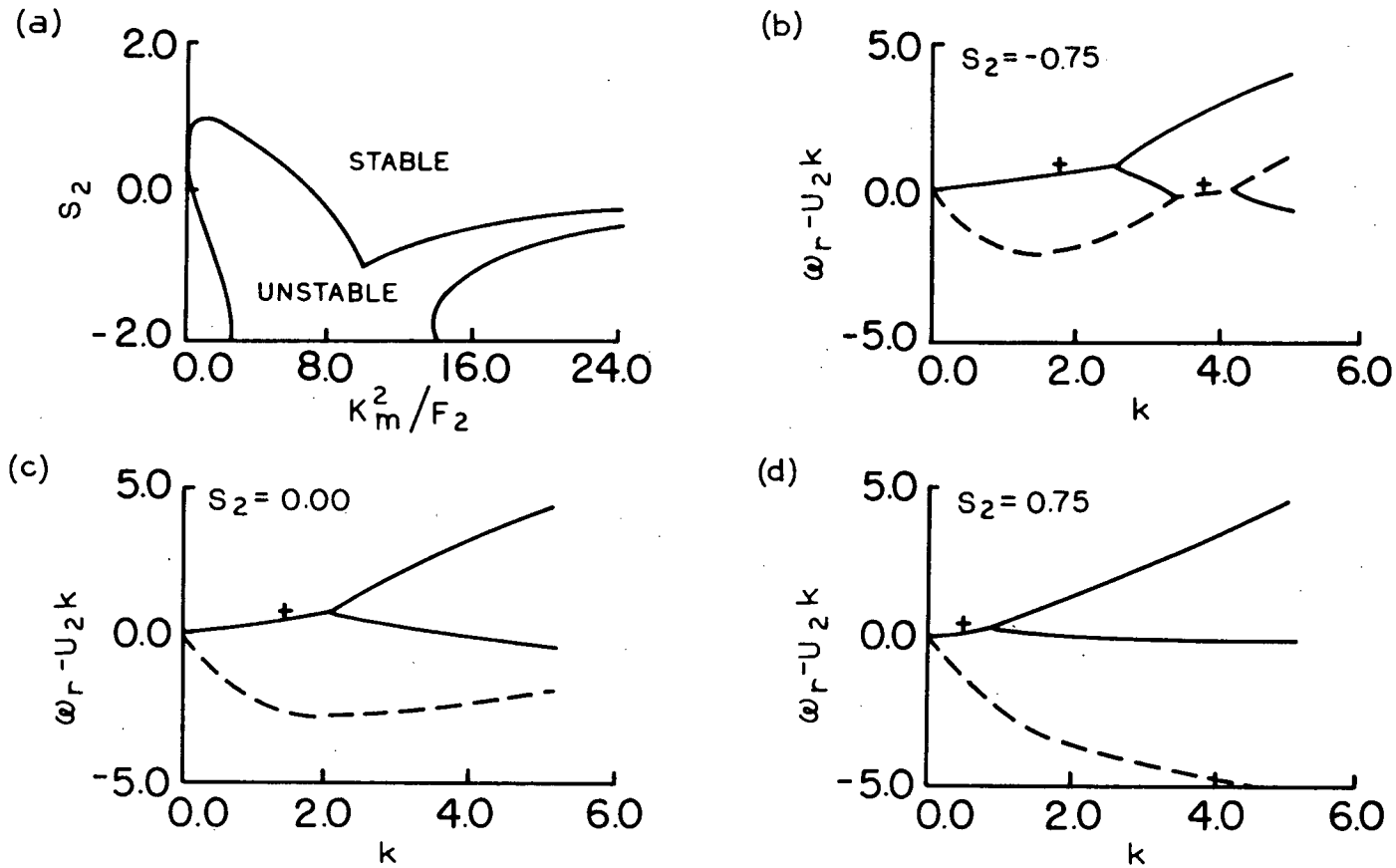

Figure 4.11:

S_2	Maximum Growth Rate	$\lvert\nu_1/\nu_2\rvert$	$\lvert\nu_3/\nu_2\rvert$	δ_1	δ_3
-0.75	0.54	1.12	0.15	59.64(+)	-64.93(-)
-0.75	0.38	0.28	1.43	-18.33(+)	82.49(+)
0.00	0.37	1.29	0.10	44.54(+)	13.14(+)
0.75	0.06	1.56	0.17	11.15(+)	- 3.66(+)

As in Figure 4.6 with $\hat{\tau} = 10$.

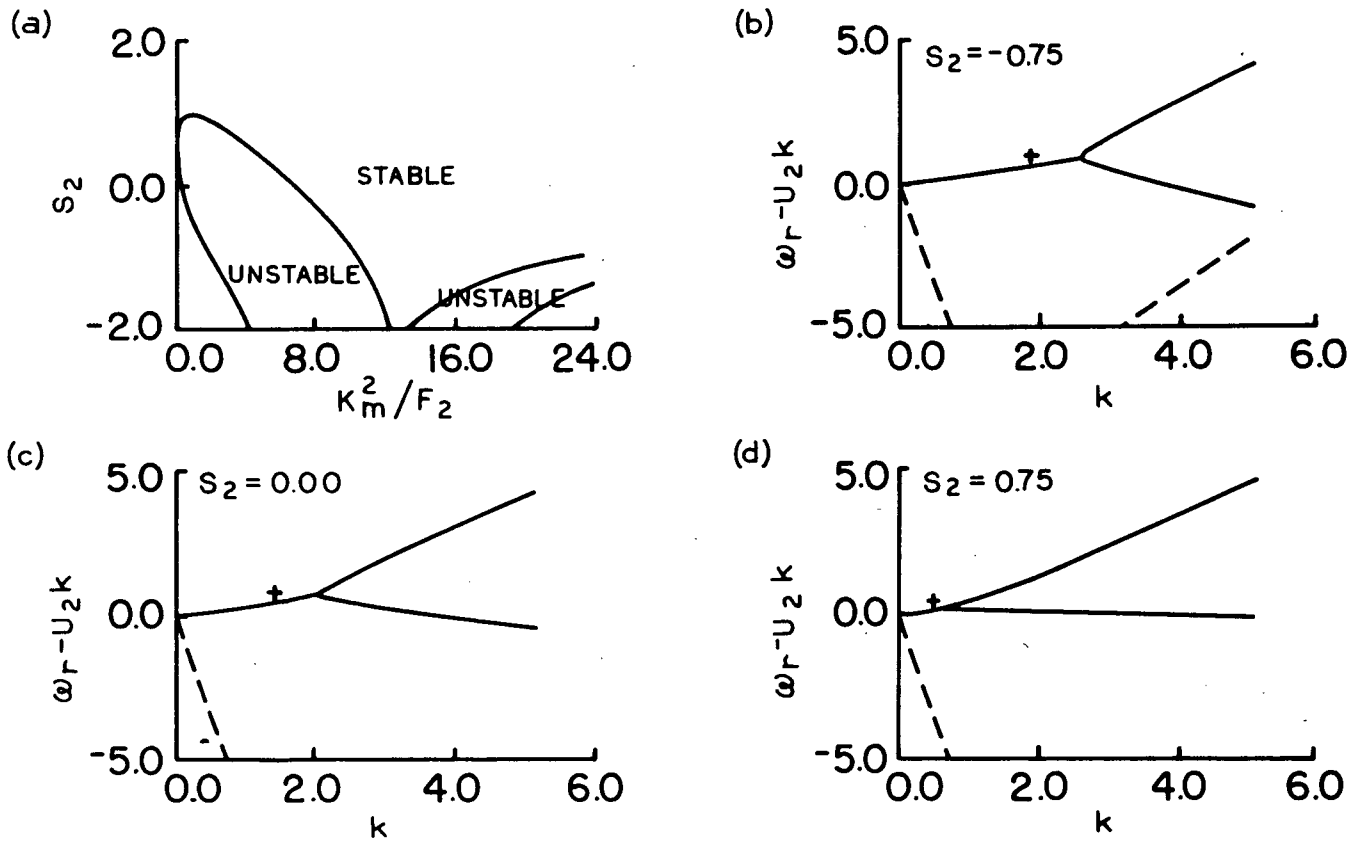

Figure 4.12:

S_2	Maximum Growth Rate	$\lvert\mu_1/\mu_2\rvert$	$\lvert\mu_3/\mu_2\rvert$	δ_1	δ_3
-0.75	0.52	1.14	0.06	62.61(+)	-56.64(-)
-0.75	0.26	0.14	2.11	-26.62(+)	-86.32(-)
0.00	0.36	1.32	0.04	43.93(+)	17.16(+)
0.75	0.05	1.64	0.07	13.89(+)	- 3.27(+)

As in figure 4.6 with $\hat{T} = 30$.

from -30 to +30 the S_2 -wave dispersion curve (which for large $\hat{T}$ is a topographic Rossby wave modified by the shears) decreases from being a generally positive root to being a negative root (consistent with the shallow water being to the right of the direction of phase propagation; see Longuet-Higgins, 1972). In decreasing from positive values at $\hat{T} = -30$ to negative values at $\hat{T} = +30$, the S_2-wave passes through and interacts with the curvature wave. For $S_2 = 0$ and 0.75 the S_2-wave root already lies below the curvature wave root at $\hat{T} = 0$ and hence no interaction takes place between these waves for $\hat{T} = 0$. For $S_2 = -0.75$ the S_2-wave does not lie below the curvature wave for the full range of k considered until $\hat{T} = +30$ and hence some interaction between these waves does occur for $\hat{T} > 0$ in the presence of large curvature in the mean velocity profile. Thus, for moderate curvature the interaction between the curvature and S_2-waves occurs for $\hat{T} < 0$ while for large curvature the interaction generally occurs for $\hat{T} > 0$. In either case the effect of topography on the direction of phase propagation is in opposition to advection in the lower layer (relative to the other layers) thus restraining the phase speed of the waves in the lower layer to remain in the range where interaction with the other waves in the system is possible.

It should be noted here that even a very large bottom slope does not cause significant reduction of the growth rates of instabilities due to the S_2- and curvature waves interacting. However, if one concentrates on the case $S_2 = -0.75$ in figures 4.6 to 4.12 (in each case the

instability at smaller k is due to such an interaction) it will be seen that topography does strongly affect both the phase and amplitudes of these waves in the lower layer. Of particular interest is the decrease in perturbation amplitude in the lower layer with increasing bottom slope. Hence, even in this case, topography has a stabilizing influence, but its significance is restricted to the lower layer where the bottom slope is strongly felt.

Finally we refer the reader to Orlansky and Cox (1973) for an alternative explanation of the stabilizing effect of bottom topography based on energy arguments involving the interchange of fluid elements within the "wedge of instability" in a continuously stratified fluid. The application to our model is simple. A large cross-channel bottom slope will cause the fluid trajectories near the bottom to also have a significant cross-channel slope and thus the release of potential energy from the lower interface is inhibited. Hence the bottom intensified waves due to the interaction of the S_2- and curvature waves are stabilized by such a slope. However, in the region of the upper interface, the fluid trajectories of the unstable waves due to the interaction of the S_1- and curvature waves are not nearly as strongly affected by the sloping bottom and hence potential energy continues to be released from the upper interface. Further, a slightly sloping bottom in the same sense as (but shallower than) the slope of the lower interface may actually increase the growth rates of the instabilities which extract potential energy from the lower interface by constraining the fluid trajectories

in this region to lie within the "wedge of instability".

Relative Layer Thicknesses

Figures 4.13 to 4.15 illustrate the effect of increasing H_1/H_2 while holding H_3/H_2 constant. Two basic effects are seen. The curvature wave and the S_1-wave tend to separate as H_1/H_2 increases causing the instabilities to shift to lower wavenumbers. The S_2-wave dispersion curve is affected little by changes in H_1/H_2 but as the other two curves separate, when the curvature and S_2-wave dispersion curves meet, an instability results.

An exactly analogous situation occurs for H_3/H_2 increasing (Figures 4.16-4.18) only in this case the curvature and S_1-wave dispersion curves come together as H_3/H_2 increases.

In general we note that as a layer thickens the perturbation velocities in that layer have a tendancy to decrease. This is due to the fact that as a layer thickens it requires more energy to maintain the same velocities in that layer, yet the thickening of a layer does not make more potential energy available for this purpose and thus a decrease in perturbation velocities in this layer will generally occur (this contrasts with the case of barotropic instability where the thickening of a layer makes more kinetic energy available). Alternative possibilities are to have smaller perturbation velocities in the other layers or to have a smaller growth rate for the wave. In general the system responds with a combination of these possibilities.

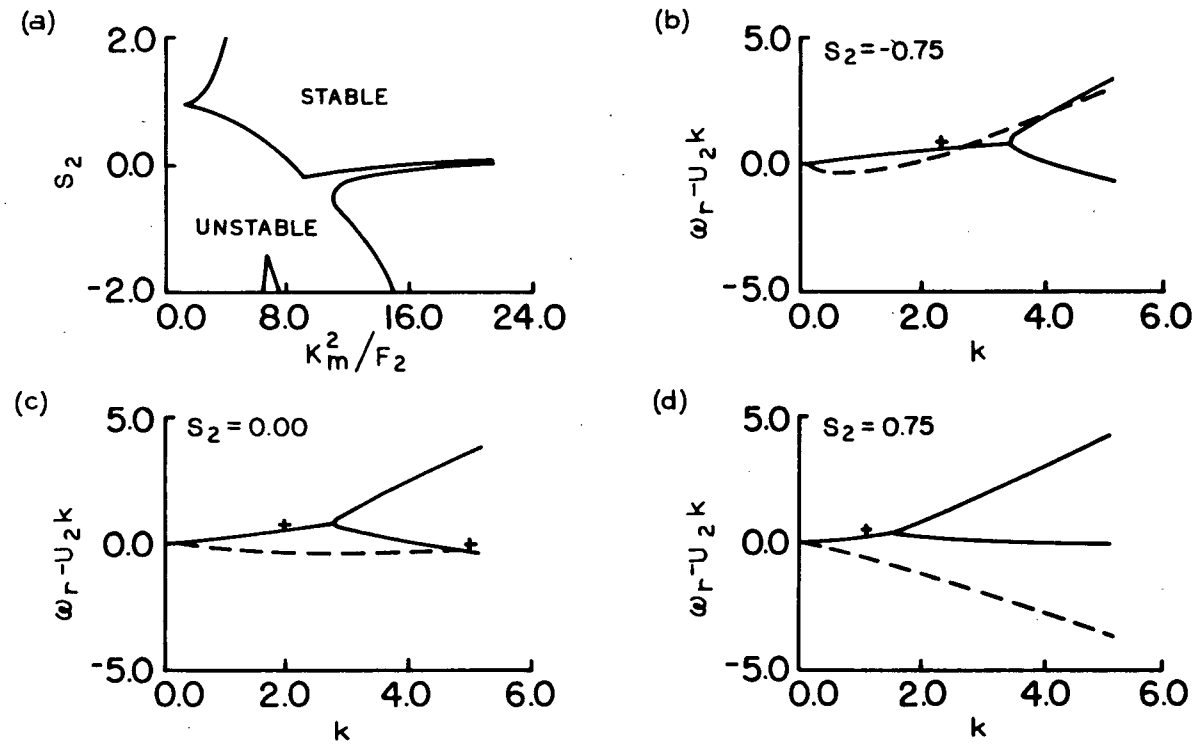

Figure 4.13:

S_2	Maximum Growth Rate	$\lvert\mu_1/\mu_2\rvert$	$\lvert\mu_3/\mu_2\rvert$	δ_1	δ_3
-0.75	0.78	1.18	0.63	72.73(+)	36.85(+)
0.00	0.54	1.67	0.27	55.24(+)	- 5.79(+)
0.00	0.06	0.34	0.63	- 8.52(+)	-82.98(-)
0.75	0.22	1.81	0.46	27.47(+)	-21.64(+)

Stability boundaries (a) for $H_1/H_2 = 0.5$, $H_3/H_2 = 1$, $\hat{T} = 0$, $\hat{\beta} = 0$ and first mode (m=1) dispersion curves corresponding to these parameter values with $F_2 = 1$ and $\delta_2 = -0.75$(b), 0.00(c), and 0.75(d) . Statistics for positions of maximum growth rate (marked by plus signs) are given in the table.

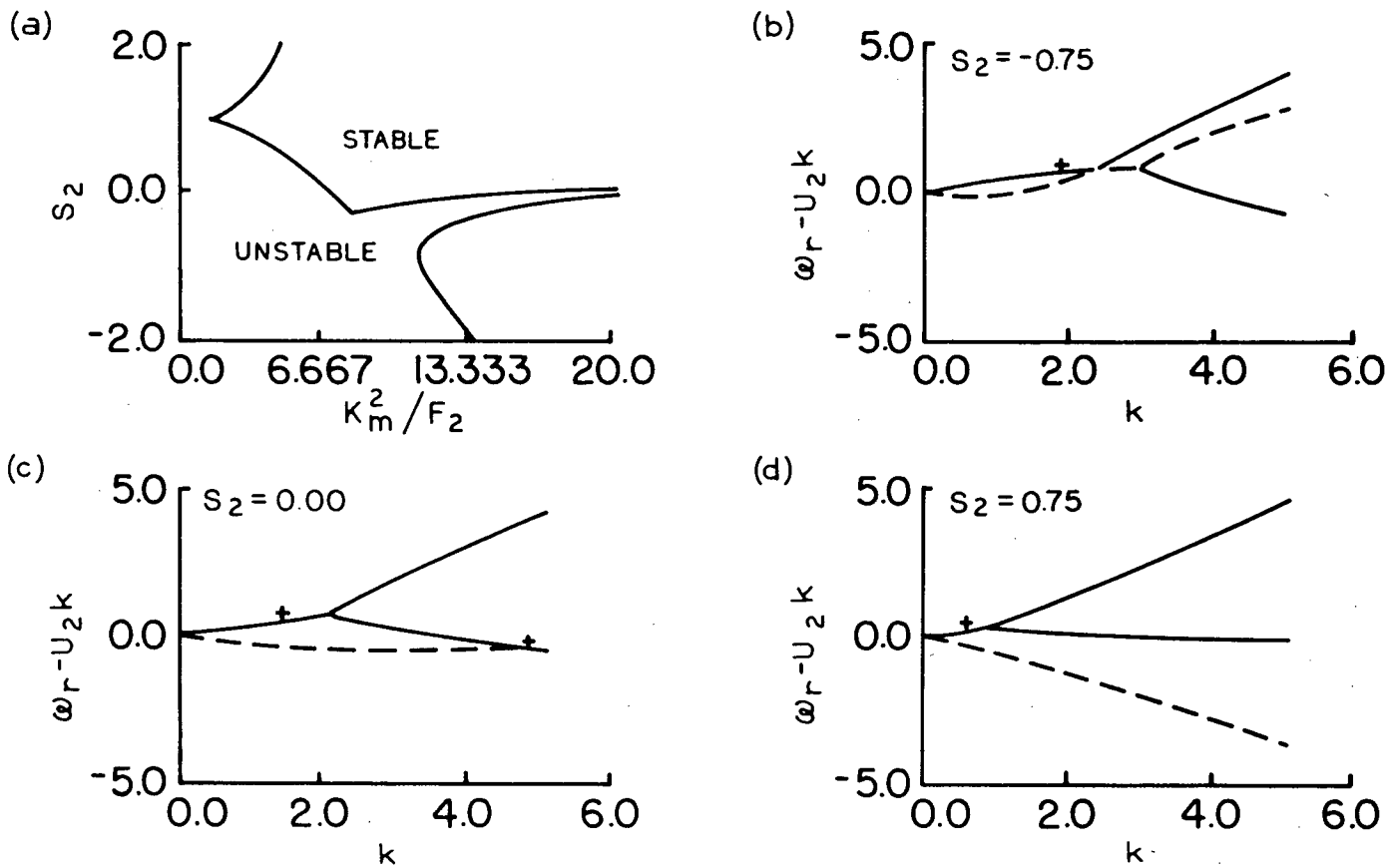

Figure 4.14:

S_2	Maximum Growth Rate	$\lvert\mu_1/\mu_2\rvert$	$\lvert\mu_3/\mu\rvert$	δ_1	δ_3
-0.75	0.64	0.88	0.51	54.87(+)	64.20(+)
0.00	0.38	1.19	0.30	48.70(+)	- 2.42(+)
0.00	0.07	0.16	0.66	- 9.28(+)	87.72(+)
0.75	0.09	1.38	0.56	19.79(+)	-11.40(+)

As in figure 4.03 with $H_1/H_2 = 1$, $H_3/H_2 = 1$.

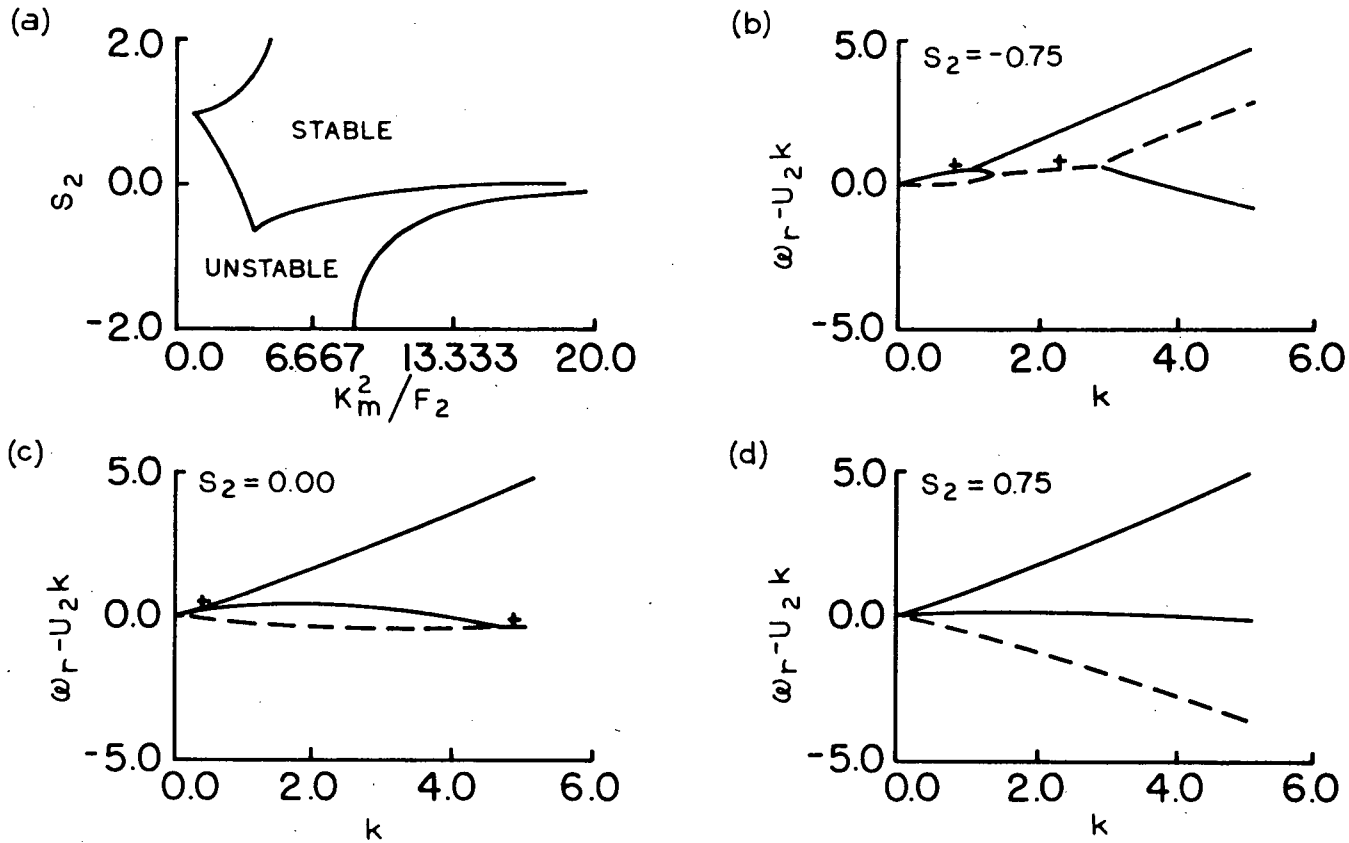

Figure 4.15:

S_2	Maximum Growth Rate	$\lvert\mu_1/\mu_2\rvert$	$\lvert\mu_3/\mu_-\rvert$	δ_1	δ_3
-0.75	0.15	0.46	0.21	32.43(+)	-69.38(-)
-0.75	0.43	0.12	0.99	-10.90(+)	72.37(+)
0.00	0.03	0.54	0.39	16.06(+)	0.10(+)
0.00	0.07	0.03	0.68	- 9.71(+)	81.61(+)

As in figure 4.13 $H_1/H_2 = 5$, $H_3/H_2 = 1$.

Values are given in order of increasing k

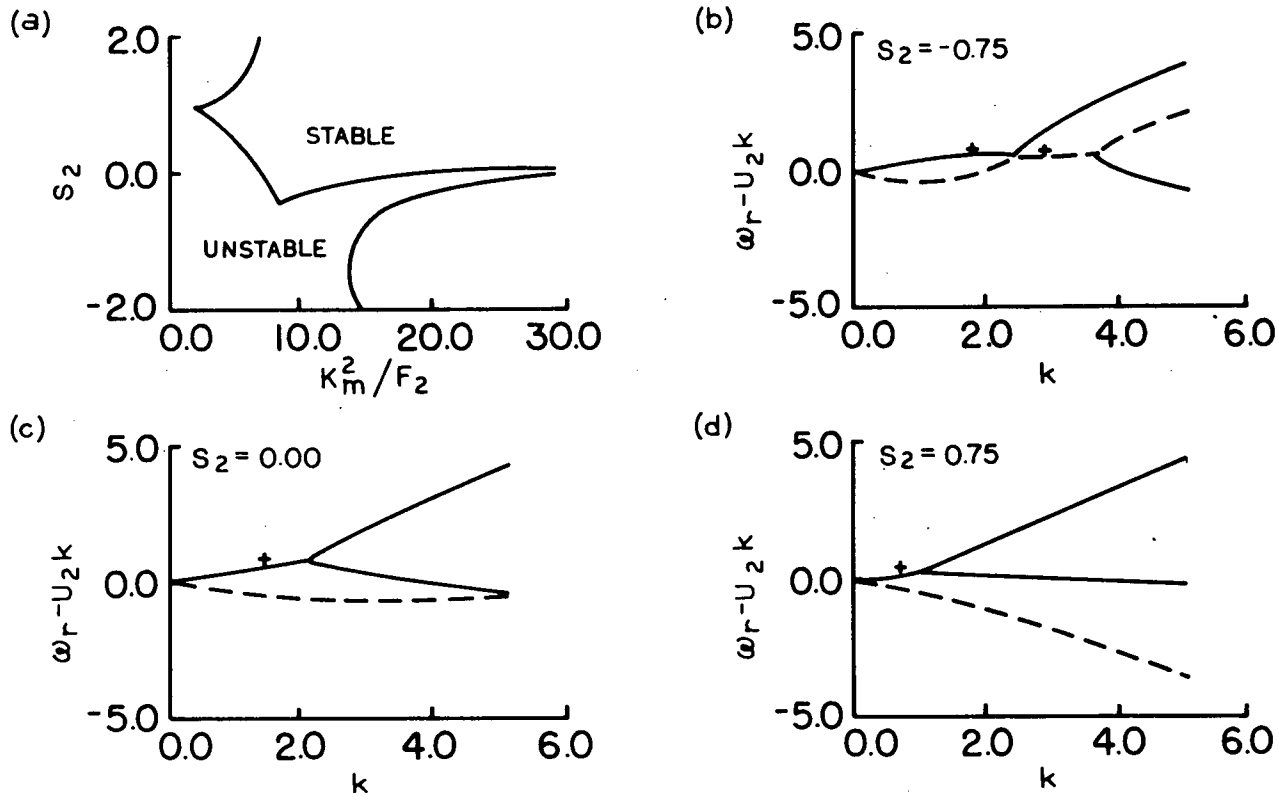

Figure 4.16:

S_2	Maximum Growth Rate	$\lvert\mu_1/\mu_2\rvert$	$\lvert\mu_3/\mu_2\rvert$	δ_1	δ_3
-0.75	0.65	0.96	0.56	49.09(+)	87.53(+)
-0.75	0.55	0.46	1.36	-10.17(+)	70.87(+)
0.00	0.39	1.14	0.38	49.54(+)	1.20(+)
0.00	0.09	0.12	1.21	-17.47(+)	74.82(+)
0.75	0.11	1.26	0.83	25.36(+)	-13.50(+)

As in figure 4.13 with $H_1/H_2 = 1$, $H_3/H_2 = 0.5$. Values are given in order of increasing k .

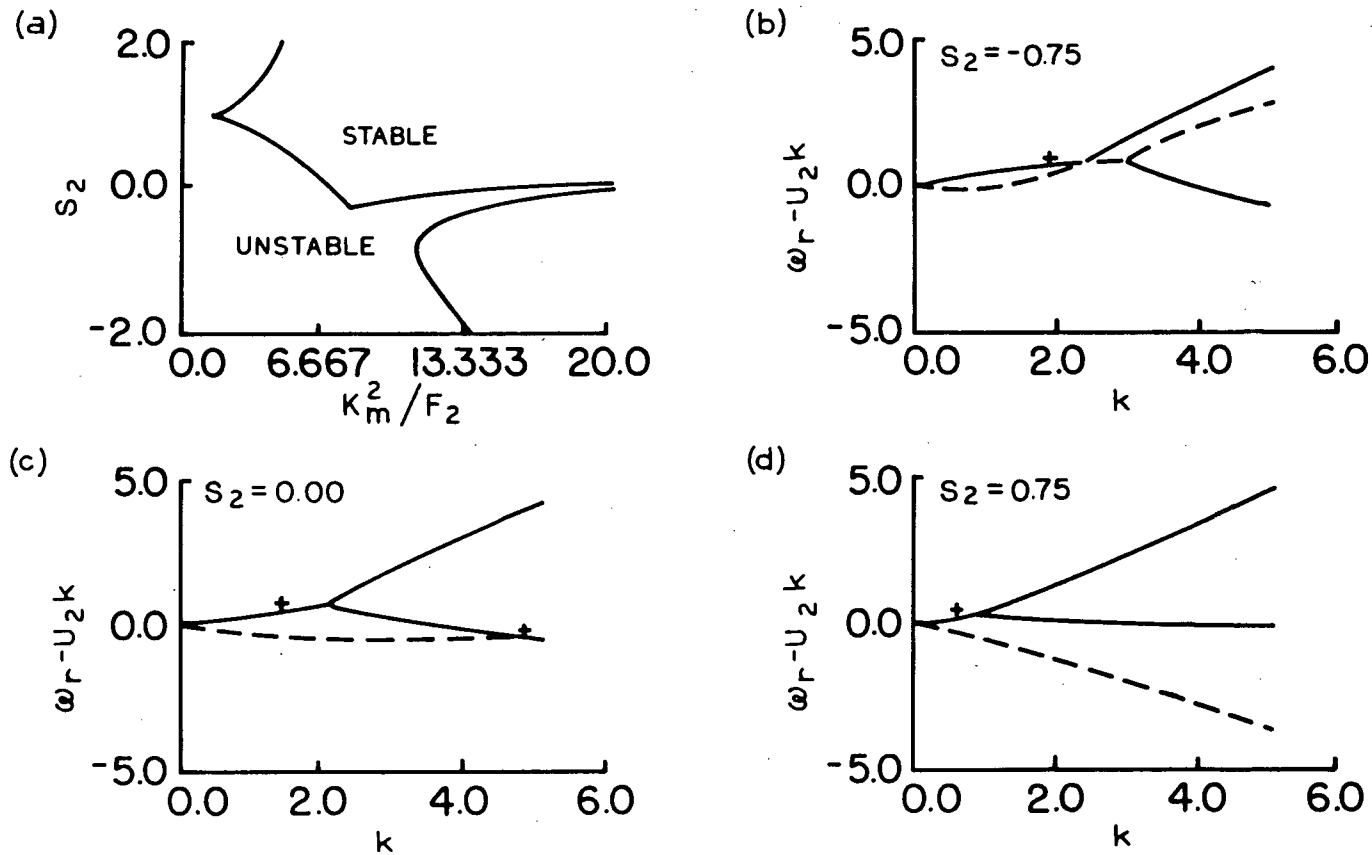

Figure 4.17:

S_2	Maximum Growth Rate	$\lvert\mu_1/\mu_2\rvert$	$\lvert\mu_3/\mu_2\rvert$	δ_1	δ_3
-0.75	0.64	0.88	0.51	54.87(+)	64.20(+)
0.00	0.38	1.19	0.30	48.70(+)	- 2.42(+)
0.00	0.07	0.16	0.66	- 9.28(+)	87.72(+)
0.75	0.09	1.38	0.56	19.79(+)	-11.40(+)

As in figure 4.13 with $H_1/H_2 = 1$, $H_3/H_2 = 1$.

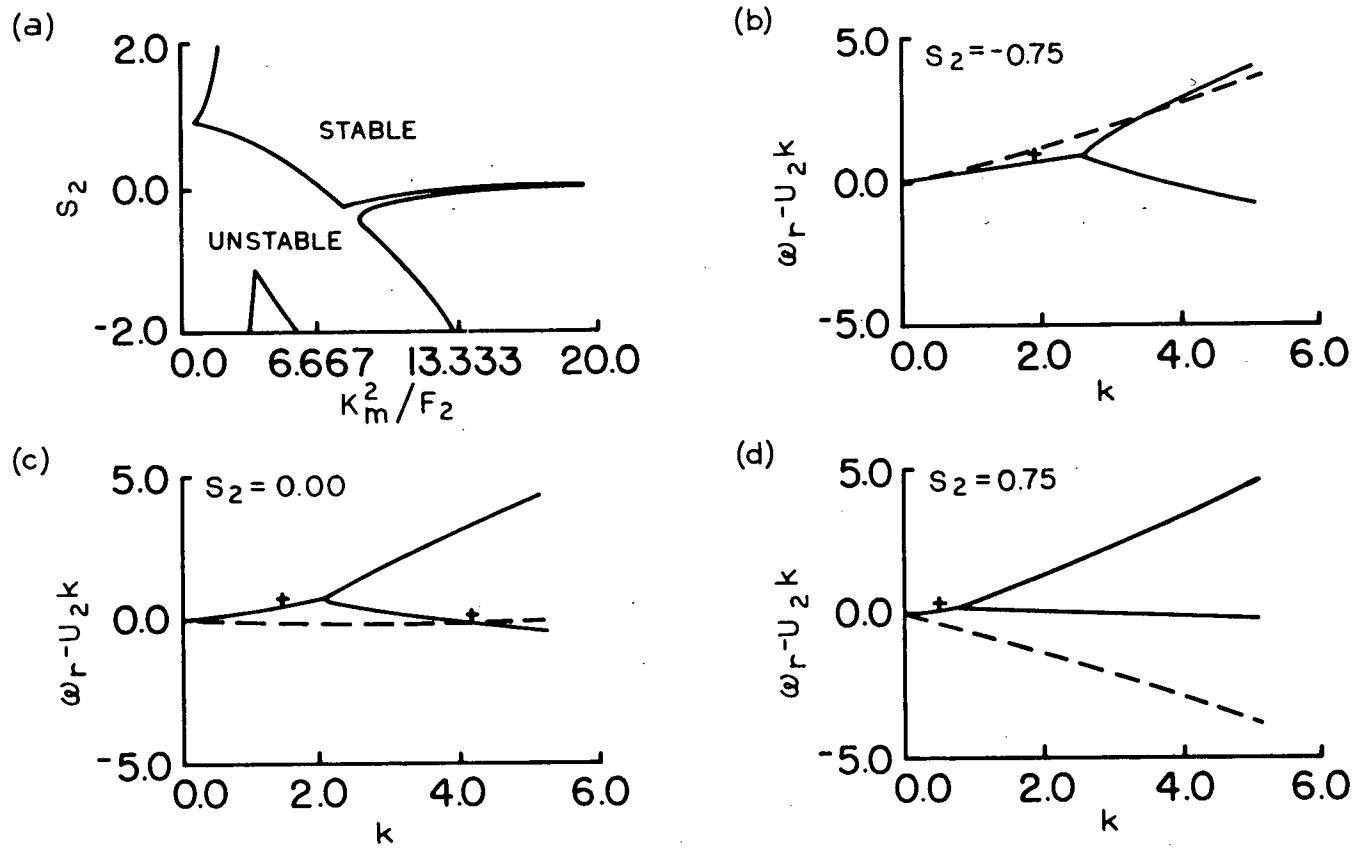

Figure 4.18:

S_2	Maximum Growth Rate	$\lvert\mu_1/\mu_2\rvert$	$\lvert\mu_3/\mu_2\rvert$	δ_1	δ_3
-0.75	0.51	1.07	0.16	67.92(+)	0.48(+)
0.00	0.37	1.29	0.11	45.81(+)	-11.30(+)
0.00	0.02	0.23	0.13	- 1.60(+)	-61.43(-)
0.75	0.06	1.57	0.15	10.95(+)	- 7.24(+)

As in figure 4.13 with $H_1/H_2 = 1$, $H_3/H_2 = 5$.

The point to be noted is that it is not always true that the case $H_1 = H_2 = H_3$ is typical.

Density Stratification

We first note that for a given channel geometry (i.e. H_2 and L fixed), F_2 $(=f_o^2 L^2/g'H_2)$ decreases as the effective density stratification increases either through a decrease in the rate of rotation or through an increase in the actual density stratification (either of these possibilities decreases the slope of the isopycnals necessary for the process of baroclinic instability).Thus through its presence in K_m^2/F_2 in (4.1) it is clear that an increase in stratification decreases the range of K_m^2 in which instabilities occur. This explains why,for the case of large curvature, the range of unstable waves found by Davey is only about half of that found here (after accounting for the difference in terminology), (see figure 4.3). This is primarily due to the over-estimation of the stabilizing effect of density stratification when considering a fluid of three layers, each of uniform density (again see the last paragraph in section 2).

One way to visualize the stabilizing effect of density stratification on these unstable rotational waves is to consider their effect on the isopycnal slopes. An increase in density stratification causes a decrease in the slope of the isopycnals in the mean state and hence a smaller "wedge of instability" (see Pedlosky, 1971; Orlansky and Cox, 1973). This naturally decreases the range of wavelengths for which instabilities may occur and generally causes a corresponding decrease in the growth rates of the most unstable waves in the system.

The strong stabilizing influence of density stratification is also seen from its effect on the influence of β and bottom slope. As seen previously , an increase in either of these parameters is generally accompanied by a decrease in the range of unstable waves as well as a decrease in the maximum growth rate of the unstable waves. Thus the presence of F_2 in the denominator of $\hat{\beta}$ and $\hat{T}$ (Equn. 4.1) clearly shows further evidence of the stabilizing effect of density stratification.

Curvature in the Mean Velocity Profile

The curvature of the mean velocity is indicated by the difference S_1-S_2 . (Note that $S_1 = S_2$ corresponds to no curvature of the mean velocity in the middle layer but over the full depth of the fluid the velocity field is of the form ⌊ . A study of part (a) of figures 41 to 418 shows that the unstable range is always small near $S_2 = 1$ (recall that $S_1 = 1$ in these figures) and that the growth rate of the most unstable wave generally increases away from $S_2 = 1$. This is in agreement with the qualitative statement made by Davey (1977) - "... the range of unstable wavelengths increases as the curvature is increased from zero". When one notes that it is the curvature wave which interacts with one of the other waves to generate an instability (at least when H_2 is significant - see section 5) and that in the limit $S_1 = S_2$ this wave tends to become energetically inactive (recall that for $F_1 = F_2 = F_3$, and $T = \beta = 0$ the curvature wave reduces to the stable root $c = U_2$), Davey's result is not surprising.

One may also consider the effect of curvature in the mean velocity profile on baroclinic instability by looking at the mean potential vorticity gradients. Setting $S_1 = S_2$ in the expressions given in (3.1) (with β, h, and the horizontal curvature of the mean velocities set equal to zero to isolate the effects of vertical curvature) we have:

$$q_{1y} = 2F_1 S_1$$

$$q_{2y} = 0$$

$$q_{3y} = -2F_3 S_1$$

Since the necessary condition for instability states only that a change in sign of q_y must occur somewhere in the fluid, this criterion is clearly satisfied. However, if the thickness of the middle layer is significant, the regions in which q_y has opposite signs are effectively isolated and instabilities are inhibited. [Note, however, that as the thickness of the middle layer is decreased relative to that of the other layers (so that F_2 becomes large relative to F_1 and F_3) the upper and lower layers will interact more strongly and thus generate significant instabilities (see section 5).] If on the other hand, $S_1 \neq S_2$ a change of sign in q_y between adjacent layers may occur and instabilities are more probable.

Finally, we note that although in our figures we have only plotted cases in which $S_2 < S_1$ so that the unstable long waves are generally due to the curvature and S_1-waves interacting, it is important to note that for $S_2 > S_1$, the S_2-wave and curvature wave will interact at long wavelengths. Thus although the relatively long unstable

waves shown in the figures of this section tend to be surface intensified, for $S_2 > S_1$, the long unstable waves will tend to be botton intensified.

5. Two-layer Models

It is of interest here to consider the cases in which one of H_1 , H_2 or H_3 vanishes. We first consider the case $H_2 \to 0$ (Figure 5.1). In this case $F_2 \to \infty$ and thus from (2.14) we see that $\psi_2 \to \frac{1}{2}(\psi_1+\psi_3)$. This in turn gives $\phi_2 \to \frac{1}{2}(\phi_1+\phi_3)$ and $U_2 \to \frac{1}{2}(U_1+U_3)$. Equations (3.1) thus reduce to (after replacing the subscript 3 by 2 to relabel the layers appropriately):

$$\begin{aligned} &\text{(a)} \quad (U_1-c)[\phi_{1yy}-k^2\phi_1-F_1(\phi_1-\phi_2)] + \phi_1 \frac{\partial q_1}{\partial y} = 0 \\ &\text{(b)} \quad (U_2-c)[\phi_{2yy}-k^2\phi_2-(\frac{H_2}{H_2-bh})F_2(\phi_2-\phi_1)] + \phi_2 \frac{\partial q_2}{\partial y} = 0 \end{aligned} \tag{5.1}$$

where $$\frac{\partial q_1}{\partial y} = \beta - U_{1yy} + F_1(U_1-U_2)$$

$$\frac{\partial q_2}{\partial y} = \beta - U_{2yy} + \frac{H_2}{H_2-bh} F_2(U_2-U_1) + \frac{b}{R_0(H_2-bh)} h_y$$

with $\phi_1 = \phi_2 = 0$ on $y = \pm 1$.

Assuming $bh << H_2$, these equations reduce to (2.2.13) of Pedlosky (1964). Hence, as expected, the case $H_2 \to 0$ simply gives the two-layer model.

Taking the limit $H_2 \to 0$ in (3.9) we see that one root of the dispersion relation for the three layer model is $C = 0$(i.e. $c = U_2 = (U_1+U_3)/2$) . Thus the roots of the dispersion relation in this case reduce to $\hat{\omega} - [(U_1+U_3)/2]k = 0$ plus those appropriate to a two-layer fluid.

Figure 21 is an example of how this transition of roots occurs.

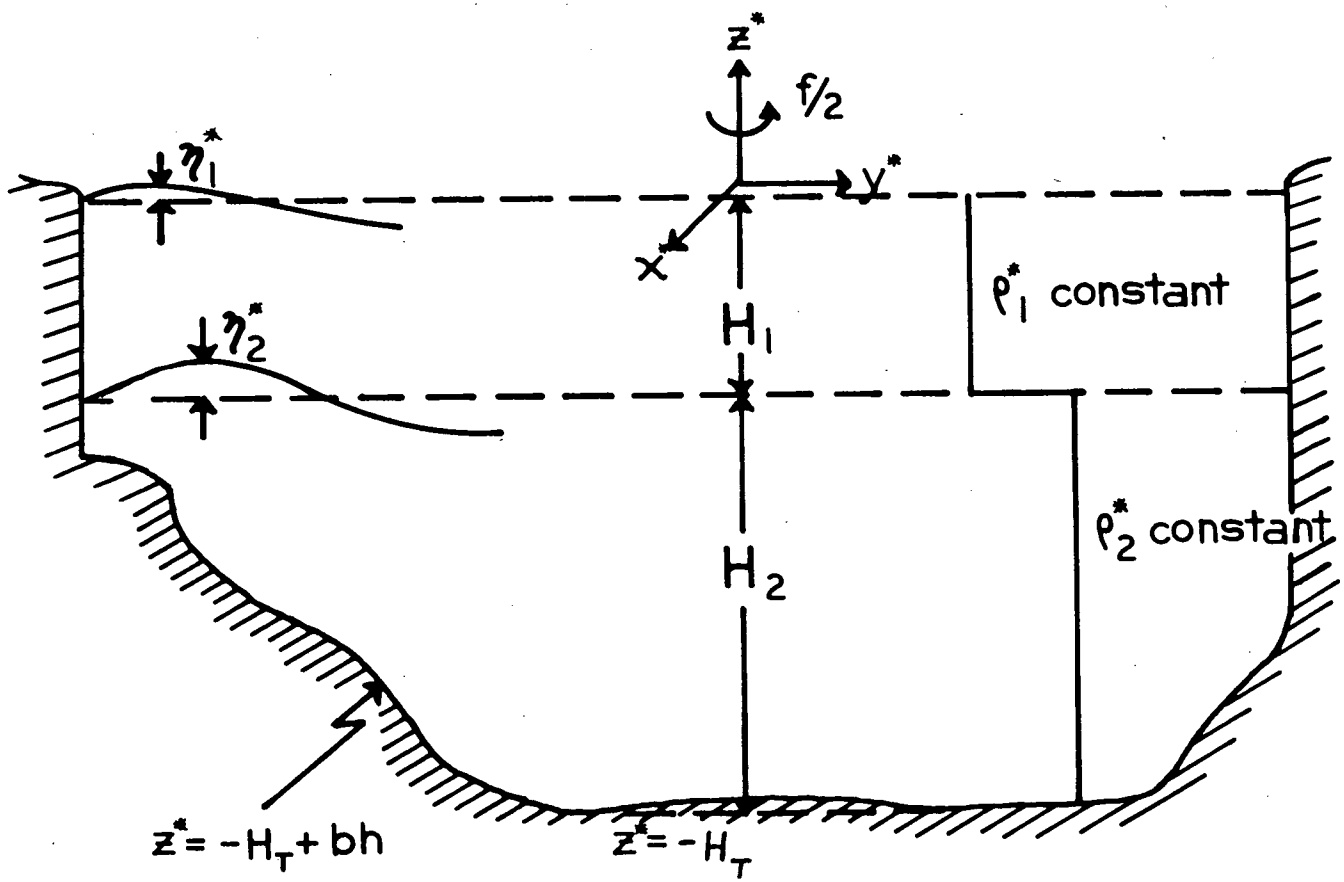

Figure 5.1: A cross-section of the two layer model obtained by letting $H_2 \to 0$.

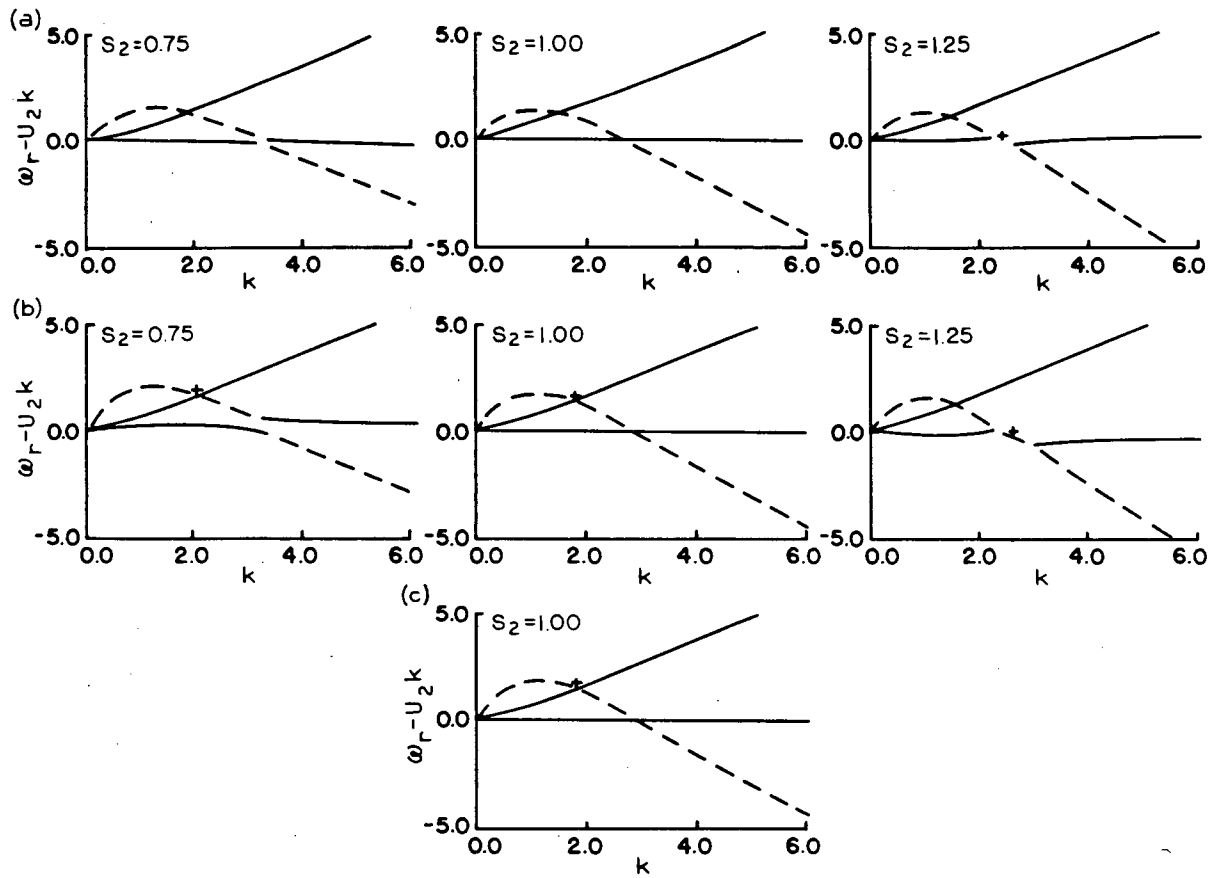

	S_2	Maximum Growth Rate	$\lvert\mu_1/\mu_2\rvert$	$\lvert\mu_3/\mu_2\rvert$	δ_1	δ_3
Figure 5.2a: H_2 = 60m	1.25	0.21	0.28	3.36	54.92(+)	-50.77(+)
Figure 5.2b:	0.75	0.12	0.60	1.54	60.19(+)	-18.52(+)
H_2 = 6m	1.00	0.06	0.61	1.65	27.42(+)	- 9.84(+)
	1.25	0.37	0.19	1.43	20.89(+)	-55.97(+)
Figure 5.2c:	1.00	0.09	0.57	1.62	42.02(+)	-13.63(+)
$H_2 = 10^{-5}$m						

Dispersion curves for the first mode (m=1) for S_1 = 1, $f_0 = 10^{-4}$rad.s^{-1}, β = 0, T = -10, L = 10km, g' = 0.02m s^{-2}, H_T = 180m and $H_1 = H_3 = (H_T - H_2)/2$

Only the case $\beta = 0$, $T = -10$ has been shown but the same general features are seen in other cases. For definiteness we have taken $f_0 = 10^{-4}$ rad s^{-1}, $L = 10$ km , $g' = 0.02$ ms^{-2}, $H_T = 180$ m , and $H_1 = H_3 = (H_T - H_2)/2$ for $H_2 = 60$ m , 6 m , and 10^{-5} m. For $S_1 = S_2$, the case $H_2 = 10^{-5}$ m is indistinguishable from the two layer model.

From figures (5.2a) and (5.2b) we see that a small change in curvature can cause considerable difference in the stability of the flow. For example in each of these cases when $S_2 = 1.25$ the curvature wave interacts with the S_2-wave to create a significant instability near $k = 2.0$. However, as $S_2 \to S_1$ the curvature wave tends to become energetically inactive and this instability diminishes. In each case we also see that the cases $S_2 = 0.75$ and $S_2 = 1.00$ are very similar at least for the choice of parameters considered here. This is, of course, only one special case and we should not try to draw any general conclusions from it. However, it is clear that the stability of the system is rather sensitive to changes in the curvature of the mean velocity field and care is needed when attempting to use a two-layer model to approximate a situation in which curvature is significant. On the other hand, when $S_2 = S_1$ the three cases considered in figures (5.2a) to (5.2c) are encouraging. Although when $H_1 = H_2 = H_3 = 60$ m (5.2a) the S_1 and S_2-waves don't interact, by the time $H_2 = 6$ m (5.2b) the stability of the 3-layer system is very near that of the two-layer system shown in figure (5.2c) (all of these cases would show better agreement if the density differences between the layers were reduced

appropriately; however, the choice of an appropriate reduction is not a trivial matter). It appears that the two-layer system should be used with great care but is useful when $S_1 \simeq S_2$ and H_2 is relatively small compared to H_1 and H_3. When $H_2 \sim H_1, H_3$ the model must be "fitted" by appropriate reduction of the total density difference.

The explanation for our result is that for the two-layer model the curvature wave reduces to an energetically inactive stationary (relative to the velocity in the middle layer) wave and the S_1- and S_2- waves can now interact (though they probably should be renamed). Thus the two-layer model is a good approximation when the middle layer is thin enough for the upper and lower layers to interact and the curvature wave does not interact significantly with the other waves.

The problem with the commonly used two-layer model is that the effect of curvature is neglected. If instead of letting $H_2 \to 0$ one lets $H_1 \to 0$ we get the situation illustrated in figure 5.3 In figure 5.4 we see that in this case the curvature wave remains active and at least for the parameters we have chosen this model is a better approximation to the three layer model than is the model consisting of two constant density layers.

For $H_1 \to 0$ we see from (2.15) that $\psi_1 \to (4\psi_2 - \psi_3)/3$. Hence $U_1 \to (4U_{2o} - U_3)/3$ and $\Phi_1 \to (4\Phi_2 - \Phi_3)/3$ so that (3.1) gives (after letting $i \to i - 1$ to relable the layers appropriately):

$$(U_{1o} - c)\,[\Phi_{1yy} - k^2\Phi_1 + 8F_1(\Phi_2 - \Phi_1)/3] + \Phi_1 \frac{\partial q_1}{\partial y} = 0$$

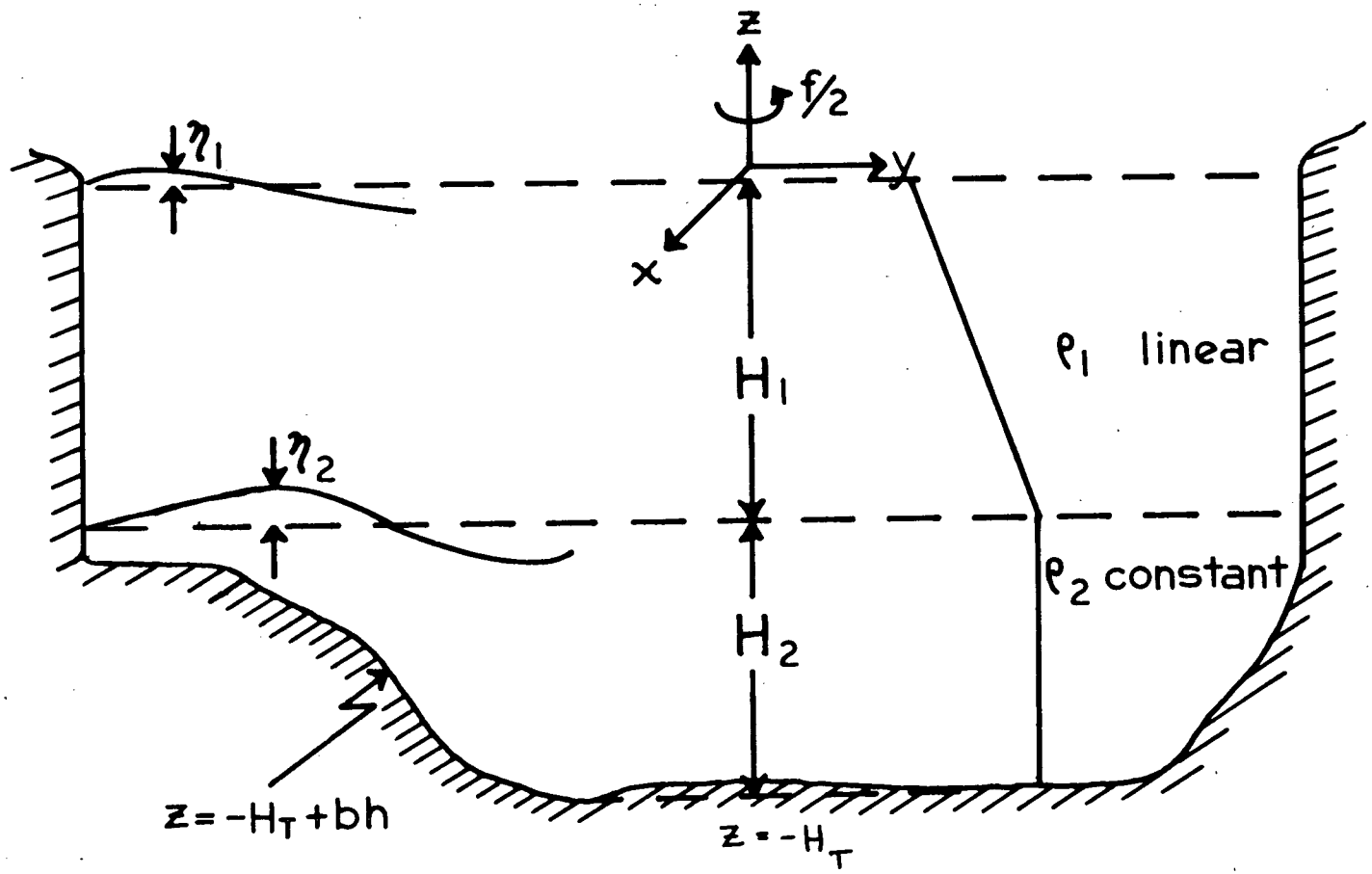

Figure 5.3: A cross-section of the two-layer model obtained by letting $H_1 \to 0$.

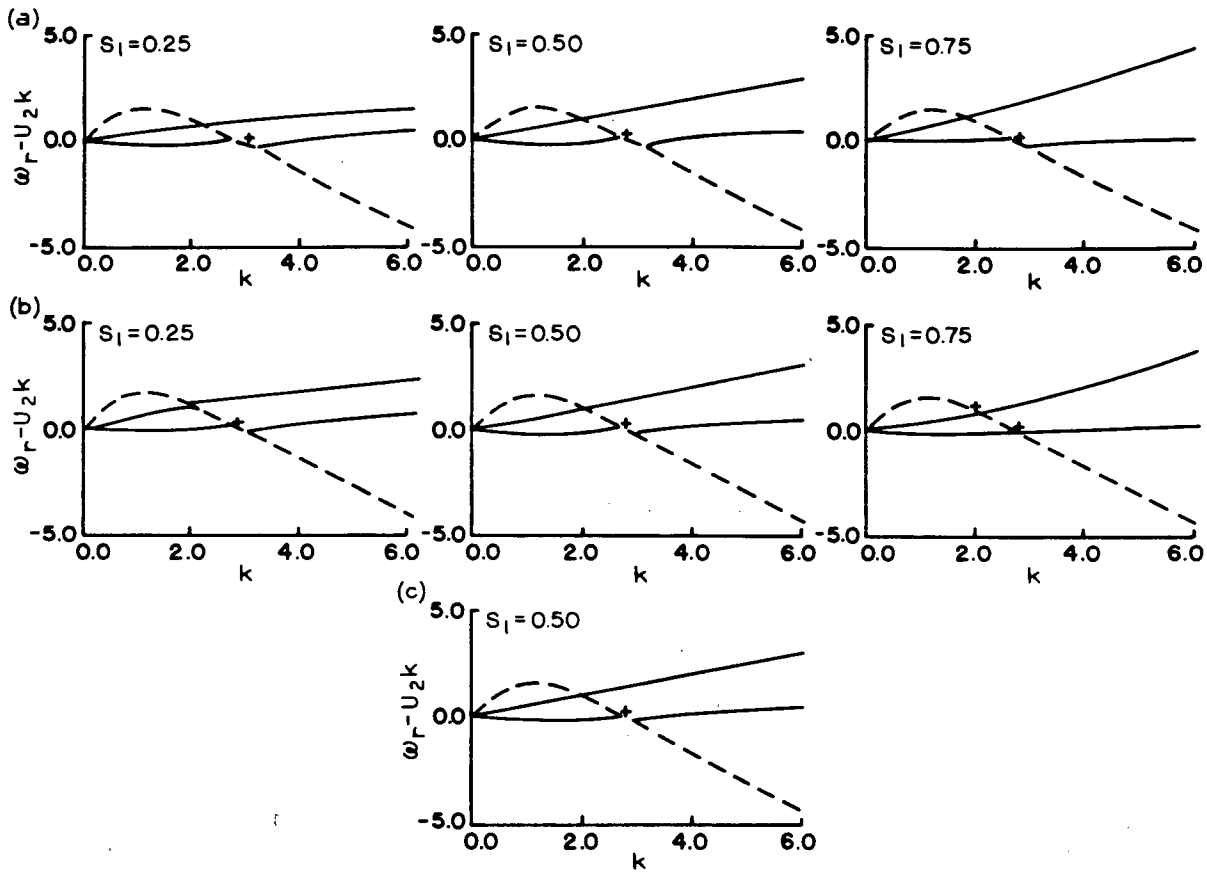

	S_1	Maximum Growth Rate	$\lvert u_1/u_2 \rvert$	$\lvert u_3/u_2 \rvert$	δ_1	δ_3
Figure 5.4a: H_1 = 60m	0.25	0.28	0.18	2.16	29.52(+)	-62.47(+)
	0.50	0.23	0.28	2.91	40.93(+)	-74.77(+)
	0.75	0.17	0.24	3.29	52.68(+)	-53.54(+)
Figure 5.4b: H_1 = 6m	0.25	0.19	0.52	2.45	26.38(+)	-78.94(+)
	0.50	0.15	1.00	2.76	38.94(+)	-75.27(+)
	0.75	0.05	3.01	3.40	-28.05(+)	23.49(+)
	0.75	0.10	1.24	3.23	50.83(+)	-59.33(+)
Figure 5.4c: $H_1 = 10^{-5}$m	0.50	0.13	1.51	2.70	36.19(+)	-82.63(+)

Dispersion curves for the first mode (m=1) for $S_2 = 1$, $f_0 = 10^{-4}$ rad.s^{-1}, $\beta = 0$, $T = -10$, $L = 10$km., $g' = 0.02$m s^{-2}, $H_T = 180$m. and $H_2 = H_3 = (H_T - H_1)/2$

$$(U_2-c)\left[\left(\frac{H_2-bh}{H_2}\right)(\Phi_{2yy}-k^2\Phi_2) + 8F_2(\Phi_1-\Phi_2)/3\right] + \Phi_2\frac{\partial q_2}{\partial y} = 0$$

where $U_{1o} = (9U_1-U_2)/8$

$$\frac{\partial q_1}{\partial y} = \beta - U_{1_{oyy}} + 3F_1(U_1-U_2)$$

$$= \beta-U_{1oyy} + 8F_1\ (U_{1o}-U_2)/3$$

$$\frac{\partial q_2}{\partial y} = \left(\frac{H_3-bh}{H_3}\right)(\beta-U_{2yy}) + 3F_2(U_2-U_1) + \frac{b}{R_oH_2}\ h_y$$

$$= \left(\frac{H_3-bh}{H_3}\right)(\beta-U_{2yy}) + 8F_2\ (U_2-U_{1o})/3 + \frac{b}{R_oH_2}\ h_y$$

(Note that these equations are identical to (5.1) with the density difference between the layers reduced by a factor of 3/8 and U_1 replaced by U_{1o}, i.e., the appropriately "fitted" two-layer model.)

Further, if one takes the limit $H_1 \to 0$ in (3.9) we see that for $\beta = 0$ the dispersion relation reduces to $C = +S_{1_o}$ (the S_1-curve whose slope tends to 3/8 (= 3/8 S_2) as $H_1 \to 0$ in figure 5.4) plus the dispersion relation for the two-layer fluid illustrated in figure 5.3.

In the case where the curvature wave interacts with the S_1-wave, the limit $H_3 \to 0$ (figure 5.5) may be of interest but we shall not consider this case here.

Due to the possible qualitative difference between the three-layer model and the two-layer model with constant densities in each layer it is suggested that care be taken when either the middle layer has significant thickness or curvature of the mean velocity profile is present. When the simplicity of a two-layer model is strongly desirable, perhaps one of the other possibilities introduced here should be considered to choose an appropriate density difference between the layers (a case where this idea is useful will be considered in Chapter IV, Section 3 of this thesis, where we consider a three-layer model with linear density variation through the upper layer, and a density discontinuity between the lower layers).

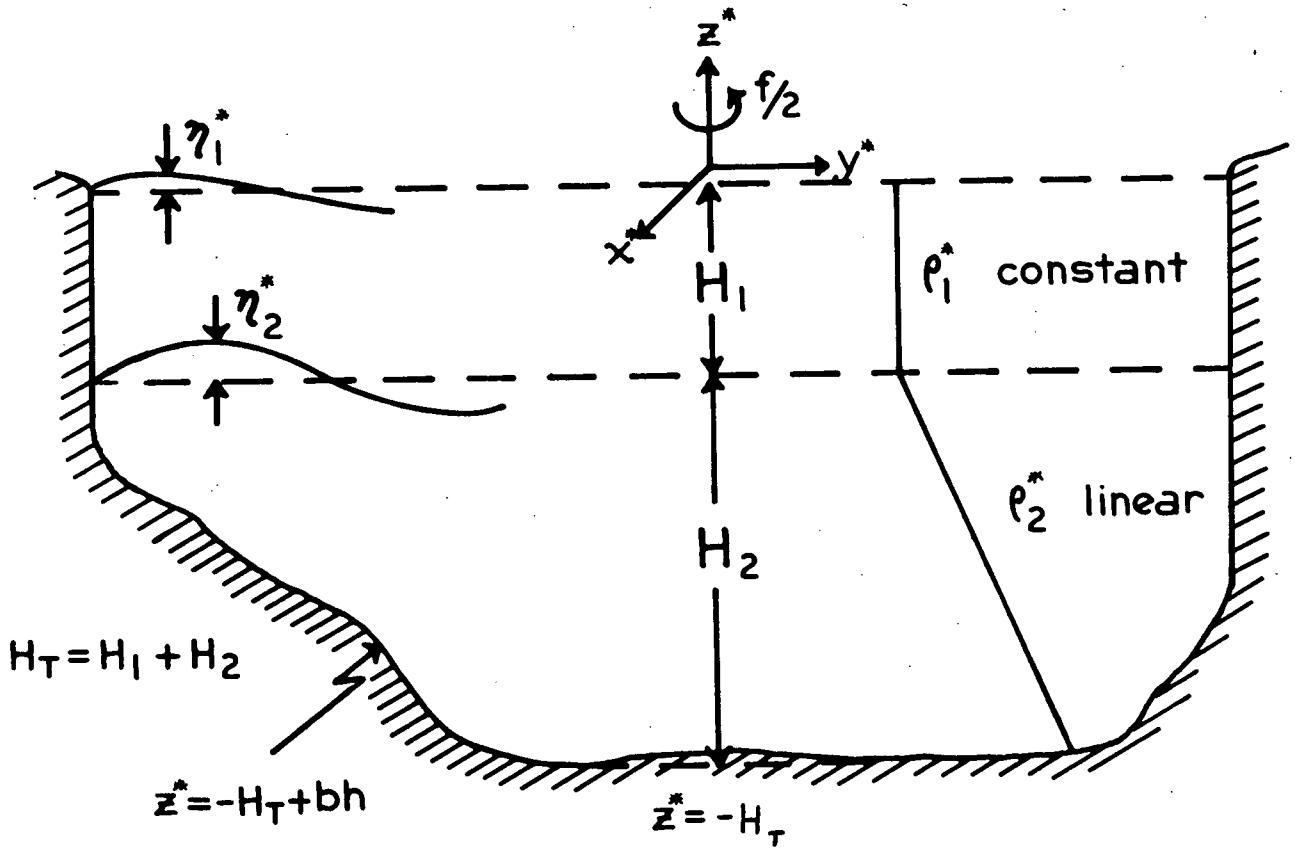

Figure 5.5: A cross-section of the two-layer model obtained by letting $H_3 \to 0$.

6. Conclusions

In general, three vertical modes may exist in the system studied here. They have been classified as shear waves here due to the role of the vertical shear in destabilizing the flow. They could equally well have been classified as vorticity waves. The S_1-wave which is strongly affected by variations in S_1 as well as β is clearly linked to $\frac{\partial q_1}{\partial y}$. Similarly the curvature and S_2-waves could be classified by their dependence on $\frac{\partial q_2}{\partial y}$ and $\frac{\partial q_3}{\partial y}$ respectively.

It is shown that when the thickness of the middle layer is significant the S_1 and S_2-waves cannot generally interact but the curvature wave is very strongly interactive with either of these waves.

Density stratification is shown to stabilize the flow both by decreasing the range of unstable wave numbers and by increasing the effect of β and topography. β stabilizes both the unstable S_1-wave and the unstable S_2-wave, while topography only has a significant stabilizing influence on the S_2-wave. Increasing either H_1 or H_3 relative to H_2 tends to stabilize the flow.

The three-layer model with uniform density in each layer is a good approximation to the model developed here in the case of zero curvature in the velocity profile but for large curvature (i.e. for $|S_1-S_2|$ large) it overestimates the density stratification and must be compensated for.

The model consisting of two constant density layers is shown to be a good approximation to the three-layer model only when the curvature in the mean velocity profile and middle layer thickness are small. In particular the agreement seems best when the shear is slightly stronger in the upper layers than in the lower layers. Improved agreement may be found by reducing the density stratification appropriately. Although

it is generally not clear how this should be done, for a linear density variation through the upper layer, it is shown that the density difference should be taken as 3/8 of the density difference through the top layer.

Appendix a

I have found it convenient to rewrite (2.25) in the following form, especially for the purpose of finding stability boundaries:

$$\alpha C^3 + \beta C^2 + \gamma C + \delta = 0$$

where $\alpha = A_6 K_m^6 + A_4 K_m^4 + A_2 K_m^2$

$A_6 = 1$

$A_4 = 3F_1 + 8F_2 + 3F_3$

$A_2 = 8(F_1F_2+F_2F_3+F_1F_3)$

$$\beta = B_6 K_m^6 + B_4 K_m^4 + B_2 K_m^2 + B_0$$

$B_6 = S_{2_o} - S_{1_o}$

$B_4 = (S_{2_o}-S_{1_o})(3F_1+8F_2+3F_3) + \frac{\partial q_1}{\partial y} + \frac{\partial q_2}{\partial y} + \frac{\partial q_3}{\partial y}$

$B_2 = 8(S_{2_o}-S_{1_o})(F_1F_2+F_2F_3+F_1F_3) + \frac{\partial q_1}{\partial y}(8F_2+3F_3)$

$$+ \frac{\partial q_2}{\partial y}(3F_1+3F_3) + \frac{\partial q_3}{\partial y}(3F_1+8F_2)$$

$B_o = 8(\frac{\partial q_1}{\partial y} F_2F_3 + \frac{\partial q_2}{\partial y} F_1F_3 + \frac{\partial q_3}{\partial y} F_1F_2)$

$$\gamma = C_6 K_m^6 + C_4 K_m^4 + C_2 K_m^2 + C_o$$

$C_6 = -S_{1_o} S_{2_o}$

$C_4 = -S_{1o}S_{2o}(3F_1+8F_2+3F_3) - S_{1o}(\frac{\partial q_2}{\partial y} + \frac{\partial q_3}{\partial y}) + S_{2o}(\frac{\partial q_1}{\partial y} + \frac{\partial q_2}{\partial y})$

$$C_2 = -8S_{1o}S_{2o}(F_1F_2+F_1F_3+F_2F_3) - S_{1o}\left(\frac{\partial q_2}{\partial y}(3F_2+3F_3) + \frac{\partial q_3}{\partial y}(3F_1+8F_2)\right)$$

$$+ S_{2o}\left(\frac{\partial q_1}{\partial y}(8F_2+3F_3) + \frac{\partial q_2}{\partial y}(3F_1+3F_3)\right)$$

$$+ \frac{\partial q_1}{\partial y}\frac{\partial q_3}{\partial y} + \frac{\partial q_1}{\partial y}\frac{\partial q_2}{\partial y} + \frac{\partial q_2}{\partial y}\frac{\partial q_3}{\partial y}$$

$$C_o = -S_{1o}\left(8F_1F_2\frac{\partial q_3}{\partial y} + 8F_1F_3\frac{\partial q_2}{\partial y}\right) + S_{2o}\left(8F_2F_3\frac{\partial q_1}{\partial y} + 8F_1F_3\frac{\partial q_2}{\partial y}\right)$$

$$+ 3F_1\frac{\partial q_2}{\partial y}\frac{\partial q_3}{\partial y} + 8F_2\frac{\partial q_1}{\partial y}\frac{\partial q_3}{\partial y} + 3F_3\frac{\partial q_1}{\partial y}\frac{\partial q_2}{\partial y}$$

$$\delta = D_4K_m^4 + D_2K_m^2 + D_0$$

$$D_4 = -S_{1_o}S_{2_o}\frac{\partial q_2}{\partial y}$$

$$D_2 = -S_{1_o}S_{2_o}\left(3F_3\frac{\partial q_2}{\partial y} + 3F_1\frac{\partial q_2}{\partial y}\right) - S_{1_o}\frac{\partial q_2}{\partial y}\frac{\partial q_3}{\partial y} + S_{2_o}\frac{\partial q_1}{\partial y}\frac{\partial q_2}{\partial y}$$

$$D_o = -S_{1_o}S_{2_o}\left(8F_1F_3\frac{\partial q_2}{\partial y}\right) + S_{1_o}\left(-3F_1\frac{\partial q_2}{\partial y}\frac{\partial q_3}{\partial y}\right) + S_{2_o}\left(3F_3\frac{\partial q_1}{\partial y}\frac{\partial q_2}{\partial y}\right)$$

$$+ \frac{\partial q_1}{\partial y}\frac{\partial q_2}{\partial y}\frac{\partial q_3}{\partial y}$$

The case of an advected topographic Rossby wave is found by letting $S_1 = S_2 = 0$, $\beta = 0$. Then

$$C = \frac{[K_m^4 + (3F_1+8F_2)K_m^2 + 8F_1F_2]T}{K_m^2[K_m^4 + (3F_1+8F_2+3F_3)K_m^2 + 8(F_1F_2+F_1F_3+F_2F_3)]}$$

and if we take the limit $F_2 \to \infty$ $(H_2 \to 0)$ we obtain the dispersion relation for a topographic planetary wave in a two-layer system

(e.g. Helbig and Mysak, 1976).

$$C = \frac{T(K_m^2+F_1)}{K_m^2(K_m^2+F_1+F_3)}$$

CHAPTER III

MIXED BAROCLINIC-BAROTROPIC INSTABILITY IN TWO- AND THREE-LAYER MODELS

1. Introduction

Pedlosky (1964b) has studied mixed baroclinic-barotropic instability in the two-layer model with upper and lower layers of uniform densities ρ_1^* and ρ_2^* respectively ($\rho_1^* < \rho_2^*$). To simplify the analysis he has considered the case in which the velocity in the lower layer is uniform across the channel. The first main purpose of this chapter is to extend the work of Pedlosky (1964b) to include the effect of horizontal shear in the lower layer (section 2). The mean velocity profile is taken to be a cosine jet in each layer with the amplitude of the velocity in the lower layer varying relative to that in the upper layer, i.e. $U_1 = U_0(1-\cos \pi(y+1))$, $U_2 = \varepsilon U_1$ with ε a constant whose value is varied. To concentrate our attention on the effects of horizontal and vertical shears of the mean currents, the effects of β and topography are not considered although they will be important in most applications.

The final sections of this chapter are concerned with a model in which the density stratification is modelled by three layers. Davey (1977) has studied pure baroclinic instability in a three-layer model similar to the two-layer model of Pedlosky. In chapter II, on the other hand, pure baroclinic instability has been studied in a three-layer model derived from the equations of motion relevant to a specialized continuously stratified fluid in which the upper and lower layers are of uniform densities ρ_1^* and ρ_3^* respectively ($\rho_1^* < \rho_3^*$) and the density of the middle

layer varies linearly from ρ_1^* to ρ_3^*. The second main purpose of this chapter is to further develope the model introduced in chapter II.

In section 3 (of this chapter) some general results analogous to those of Pedlosky (1964a,b) for the two-layer model are presented for the three-layer model. The energy equation is discussed, bounds on phase speeds and growth rates of unstable waves are found and the condition for marginally stable waves with phase speed within the range of the mean velocity is presented. Section 4 is concerned with some specific results on mixed baroclinic-barotropic instability in the three-layer model. The flow in the lower layer is assumed to be uniform (and thus set equal to zero) while the velocity profiles in the upper layers are chosen as in the study of the two-layer model, i.e. $U_1 = U_0(1-\cos \pi (y+1))$, $U_2 = \varepsilon U_1$. By varying ε, mixed baroclinic-barotropic instability is examined. Finally some general conclusions are made in section 5.

2. The Two-layer Model

The two-layer model introduced by Phillips (1951) to study the stability of quasi-geostrophic flows has been extensively used in both meteorology and oceanography. The reason for its popularity is the simplifications which result in replacing a singular non-separable partial differential equation with a pair of coupled, singular ordinary differential equations. The analysis is often further simplified by making the assumption that the mean flow in the lower layer is uniform (both vertically and horizontally) and hence without further loss of generality it is set equal to zero. The main

purpose of this section is to investigate the effects of non-uniform flow in the lower layer. The analysis will generally be restricted to the case $\beta = 0$. Killworth (1978) has pointed out that the effect of β is mainly quantitative rather than qualitative except in cases where β is sufficiently large to stabilize the flow. This is particularly relevant to the very long waves which may be stabilized by a relatively small value of β and hence we will restrict our attention to unstable waves at moderate wavelengths.

We begin with a brief discussion of the cases in which the mean currents vary over a horizontal length scale which is either small or large compared to the local internal deformation radius in each layer. This is followed by a detailed discussion of the case in which these length scales are of the same order. The case of a cosine jet in the upper layer of a two-layer fluid with $U_2 \equiv 0$ (first studied by Pedlosky, 1964b) is further considered followed by a discussion of the case $U_2 \equiv U_1$. For these cases some simple analytical results are discussed. The remainder of this section consists of a numerical study of the effects of horizontal shear in the lower layer.

The effect of taking $U_2 \neq 0$ will, of course, depend on the horizontal length scale of the motion. More precisely, it depends on the ratio of the horizontal length scale of the mean flow to the internal (Rossby) radius of deformation. This fact is clear from the equations for the non-dimensional (complex) amplitudes of the stream functions for the two layers.

$$(U_1-c)[\phi_{1yy}-k^2\phi_1+F_1(\phi_2-\phi_1)] + \phi_1[\beta-U_{1yy}+F_1(U_1-U_2)] = 0$$

$$(U_2-c)[\phi_{2yy}-k^2\phi_2+F_2(\phi_1-\phi_2)] + \phi_2[\beta-U_{2yy}+F_2(U_2-U_1)] = 0 \qquad (2.1)$$

where the nondimensional quantities are related to the corresponding dimensional (starred) quantities as in section 2 of chapter II. i.e.:

$$(x^*,y^*) = L(x,y)$$

$$(c^*,U_{1,2}^*) = U\,(c,U_{1,2})$$

$$k^* = k/L$$

$$\phi_i^* = UL\phi_i$$

$$\beta^* = \beta U/L^2 \qquad (f=f_0+\beta^* y^*) \tag{2.2}$$

in which L and U are typical horizontal length and velocity scales, f_o is the local value of the Coriolis parameter, g' is the reduced gravity ($g'=[(\rho_2^*-\rho_1^*)/\rho_2^*]\cdot g$), H_1, H_2 are the thicknesses of the upper and lower layers in the absence of motion respectively. Finally, $F_i = f_0^2L^2/g'H_i$ is the square of the ratio of the horizontal length scale of the mean flow to the internal deformation radius of the i^{th} layer. We note that the definition of the internal deformation radius introduced here is not equivalent to the usual definition ($r_{int}=\sqrt{\frac{g'H_1H_2}{f_0^2(H_1+H_2)}}$) but it has the same basic properties and we will find it very convenient to refer to the quantity $\sqrt{g'H_i}/f_0$ as the internal deformation radius of the i^{th} layer.

We will briefly consider the cases $F_i \ll 1$, $F_i \sim 1$ and $F_i \gg 1$ separately. A more detailed treatment of these limiting cases may be found in Killworth (1978).

Case I: $F_i \ll 1$ $(i=1,2)$.

Assuming that F_1 and F_2 are of the same order, the following expansions are appropriate:

$$\phi_i = \phi_i^0 + \phi_i^1 F_1 + \ldots$$

$$c = c^0 + c^1 F_1 + \ldots \tag{2.3}$$

Substituting these expansions in (2.1), we find that to leading order in F_1 , ϕ_1^0 , ϕ_2^0 and c^0 satisfy:

$$(U_1-c^0)[\phi_{1yy}^0-k^2\phi_1^0] + \phi_1^0[\beta-U_{1yy}] = 0$$

$$(U_2-c^0)[\phi_{2yy}^0-k^2\phi_2^0] + \phi_2^0[\beta-U_{2yy}] = 0 \ . \tag{2.4}$$

Hence, in this case the equations decouple, each layer yielding a Rayleigh instability problem. If $U_1 \neq U_2$, an eigenvalue of the first equation will not generally be an eigenvalue of the second equation so that the perturbation motion is generally trapped in one layer where instability may occur due to pure barotropic instability. (To next order in F_1 there will, of course, generally be motion forced in the other layer). In this case, only the form of the mean velocity in the layer in which instability occurs is of any consequence. A typical example of this type of instability is shown in Figure 2.1 where we have taken $f_0 = 10^{-4}\ s^{-1}$, $\beta = 0$, $L = 57.735$ km, $g' = 0.66\ m\ s^{-2}$, $H_1 = H_2 = 5$ km $(F_1=F_2=0.01)$, $U_1 = U_0(1-\cos \pi(y+1))$ and $U_2 = -U_1$. We note that with the exception of L these parameter values have been chosen to model atmospheric flows. This choice was made in order to facilitate comparison with the studies of Pedlosky (1964a,b) and Brown (1969a,b), however the results only depend on the values of F_1 and F_2 and are

immediately applicable to appropriate oceanic flows. For these parameter values, the layers are essentially uncoupled and ϕ_1 and ϕ_2 satisfy, to a good approximation:

$$[(U_0-c)-U_0\cos\,\pi(y+1)][\phi_{1yy}-k^2\phi_1] + \phi_1[-\pi^2 U_0\cos\,\pi(y+1)] = 0$$

$$[(\varepsilon U_0-c)-\varepsilon U_0\cos\,\pi(y+1)][\phi_{1yy}-k^2\phi_1] + \phi_2[-\pi^2\varepsilon U_0\cos\,\pi(y+1)] = 0 \qquad (2.5)$$

Since we have taken $\beta = 0$, the growth rate of any instability will simply be proportional to the maximum velocity in that layer. This is the only role of ε at these very small horizontal length scales. Further details on this type of instability can be found in Lin (1945, parts I, II, III), Pedlosky (1964b), Drazin and Howard (1966), Brown (1969a,b) and Kuo (1973) as well as a multitude of others.

Case II: $F_i \gg 1$ $(i=1,2)$.

In this case the horizontal length scale is much greater than the internal deformation radius and we expect any instability to be basically baroclinic in nature. This being the case, the appropriate horizontal length scale for the perturbation is the internal deformation radius rather than the scale on which the mean flow varies. Hence we introduce the following transformations

$$y' = y(F_1)^{1/2}$$

$$k' = k(F_1)^{-1/2} \qquad (2.6)$$

and expand ϕ_i and c as:

$$\phi_i = \phi_i^0 + \phi_i^1 F_1^{-1} + \ldots$$

$$c = c^0 + c^1 F_1^{-1} + \ldots \quad . \qquad (2.7)$$

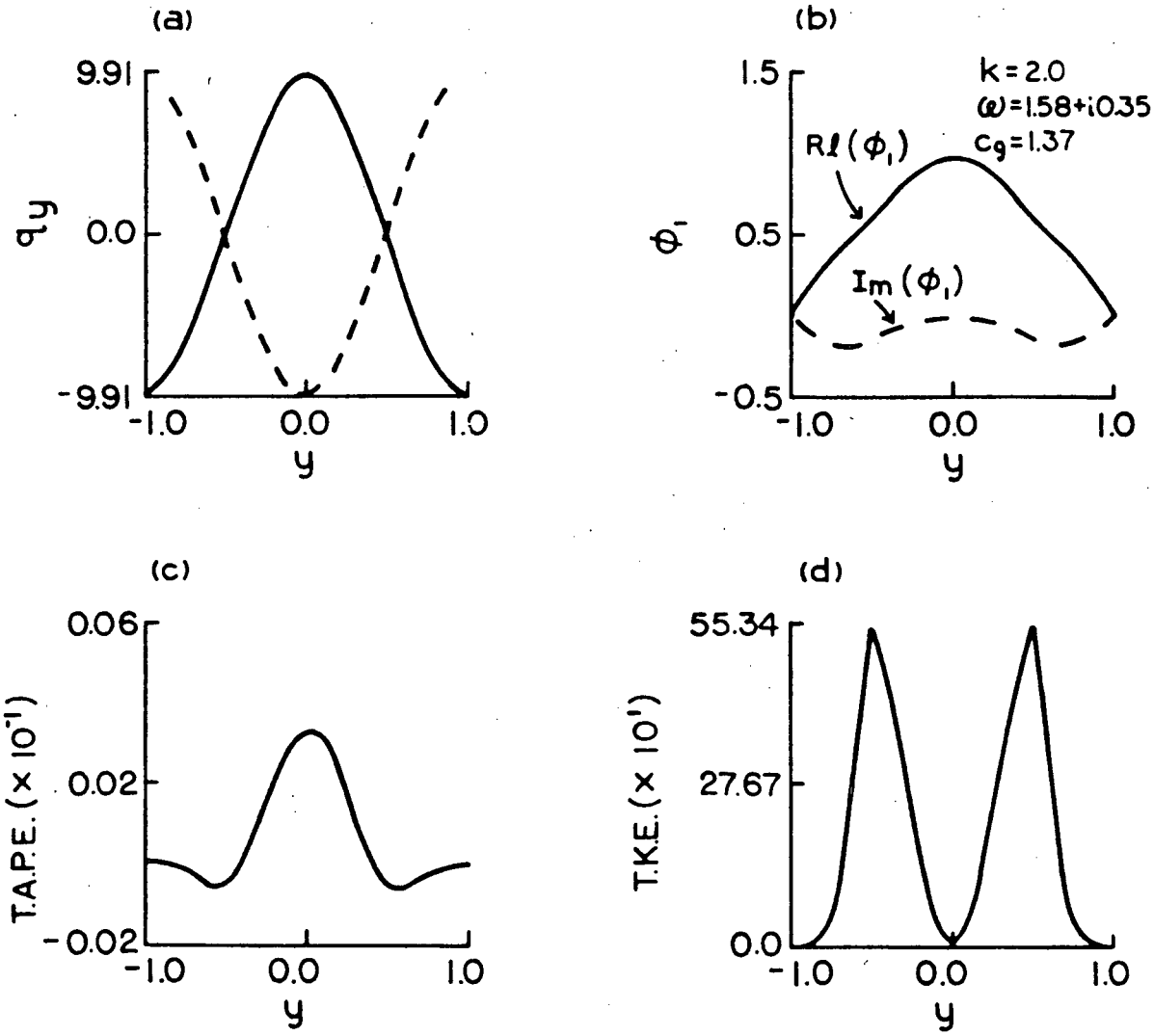

Figure 2.1: (a)Mean potential vorticity gradients in the upper layer (solid line) and the lower layer (dashed line). (b)Complex amplitude for the stream function in the upper layer ($\phi_2 \simeq 0$). (c)Transfer of Available Potential Energy (T.A.P.E.). (d)Transfer of Kinetic Energy (T.K.E.) in the upper layer. Since $\phi_2 \simeq 0$, the transfer in the lower layer is very small. $f_o = 10^{-4} s^{-1}$, $\beta = 0.0$, L=57.735 km, $g' = 0.66$ ms^{-2}, $H_1 = H_2 = 5$ km ($F_1 = F_2 = 0.01$), $U_1 = 1 - \cos\pi(y+1)$, $U_2 = -U_1$.

Making these substitutions in (2.1), we find that to leading order, ϕ_1^0 and ϕ_2^0 satisfy:

$$(U_1-c^0)[\phi^0_{1y'y'}-k'^2\phi_1^0+(\phi_2^0-\phi_1^0)] + \phi_1^0[\beta+(U_1-U_2)] = 0$$

$$(U_2-c^0)[\phi^0_{2y'y'}-k'^2\phi_2^0+H_1/H_2(\phi_1^0-\phi_2^0)] + \phi_2^0[\beta+H_1/H_2(U_2-U_1)] = 0 \qquad (2.8)$$

These equations constitute the justification for considering local values of the mean flow in studies of baroclinic instability and are valid for $(r_i/L)^2 << 1$. The study of these equations amounts to the study of the effect of weak horizontal shear on baroclinic instability. Further comments relevant to this case will be made in the following section, but here I will just note that for this case, the marginally stable waves marking the short wave cut-off will be baroclinic in nature as opposed to the expected barotropic nature conjectured by Pedlosky (1964b). This is due to the fact that the short wave cut-off for barotropic instability is proportional to the horizontal length scale of the mean shear while that for baroclinic instability is roughly proportional to the internal deformation radius. Thus for $(r_i/L)^2 << 1$ we expect the short unstable waves to be baroclinic in nature. This prediction is, in fact, verified by numerical computation.

It must be noted here that the horizontal shear may influence the cross-channel structure of the most unstable waves even for $(r_i/L)^2 << 1$. The marginally stable waves at the short wave cut-off will have a meridional scale of the order of the internal Rossby radius and hence are unaffected by the horizontal shear. However, Simmons (1974) has shown that the meridional length scale appropriate to the most unstable wave is $(Lr_i)^{1/2}$ and hence one must be careful not to neglect the effects of horizontal shear when these waves are to be studied. Of course if one is interested in the local (on

the scale of r_i) stability properties of the flow then it is reasonable to consider the case of no horizontal shear but this will not give any information on the meridional structure of the waves occurring on the much larger scales.

Case III: $F_i \sim 1$ (i=1,2)

This is the case of greatest interest here. Pedlosky (1964b) has considered the case of a cosine jet in the upper layer with $U_2 \equiv 0$ and has given the stability boundary corresponding to the short wave cut-off. In the interest of completeness, the full stability boundary is given in figure 2.2 which has been found by the methods described in appendix a. For the case $U_2 \equiv 0$, Pedlosky was also able to demonstrate numerically that the minimum value of U_0 at which instability occurs is precisely that value for which the necessary condition for instability is just satisfied (i.e. precisely the minimum value of U_0 for which q_y changes sign somewhere). It turns out that this result is relatively easy to prove analytically for the cosine jet and that this point on the stability boundary corresponds to c=0, $k = \frac{\sqrt{3}}{2}\pi$ (see appendix b). It is interesting to note that this value of k gives precisely the short wave cut-off for pure barotropic instability (the reason for this result becomes clear in appendix b).

Finally it is of interest to look at the case $F_1 = F_2$, $U_1 = U_2$ analytically. The stability boundary for this case in U_0 vs. k space is given in figure 2.3 for $f_0 = 10^{-4} s^{-1}$, $\beta = 0.0$, $L = 1000$ km , $g' = 0.66$ m s^{-2} , $H_1 = H_2 = 5$ km , $U_1 = U_2 = U_0(1-\cos \pi(y+1))$. For $F_1 = F_2$ and $U_1 = U_2$ our equations reduce to

$$(U_1-c)[\phi_{1yy}-k^2\phi_1+F_1(\phi_2-\phi_1)] + \phi_1[\beta- U_{1yy}] = 0$$

$$(U_1-c)[\phi_{2yy}-k^2\phi_2+F_1(\phi_1-\phi_2)] + \phi_2[\beta-U_{1yy}] = 0 \qquad (2.9)$$

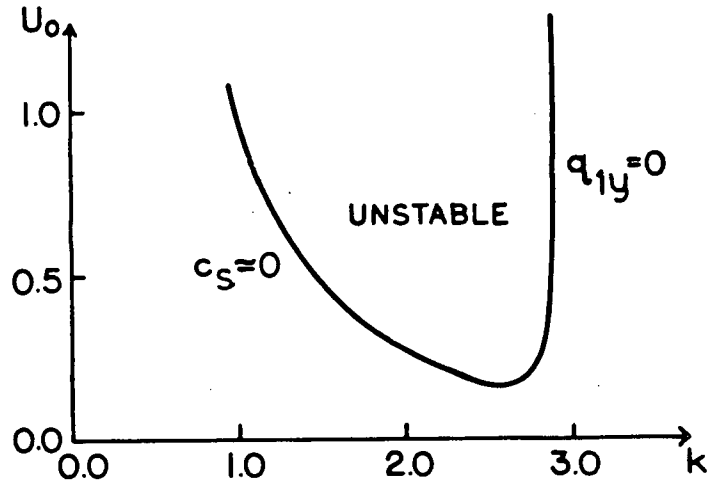

Figure 2.2: Stability boundary corresponding to the parameter values $f_o = 10^{-4}s^{-1}$, $\beta = 1.5$, $L = 1{,}000$ km , $g' = 0.66$ m.s.$^{-2}$, $H_1 = H_2 = 5$ km. $(F_1 = F_2 = 3)$, $U_1 = U_0(1-\cos \pi(y+1))$, $U_2 \equiv 0$.

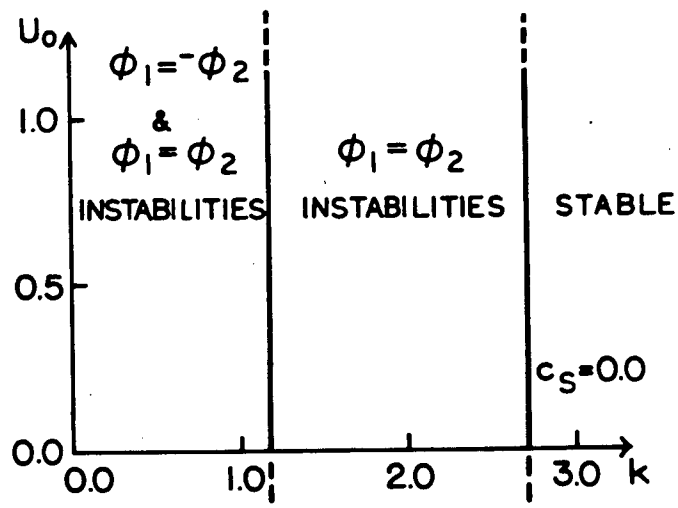

Figure 2.3: Stability boundary corresponding to the parameter values $f_0 = 10^{-4}s^{-1}$, $\beta = 0.0$, $L = 1{,}000$ km., $g' = 0.66$, $H_1 = H_2 = 5$ km. $(F_1 = F_2 = 3)$, $U_1 = U_2 = U_0(1-\cos \pi(y+1))$.

The phase speed at the short wave cut-off is given by $c = U_1(y_s)$ where $q_{1y}(y_s) = 0$ (see Pedlosky 1964b). This gives $c = U_0 - \beta/\pi^2$ which reduces our equations to:

$$\phi_{1yy} - k^2\phi_1 + F_1(\phi_2 - \phi_1) + \pi^2\phi_1 = 0$$

$$\phi_{2yy} - k^2\phi_2 + F_2(\phi_1 - \phi_2) + \pi^2\phi_2 = 0 \qquad (2.10)$$

Substituting $\phi_i = A_i \sin \frac{n\pi}{2}(y+1)$, $(i=1,2)$ we find that the condition for a non-trivial solution is:

$$k^2 = \begin{cases} \pi^2 - \left(\frac{n\pi}{2}\right)^2 - 2F_1 \\ \pi^2 - \left(\frac{n\pi}{2}\right)^2 \end{cases}$$

Clearly only $n = 1$ gives $k^2 > 0$, so the short wave cut-off is given by

$$k^2 = \frac{3\pi^2}{4} \quad \text{or} \quad k^2 = \frac{3\pi^2}{4} - 2F_1$$

The significance of these two cut-off values has been clearly pointed out by Dr. J. Pedlosky (thesis report). His comments are as follows. "When the mean flow is barotropic the perturbations can be resolved on the N vertical resting state modes of the system. The stability problem then reduces to the classical barotropic stability problem with k^2 replaced by $k^2 + \mu_n^2$ where μ_n is the vertical wave number of the mode. Since $c = c(k^2 + \mu_n^2)$, while the growth rate is kc_i it is apparent that the maximum instability (which is always barotropic) must correspond to the barotropic mode which has $\mu_n = 0$. The short wave cut-off for the n^{th} mode is at $(k_B^2 - \mu_n^2)^{\frac{1}{2}}$ where k_B is the barotropic cut-off." In the preceding work N = 2. The short wavelength

cut-off for the barotropic mode, k_B, is $\sqrt{3}\pi/2$ and that for the first baroclinic mode, which has $\phi_1 = -\phi_2$, is $(3\pi^2/4 - 2F_1)^{\frac{1}{2}}$. The corresponding regions of instability are marked appropriately in figure 2.3.

To consider the effects of varying U_2 in general we consider the following parameter values: $f_0 = 10^{-4}$ s^{-1}, $\beta = 0$, $L = 2{,}000$ km, $g' = 0.66$ ms^{-2}, $H_1 = H_2 = 5$ km ($F_1 = F_2 = 12$), with $U_1 = (1-\cos \pi(y+1))$, $U_2 = \varepsilon U_1$. Note that in the absence of both β and topography, the value of U (the horizontal velocity scale) is irrelevant. The choice of these parameter values gives the ratio of terms involving the vertical shear of the mean currents to those involving the horizontal shear of the mean currents to be of order unity (i.e. $F_1(U_1-U_2) \sim U_{1yy}$). Further, the choice of a cosine jet is appropriate since we wish to consider a case in which both baroclinic and barotropic instabilities are possible.

Figure 2.4 gives approximate stability boundaries in ε vs. k space for the parameter values given above (see appendix a for a further discussion of the stability boundaries). Probably the only meaningful conclusion which can be drawn from this figure is that, as expected, away from $\varepsilon = 1.0$ the short wave cut-off for unstable waves is shifted to higher wavenumbers due to the presence of vertical shear. The unstable regions beyond the short dashed line are probably not meaningful. We will first consider a series of cases in which both energy sources are expected to be important ($k = 1.5$, ε varying) and then we will look briefly at larger values of k ($k = 3.5$). In each case, attention will be focused on the most unstable waves.

The most unstable wave for $k = 1.5$, $\varepsilon = -1$ (strong vertical shear)

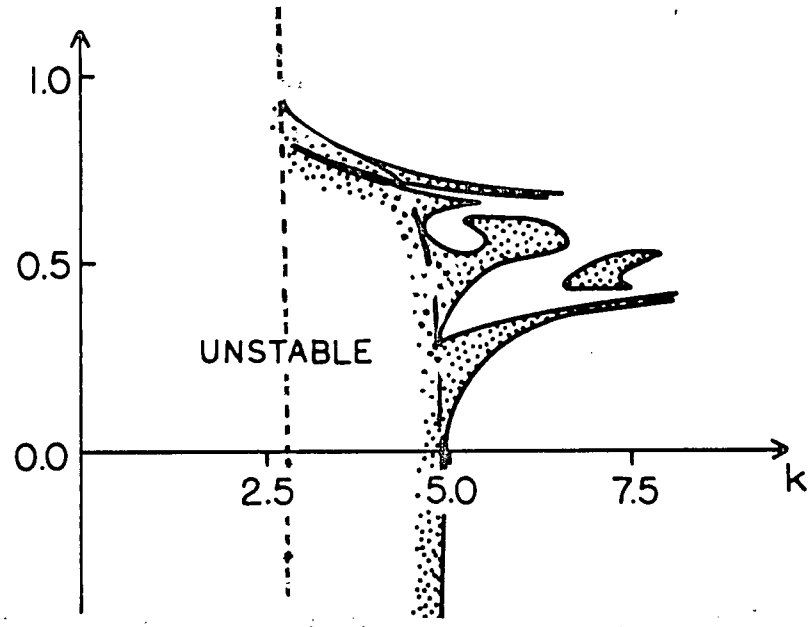

Figure 2.4: Approximate stability boundaries in ε vs. k space for the two-layer model with parameter values: $f_0 = 10^{-4}s^{-1}$, $\beta = 0.0$, $L = 2{,}000$ km., $g' = 0.66$ m.s.$^{-2}$, $H_1 = H_2 = 5$ km. $(F_1 = F_2 = 12)$, $U_1 = 1-\cos \pi(y+1)$, $U_2 = \varepsilon U_1$. Also shown here is the stability boundary appropriate to $(L/r_i)^2 << 1$ (short dashed line). Note: These boundaries are qualitative. The long dashed line indicates that value of k below which the apparent instabilities are likely real. Beyond this line the apparent instabilities have very small growth rates and details of the boundaries shown should not be taken seriously.

has $\omega = 0.00 + i\ 1.50$ and is illustrated in figure 2.5. It's energy source is almost purely baroclinic with only a very small contribution from barotropic sources (Transfer of Kinetic Energy [TKE] < 1/50 Transfer of Available Potential Energy [TAPE]). As one might have expected, this wave has zero phase and group velocities making it a very special case and hence probably only of limited use in modelling. Other apparent instabilities at $k = 1.5$, $\varepsilon = -1$ have very small growth rates: $\omega = 0.37 + i\ 0.09$ - mixed energy source extracting potential energy from the interface and kinetic energy from the upper layer in roughly equal amounts and $\omega = -0.37 + i\ 0.09$ with the same properties as above but its source of kinetic energy is the lower layer.

The most unstable wave at $\varepsilon = -0.5$ $(k = 1.5)$ has $\omega = 0.43 + i\ 1.10$ and is illustrated in figure 2.6. In this case the net conversion of kinetic energy in the upper layer is nearly zero while that in the lower layer is again very small compared to the conversion of potential energy. The only other instability found at $k = 1.5$ is a bottom intensified wave (perturbation energy of lower layer $\simeq 4\times$ perturbation energy of upper layer) whose energy source is mainly barotropic instability in the lower layer with TAPE < TKE/2 in the lower layer. The TKE in the upper layer is small and negative.

At $\varepsilon = 0.0$ the most unstable wave has $\omega = 0.84 + i\ 0.56$ and is illustrated in figure 2.7. It is a potential energy converting wave losing a small amount of kinetic energy to the mean flow in the upper layer. (The conversion of kinetic energy in the lower layer vanishes since $U_2 \equiv 0$). Also significant at $\varepsilon = 0.0$ is the unstable wave shown in figure 2.8. It has the same basic energy conversion properties as the most unstable wave but the TAPE is more evenly distributed across the channel and this is

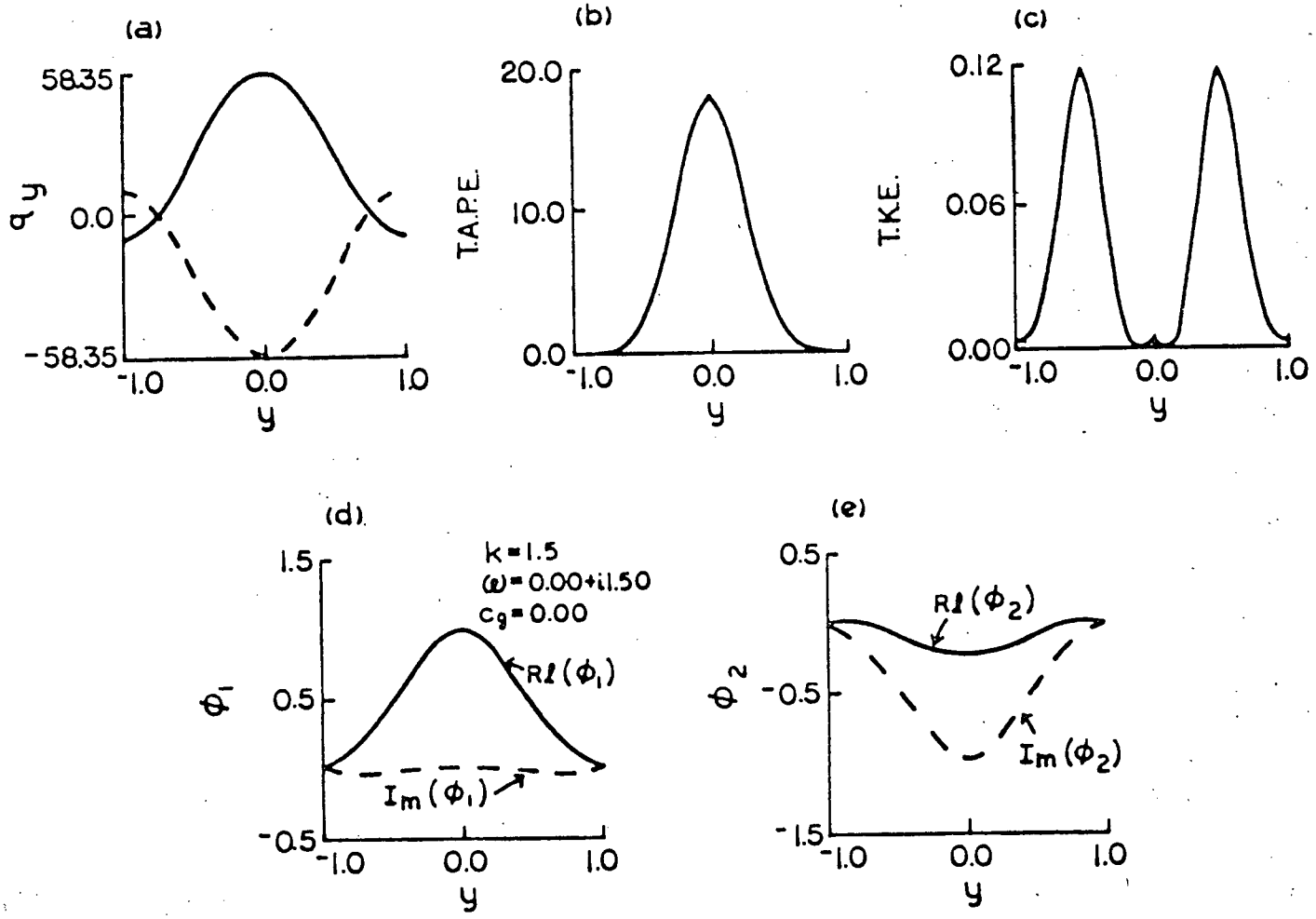

Figure 2.5: (a)Mean potential vorticity gradients in the upper layer (solid line) and lower layer (dashed line). (b)Transfer of available potential energy. (c)Transfer of kinetic energy in the upper layer (=transfer in the lower layer which is indicated by a dashed line in this and future figures). (d)Complex amplitude of the stream function in the upper layer. (e)Complex amplitude of the stream function in the lower layer. Parameter values as in figure 2.4; ε=-1.00, k=1.5 .

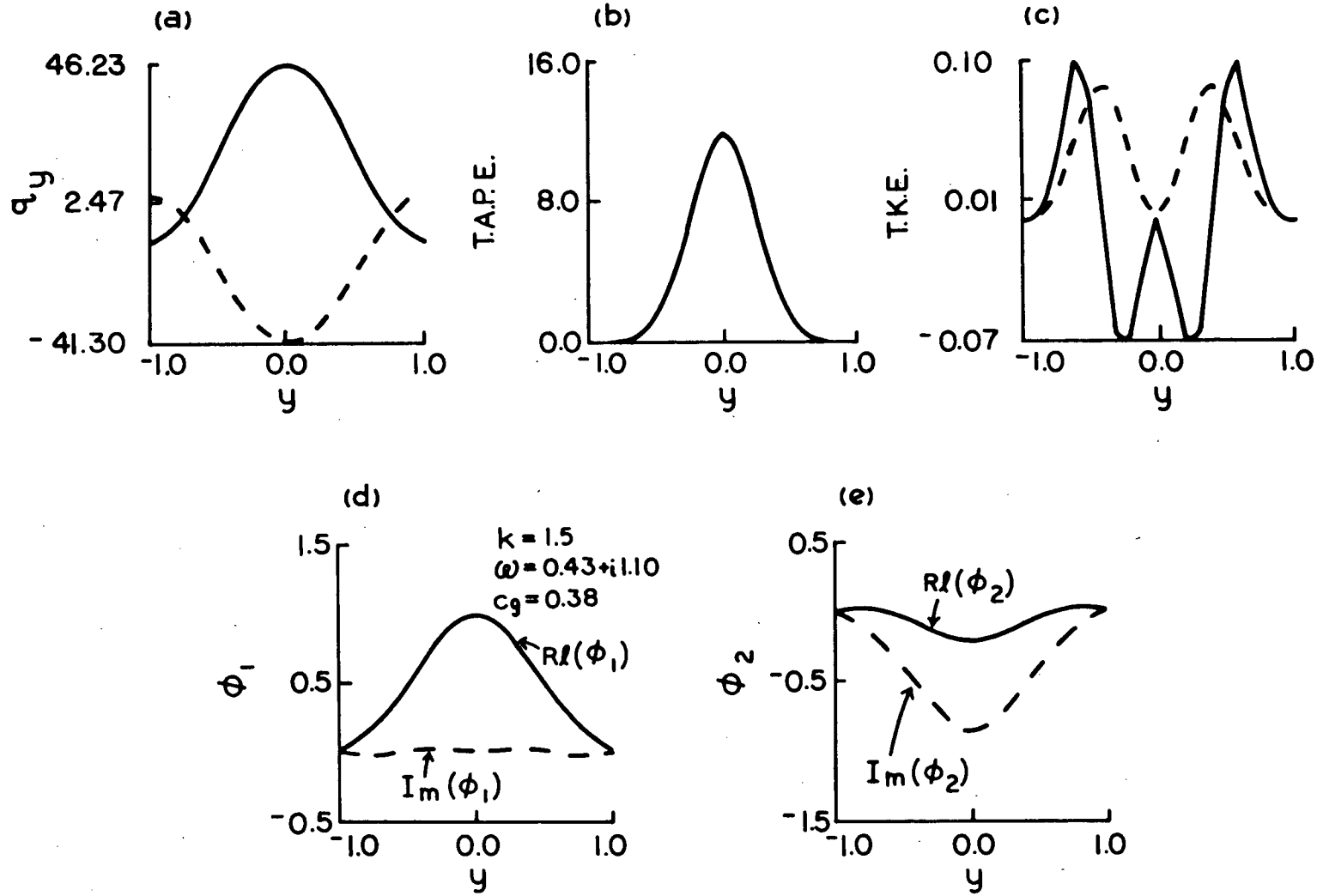

Figure 2.6: As in figure 2.5 but $c = -0.5$.

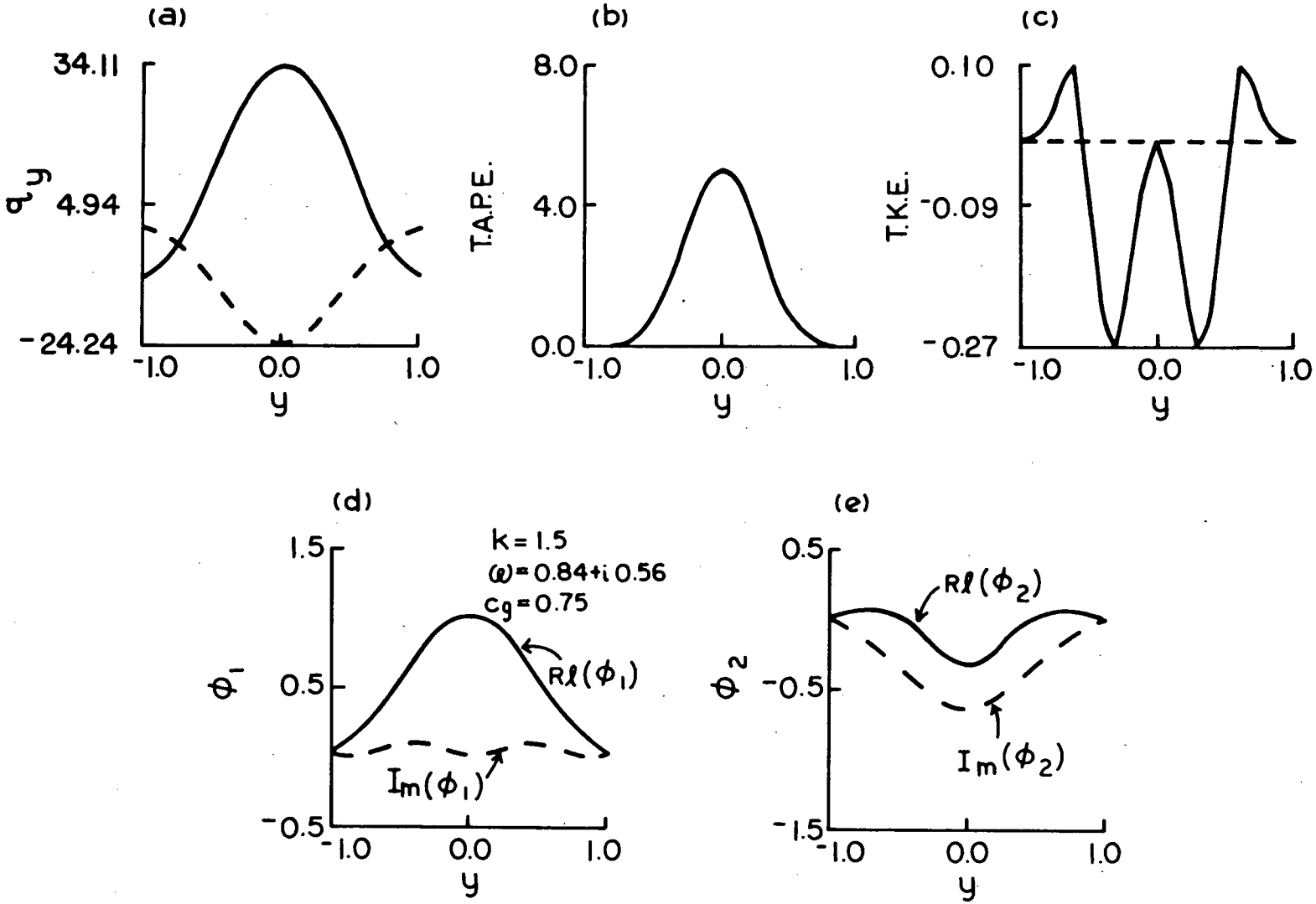

Figure 2.7: As in figure 2.5 but $\varepsilon = 0.0$.

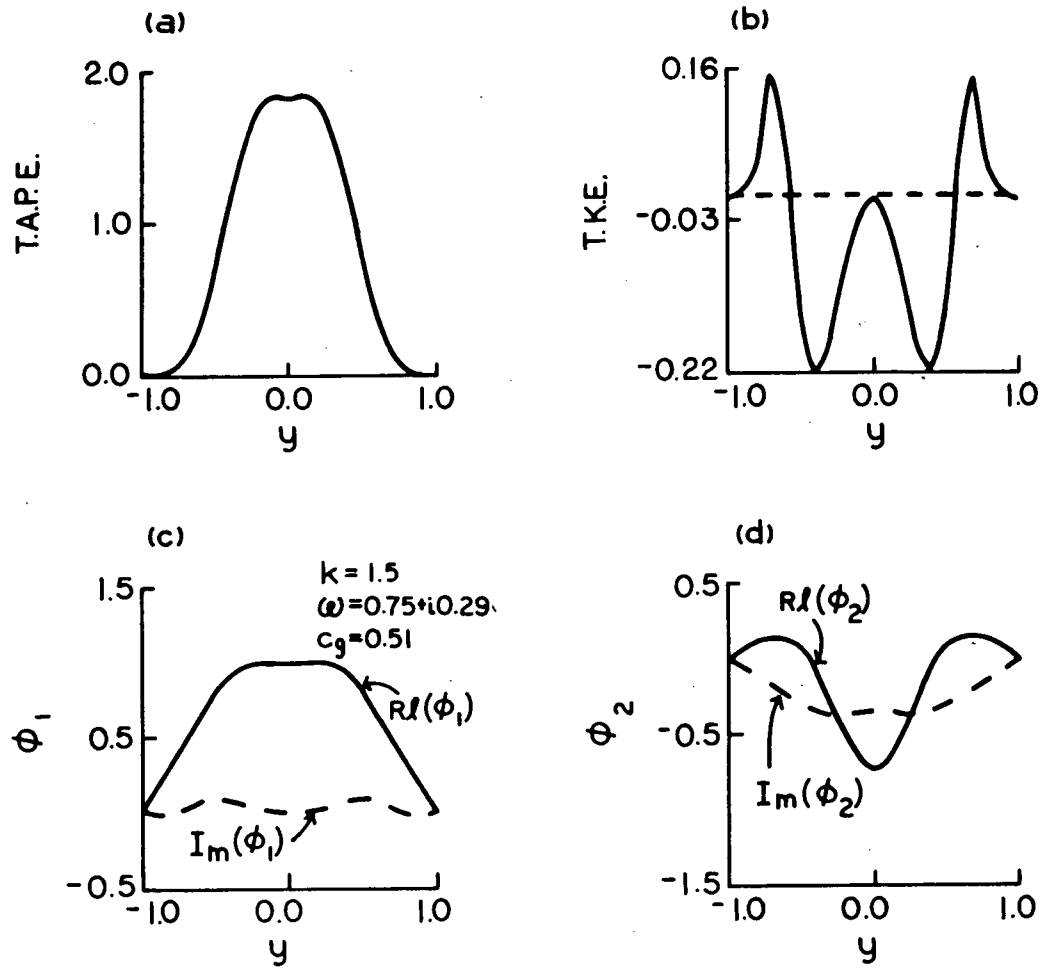

Figure 2.8: As in figure 2.7 - a second significant instability at the same position in parameter space.

reflected in the form of the eigenfunctions (especially ϕ_1). This wave is basically a higher mode instability.

The most unstable wave at $\varepsilon = 0.5$ (k=1.0) has $\omega = 0.76 + i\ 0.34$ and is illustrated in figure 2.9. Unlike the most unstable waves of previous cases this wave has substantial energy conversion contributions from barotropic instability especially in the upper layer. In fact the TAPE $\simeq$ TKE . One significant consequence of the TKE in the upper layer is that the wave is considerably intensified in the upper layer. (When considering baroclinic-barotropic instability in the three-layer model we will see that an apparently insignificant conversion of kinetic energy may cause significant intensification in the corresponding layer). A second significant instability also occurs at $\varepsilon = 0.5$. It is illustrated in figure 2.10. This wave extracts most of its energy from the tilt of the interface near the centre of the channel and is itself somewhat concentrated towards the centre of the channel. The growth rate of this wave is considerably reduced by a loss of kinetic energy to the upper layer. The perturbation is, however, not significantly intensified in either layer.

At $\varepsilon = 1.0$, the only source of energy for the perturbations is the horizontal shear of the mean currents. This case has already been considered in some detail analytically. Since $F_1 = F_2 \simeq 12$ for the case considered here, the wave with $\phi_1 = -\phi_2$ is not present (recall that the short wave cut-off with this class of waves is given by $k^2 = \frac{3\pi^2}{4} - 2F_1$) and hence the only unstable wave found here has $\phi_1 = \phi_2$ (see figure 2.11). This wave has $\omega = 0.93 + i\ 0.39$ and actually grows somewhat faster than the corresponding wave at $\varepsilon = 0.5$ ($\omega = 0.76 + i\ 0.34$).

In conclusion we note that at $k = 1.5$, $F_1 = F_2 \simeq 12$ the most unstable

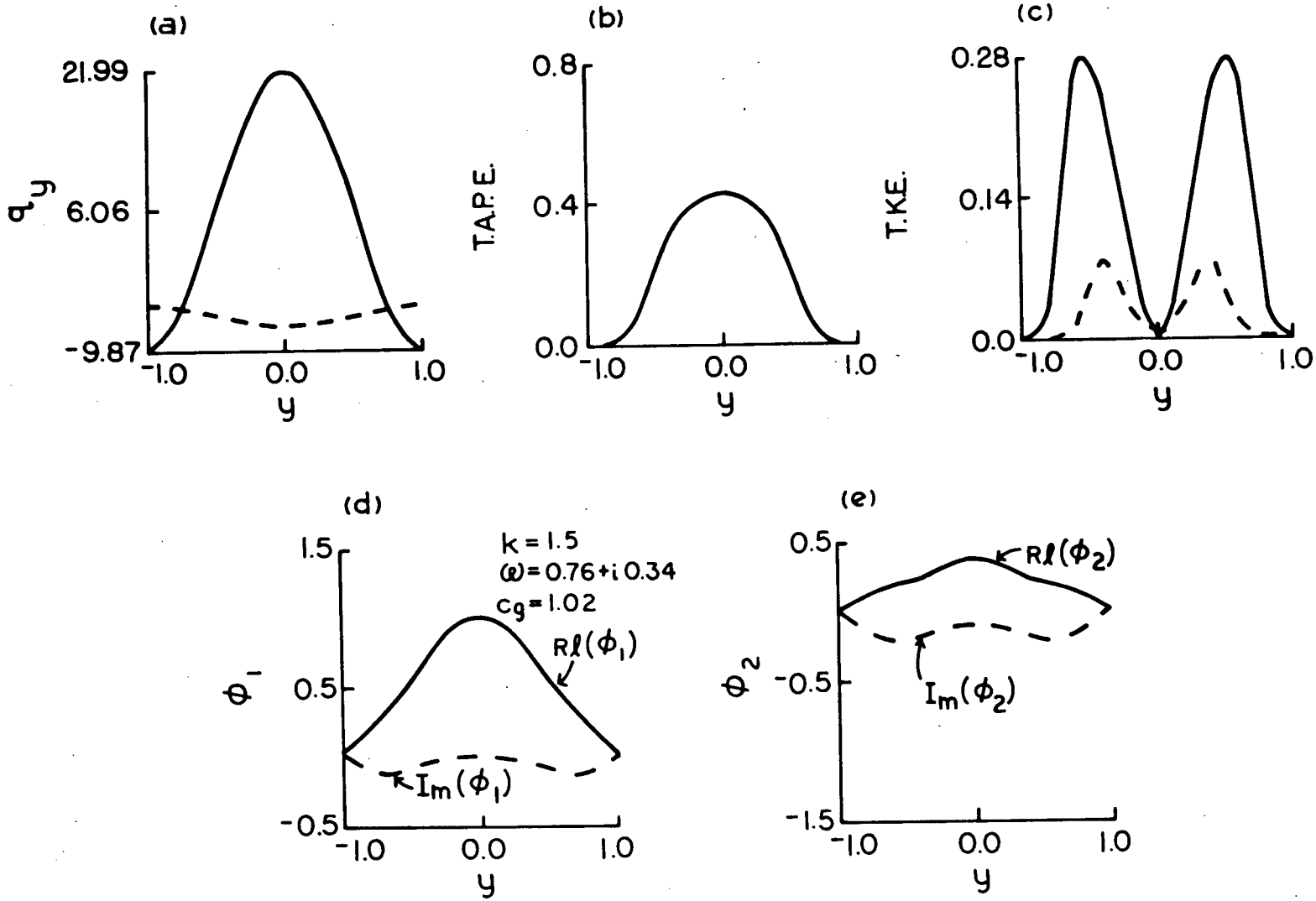

Figure 2.9: As in figure 2.5 but $\epsilon = 0.5$.

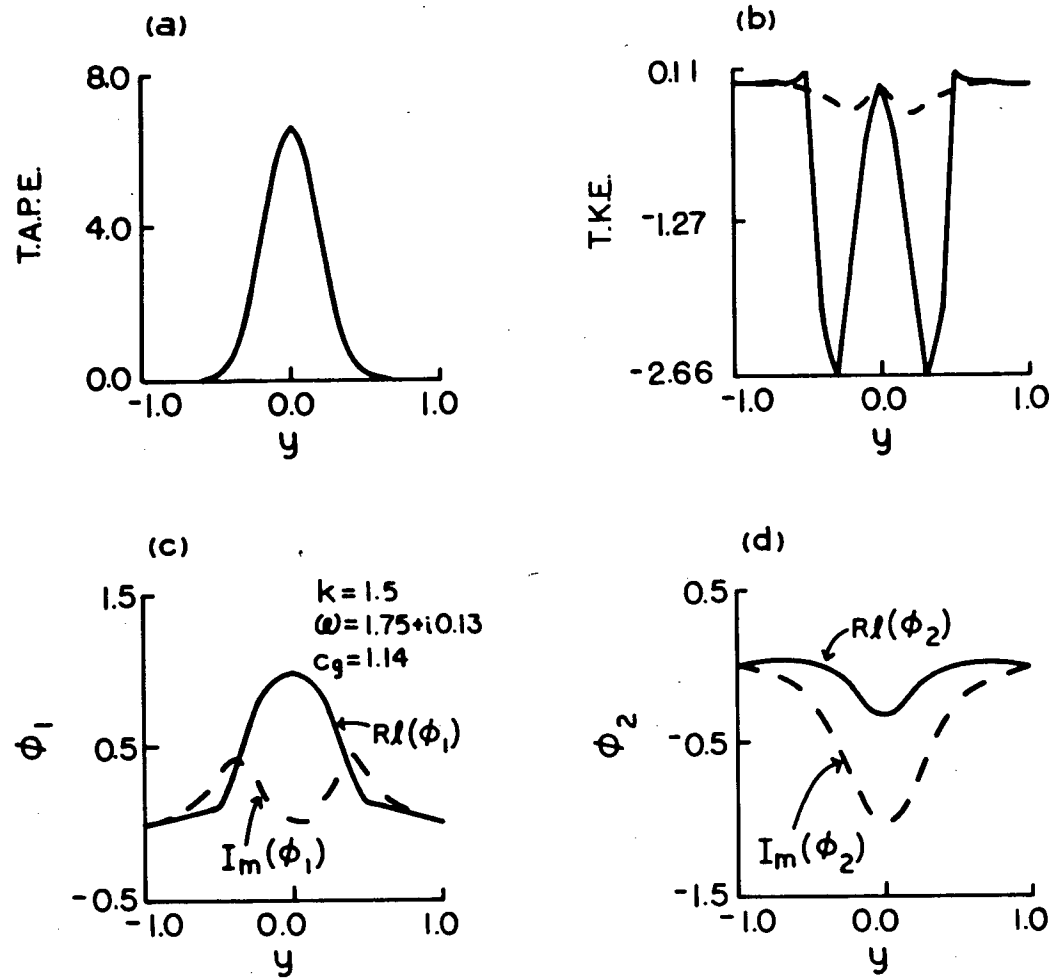

Figure 2.10: As in figure 2.9 - a second significant instability at the same position in parameter space.

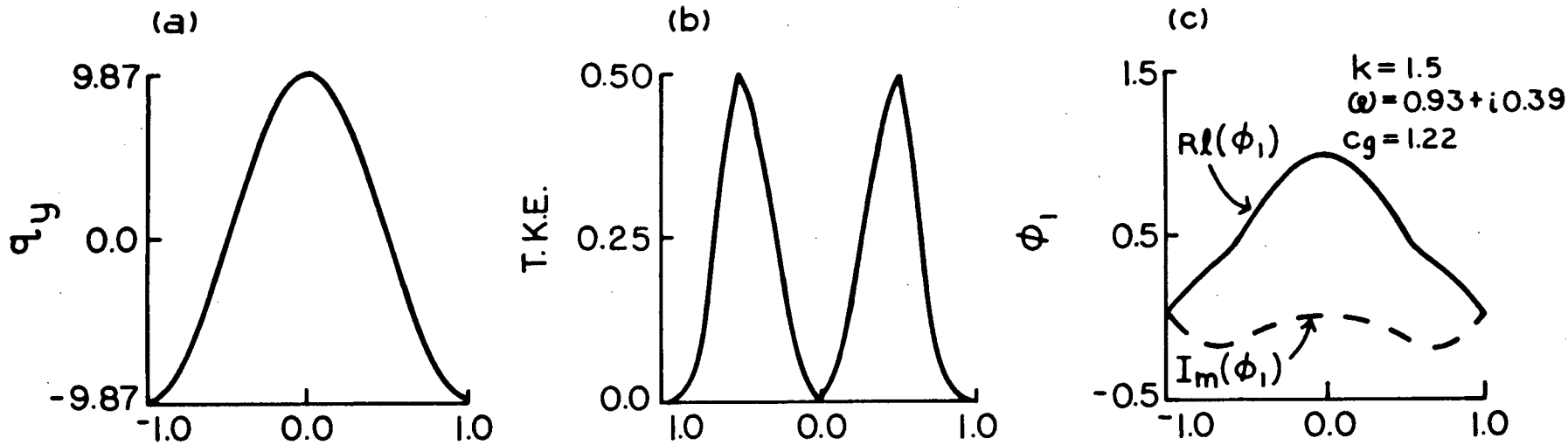

Figure 2.11: (a) q_{1y} ($\equiv q_{2y}$) (b) T.K.E. (T.A.P.E.$\equiv$0) (c) $\phi_1(\equiv\phi_2)$ Parameter values as in figure 2.4; ϵ = 1.0 , k = 1.5

waves with $\varepsilon \leq 0$ are essentially baroclinic energy converting waves extracting energy from the tilt of the interface and losing small amounts of kinetic energy to the mean flow. For this type of instability, the most important quantity to estimate is the magnitude of the vertical shear. For $\varepsilon > 0$ however, this is not the case. The most unstable waves have significant contribution from kinetic energy conversions and taking $\varepsilon = 0.0$ as a first approximation may give very misleading results.

Finally, let us consider the instabilities present at values of k greater than that corresponding to the short wave cut-off for barotropically unstable waves. In particular we have considered $k = 3.5$. At values of ε where instabilities occur at $k = 3.5$ the energy source is almost purely baroclinic, however a significant loss of kinetic energy to the mean flow may occur for $\varepsilon > 0$. Two effects thus serve to stabilize the flow near $\varepsilon = 1$. The first is that the net conversion of potential energy is roughly proportional to the mean vertical shear and hence decreases as $\varepsilon = 1$ is approached. The second effect is that the loss of kinetic energy to the mean currents increases as $\varepsilon = 1$ is approached. Both of these effects will be noted on comparing figure 2.12 (ε=0.0) with figure 2.13 (ε=0.5).

We thus conclude that even in the case where we are interested in waves considerably shorter than the short wave cut-off for barotropically unstable waves, the neglect of horizontal shear in the lower layer may be significant (especially for $\varepsilon > 0$) in that we are neglecting a potential stabilizing effect. However, we note again (as in the case of "small" k) that for $\varepsilon < 0$ this effect is probably not very significant and the study of baroclinically unstable waves is reasonably approximated by setting $\varepsilon = 0.0$.

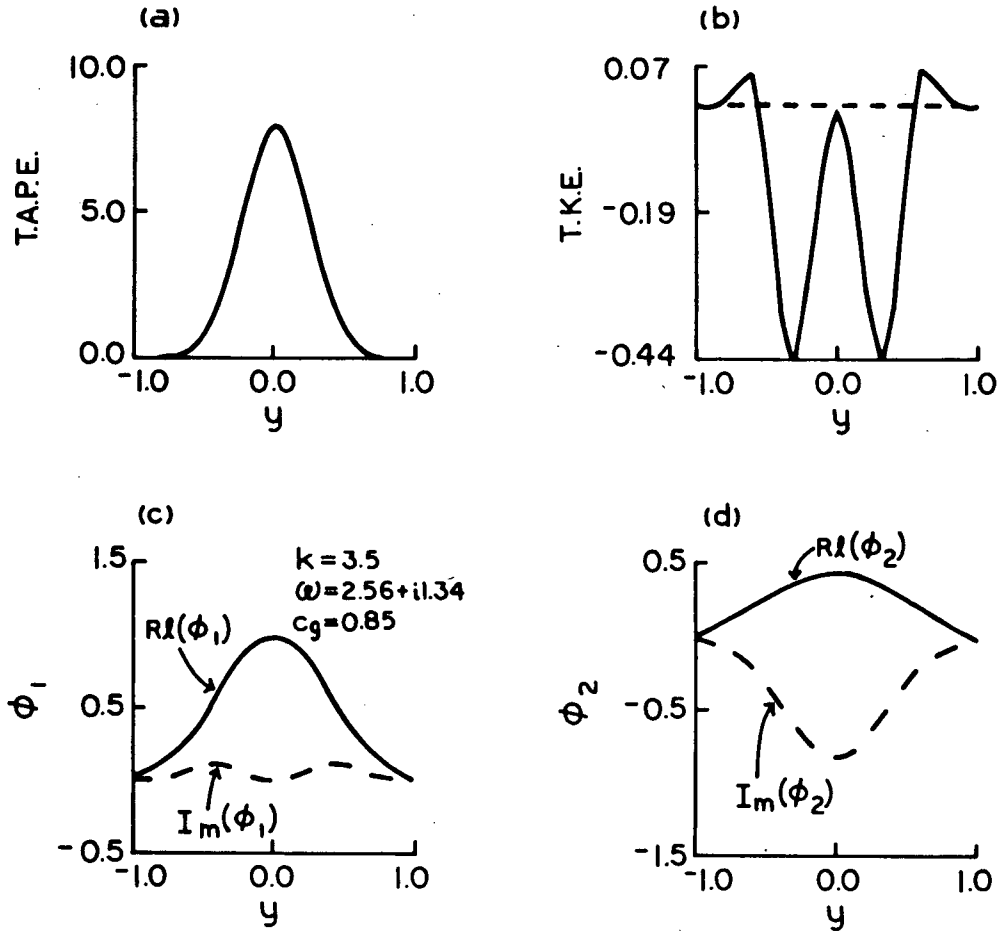

Figure 2.12: Parameter values as in figure 2.4; k = 3.5 , ε = 0.0 .

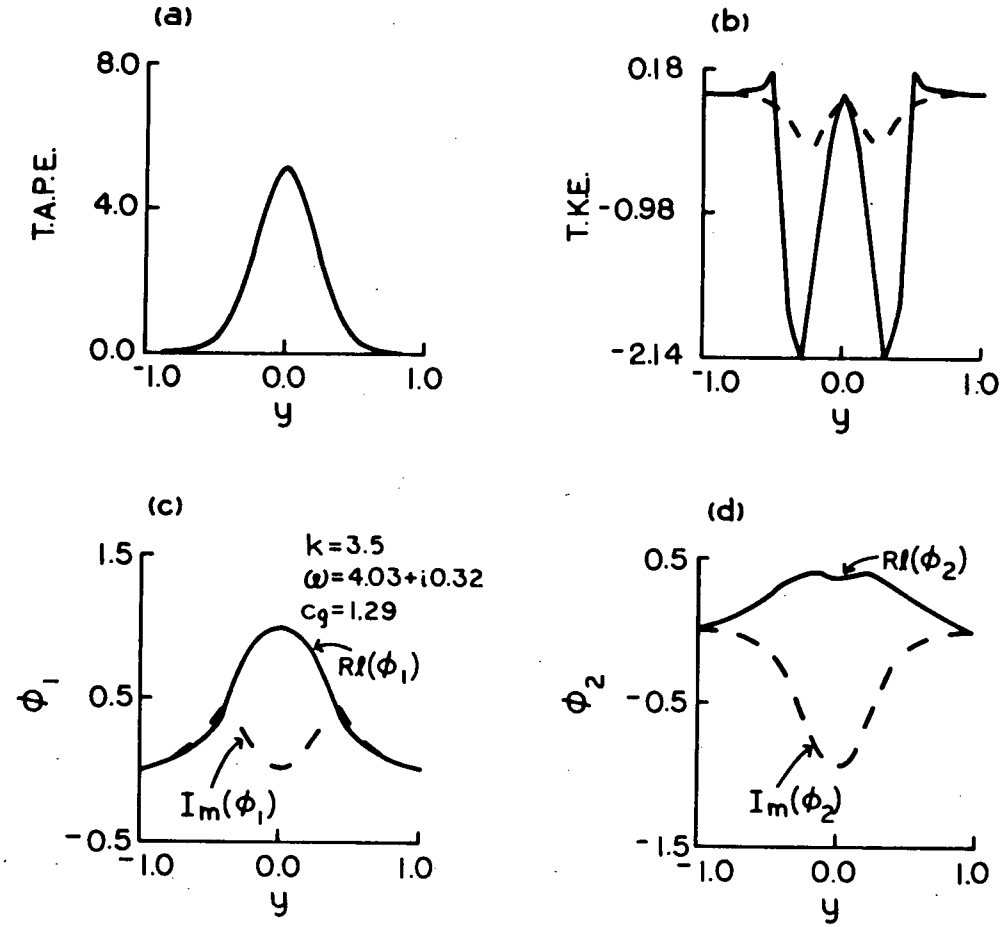

Figure 2.13: Parameter values as in figure 2.4; k = 3.5 , c = 0.5 .

3. The Three-layer Model (Qualitative Results)

In chapter II a three-layer model was derived from the equations of motion for a continuously stratified fluid with densities of the upper and lower layers given by ρ_1^* and ρ_3^* respectively ($\rho_3^*>\rho_1^*$) and ρ_2^* varies linearly from ρ_1^* to ρ_3^* (Figure 2.1 chapter II). There it was found that for $bh/H_3<<1$ the linearized equations expressing the conservation of potential vorticity for the model described above are:

$$\left(\frac{\partial}{\partial t} + U_{1o}\frac{\partial}{\partial x}\right)[\nabla_H^2\xi_1 - F_1(3\xi_1-4\xi_2+\xi_3)] + \xi_{1x}\, q_{1y} = 0$$

$$\left(\frac{\partial}{\partial t} + U_{2o}\frac{\partial}{\partial x}\right)[\nabla_H^2\xi_2 + 4F_2(\xi_1-2\xi_2+\xi_3)] + \xi_{2x}\, q_{2y} = 0$$

$$\left(\frac{\partial}{\partial t} + U_{3o}\frac{\partial}{\partial x}\right)[\nabla_H^2\xi_3 - F_3(\xi_1-4\xi_2+3\xi_3)] + \xi_{3x}\, q_{3y} = 0 \qquad (3.1)$$

where

$$q_{1y} = \beta - U_{1yy} + 2F_1(2U_1-3U_2+U_3)$$

$$q_{2y} = \beta - U_{2oyy} - 6F_2(U_1-2U_2+U_3)$$

$$q_{3y} = \beta - U_{3yy} + 2F_3(U_1-3U_2+2U_3) + (b/R_0H_3)h_y \qquad (3.2)$$

are the northward gradients of the potential vorticity of the mean currents in each layer. Subscripts 1, 2 and 3 refer to quantities defined in the upper, middle and lower layers respectively and the additional subscript o indicates that the quantity is to be evaluated at the middle of the appropriate layer. Note that since quantities in the upper and lower layers are vertically uniform, $U_{1o} \equiv U_1$, $U_{3o} \equiv U_3$ but (c.f. chapter II):

$$U_{2o} = (6U_2 - U_1 - U_3)/4. \tag{3.3}$$

The purpose of this section is to extend the qualitative results of Pedlosky (1964a,b) to the three-layer case.

(a) The Energy Equation

In chapter II it was found that if the i^{th} equation of (3.1) is multiplied by ξ_i/F_i and integrated across the channel and over a wavelength in the x-direction, a region we have referred to as R, the following energy equation is derived.

$$\frac{\partial}{\partial t}\int_R \left[\frac{(\nabla_H\xi_1)^2}{2F_1} + \frac{(\nabla_H\xi_2)^2}{2F_2} + \frac{(\nabla_H\xi_3)^2}{2F_3} + (\xi_1-\xi_2)^2 + (\xi_2-\xi_3)^2 + \frac{1}{2}(\xi_1-2\xi_2+\xi_3)^2\right] dxdy$$

$$= \int_R \left[U_{1y}\xi_{1x}\xi_{1y}/F_1 + U_{2oy}\xi_{2x}\xi_{2y}/F_2 + U_{3y}\xi_{3x}\xi_{3y}/F_3\right] dxdy \tag{3.4}$$

$$+ \int_R \left[4\xi_1\xi_{2x}(U_1-U_{2o}) + \xi_3\xi_{1x}(U_1-U_3) + 4\xi_2\xi_{3x}(U_{2o}-U_3)\right] dxdy$$

This equation expresses the fact that the local rate of change of total perturbation energy is due to one (or both) of two distinct energy conversion mechanisms. The first of these mechanisms extracts energy from the mean flow made available to the perturbations by the horizontal shear of the mean currents. When this is the dominant energy source for the perturbations the instability is referred to as barotropic instability. If, on

the other hand, the perturbations extract energy principally from the available potential energy of the mean currents (due to the effect of rotation on a vertically sheared, stratified fluid) the instability is known as baroclinic instability. In this chapter we are basically interested in the mixed baroclinic-barotropic instability case where both mechanisms may be significant.

(b) Necessary Conditions for Instability

The necessary conditions for instability have been given in chapter II (equations 3.5 and 3.6). The first of these is:

$$c_i \int_{-1}^{1} \sum_{i=1}^{3} \frac{q_{iy} |\Phi_i|^2}{F_i |U_{io} - c|^2} = 0 \ , \tag{3.5}$$

which implied that for unstable waves (i.e. for $\mathrm{Im}(c) \neq 0$) the potential vorticity gradient must change sign somewhere, either within a layer or in going from one layer to another. An enlightening interpretation of this condition has been given by Pedlosky (1964a). Basically (3.5) results from the fact that in the absence of external forcing, momentum can be redistributed between the mean and the perturbations but no net change in momentum may occur.

The second necessary condition for instability is:

$$kc_i \int_{-1}^{1} \sum_{i=1}^{3} \left(|\Phi_{iy}|^2 + k^2 |\Phi_i|^2 \right)/F_i + 2\left[|\Phi_1-\Phi_2|^2 + |\Phi_2-\Phi_3|^2 + \tfrac{1}{2}|\Phi_1-2\Phi_2+\Phi_3|^2\right] \, dy$$

$$= kc_i \int_{-1}^{1} \sum_{i=1}^{3} \frac{U_i |\Phi_i|^2}{F_i |U_{io}-c|^2} \frac{\partial q_i}{\partial y} \, dy \qquad (3.6)$$

It can be shown (see Pedlosky 1964a) that (3.6) is equivalent to the statement

$$\frac{\partial}{\partial t}[\text{Perturbation Energy}] \propto \pi c_i \int_{-1}^{1} \sum_{i=1}^{3} \frac{U_{io} |\Phi_i|^2 q_{iy}}{F_i |U_{io}-c|^2} \, dy \exp(2kc_i t) \qquad (3.7)$$

For an unstable wave, the left hand side of (3.7) is positive and hence we see that the product $U_{io} \frac{\partial q_i}{\partial y}$ must be somewhere positive for instability to occur. This result may also be seen directly from (3.6), but the form (3.7) (and its derivation) is more satisfying physically.

(c) Bounds on Phase Speeds and Growth Rates

In this section bounds will be found for the phase speeds and growth rates of unstable waves in the three-layer model studied here (β and topographic effects are now included). Since the details are somewhat more complicated than for the two-layer model a full derivation will be given.

We begin with Eq. 3.1 from chapter II with $bh \ll H_3$.

$$(U_{1o}-c)\ [\Phi_{1yy}-k^2\Phi_1-F_1(3\Phi_1-4\Phi_2+\Phi_3)] + \Phi_1 q_{1y} = 0$$

$$(U_{2o}-c)\{\Phi_{2yy}-k^2\Phi_i+4F_2(\Phi_1-2\Phi_2+\Phi_3)] + \Phi_2 q_{2y} = 0$$

$$(U_{3o}-c)[\Phi_{3yy}-k^2\Phi_3-F_3(\Phi_1-4\Phi_2+3\Phi_3)] + \Phi_3 q_{3y} = 0\ . \qquad (3.8)$$

Since for unstable waves, $Im(c)\neq 0$, it is permissible to make the transformations

$$\Phi_i = (U_{io}-c)\theta_i \qquad (i=1,2,3). \qquad (3.9)$$

From (3.8) it can be shown that the equations satisfied by θ_1, θ_2 and θ_3 are:

$$\frac{d}{dy}\left[\frac{(U_1-c)^2}{F_1}\frac{d\theta_1}{dy}\right]-k^2\frac{(U_1-c)^2}{F_1}\theta_1 - (U_1-c)\left[3(U_1-c)\theta_1-4(U_{2o}-c)\theta_2+(U_3-c)\theta_3\right]$$

$$+\frac{(U_1-c)}{F_1}[\beta+2F_1(2U_1-3U_2+U_3)]\theta_1 = 0$$

$$\frac{d}{dy}\left[\frac{(U_{2o}-c)^2}{F_2}\frac{d\theta_2}{dy}\right]-k^2\frac{(U_{2o}-c)^2}{F_2}\theta_2+4(U_{2o}-c)[(U_1-c)\theta_1-2(U_{2o}-c)\theta_2+(U_3-c)\theta_3]$$

$$+\frac{(U_{2o}-c)}{F_2}[\beta-6F_2(U_1-2U_2+U_3)]\theta_2=0$$

$$\frac{d}{dy}\left[\frac{(U_3-c)^2}{F_3}\frac{d\theta_3}{dy}\right]-k^2\frac{(U_3-c)^2}{F_3}\theta_3-(U_3-c)[(U_1-c)\theta_1-4(U_{2o}-c)\theta_2+3(U_3-c)\theta_3]$$

$$+\frac{(U_3-c)}{F_3}[\beta+2F_3(U_1-3U_2+2U_3)+(b/R_0H_3)h_y]\theta_3=0 \qquad (3.10)$$

If the i^{th} equation is multiplied by θ_i^* (where a * is used to represent the complex conjugate), integrated from $y=-1$ to $y=+1$, and the three equations added, the imaginary part of the resulting equation gives:

$$c_r(\overline{\mathcal{P}_1+\mathcal{P}_2+\mathcal{P}_3})=\overline{U_1\mathcal{P}_1}+\overline{U_2\mathcal{P}_2}+\overline{U_3\mathcal{P}_3}-\frac{\beta}{2}(\overline{J_1+J_2+J_3})-\frac{b}{2R_0H_3}\overline{h_yJ_3} \qquad (3.11)$$

where

$$\mathcal{P}_1=\frac{|\theta_{1y}|^2+k^2|\theta_1|^2}{F_1}+2|\theta_1-\theta_2|^2-\frac{1}{2}|\theta_1-\theta_3|^2$$

$$\mathcal{P}_2=\frac{|\theta_{2y}|^2+k^2|\theta_2|^2}{F_2}+2|\theta_1-\theta_2|^2+2|\theta_2-\theta_3|^2$$

$$\mathcal{P}_3=\frac{|\theta_{3y}|^2+k^2|\theta_3|^2}{F_3}+2|\theta_2-\theta_3|^2-\frac{1}{2}|\theta_1-\theta_3|^2$$

$$J_i=\frac{|\theta_i|^2}{F_i} \qquad (i=1,2,3) \qquad (3.12)$$

and an overbar denotes integration from $y=-1$ to $y=+1$. (3.11) is

directly analogous to (4.2.5) of Pedlosky (1964a). However, further analysis is complicated by the possibility of one of $\mathcal{P}_1$ or $\mathcal{P}_3$ being negative in some region (It seems plausible that $\mathcal{P}_1$, $\mathcal{P}_2$, $\mathcal{P}_3$ are always positive for an unstable wave but I have been unable to prove this. If this result could be proved, bounds identical to those given by Pedlosky would follow in the same manner as in the two-layer case). To proceed further, we let $U_{2o} = (U_1+U_3)/2 + \delta U$ and rewrite (3.11) in the form:

$$c_r(\overline{\mathcal{P}_1+\mathcal{P}_2+\mathcal{P}_3}) = \overline{U_1(\mathcal{P}_1+\tfrac{1}{2}\mathcal{P}_2)} + \overline{U_3(\mathcal{P}_3+\tfrac{1}{2}\mathcal{P}_2)} + \overline{\delta U\cdot\mathcal{P}_2} - \frac{\beta}{2}(\overline{J_1+J_2+J_3}) - \frac{b}{2R_0H_3}\overline{h_yJ_3} \quad (3.13)$$

Now, using the identity

$$|a|^2 + |b|^2 = \frac{|a+b|^2}{2} + \frac{|a-b|^2}{2} \quad (3.14)$$

it is easily seen that $\overline{\mathcal{P}_1 + \frac{1}{2}\mathcal{P}_2}$ and $\overline{\mathcal{P}_3 + \frac{1}{2}\mathcal{P}_2}$ are positive definite quantities (e.g. $\mathcal{P}_1 + \frac{1}{2}\mathcal{P}_2 = |\theta_1-\theta_2|^2 + |\theta_2-\theta_3|^2 - \frac{1}{2}|\theta_1-\theta_3|^2 +$ positive quantities $=$ $\frac{1}{2}|\theta_1-2\theta_2+\theta_3|^2 +$ (positive quantities)).

Now, since for any reasonably well behaved function g which vanishes on $y = \pm 1$ we have

$$\int_{-1}^{1}|g_y|^2dy \geq (\tfrac{\pi}{2})^2\int_{-1}^{1}|g|^2dy \ , \quad (3.15)$$

it is easily shown that

$$\overline{\mathcal{P}_1+\mathcal{P}_2+\mathcal{P}_3} \geq (k^2+(\tfrac{\pi}{2})^2)\ (\overline{J_1+J_2+J_3}) \geq (k^2+(\tfrac{\pi}{2})^2)\ \overline{J_3} \quad (3.16)$$

and using (3.14)

$$\overline{\hat{P}_1+\hat{P}_2+\hat{P}_3} \geq \overline{\hat{P}_2} \quad . \tag{3.17}$$

By considering the cases $c_r \geq U^{1,3}_{max} \equiv \max(U_1,U_3)$ (note that this is not necessarily greater than the maximum of U_{2o}) and $c_r \leq U^{1,3}_{min} = \min(U_1,U_3)$ and using (3.13), (3.15) - (3.17) the following bounds are readily found for c_r (the details are analogous to those of Pedlosky 1964a).

$$U^{1,3}_{min} + \min(\delta U_{min},0) - \frac{\beta}{2(k^2+(\frac{\pi}{2})^2)} - \frac{b}{2R_0H_3}\frac{\max(h_{ymin},0)}{(k^2+(\frac{\pi}{2})^2)}$$

$$\leq c_r \leq U^{1,3}_{max} + \max(\delta U_{max},0) - \frac{b}{2R_0H_3}\frac{\min(h_{ymax},0)}{(k^2+(\frac{\pi}{2})^2)} \tag{3.18}$$

In the case in which $U_{2o} = (U_1+U_3)/2$, these bounds reduce to the same form as found by Pedlosky (1964a) for the two-layer model.

To derive a semi-circle theorem applicable to our model the real part of the equation corresponding to (3.11) is used. This equation can be arranged into the form:

$$\overline{U_1^2\hat{P}_1} + \overline{U_{2o}^2\hat{P}_2} + \overline{U_3^2\hat{P}_3} = (c_r^2+c_i^2)\,\overline{\hat{P}_1+\hat{P}_2+\hat{P}_3} + 2\overline{|\theta_1-\theta_2|^2(U_1-U_{2o})^2} + 2\overline{|\theta_2-\theta_3|^2(U_{2o}-U_3)^2}$$

$$-\frac{1}{2}\overline{|\theta_1-\theta_3|^2(U_1-U_3)^2} + \beta(\overline{U_1J_1+U_{2o}J_2+U_3J_3}) + \overline{U_3(bh_y/R_0H_3)J_3} \tag{3.19}$$

Further considerations will be restricted to the case in which $U_{2o} = (U_1+U_3)/2$ (in any case where $\hat{P}_i > 0$, i = 1,2,3 , this restriction is not necessary).

Now, letting $a = U_{max}$, $d = U_{min}$ and using $\overline{\hat{P}_1+\frac{1}{2}\hat{P}_2} \geq 0$, $\overline{\hat{P}_3+\frac{1}{2}\hat{P}_2} \geq 0$ we have:

$$0 \geq \overline{(U_1-a)(U_1-d)(\mathcal{P}_1+\tfrac{1}{2}\mathcal{P}_2)} + \overline{(U_3-a)(U_3-d)(\mathcal{P}_3+\tfrac{1}{2}\mathcal{P}_2)}$$

$$= \overline{U_1^2\mathcal{P}_1+U_{2_0}^2\mathcal{P}_2+U_3^2\mathcal{P}_3} - (a+d)\,\overline{(U_1\mathcal{P}_1+U_{2_0}\mathcal{P}_2+U_3\mathcal{P}_3)} + ad\overline{(\mathcal{P}_1+\mathcal{P}_2+\mathcal{P}_3)} + \overline{((U_1-U_3)/2)^2\mathcal{P}_2}$$

$$= (c_r^2+c_i^2)\,\overline{(\mathcal{P}_1+\mathcal{P}_2+\mathcal{P}_3)} + \beta\overline{(U_1J_1+U_{2_0}J_2+U_3J_3)} + \overline{U_3(bh_y/R_0H_3)J_3}$$

$$- (a+d)\{c_r\overline{(\mathcal{P}_1+\mathcal{P}_2+\mathcal{P}_3)}+\tfrac{\beta}{2}\overline{(J_1+J_2+J_3)} + \frac{b}{2R_0H_3}\overline{h_yJ_3}\} + ad\overline{(\mathcal{P}_1+\mathcal{P}_2+\mathcal{P}_3)} + \tfrac{1}{4}\overline{(U_1-U_3)^2\mathcal{P}_2}$$

$$+ \tfrac{1}{2}\overline{(U_1-U_3)^2|\theta_1-\theta_2|^2} + \tfrac{1}{2}\overline{(U_1-U_3)^2|\theta_2-\theta_3|^2} - \tfrac{1}{2}\overline{(U_1-U_3)^2|\theta_1-\theta_3|^2} \qquad (3.2)$$

where (3.11) and (3.19) have been used in the second equality. Using (3.14) and the definition of $\mathcal{P}_2$ (cf. (3.12)) the sum of the last four terms in (3.20) is easily seen to be positive. Hence (3.20) gives:

$$\left\{\left[c_r-\left(\frac{a+d}{2}\right)\right]^2+c_i^2\right\}\overline{(\mathcal{P}_1+\mathcal{P}_2+\mathcal{P}_3)} \leq \left(\frac{a-d}{2}\right)^2\overline{(\mathcal{P}_1+\mathcal{P}_2+\mathcal{P}_3)}$$

$$+ \beta\left\{\left(\frac{a+d}{2}\right)\overline{(J_1+J_2+J_3)} - \overline{(U_1J_1+U_{2_0}J_2+U_3J_3)}\right\} + \overline{\left(\frac{a+d}{2}-U_3\right)\frac{b}{R_0H_3}h_yJ_3}$$

$$\leq \left(\frac{a-d}{2}\right)^2\overline{(\mathcal{P}_1+\mathcal{P}_2+\mathcal{P}_3)} + \beta\left(\frac{a-d}{2}\right)\overline{(J_1+J_2+J_3)} + \frac{b}{R_0H_3}\max\left\{\left(\frac{a+d}{2}-U_3\right)h_y\right\}\bar{J}_3$$

Using (3.16), we finally have:

$$\left[c_r - \left(\frac{U_{max}+U_{min}}{2}\right)\right]^2 + c_i^2 \leq \left(\frac{U_{max}-U_{min}}{2}\right)^2 + \frac{\beta(U_{max}-U_{min})}{2\left(k^2+(\frac{\pi}{2})^2\right)}$$

$$+ \frac{b}{R_0H_3}\max\left\{\left[\frac{U_{max}+U_{min}}{2}-U_3\right]h_y\right\}\left[k^2+(\tfrac{\pi}{2})^2\right]^{-1} \qquad (3.21)$$

Using $\max\left\{\left[\frac{U_{max}+U_{min}}{2}-U_3\right]h_y\right\} \leq \frac{1}{2}(U_{max}-U_{min})\,|h_y|_{max}$ this can be replaced

by the convenient form:

$$\left[c_r - \left(\frac{U_{max}+U_{min}}{2}\right)\right]^2 + c_i^2 \leq \left(\frac{U_{max}-U_{min}}{2}\right)^2 + (\beta+(b/R_0H_3)|h_y|_{max})\frac{(U_{max}-U_{min})}{2\left(k^2+(\frac{\pi}{2})^2\right)} \quad (3.22)$$

Although (3.22) has only been derived for the case $U_{2o} = (U_1+U_3)/2$, comparison with the corresponding relations found for the two-layer and continuous cases (Pedlosky, 1964a) suggests that it is probably valid in general. A proof of this result appears to depend on P_1, P_2 and P_3 being independently positive, a proof of which I have been unable to produce.

To find a bound on the growth rate which does not increase as β increases we again follow the work of Pedlosky (1964a). Multiplying the i^{th} equation of (3.8) by ϕ_i^*/F_i, integrating from $y = -1$ to $y = +1$ and taking the imaginary part of the sum of these equations we have:

$$c_i \int_{-1}^{1}\left\{\frac{|\phi_{1y}|^2+k^2|\phi_1|^2}{F_1} + \frac{|\phi_{2y}|^2+k^2|\phi_2|^2}{F_2} + \frac{|\phi_{3y}|^2+k^2|\phi_3|^2}{F_3}\right.$$

$$\left. + 2[|\phi_1-\phi_2|^2+|\phi_2-\phi_3|^2+\frac{1}{2}|\phi_1-2\phi_2+\phi_3|^2]\right\}dy$$

$$= \int_{-1}^{1}\left\{2i(U_1-U_{2o})(\phi_1^*\phi_2-\phi_1\phi_2^*)-\frac{i}{2}(U_1-U_3)(\phi_1^*\phi_3-\phi_1\phi_3^*)+2i(U_{2o}-U_3)(\phi_2^*\phi_3-\phi_2\phi_3^*)\right\}dy$$

$$- \frac{i}{2}\int_{-1}^{1}\left\{\frac{U_{1y}}{F_1}(\phi_1^*\phi_{1y}-\phi_1\phi_{1y}^*) + \frac{U_{2o}y}{F_2}(\phi_2^*\phi_{2y}-\phi_2\phi_{2y}^*) + \frac{U_{3y}}{F_3}(\phi_3^*\phi_{3y}-\phi_3\phi_{3y}^*)\right\}dy \quad (3.23)$$

Now, using

$$|\phi_i\phi_j| \leq |\phi_i|^2 + |\phi_j|^2 \quad (3.24)$$

and

$$2k|\phi_i\phi_{iy}| \leq k^2|\phi_i|^2 + |\phi_{iy}|^2 \tag{3.25}$$

we obtain the following inequality

$$|kc_i| \leq \frac{2(F_1+F_2)k\left|U_1-U_{2o}\right|_{max}}{\left[k^2+(\frac{\pi}{2})^2\right]} + \frac{(F_1+F_3)k\left|U_1-U_3\right|_{max}}{2\left[k^2+(\frac{\pi}{2})^2\right]} + \frac{2(F_2+F_3)k\left|U_{2o}-U_3\right|_{max}}{\left[k^2+(\frac{\pi}{2})^2\right]}$$

$$+ \frac{\left|U_{1y}\right|_{max}}{2} + \frac{\left|U_{2y}\right|_{max}}{2} + \frac{\left|U_{3y}\right|_{max}}{2} \tag{3.26}$$

This method of bounding the growth rate has been interpreted by Pedlosky (1964a) as simply the bound obtained by majorizing the energy conversion terms due to vertical and horizontal shears.

A final bound on the growth rate can be found from (3.8). Multiplying the i^{th} equation by $\phi_i^*/F_i(U_{i_0}-c)$, integrating from $y = -1$ to $y = +1$, summing, extracting the real part and using (3.5) we have:

$$\int_{-1}^{1}\left\{\sum_{i=1}^{3}\frac{U_{io}|\phi_i|^2}{|U_{io}-c|^2}\frac{\partial q_i}{\partial y}\frac{1}{F_i}\right\}dy = \int_{-1}^{1}\left\{\sum_{i=1}^{3}\frac{|\phi_{iy}|^2+k^2|\phi_i|^2}{F_i}\right.$$

$$\left. + 2[|\phi_1-\phi_2|^2+|\phi_2-\phi_3|^2+\tfrac{1}{2}|\phi_1-2\phi_2+\phi_3|^2]\right\}dy \tag{3.27}$$

Since we have shown that, for this case, $(U_{io}\frac{\partial q_i}{\partial y})_{max} > 0$ for instability (cf (3.6)) the following bound is easily derived from (3.27).

$$(kc_i)^2 \leq (k^2/k^2+(\tfrac{\pi}{2})^2)(U\tfrac{\partial q}{\partial y})_{max} \tag{3.28}$$

Finally, if $|U-c_r| \geq \delta$ (i.e. if c_r lies outside the range of U)

this bound can be replaced by:

$$(kc_i)^2 \leq (k^2/k^2+(\tfrac{\pi}{2})^2)(U\frac{\partial q}{\partial y})_{max} - (k\delta)^2 \qquad (3.29)$$

(d) Marginally Stable Waves

The condition for marginally stable waves whose phase speed lies in the range of the mean velocity of one or more of the layers is derived in exactly the same manner as for the two-layer case (cf Pedlosky, 1964b) and hence only the final result shall be given. It is

$$\sum_{i=1}^{3} \sum_{\substack{\text{critical points} \\ \text{in the } i^{th} \text{ layer}}} \frac{|\phi_i|^2}{F_i|U_{iy}|}\frac{\partial q_i}{\partial y} = 0 \qquad (3.30)$$

A critical point in the i^{th} layer is defined as the point y_c where $U_{io}(y_c) = c_r$. The result (3.30) is identical in form to that corresponding to a two-layer fluid.

With the results of this section in hand we now proceed to consider the effects of mixed baroclinic-barotropic instability in the three-layer model.

4. Baroclinic-barotropic instability in the three-layer model (A numerical study)

In this section we consider the three-layer model discussed above with $U_3 \equiv 0$ and $U_2 = \varepsilon U_1$ where $U_1 = U_0(1-\cos \pi(y+1))$. In many respects the work done here is similar to that of section 2 on the two-layer model but one must bear in mind that the vertical shear between the lower layers is an important energy source for baroclinic instability (especially near $\varepsilon = 1.0$) . As in section 2 we are interested in the effect of varying $\varepsilon(=U_2/U_1)$ and we look at this effect in the three cases, $F_i << 1, F_i >> 1$ and $F_i \sim 1$.

Cases I, II: $F_i << 1$ and $F_i >> 1$ $(i=1,2,3)$

These cases may be studied in exactly the same manner as was done for the two-layer model. For $F_i << 1$, i=1,2,3 (horizontal length scale of the mean currents much smaller than the internal deformation radii) the three equations decouple to leading order in F_1 , and for each layer there is the possibility of barotropic instability. For $F_i >> 1$, i=1,2,3 the main energy source for unstable waves is the tilt of the two interfaces, and the most unstable waves are essentially the same as the corresponding waves in the absence of horizontal shear (this has been verified by direct numerical studies). This case has been studied in some detail in chapter II.

Case III: $F_i \sim 1$ (i=1,2,3)

This is the case of greatest interest here for it is in this case that both baroclinic and barotropic energy sources are likely to be important. To facilitate comparison with the work on the two-layer model in section 2 the following parameter values were chosen. $f_0 = 10^{-4}s^{-1}$, $\beta = 0.0$, $g' = 1.00ms^{-2}$ (Note that this is somewhat larger than for the two-layer case), $H_1=H_2=H_3=$ 3333.33m (Note that $H_T = 10$ km as in the two-layer case) and L = 2000 km. The choice of g' is such that F_i (i=1,2,3) are all equal to the corresponding parameters in the two-layer model (i.e. $F_1=F_2=F_3=12$). Since away from $\varepsilon = 0.5$ it was found that baroclinic energy sources strongly dominated the barotropic sources for these parameter values, L = 1,000 km was also considered in some detail. This is of considerable importance in itself since it indicates the fact that the baroclinic energy source is apparently considerably stronger for the three-layer model than for the two-layer model. The explanation for this appears to lie in the fact that the term involving U_{zz} in the equation expressing the conservation of potential vorticity is poorly estimated in a two-layer model but somewhat better estimated using the three-layer model. In fact it was shown in chapter II that the two-layer model corresponds to the limit of the three-layer model as $H_2 \to 0$ with $U_2=(U_1+U_3)/2$ (i.e. with the finite difference approximation to U_{zz} in the middle layer set identically equal to zero).

Approximate stability boundaries for these two cases are given in figure 4.1. Several general features of these boundaries deserve some explanation. Possibly the most striking feature is the cusp at $\varepsilon = 0.5$. This feature has been discussed above and is due to the fact that the vertical

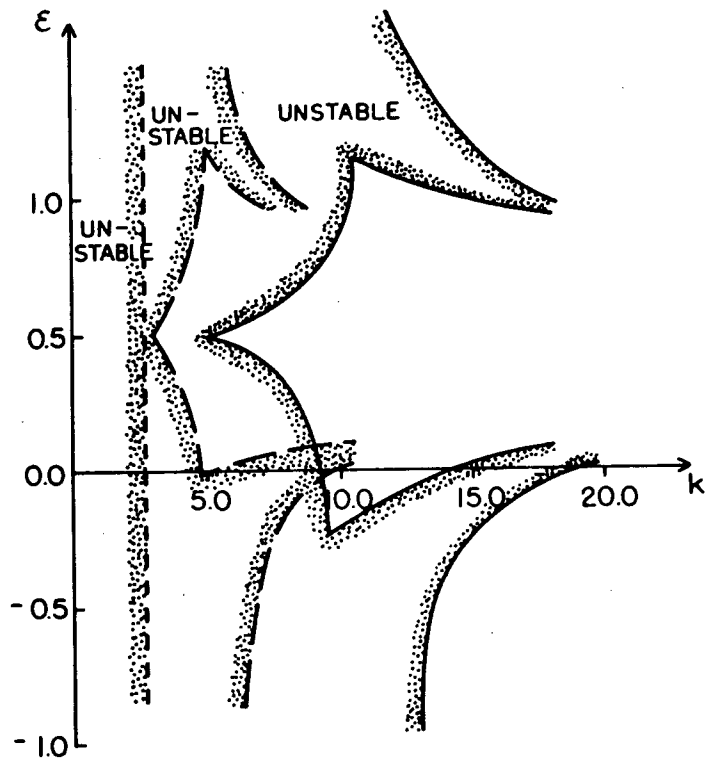

Figure 4.1: Approximate stability boundaries in c vs. k space for the three-layer model. $f_0 = 10^{-4} s^{-1}$, $\beta = 0.0$, $g' = 1.0$, $H_1 = H_2 = H_3 = 3333.33$ m.; L = 57,735 km - approximately vertical line; L = 1,000 km - dashed line; L = 2,000 km - solid line.

curvature of the mean flow is small here. The branches extending to large values of k near $\varepsilon = 0.0$ and $\varepsilon = 1.0$ have been explained by Davey (1977) in a study of pure baroclinic instability (no horizontal shear) in a similar three-layer model. At these short wavelengths, the layers are only weakly coupled and a tilt of one interface acts as effective topography for the two layers above or below as the case may be. The branches may thus be related to similar features of a two-layer model with topography. We also note that instabilities extend to much shorter wavelengths in a three-layer model than they do in the corresponding two-layer model (compare figure 4.1 with figure 2.4). This feature is expected since in the three-layer model, the minimum vertical scale of the motion is two thirds that of the corresponding two-layer case, and we know that for baroclinic instability to occur the vertical and horizontal length scales must be related such that, on the average, the slope of the fluid trajectories in the y-z plane lie within the "wedge of instability" (see Pedlosky, 1971; Hide and Mason, 1974). Finally, we note that the stability boundaries for $L = 1{,}000$ km and $L = 2{,}000$ km are nearly identical outside of a factor of two due to scaling with respect to the half-channel width. If the horizontal length scale had been chosen as the internal deformation radius for the system the two stability boundaries would nearly overlap. This is due to the fact that by $L = 1000$ km, the short wave cut-off is dictated almost entirely by baroclinic instability with the short wave cut-off for barotropically unstable waves occurring at much smaller values of k.

In order to study the effects of varying ε we shall consider the three values $\varepsilon = 0.5$, 0.75 and 1.0 for different values of k. The main emphasis will be on the case $L = 1{,}000$ km but any significant

differences between $L = 2{,}000$ km and $L = 1{,}000$ km will be pointed out.

At $k = 1.0$, $\varepsilon = 0.5$ the most unstable wave has changed from a layer-limited barotropic instability at $L \ll r_i$ to a baroclinically unstable wave with substantial energy input from barotropic instability at $L = 1{,}000$ km $((L/r_i)^2 \sim 3)$ (figure 4.2). Due to the influence of barotropic instability in the upper layer this wave is substantially intensified in the upper layer. Even at $L = 2{,}000$ km $((L/r_i)^2 \sim 12)$ where the net transfer of available potential energy is of order six times the net transfer of kinetic energy, the eigenfunctions of the most unstable wave are very similar to those in figure 4.2. Also present when $L = 2{,}000$ km is a baroclinically unstable wave which loses energy to the mean flow through the horizontal Reynolds stresses. This wave is shown in figure 4.3. It is significant that this wave is equally as strong in the upper and lower layers and considerably diminished in the middle layer. Also considered for $\varepsilon = 0.5$ was the case $k = 2.5$. At $L = 1{,}000$ km the most unstable wave had approximately equal contributions from baroclinic and barotropic energy sources with the major source of potential energy being the tilt of the lower interface and the major source of kinetic energy being the shear of the mean currents in the upper layer as expected (figure 4.4). By $L = 2{,}000$ km the situation is quite different (figure 4.5). The transfer of kinetic energy represents a loss from the perturbations in both of the upper layers and the energy source is baroclinic.

The most unstable wave at $k=1.0$, $\varepsilon=0.75$ has $\omega=0.33 + i\ 0.26$ and is shown in figure (4.6). Comparing this with figure 4.2 ($\varepsilon=0.5$) we see that the phase speeds, growth rates and eigenfunctions for these two cases are very similar. The relative magnitudes of the net TAPE and TKE are also very similar, but their distribution is quite different. At $\varepsilon = 0.5$

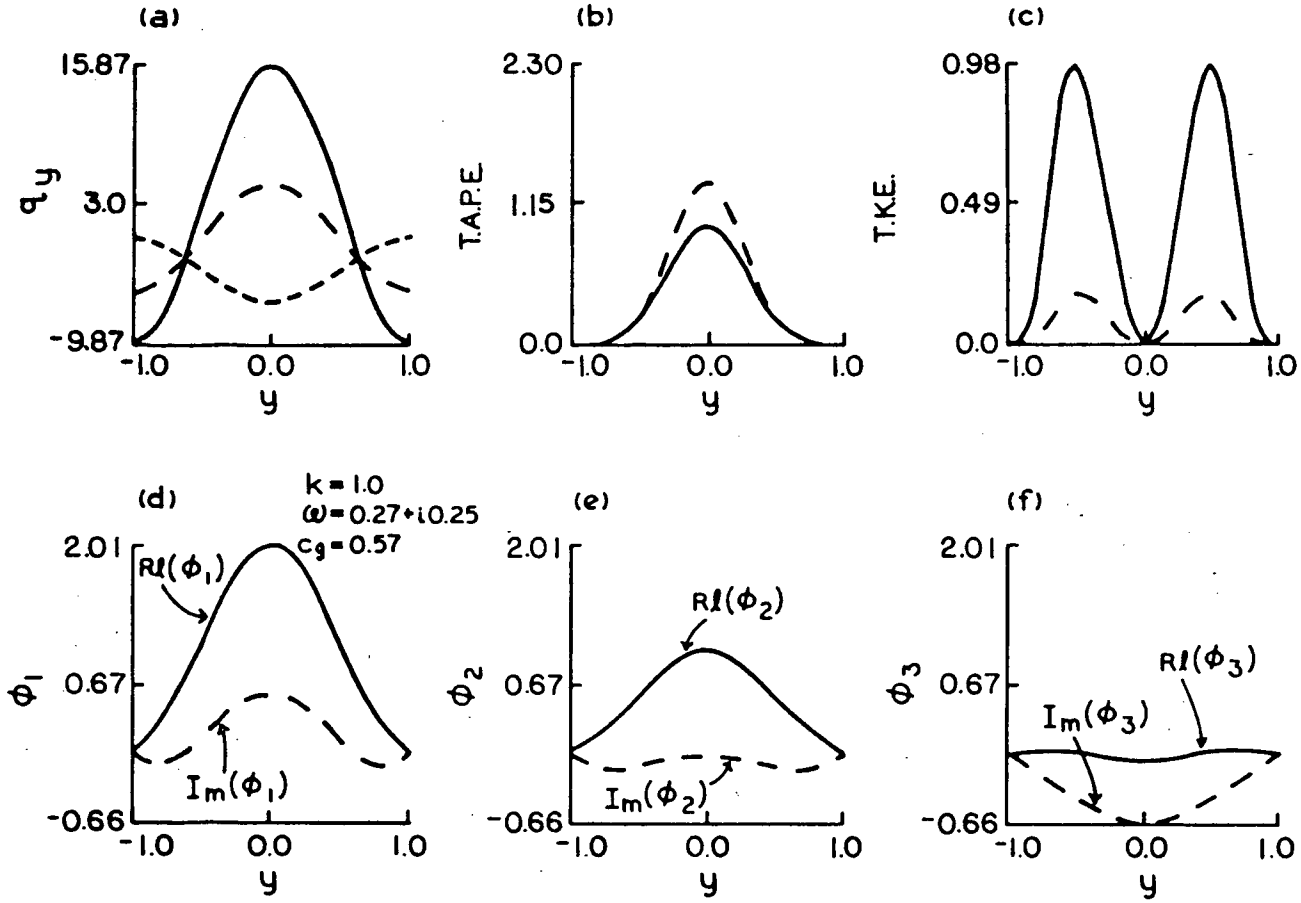

Figure 4.2: (a)The mean potential vorticity gradients in the upper layer (solid line); the middle layer (long dashes); the lower layer (short dashes). (b)Transfer of available potential energy due to shear between the upper layers (solid line) and that due to shear between the lower layers (dashed line). (c)The transfer of kinetic energy in the upper layer (solid line) and in the middle layer (dashed line). The transfer in the bottom layer is zero since $U_3 \equiv 0$. (d)The complex amplitude for the stream function in the upper layer. (e)The complex amplitude for the stream function in the middle layer. (f)The complex amplitude for the stream function in the bottom layer. $f_o = 10^{-4} s^{-1}$, $\beta = 0.0$, L= 1,000km, $g' = 1.00 ms^{-2}$, $H_1 = H_2 = H_3 = 3333.33m$ ($F_1 = F_2 = F_3 \simeq 3$), $U_1 = 1 - \cos\pi(y+1)$, $U_2 = \varepsilon U_1$, $\varepsilon = 0.5$.

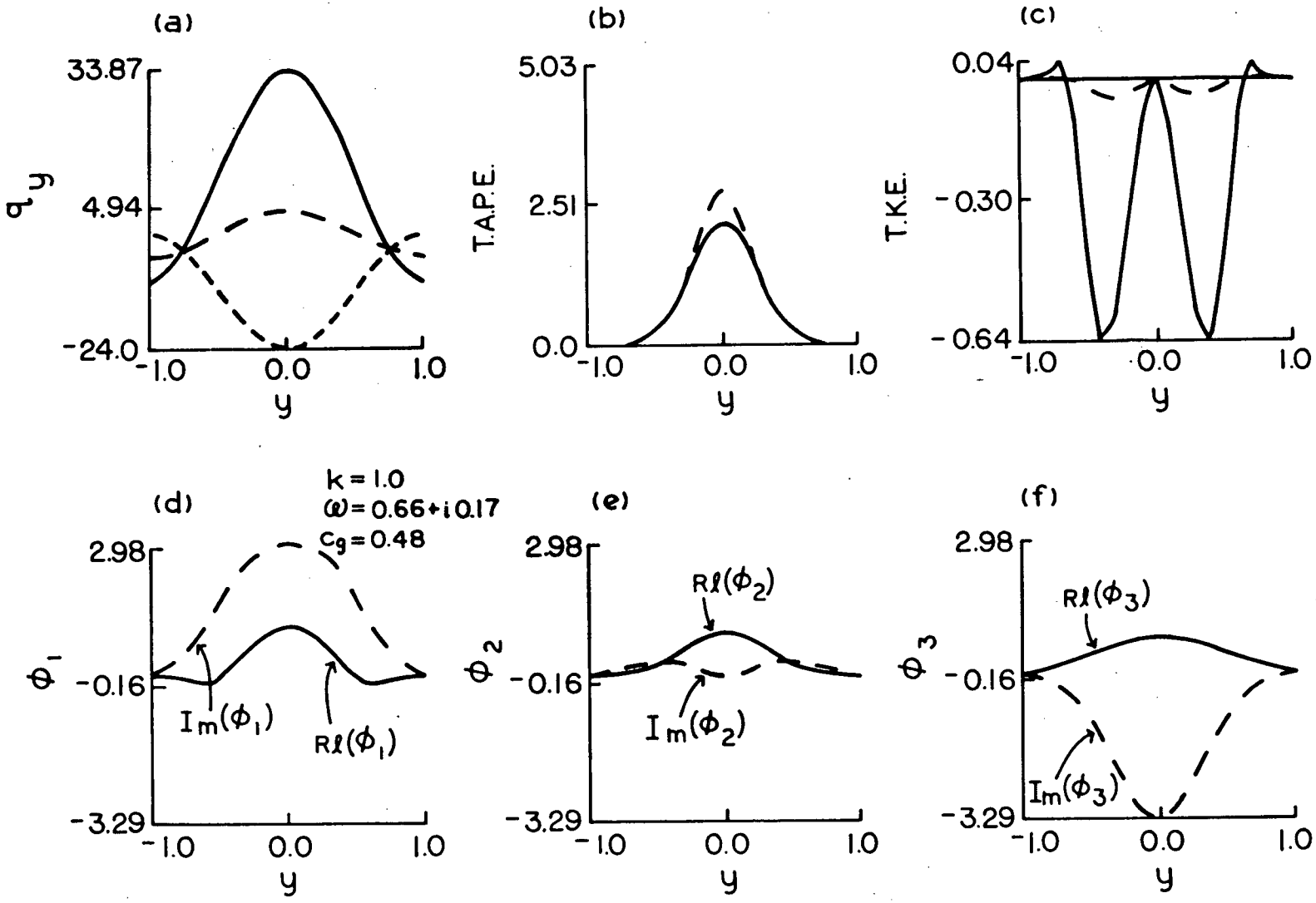

Figure 4.3: As in figure 4.2 but L = 2,000 km.

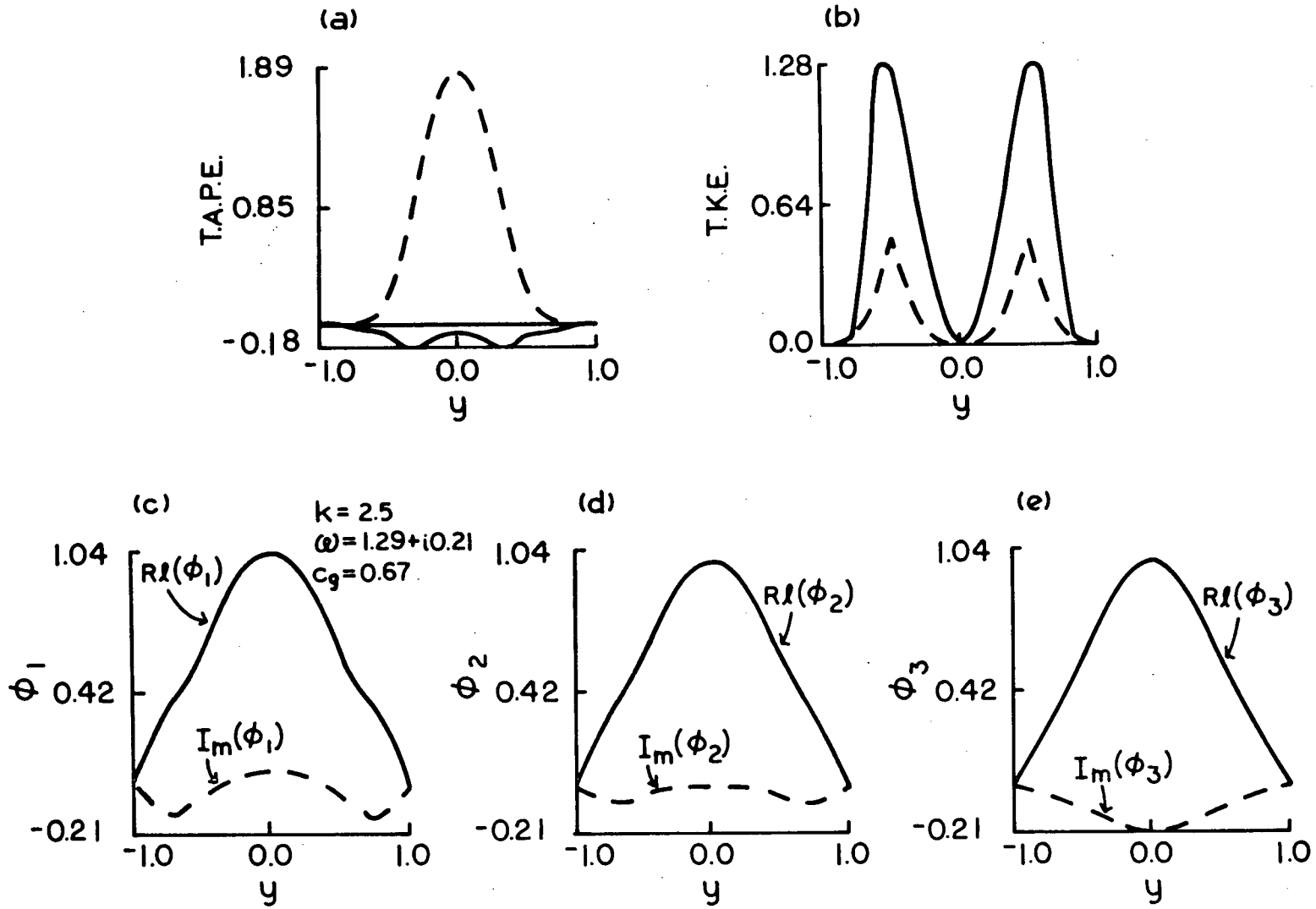

Figure 4.4: As in figure 4.2 - the instability at larger k .

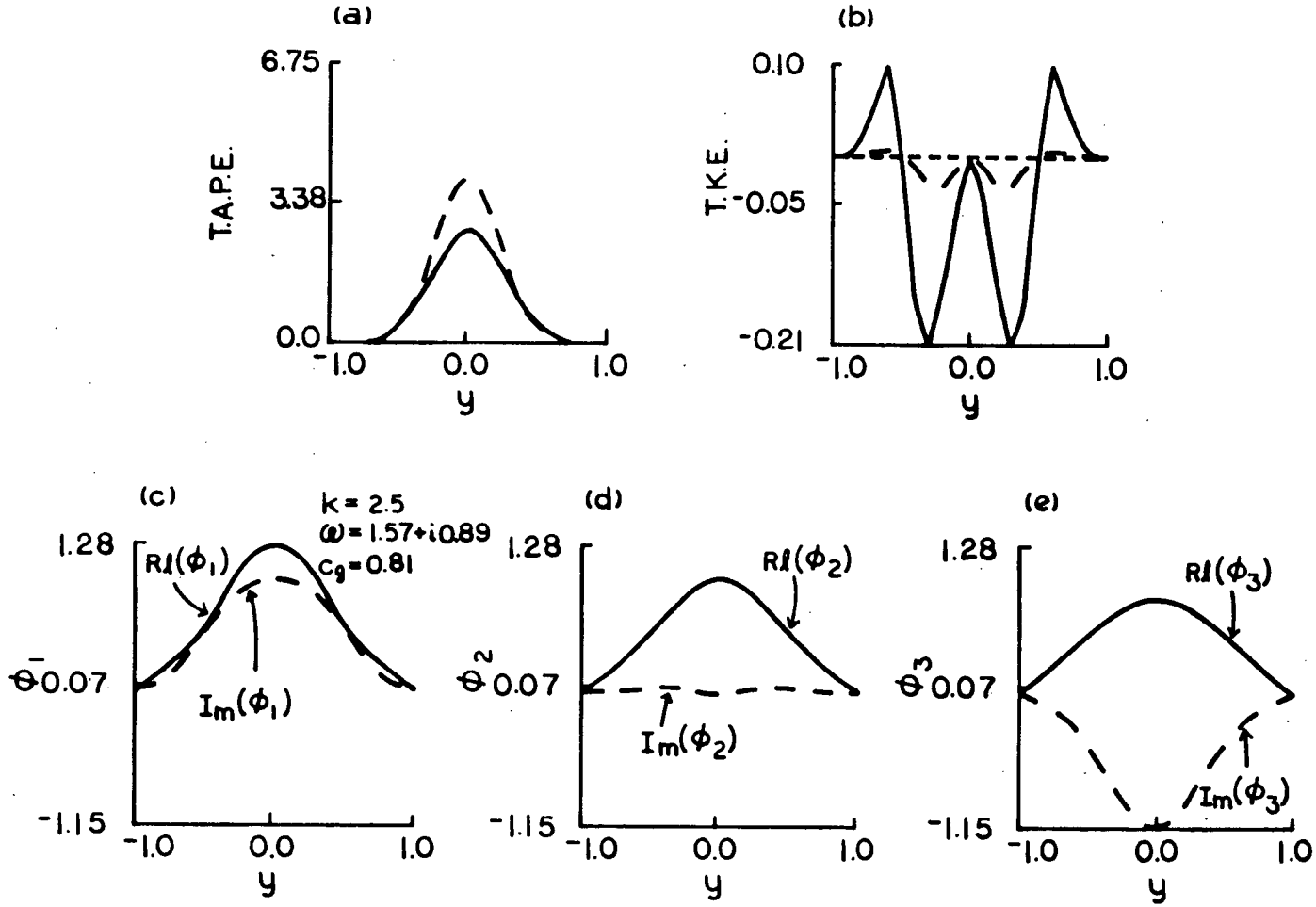

Figure 4.5: As in figure 4.3 - the instability at larger k .

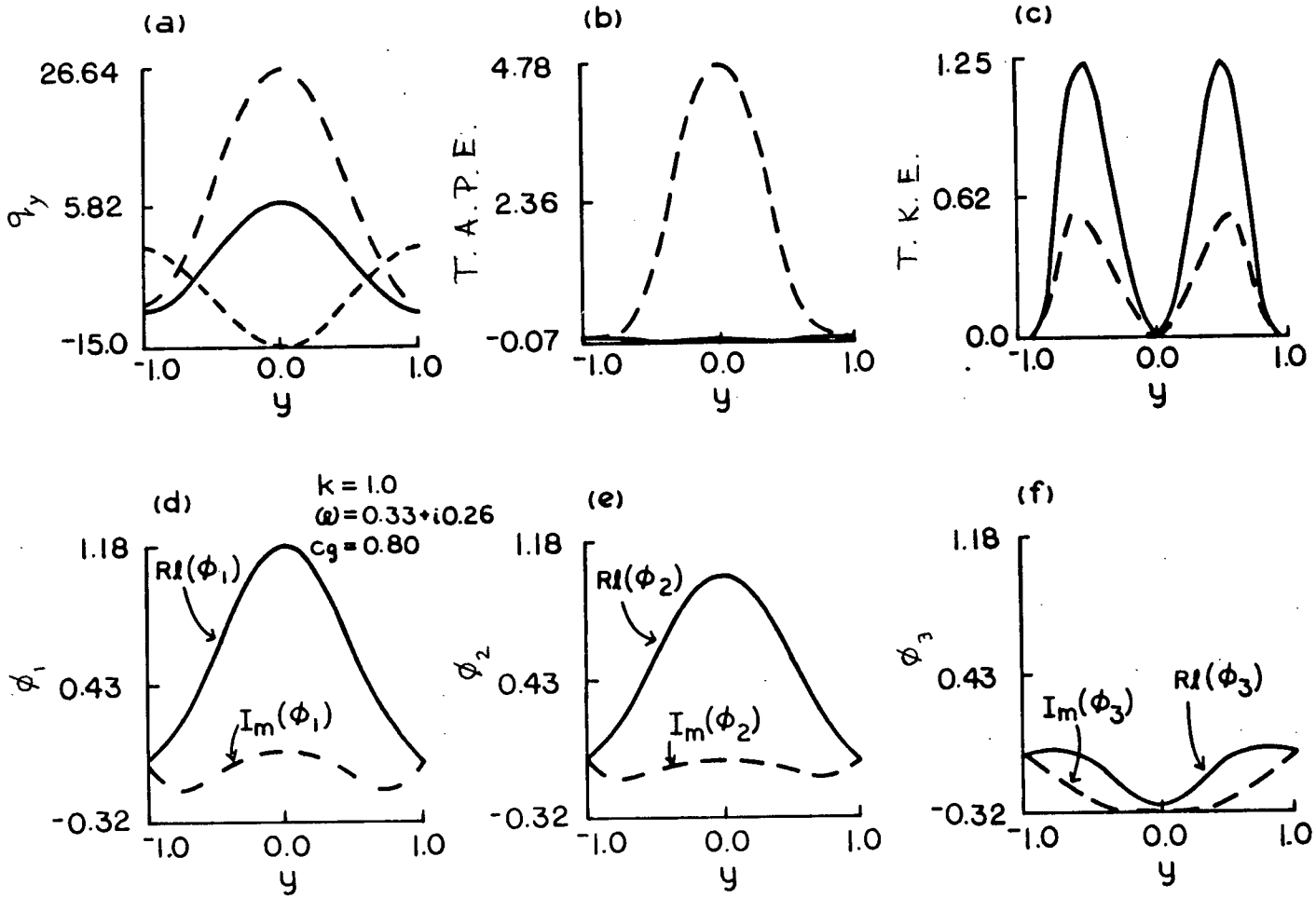

Figure 4.6: As in figure 4.2 but $\epsilon = 0.75$.

the source of potential energy is almost equally distributed between the upper and lower interfaces whereas at $\varepsilon = 0.75$ the tilt of the lower interface is the main source of potential energy. Also, with the increase in U_2 the TKE in the middle layer is substantially increased. Unlike the case $\varepsilon = 0.5$ the most unstable wave at $L = 1{,}000$ km still remains at $L = 2{,}000$ km with relatively minor changes in phase speed, growth rate and eigenfunctions. However, as expected the relative magnitude of the TKE is considerably reduced compared to the TAPE (compare figures 4.6 and 4.7). One point of considerable interest is clear from these figures (especially figure 4.7). Although the major source of energy for the perturbations is the tilt of the lower interface, the wave is intensified in the upper layers. In the absence of horizontal shear, the unstable wave here would be intensified in the lower layers. It appears that a relatively small TKE is capable of a very significant vertical redistribution of energy in the growing perturbation. This behaviour has frequently been observed in this study and appears to be of major importance whenever the TKE represents a source of energy for the perturbations. This behaviour will be observed again for $\varepsilon = 1.0$ in figure 4.10.

Although the most unstable wave at $L = 1{,}000$ km is still present at $L = 2{,}000$ km it no longer has the largest growth rate. The wave with the largest growth rate is due to baroclinic instability and loses very small amounts of kinetic energy (relative to the TAPE) in both of the upper layers (figure 4.8).

Now, if one considers $k = 3.5$ (with $\varepsilon = 0.75$ still), things are much as expected. We are well beyond the short wave cut-off for barotropic instability and the waves are not substantially influenced by the presence

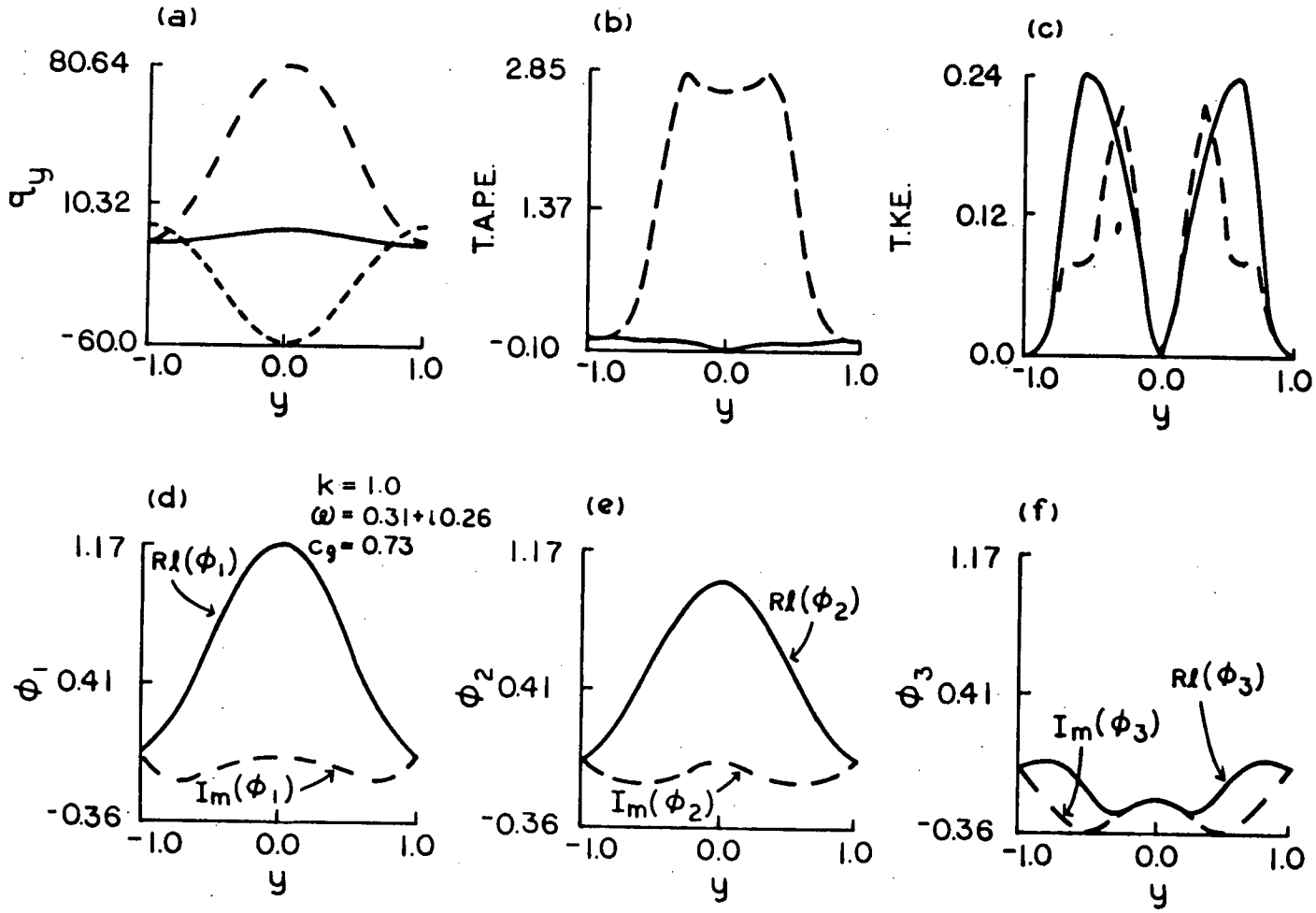

Figure 4.7: As in figure 4.2 but L = 2,000 km., ε = 0.75 .

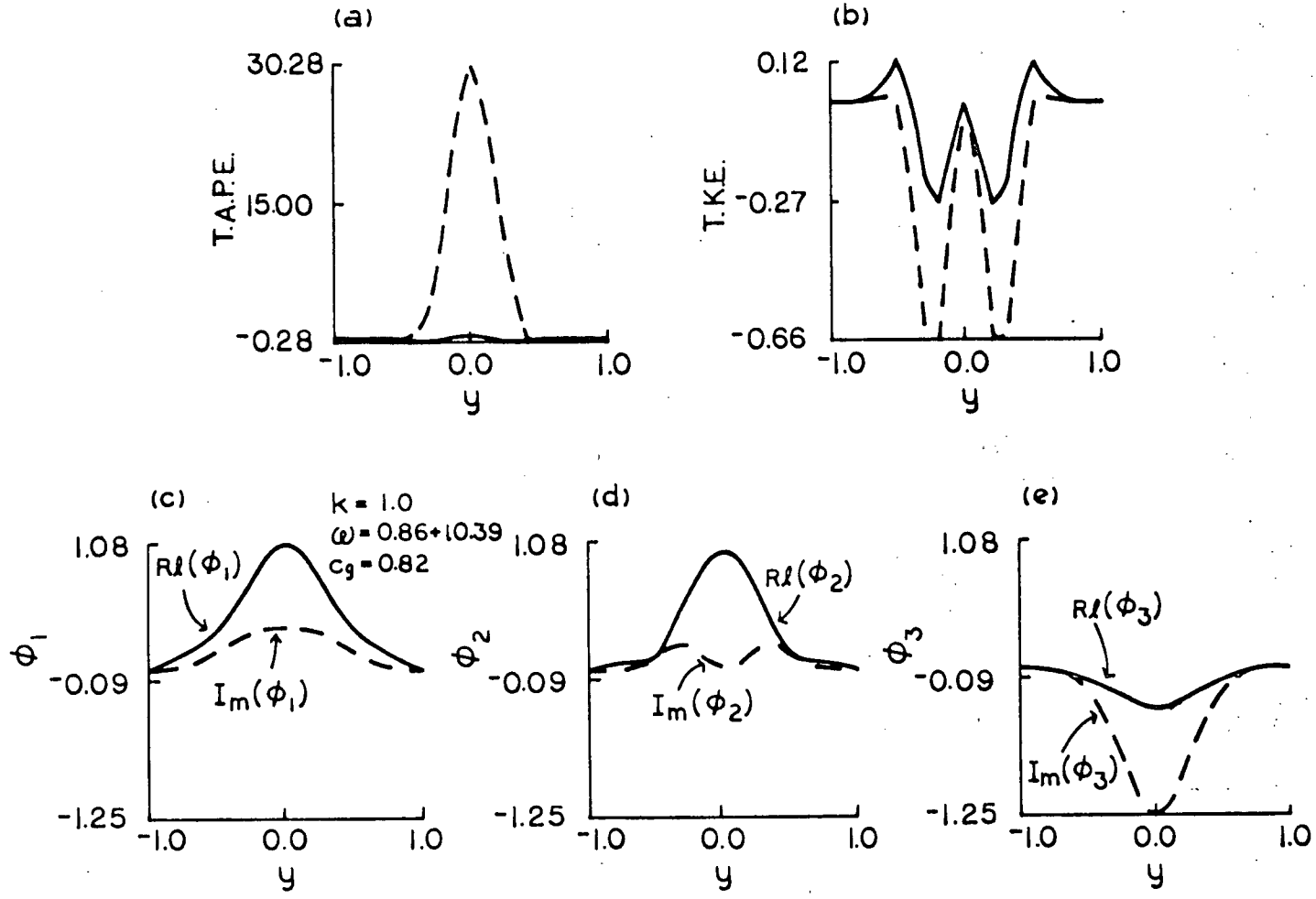

Figure 4.8: As in figure 4.7.

of the horizontal shear. As shown in figure 4.9 the most unstable wave for L = 1,000 km is a bottom intensified baroclinically unstable wave extracting its energy primarily from the tilt of the lower interface. There is a small gain through the Reynolds stresses in the upper layer, and a loss in the lower layer but neither of these appear to have any significant effect. The only major difference at L = 2,000 km is that both the phase speed and the growth rates are substantially increased (ω = 3.06+i 1.94 for the most unstable wave at L = 2,000 km compared to ω = 2.35+i 0.72 at L = 1,000 km). The energy transfer properties and eigenfunctions are not substantially altered although the eigenfunction is slightly less intensified in the lower layers. The explanation for the seemingly large discrepancy in phase speed (we expect the growth rate to be increased) lies in the fact that we are comparing waves with the same non-dimensional wavelength when scaled with the horizontal length scale of the mean currents when the appropriate length scale is the internal deformation radius. In fact the phase speed of the most unstable wave at k = 7.0, L = 2,000 km is very near that for k = 3.5, L = 1,000 km as it should be. The eigenfunctions and energy transfer properties of these two waves are also in excellent agreement.

Finally, we consider ε = 1.0 . This case is in fact very similar to ε = 0.75 and hence will only be considered briefly. The figure corresponding to figure 4.7 (ε = 0.75) is given in figure 4.10. We see that the only differences that occur are quantitative and due mainly to the increase in TKE in the middle layer. The figures corresponding to figures 4.6, 4.8 and 4.9 show similar agreement and will not be reproduced. In figure 4.10 we see that the effect of the small TKE in redistributing the energy of the perturbation is again surprisingly strong. In fact, the effect is so strong that in spite of the fact that

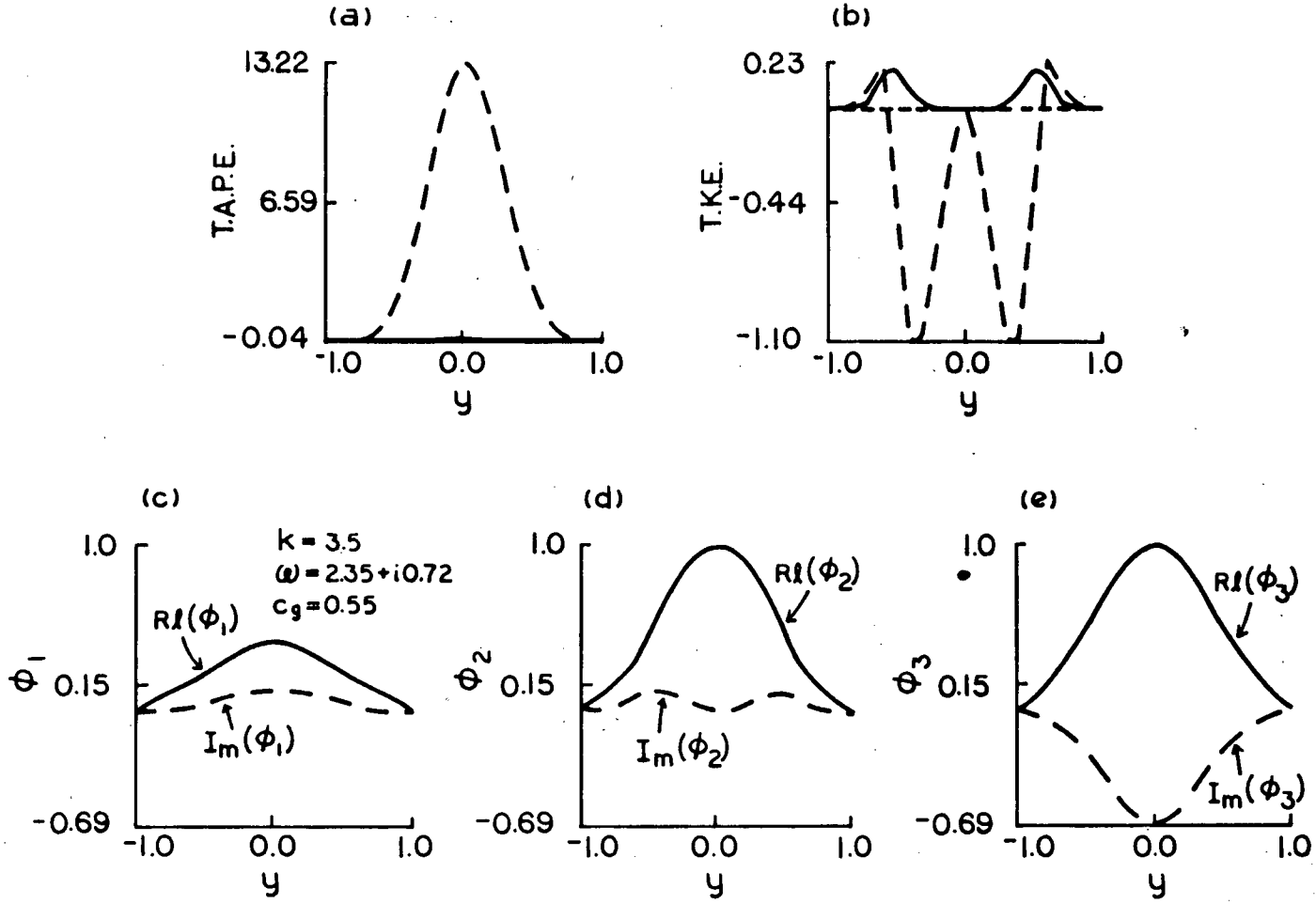

Figure 4.9: As in figure 4.6.

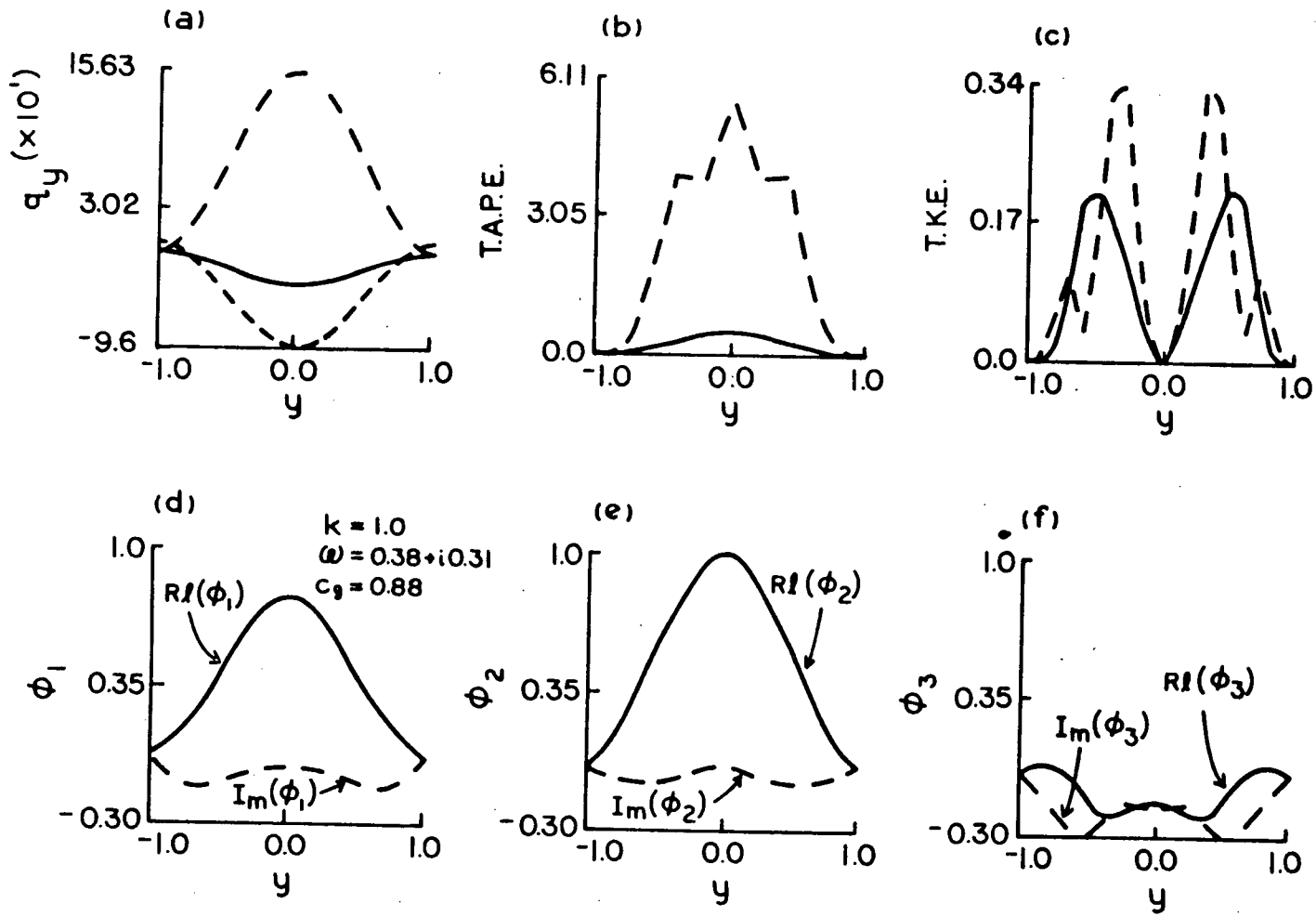

Figure 4.10: As in figure 4.7 but L = 2,000 km., ε = 1.0 .

TAPE $\sim 10 \times$ TKE it is still reasonable to refer to these waves as barotropically unstable waves modified by baroclinic effects.

The final case of interest is the instabilities associated with the branch extending to the right near $\varepsilon = 0.0$ and $\varepsilon = 1.0$ in figure 4.1. As mentioned earlier this branch has been explained by Davey (1977) as a result of the layers effectively decoupling and the tilt of one or the other of the interfaces acting similar to bottom topography. No attempt was made to study these waves in detail as the growth rates of these waves were very small and it would take a large number of cross-channel modes to properly resolve them. Studies with 10 symmetric cross-channel modes did however indicate that Davey's conclusions are correct.

5. Conclusions

We have considered baroclinic-barotropic instability in two- and three-layer models. For the case of a mean flow with a short horizontal length scale ($(L/r_i)^2 << 1$) it is shown that the study of barotropic instability is appropriate with the thickness of the layer in which the large horizontal shear occurs used as the fluid depth. From the proof given in section 2 it is clear that this result holds for any region (layer) in which the condition $(L/r_i)^2 << 1$ holds. This result may be immediately extended to a continuously stratified fluid. The condition $(L/r_i)^2 << 1$ simply states that the vertical stability of the fluid is so large that the process of baroclinic instability is inhibited (i.e. that the rotation rate is so small or the density stratification so strong that the isopycnal slopes are insufficient for significant amounts of potential energy to be released by the process of baroclinic instability), however the process of barotropic instability involves only horizontal exchanges of fluid (and vorticity) and hence is affected little by the vertical stability. Thus in a region of high vertical stability, "layer limited" barotropic instability is possible. This fact is very significant since averaging over the depth of the fluid may eliminate or greatly diminish the instability if the large horizontal shears occur over a limited depth of the fluid, thus such averaging is not recommended in the study of cases where the process of barotropic instability is believed to be dominant. A better approximation would be to consider the region in which $(L/r_i)^2 << 1$ separately.

Now, as $(L/r_i)^2$ increases the mechanism of baroclinic instability becomes increasingly important. Since baroclinic instability occurs on the scale of the internal deformation radius, and barotropic instability occurs on the scale of the horizontal shear of the mean currents, for

$(L/r_i)^2$ small, baroclinic instability will be limited to very large length scales (i.e. very small $k = k^* L$). Further, the growth rates of such baroclinically unstable waves will be small relative to those of barotropically unstable waves in the system. However, for $(L/r_i)^2 \sim 1$ substantial baroclinic and barotropic instabilities may occur at the same wavelengths and the interaction can be strong. The (basically) baroclinically unstable waves generally lose kinetic energy to the mean flow through the horizontal of Reynold's stresses while the barotropically unstable waves extract additional energy from the mean state through the process of baroclinic instability. As expected, the main effect of the losses due to the Reynold's stress on the baroclinically unstable waves (both above and below the long wave cut-off for barotropic instability) is to reduce the growth rates of the waves. It appears that the study of these waves may be reasonably undertaken by taking the shear between the layers to be an appropriate mean value across the channel. However this approximation eliminates the second class of instabilities (the basically barotropically unstable waves) which we have seen may have significant growth rates even for $(L/r_i)^2$ large due to their ability to extract potential energy from the mean flow. A very interesting property of these waves is that their vertical energy distribution appears to be dictated primarily by the transfer of kinetic energy even when their dominant energy source is the transfer of available potential energy.

For $(L/r_i)^2 >> 1$ the barotropically unstable waves are limited to very long wavelengths (relative to those of the most unstable baroclinic waves) where the growth rates are much smaller than for the shorter baroclinically unstable waves. Thus for $(L/r_i)^2 >> 1$ the flow will be essentially baroclinically unstable and may be studied by considering uniform shears across the

channel. It is, however, important to note that the condition $(L/r_i)^2 >> 1$ must be strongly satisfied before such a study is justified (the studies with the cosine jet suggest that this condition is more accurately stated as $(L/r_i)^2 >> \pi^2$) .

Finally, we mention the work of section 3 in which the three layer model of chapter II is further developed. The energy equation is discussed, necessary conditions for instability derived, bounds on phase speeds and growth rates are found and the condition for marginally stable waves with phase speed within the range of the mean currents is discussed. All of these results are essentially identical to the corresponding work done on the two-layer model (Pedlosky, 1964a,b) although the bounds on the phase speeds are somewhat weaker unless $U_2 = (U_1+U_3)/2$.

The work done here suggests that in most cases of real oceanic flows the study of instabilities should include the effects of both horizontal and vertical shears (as well as the effects of topography and β which have not been considered here). All of these aspects are considered in chapter IV in which the three-layer model is applied to real ocean situations.

Appendix a - Method of Solution

We have already seen in chapter II how a simple analytical solution of (3.40) (with $\phi_i = 0$ on $y = \pm 1$, $i = 1,2,3$) may be found for the case

$$U_{i_0} = \text{constant}$$

$$h_y = \text{constant}$$

Under these restrictions solutions are found in the form $\phi_i = \mu_i \sin \frac{m\pi}{2}(y+1)$ with the μ_i's being determined from the differential equations. In order to extend this method to more general cases the following expansions are made.

$$U_i(y) = u_{i_0} + \sum_{k=1}^{\infty} u_{i_k} \cos \frac{k\pi}{2}(y+1)$$

$$U_{iyy}(y) = uc_{i_0} + \sum_{k=1}^{\infty} uc_{i_k} \cos \frac{k\pi}{2}(y+1)$$

$$bh_y/H_3 = hs_0 + \sum_{\ell=1}^{\infty} hs_\ell \cos \frac{\ell\pi}{2}(y+1)$$

$$\phi_i = \sum_{m=1}^{\infty} \mu_{im} \sin \frac{m\pi}{2}(y+1) \qquad \text{(A.1)}$$

The second of these expansions permits the study of cases in which the differentiated series for the first case may be slowly or non-convergent.

Substitution of (6.1) in (3.10) results in an infinite dimensional matrix eigenvalue problem of the form:

$$(\underline{\underline{A}} - c\underline{\underline{B}})\underline{\Phi} = \underline{0} \qquad \text{(A.2)}$$

where c is the (complex) phase speed, $\underline{\underline{A}}$ and $\underline{\underline{B}}$ are square matrices, and $\underline{\Phi}$ is a column matrix containing the coefficients for the eigenfunction

expansions. The components of these matrices are given below.

$$a_{3j-2,3m-2} = -\frac{1}{2}(K_m^2-F_1)(u_{1_{|m-j|}}-u_{1_{m+j}}) - 3F_1(u_{2_{|m-j|}}-u_{2_{m+j}}) + F_1(u_{3_{|m-j|}}-u_{3_{m+j}})$$

$$-\frac{1}{2}(uc_{1,|m-j|}-uc_{1,m+j}) + (\beta-K_m^2 u_{1_0}-uc_{1_0}+F_1(u_{1_0}-6u_{2_0}+2u_{3_0}))\delta_{mj}$$

$$a_{3j-2,3m-1} = 2F_1(u_{1_{|m-j|}}-u_{1_{m+j}}) + 4F_1 u_{1_0}\delta_{mj}$$

$$a_{3j-2,3m} = -F_1/2(u_{1_{|m-j|}}-u_{1_{m+j}}) - F_1 u_{1_0}\delta_{mj}$$

$$a_{3j-1,3m-2} = 2F_2(u_{2o_{|m-j|}}-u_{2o_{m+j}}) + 4F_2 u_{2o_0}\delta_{mj}$$

$$a_{3j-1,3m-1} = -\frac{1}{2}(K_m^2+8F_2)(u_{2o_{|m-j|}}-u_{2o_{m+j}}) - \frac{1}{2}(uc_{2o_{|m-j|}}-uc_{2o_{m+j}})$$

$$-3F_2(u_{1_{|m-j|}}-u_{1_{m+j}}-2u_{2_{|m-j|}}+2u_{2_{m+j}}+u_{3_{|m-j|}}-u_{3_{m+j}})$$

$$+ (\beta-(K_m^2+8F_2)u_{2o_0}-uc_{2o_0}-6F_2(u_{1_0}-2u_{2_0}+u_{3_0}))\delta_{mj}$$

$$a_{3j-1,3m} = 2F_2(u_{2o_{|m-j|}}-u_{2o_{m+j}}) + 4F_2 u_{2o_0}\delta_{mj}$$

$$a_{3j,3m-2} = -F_3 u_{3_0}\delta_{mj} - F_3/2(u_{3_{|m-j|}}-u_{3_{m+j}})$$

$$a_{3j,3m-1} = 4F_3 u_{3_0}\delta_{mj} + 2F_3(u_{3_{|m-j|}}-u_{3_{m+j}})$$

$$a_{3j,3m} = -K_m^2/2(u_{3_{|m-j|}}-u_{3_{m+j}}) - \frac{1}{2}(uc_{3_{|m-j|}}-uc_{3_{m+j}})$$

$$+ F_3(u_{1_{|m-j|}}-u_{1_{m+1}}-3u_{2_{|m-j|}}+3u_{2_{m+j}}+\frac{1}{2}u_{3_{|m-j|}}-\frac{1}{2}u_{3_{m+j}})$$

$$+ (\beta-K_m^2 u_{3_0}-uc_{3_0}+2F_3(u_{1_0}+3u_{2_0}+\frac{1}{2}u_{3_0})+hs_0/R_o)\delta_{mj} + (\frac{1}{2R_o})(h_{s_{|m-j|}}-h_{s_{m+j}})$$

$$b_{3j-2,3m-2} = -(K_m^2+3F_1)\delta_{mj}$$

$$b_{3j-2,3m-1} = 4F_1\delta_{mj}$$

$$b_{3j-2,3m} = -F_1\delta_{mj}$$

$$b_{3j-1,3m-2} = 4F_2\delta_{mj}$$

$$b_{3j-1,3m-1} = -(K_m^2+8F_2)\delta_{mj}$$

$$b_{3j-1,3m} = 4F_2\delta_{mj}$$

$$b_{3j,3m-2} = -F_3\delta_{mj}$$

$$b_{3j,3m-1} = 4F_3\delta_{mj}$$

$$b_{3j,3m} = -(3F_3+K_m^2)\delta_{mj}$$

$$\Phi_{3m-2} = \mu_{1m} \qquad \Phi_{3m-1} = \mu_{2m} \qquad \Phi_{3m} = \mu_{3m}$$

where $K_m^2 = k^2 + (\frac{m\pi}{2})^2$

$$u_{2o_j} = (6u_{2j}-u_{1j}-u_{3j})/4$$

$$uc_{2o_j} = (6uc_{2j}-uc_{1j}-uc_{3j})/4$$

This system was approximately solved by truncating the eigenfunction expansions at a point where the eigenfunction expansions appeared to have settled down. For the most unstable waves, only a few modes were generally required although the number varied with the form of the mean currents. In this paper, only symmetric velocity profiles are considered and we have

taken $h \equiv 0$. Under these restrictions, the solutions of (3.10) are either symmetric or anti-symmetric in y (since the coefficients in 3.10 are then even functions of y) and these two classes of solutions can be considered separately (at a considerably reduced expense). Since the symmetric modes were generally the most unstable, only these modes are discussed. In practice, ten symmetric modes were used in all the calculations presented in this paper (i.e. ϕ_i was approximated by $\phi_i = \sum_{m=1}^{10} \mu_{i_{2m-1}} \sin\frac{(2m-1)\pi}{2}(y+1))$. This is considerably more than is generally required.

Finally, we note that for cases such as those presented in figures 2.2 and 2.3, the value of c at the short wave cut-off is known exactly from the work on marginally stable waves (3(d)). In this case it is preferable to fix c in (3.10) and solve the resulting eigenvalue problem with k^2 as the eigenvalue. This eigenvalue problem is simply expressed in terms of the definitions given by (A.3). It is given by:

$$(\underline{\underline{\bar{A}}} - k^2\underline{\underline{\bar{B}}})\underline{\Phi} = \underline{0}$$

where $\underline{\underline{\bar{A}}}$ and $\underline{\underline{\bar{B}}}$ are given by the following. First, set $K_m^2 = (\frac{m\pi}{2})^2$ instead of $(\frac{m\pi}{2})^2 + k^2$ in (A.3). Then $\underline{\underline{\bar{A}}} = \underline{\underline{A}} - c_s\underline{\underline{B}}$ and $\underline{\underline{\bar{B}}}$ is given by

$$b_{i,j} = 0 \quad (i \neq j)$$

$$b_{3j-2,3m-2} = \frac{1}{2}(u_{1_{|m-j|}} - u_{1_{m+j}}) + (u_{1_0} - c_s)\delta_{mj}$$

$$b_{3j-1,3m-1} = \frac{1}{2}(u_{2o_{|m-j|}} - u_{2o_{m+j}}) + (u_{2o_0} - c_s)\delta_{mj}$$

$$b_{3j,3m} = \frac{1}{2}(u_{3_{|m-j|}} - u_{3_{m+j}}) + (u_{3_0} - c_s)\delta_{mj}$$

Finally the approximate stability boundaries presented in figures (2.4)

and (4.1) need some further discussion. The method used in this paper to study unstable waves is not well suited to the calculation of stability boundaries due to the singular nature of the governing differential equations (and hence the resulting eigenvalue problem) for $c_i=0$ (or ≈ 0). For this reason we stress that while we may use the method employed here to study the most unstable waves, the stability boundaries calculated by this method are qualitative in nature and small details should not be taken seriously. In fact the unstable wave associated with the branches extending to the right in both figures 2.4 and 4.1 have very small growth rates and are not very well resolved. Due to the inherent qualitative nature of these boundaries, figure 4.1 was calculated using only 3 symmetric modes and checked at several points with 10 modes for qualitative accuracy (the results agree quite well). In spite of the qualitative nature of these figures, they do contain much useful information.

Appendix b

In this appendix it is shown that the minimum value of U_o at which instability occurs in a two-layer model with $U_1 = U_o(1-\cos \pi(y+1))$, $U_2 \equiv 0$ is precisely the minimum value for which q_y changes sign somewhere. Since the phase speed at the high wavenumber cut-off is given by $c = U_1(y_s)$ where y_s is given by $q_{1_y}(y_s) = 0$ and the low wavenumber cut-off consists of retrograde waves the minimum value of U_o for which instability occurs must have $c = 0$. The equation for the second layer then gives $\phi_2 \equiv 0$ (i.e. we are essentially considering a case of barotropic instability) and the upper layer equation reduces to

$$U_1[\phi_{1yy}-k^2\phi_1-F_1\phi_1] + \phi_1[\beta-U_{1yy}+F_1U_1] = 0$$

It is now easily verified that for $U_o = \beta/\pi^2$ (the minimum value for which $q_y = 0$ somewhere and also precisely that value which makes $q_{1_y} \propto U_1$) $\phi_1 = A \sin\frac{n\pi}{2}(y+1)$ is a solution for $k^2 = \pi^2 - (\frac{n\pi}{2})^2$. Clearly only the first mode can be unstable and the value of k corresponding to the minimum value of U_o on the stability boundary is $k = (\sqrt{3}/2)\pi$.

CHAPTER IV

OCEANIC APPLICATIONS

1. Introduction

Energetic current fluctuations with periods longer than a day have been observed in many regions of the ocean during the past decade. Probably the most accepted explanation for the presence of these fluctuations is that potential energy (available from the tilt of the isopycnals in a rotating stratified fluid in the presence of vertical shear) may be released to perturbations at these frequencies by the process of baroclinic instability (Charney (1947), Eady (1949), Green (1960), Pedlosky (1964)). A second possible energy source for these fluctuations is the kinetic energy of the mean currents made available by horizontal shear in these currents. When this is the principle source of energy for the perturbations the mechanism by which energy is extracted is known as barotropic instability (Lin (1945), Kuo (1949, 1973), Drazin and Howard (1966)). Using the model developed in chapter II, both of these energy sources are included in a study of the stability of the current systems in Juan de Fuca Strait and the northern region of the California Undercurrent (off Washington and Vancouver Island). In each case, it is found that the major source of energy is the potential energy due to sloping isopycnals and that the main influence of horizontal shear in the mean currents is to limit the region in which the vertical shear is such that energy is released to the perturbations. Mysak (1977) has studied pure baroclinic instability in a two-layer model of the California Undercurrent and found results consistent with observations. Through a study of the stability of a three-layer system including horizontal shear and non-constant bottom slope, the results of Mysak's study are extended and several questions raised in his paper are examined. In particular we find that replacing the upper layer of strongly stratified

fluid with a rigid lid is valid in the study of the waves examined by Mysak. However, this approximation filters out a very important class of instabilities which extract potential energy from the tilt of the upper interface, and it appears likely that this class of instability may be responsible for the observed wave-like perturbations in the region of the California Undercurrent.

2. Juan de Fuca Strait

Juan de Fuca Strait consists of two basins separated by an effective sill extending southward from Victoria at a depth of about 100 m (see figure 2.1). Although we will principally concentrate on the western basin, we will find that the most unstable waves in the strait are strongly surface intensified and hence the sill probably does not act as a barrier to these waves. The western basin is approximately 20 km across and 90 km long with a relatively uniform rectangular cross-section throughout its length. The most complete measurements of the currents in this basin have been presented by Fissel and Huggett (1976), Fissel (1976), Cannon and Laird (1978) and Holbrook and Halpern (1978). The reports by Fissel and Huggett, and Fissel are concerned with the same set of measurements collected in the period from late May to mid-July 1975. The positions at which these measurements were taken are shown in figures 2.1 (circles) and 2.2. Figure 2.2 also includes the values of the mean long-strait currents during the measurement period. The average density profile across this cross-section, measured during a cruise on June 14-15, 1975 is indicated in figure 2.3 together with the approximate density stratification corresponding to the model developed in chapters II and III of this thesis. The approximation is clearly quite reasonable. A more complete set of measurements of the mean currents than those given in figure 2.2 (appropriate to the nearby cross-section indicated by the x's in figure 2.1), measured during the same season (June-August 1977), has been presented by Cannon and Laird (1978) and is reproduced in figure 2.4. These two sets of mean current measurements appear to be

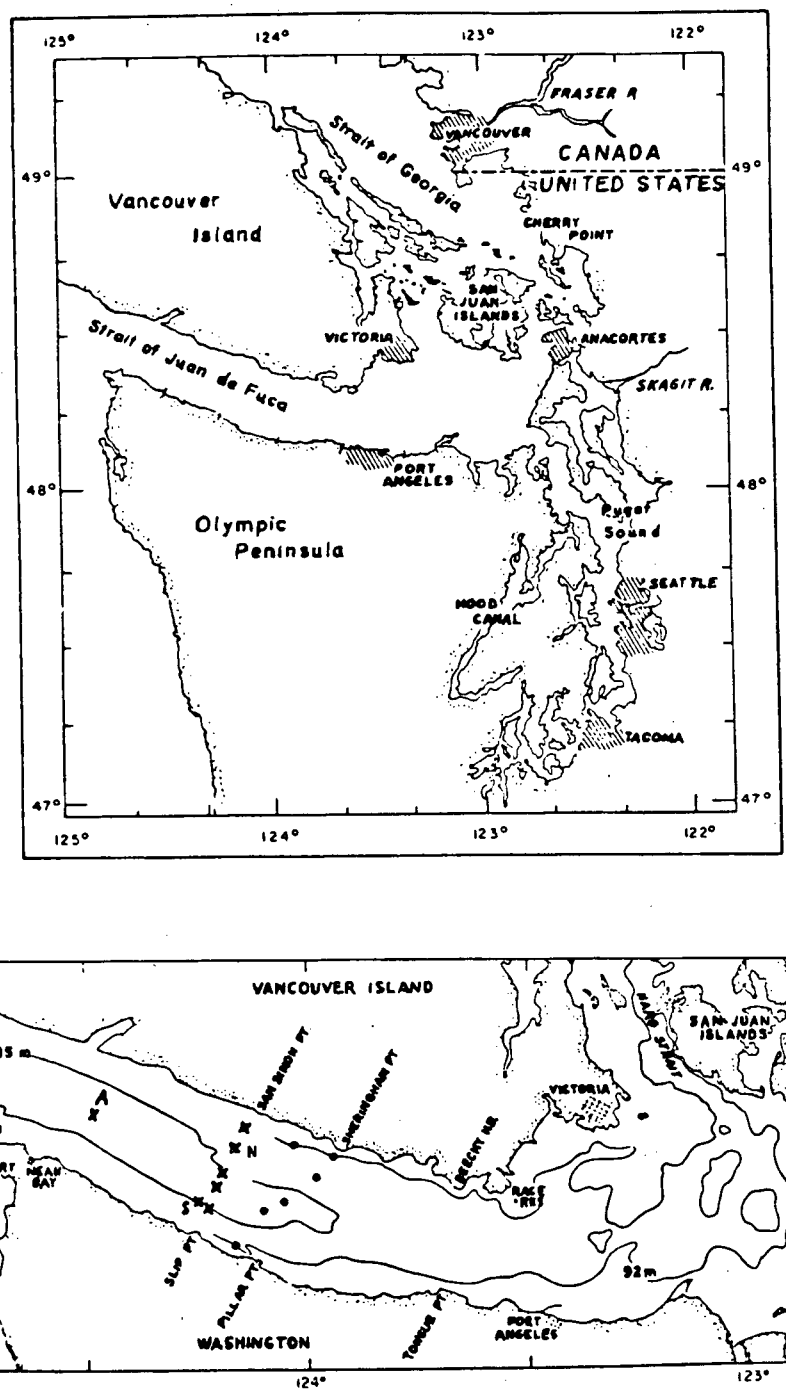

Figure 2.1: (top) Juan de Fuca Strait and nearby geographical features. (bottom) Juan de Fuca Strait with positions at which Fissel's data (•) and one section of Cannon and Laird's data (x) were collected. (from Cannon and Laird, 1978)

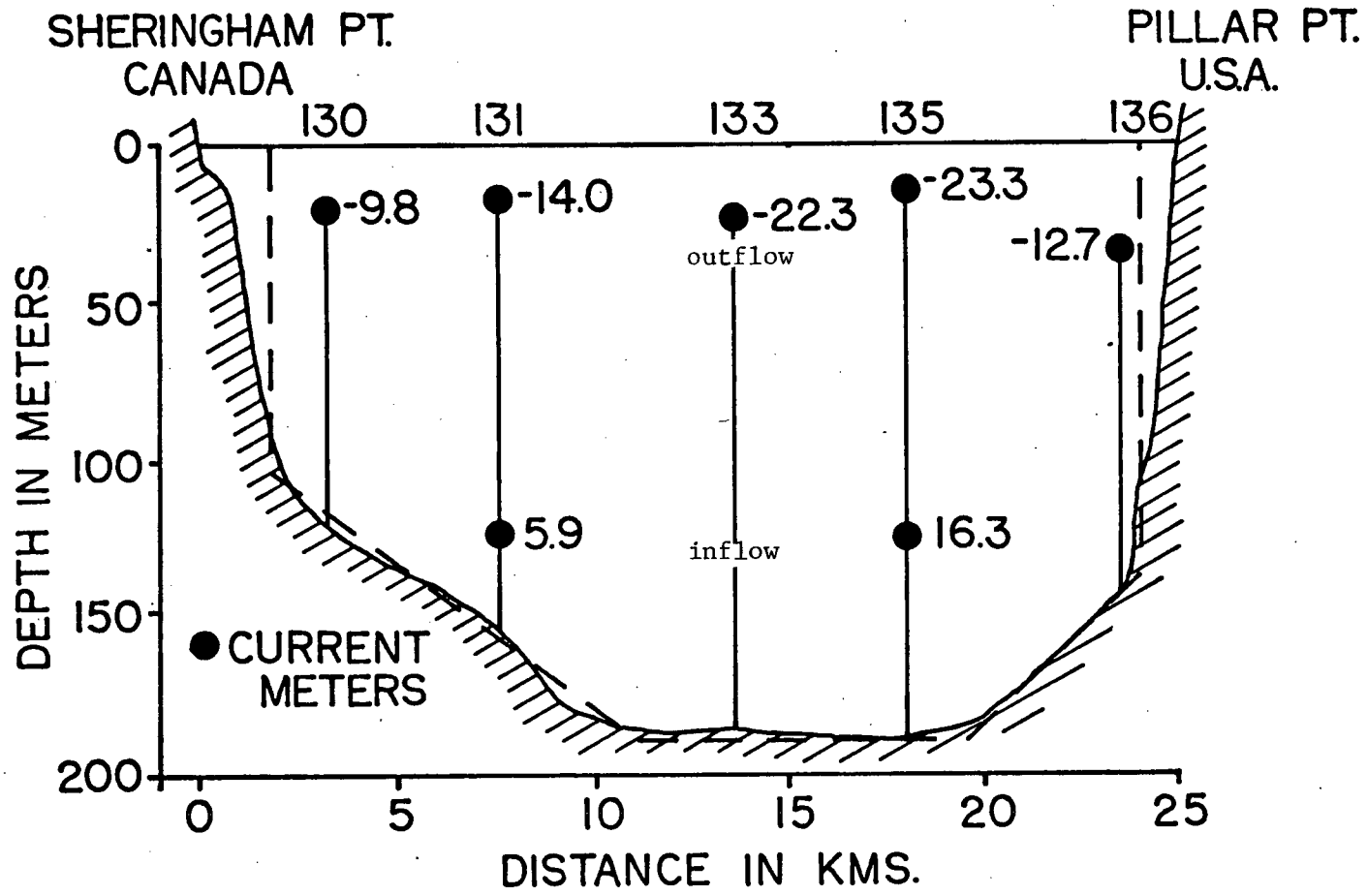

Figure 2.2: The cross-section of Juan de Fuca Strait at which Fissel's data were collected. Numbers above each station are used to indicate the station considered in figure 2.5. Along-channel velocities are given in cm s^{-1}. The dashed line indicates the topography used in the model of the strait. (from Fissel, 1976)

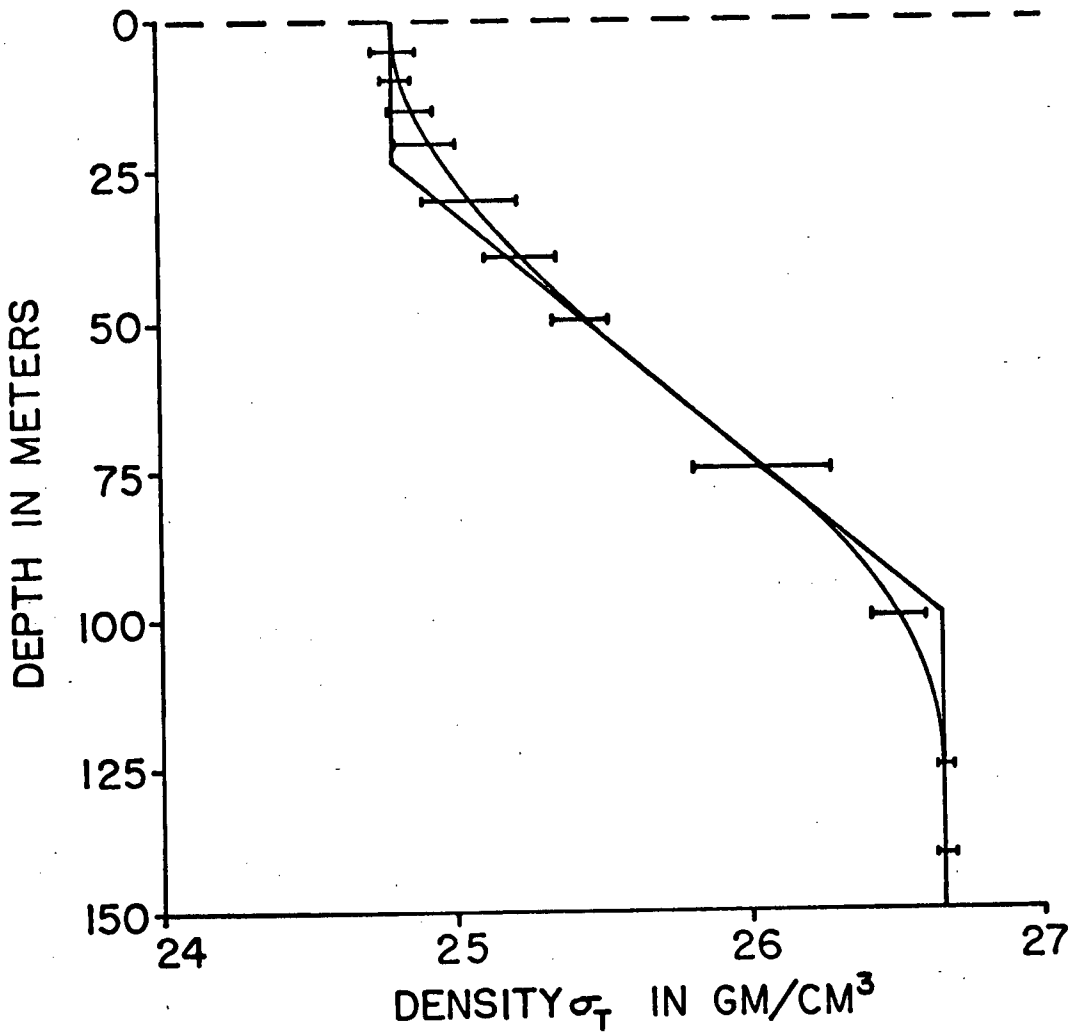

Figure 2.3: The mean density profile on June 14-15, 1975 across the section at which Fissel's data was collected (from Fissel and Huggett, 1976)

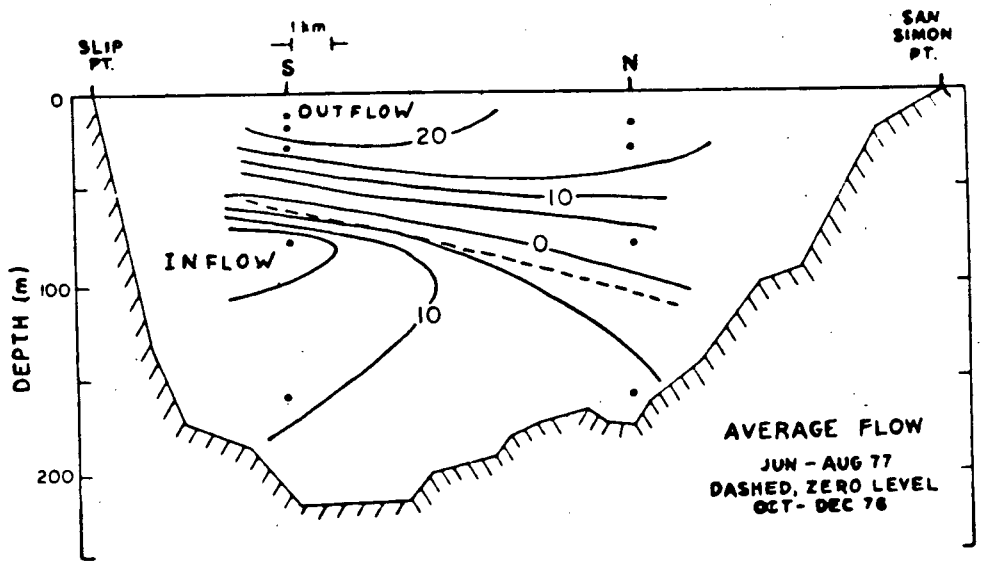

Figure 2.4: Along-channel total-record average currents (cm/sec.) through the cross-section marked by x's in figure 2.1 (from Cannon and Laird, 1978)

reasonably consistent and hence in our studies we shall use the more complete set of values presented in figure 2.4.

Fissel (1977) defines the residual currents as the flow remaining after currents with frequencies greater than 0.8 cycles per day have been removed. His analysis shows that the residual currents in Juan de Fuca Strait between Sheringham Point and Pillar Point have the following properties:

(1) 80% of the total variance of the residual currents is concentrated at frequencies less than 0.25 cycles per day,

(2) the amplitude fluctuations in the up-strait component of the residual currents are larger by a factor of two than those of the cross-strait currents,

(3) the amplitude fluctuations of the residual currents at 20m depth are considerably larger (by a factor of two or three) than the fluctuations at 120 m depth,

(4) the residual up-strait currents are poorly correlated at the lowest frequencies where most of their activity occurs. Even fluctuations of the current at pairs of stations that are adjacent to one another (with a typical separation of 4km) are not consistently correlated at the 90% significance level. Verification of the first three statements above can be found in figure 2.5 which gives the spectral densities of the residual currents measured at the various stations shown in figure 2.2. The fourth statement is discussed further at the end of this section. The principal subject of this section is the study of the stability of the mean currents to low-frequency quasi-geostrophic wave perturbations.

The model used to study the stability of the mean currents

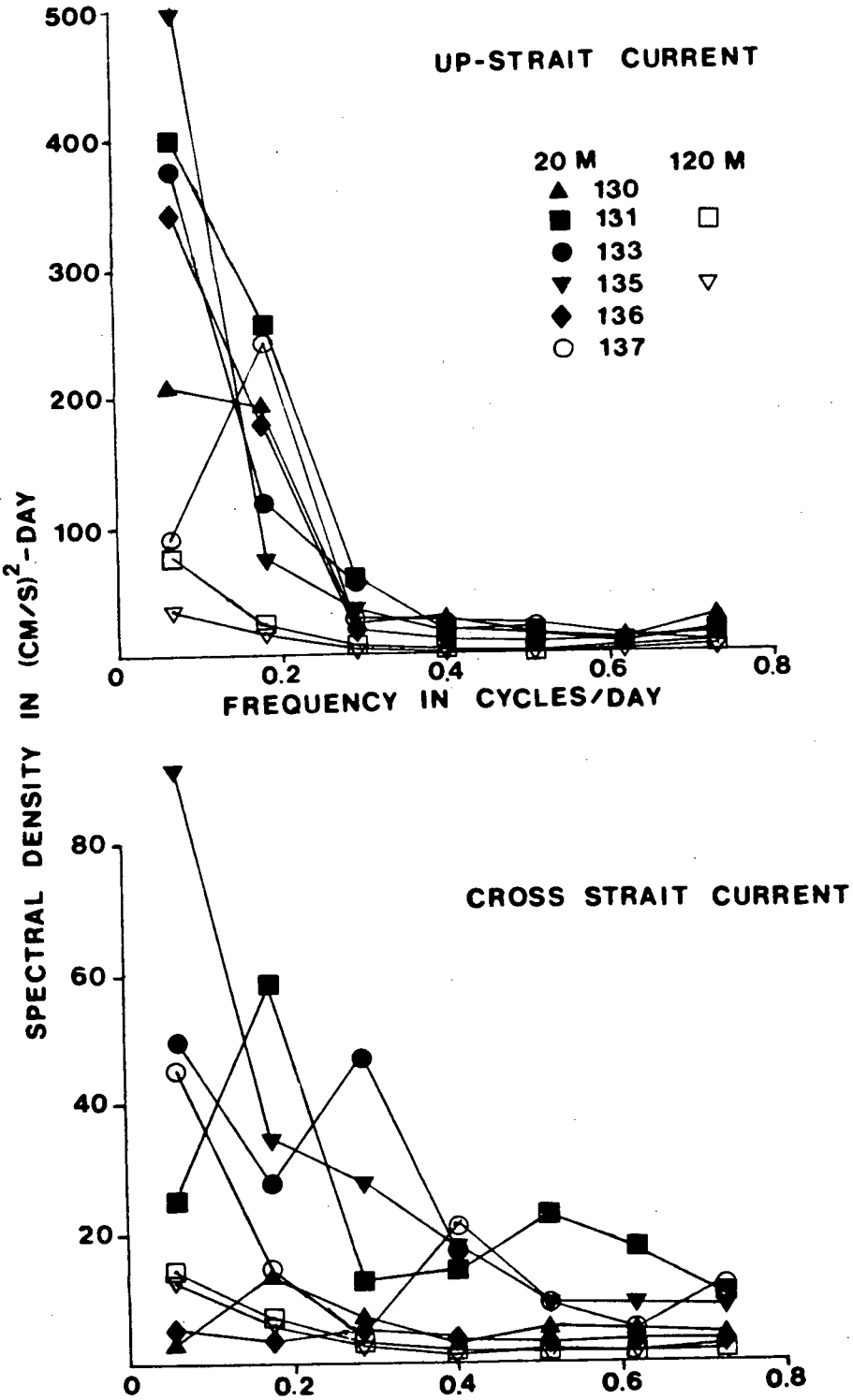

Figure 2.5: The power spectral density of the residual currents for the current meter stations of Fissel (1976). Stations 130-136 are shown in figure 2.2 and station 137 is the additional station a few kilometers to the west of Sheringham Point seen in figure 2.1 (bottom). (from Fissel, 1976).

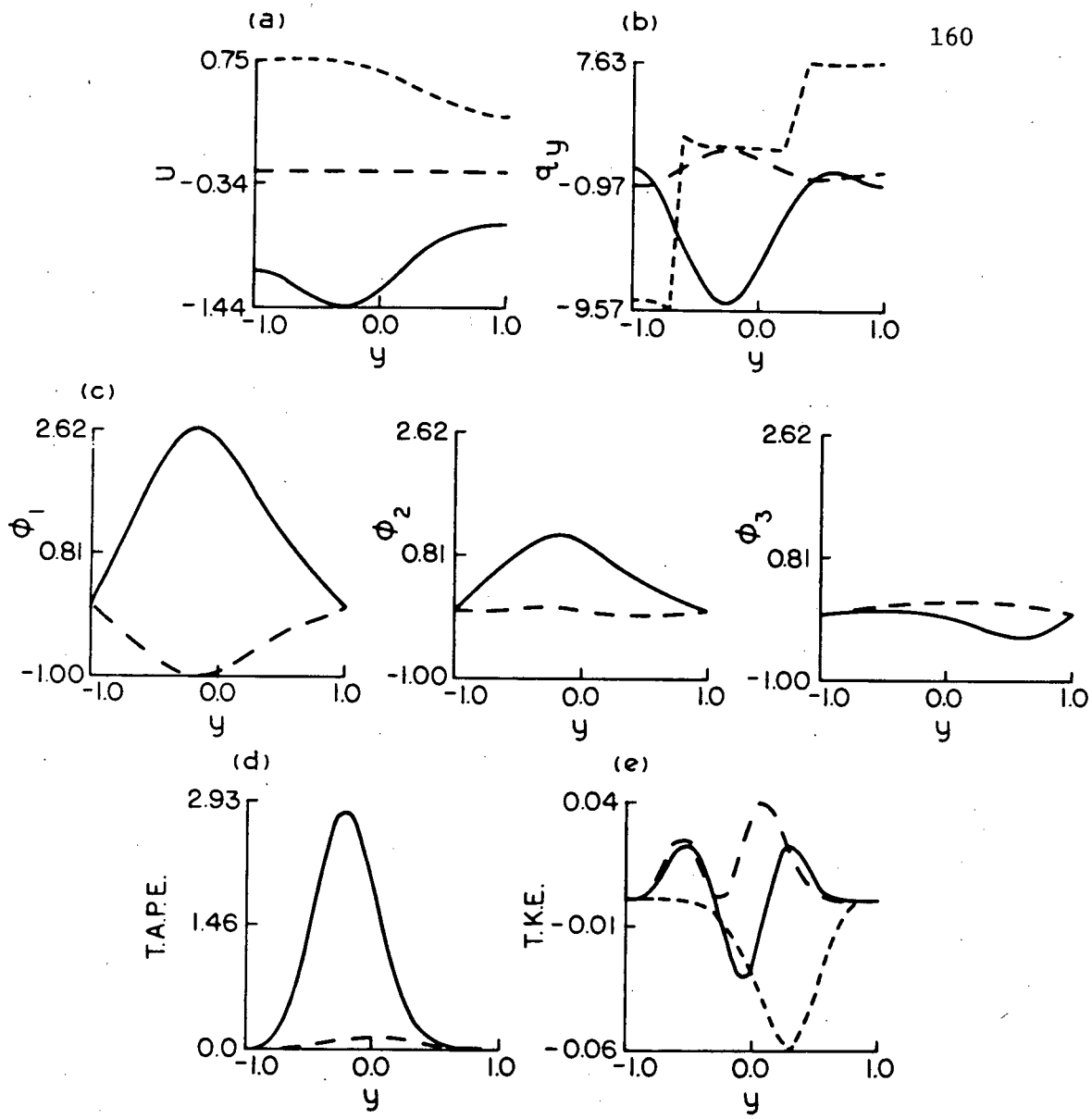

Figure 2.6: (a) Approximation to the mean currents used to model Juan de Fuca Strait; (b) the mean potential vorticity gradients corresponding to the three layers of our model: upper layer-solid line, middle layer-long dashes, lower layer-short dashes; (c) the eigenfunction corresponding to the most unstable wave in the model; (d) the transfer of available potential energy corresponding to this wave: the solid line corresponds to the transfer of energy due to the shear between the upper layers and the dashed line to that due to the shear between the lower layers; (e) the transfer of kinetic energy for this wave: solid line corresponds to the upper layer, long dashed line to the middle layer and the short dashed line to the bottom layer.

Table 2.1: Properties of the most unstable wave found in the three-layer model of Juan de Fuca Strait. This wave is illustrated in figure 2.6. (A positive value of c or c_g corresponds to an eastward velocity.)

Model	U_1, U_2, U_3 (x 16 cm sec^{-1})	Period (days)	Wavelength (km)	e-folding time (days)	Phase velocity (km day^{-1})	Group velocity (km day^{-1})
Figure 2.6	figure 2.7a	13.7	76	6.6	-5.5	-6.8

in Juan de Fuca Strait to propagating quasi-geostrophic perturbations has been derived in Chapter II, section 2. A three-layer model was derived from the equations of motion for a continuously stratified fluid with densities of the upper and lower layers given by ρ_1^* and ρ_3^* respectively and ρ_2^* varies linearly from ρ_1^* to ρ_3^* over the middle layer in the absence of motion (the basic state density approximation is shown in figure 2.1 chapter II). There it was found that the linearized equations expressing the conservation of potential vorticity for the model described above are:

$$(U_{1o}-c)[\phi_{1yy} - k^2\phi_1 - F_1(3\phi_1-4\phi_2+\phi_3)] + \phi_1 q_{1y} = 0$$

$$(U_{2o}-c)[\phi_{2yy} - k^2\phi_2 + 4F_2(\phi_1-2\phi_2+\phi_3)] + \phi_2 q_{2y} = 0 \qquad (2.1)$$

$$(U_{3o}-3)[(\frac{H_3-bh}{H_3})(\phi_{3yy}-k^2\phi_3) - F_3(\phi_1-4\phi_2+3\phi_3)] + \phi_3 q_{3y} = 0$$

where $q_{1y} = \beta - U_{1yy} + 2F_1(2U_1 - 3U_2 + U_3)$

$$q_{2y} = \beta - U_{2yy} - 6F_2(U_1-2U_2+U_3)$$

$$q_{3y} = (\frac{H_3-bh}{H_3})(\beta-U_{3yy}) + 2F_3(U_1-3U_2+2U_3) + (b/R_0H_3)hy$$

In the study made here and in that made in the next section the effect of β is very small and hence it is neglected. In fact, as pointed out by Dr. Roland de Szoeke (private communication), this is probably generally true for the study of baroclinic instability in the oceans since the effect of β is not likely to be strongly felt on the scale of the internal deformation radius of the oceans. This is, of course, not true for atmospheric flows where the internal deformation radius is much larger.

The bottom topography and density stratification used in our model are shown in figures (2.2) and (2.3). The structure of the mean currents (averaged over each layer) are modelled by the approximation shown in figure (2.6a) . Also shown in this figure (part (b)) are the mean potential vorticity gradients. The form of the potential vorticity gradients is of great interest in the study of either barotropic or baroclinic instability. If the potential vorticity gradient changes sign within a given layer then the possibility of barotropic instability extracting its energy from the kinetic energy of the mean currents is introduced. A change of sign in going from one layer to another introduces the possibility of baroclinic instability in which energy is extracted from the available potential energy due to the tilt of an interface. As can be seen from the figures showing the transfer of available potential energy (T.A.P.E.) and the transfer of kinetic energy (T.K.E.) for the most unstable waves found (figure 2.6) the major source of energy is potential energy and its release is centred on the region in which $q_{1y} \times q_{2y}$ is large and negative $(-.7 \leq y \leq .3)$.

The T.K.E. is very small but it is interesting that its largest effect is a loss of energy in the lower layer due to the stabilizing effect of topography. The eigenfunctions corresponding to the most unstable wave in this system are shown in figure 2.6(c). It is interesting to note that the transfer of potential energy is strongly intensified in the region of maximum vertical shear (see Fig. 2.6(a) and (d)) in spite of the fact that the channel is only about two internal deformation radii in width. Hence averaging the mean currents over a couple of internal (Rossby) radii of deformation is not justified if large horizontal shears are present. Further, it is interesting that with horizontal shear included, the stability of the system was found to be relatively insensitive to small changes in the mean currents. A case in which the stratification and mean currents of the flow are retained as in figures 2.3 and 2.6 but topography is totally neglected (i.e. the bottom is assumed flat) was also studied. The results for the most unstable wave were not significantly different from those given in figure 2.6 and table 2.1, which gives the properties of the most unstable wave illustrated in figure 2.6. These results are encouraging as they indicate that the changes in mean currents and bottom topography which occur over the length of the channel may be reasonably neglected. Note, however, that although this is the case for the study made here, in the general situation these results will not always be true. (eg. if the main source of energy was the tilt of the lower interface, effects of bottom topography would be significant).

Table 2.1 gives the properties of the most unstable wave found in Juan de Fuca Strait. Though the observations are seriously limited, we see

that the predictions of our model are at least consistent with what is known. The period is in the right general range, and the wavelength is such that the ratio of long-strait to cross-strait energy is of order four, as observed. The e-folding time and group velocity are such that the perturbation velocities e-fold in the time that the group travels about 45 km (i.e. about two channel widths). Hence the growth rate is certainly sufficiently large to have significant influence on the low-frequency motions in the strait. Finally, from figure 2.6(c), we see that the perturbation is predicted to be surface intensified as observed. We thus conclude that the low-frequency motions observed in the strait may be at least partially due to baroclinic instability of the mean currents, however, we have not yet explained the observed lack of coherence between the stations. It seems likely that it is due to several processes occurring simultaneously. Some possibilities are:

(1) influence from low-frequency motions in the Strait of Georgia,

(2) influence of varying outflow from Puget Sound and Frazer River,

(3) effects due to the proximity of boundaries for the near-shore stations,

(4) wind forcing over the ocean causing a "piling up" of water along the coast creating an adverse pressure gradient in the upper layer,

(5) the diffraction of shelf waves or other waves propagating up the coast (which may be generated many kilometers to the south) into Juan de Fuca Strait,

(6) the effects of non-linearity and geostrophic turbulence,

(7) the effects of strong "high-frequency" ($\omega \sim f$) tides.

The most significant of these are probably the last four. Cannon et al (1978) have found that, during the winter, deceleration of the along-channel

currents generally occurred during strong southerly winds off the coast and during increasing sea surface height at Neah Bay. They found that significant correlations existed between:

(1) the along-channel 4-m currents at Site A (Fig. 2.1) and the north-south Pacific winds with currents lagging winds by 42 hours (process (8));

(2) the along channel 4-m currents at Site A and the sea surface height at Neah Bay with currents lagging sea-surface height by 6 hours (process (9)); and

(3) the north-south Pacific winds and sea surface height at Neah Bay with sea-surface height lagging winds by 24 hours (the winds are apparently either generating or reinforcing wave motions on the shelf). These observations certainly support the assumption that motions on the shelf and winds over the open ocean have significant influence on the currents in the Strait.

Without doubt the effects of non-linearity are also strong. The study made here assumes that the perturbations are much smaller than the mean currents and predicts that these small perturbations will grow at the expense of the potential energy of the tilting isopycnals. However, when the perturbation velocities become comparable with the mean velocities (observations in Juan de Fuca Strait show that perturbation velocities $\sim$ mean velocities $\sim$ 20 cm s^{-1}) the governing equations for the "perturbations" become highly non-linear and the effects of geostrophic turbulence probably dominate the flow. Though the effect of strong non-linearity on a realistic channel flow is not well understood it is certain that some or all of the low- (and high-) frequency waves will interact and tend to initiate an energy cascade to-

ward larger scales (Charney, 1971). Due to the proximity of boundaries, the studies of geostrophic-turbulence in the open ocean are not directly applicable since they rely strongly on the assumption of isotropy. However, the basic dynamics are probably similar and interactions are undoubtedly strong. Such strong non-linear interactions almost certainly act to decrease the coherence between stations.

Finally we must consider the possible effects of strong, "high-frequency" (diurnal and semi-diurnal) tidal currents. The inclusion of tidal currents in our model introduces some interesting effects. The Rossby number corresponding to the tides in the channel is not small and the scaling used in our model must be revised. The result is that we must consider the effect of an imposed high-frequency ageostrophic wave on the low-frequency geostrophic waves studied in this thesis. To study this problem, the full ageostrophic equations must be considered and no simple solutions appear possible. Rao and Simmons (1970) have shown that instability can occur as a result of a coupling between an internal gravitational mode (an ageostrophic wave) and a rotational wave (the high-frequency analogue of the geostrophic waves studied here). However, this instability occurs at much higher frequencies than those considered in this thesis and gives little insight into the above mentioned problem other than to demonstrate that interaction is possible. Since the tidal frequencies are much greater than those of the low-frequency quasi-geostrophic instabilities studied here, it has been assumed that their effect on these instabilities is negligible. However, this is by no means obvious and a more complete study including ageostrophic effects would certainly be enlightening.

We thus conclude that although baroclinic instability is probably significant in Juan de Fuca Strait, it is not likely the dominant energy source for the observed low-frequency motions. It seems quite likely that the effects of motions on the continental shelf are of at least equal importance and that the effects of tides are also strong. Finally, due to the large "perturbation" velocities in the strait, the effects of non-linearity are certainly important and must be included before any firm conclusions can be made.

3. The California Undercurrent off Vancouver Island

The California current is a broad eastern boundary current off the west coast of Canada and the United States formed at mid-latitudes where the eastward flowing Subarctic Current (west wind drift) separates into northern and southern components. The northern component forms the Alaska Current while the southern component forms the California current. At intermediate depths beneath this weak (~ 5-10 cm s^{-1}, Tabata (1975), Reed and Halpern (1976), Bernstein, Breaker and Whritner, (1976), Halpern, Smith and Reed (1978)) current, a strong (mean speed of order 10 cm s^{-1} with maximum speeds as high as 100cm s^{-1} ; Tabata, 1975), narrow (~ 50 km) poleward flowing jet known as the California Undercurrent occurs. The major features of this current system have been discussed by Mysak (1977) and will be summarized here. The undercurrent extends all the way from California up to Vancouver Island and its water properties suggest that it has its origin in the North Equatorial Counter Current (Tabata, 1975). Off California it consists of approximately an equal mixture of Pacific Equatorial water and subartic water, but further north the percentage of equatorial water is significantly reduced.

Off California where extensive measurements have been made, meso-scale eddy-like formations have frequently been observed through the analysis of hydrographic data (eg. Wooster and Jones, 1970; Wickham, 1975). Further, the formation of these eddies has been observed through the use of satellite-borne infrared scanners (Bernstein, Breaker and Whritner, 1977). Though our primary interest is with the flow off Vancouver Island, the analysis produced below may also be used to explain the presence of these eddies.

Off Vancouver Island, the data base is far more limited than off California; however, as seen in figure 3.1 such mesoscale eddies as those observed further south are again observed here. We shall show that, as first suggested by Mysak (1977), the presence of these eddies may be explained in terms of baroclinic instability of the undercurrent.

The presence of the undercurrent in these northern regions is now fairly well established. It has been observed over the slope and shelf off Oregon by Huyer (1976), who suggests it may be a part of the wind-induced coastal upwelling regime. (It had earlier been shown (Pedlosky, 1974) that a deep topographically controlled poleward undercurrent is part of the steady-state response of a wind-driven flow in a rotating stratified fluid in a channel with a sloping bottom.) Halpern et al (1978) have also noted the existence of a northward flow over the depth range of 200-500m over the slope off Oregon in the first half of July. Dodimead et al (1963) found a northward flow during winter in the same depth range, and Ingraham (1967) observed that within about 200 km of the shore there was a net northward volume transport relative to 1500 m. Over the depth range of 200-500m the maximum current speeds were estimated to be 10-20 cm s^{-1}. Finally, Reed and Halpern (1976) and S. Tabata (see Mysak 1977) have found a northward flow during early fall at intermediate depths in the latitude range 46-50°N.

Maps of geopotential topography at four levels off Washington and the southern part of Vancouver Island as computed by Reed and Halpern (1976) are shown in figure 3.2. The 10/1000 db map shows a weak ($\sim$ 5cm s^{-1}) southward flow over the continental slope which is apparently considerably reduced as one moves further from the coast. The remaining maps all show

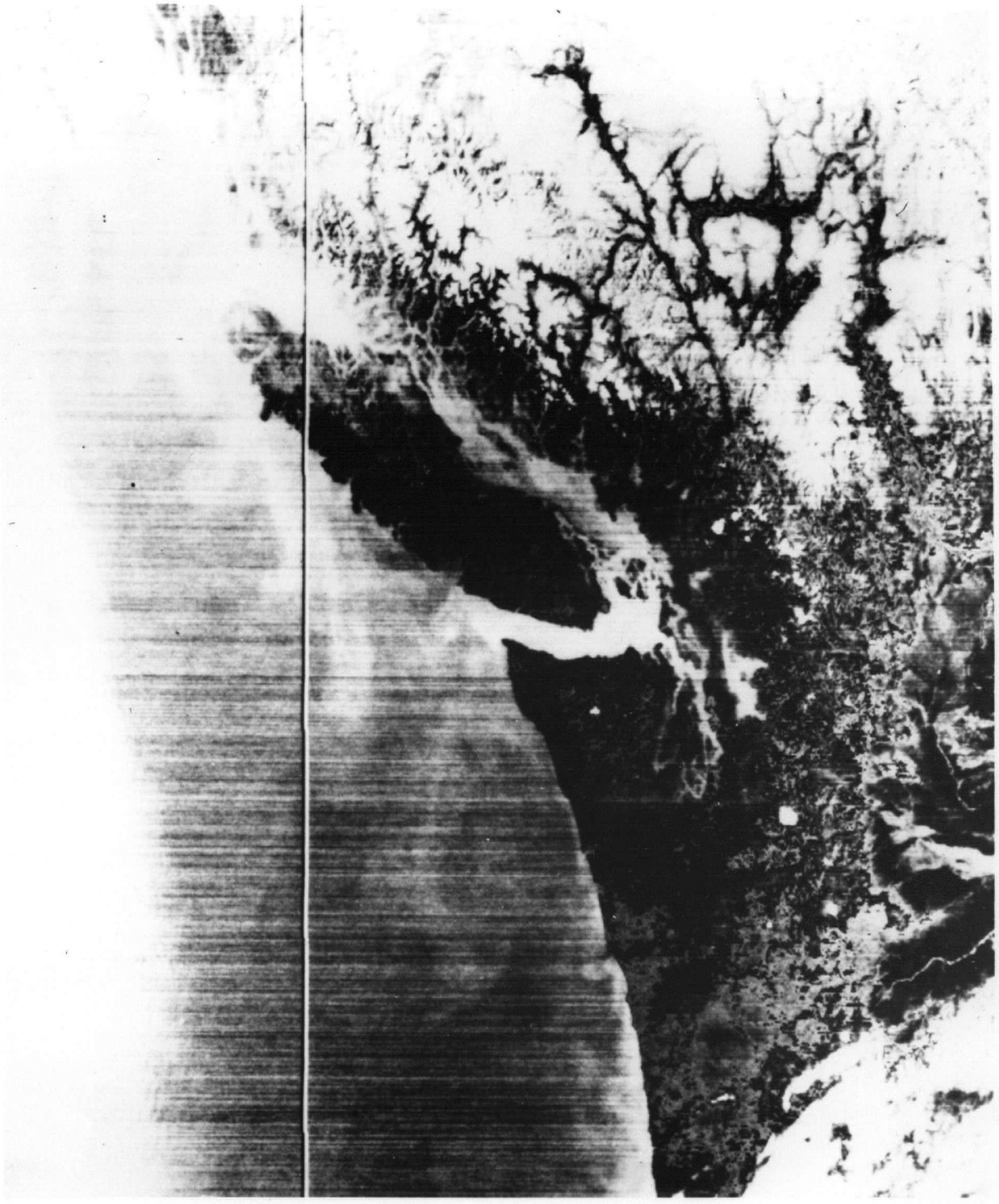

Figure 3.1: Enhanced infrared image of sea surface showing spatial structure of surface temperature on 10 September, 1975 off the west coast of British Columbia and Washington. The dark areas are warm water and the grey-white, cold water (after Gower and Tabata, 1976.)

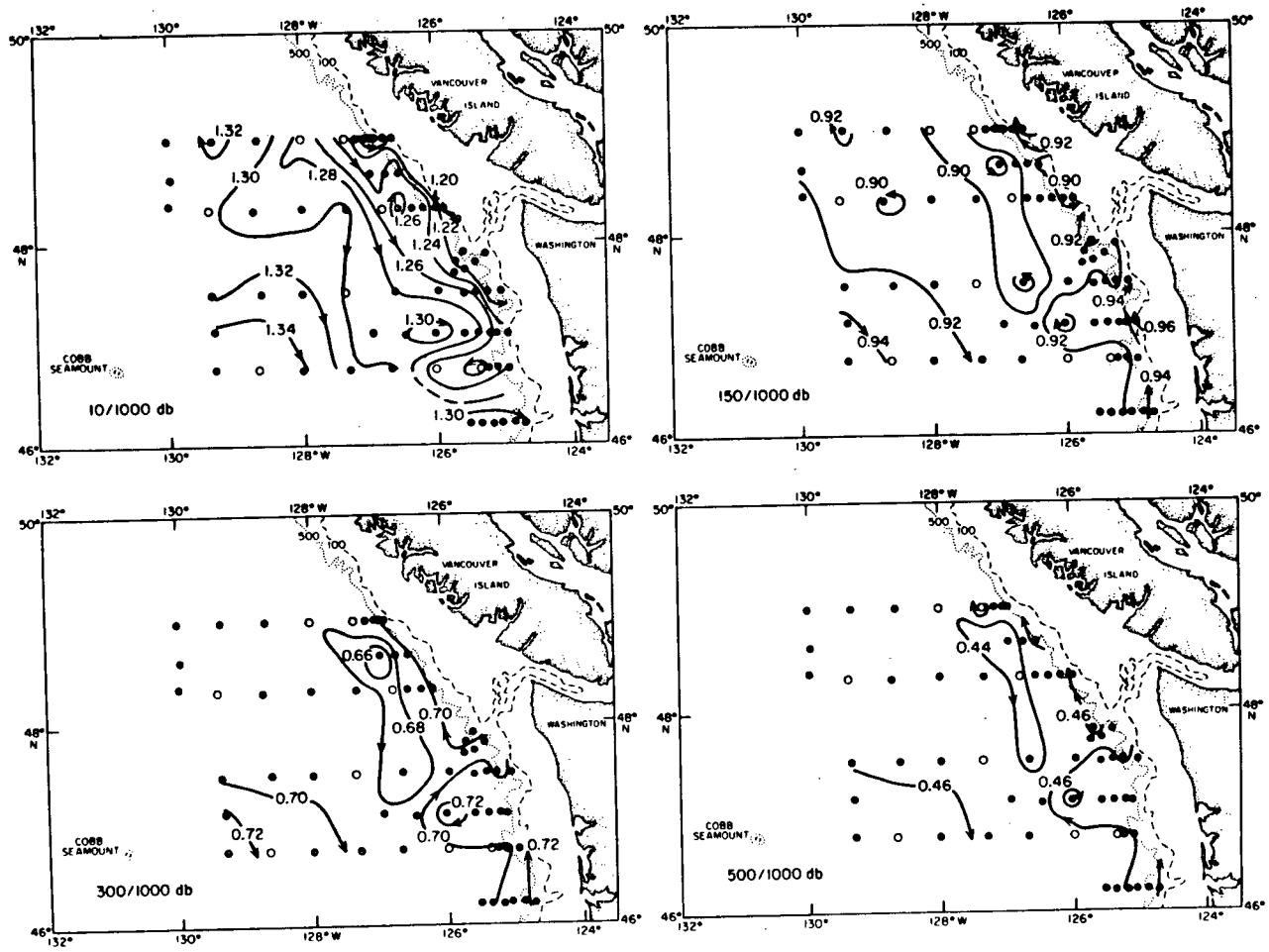

Figure 3.2: Geopotential topography (dyn m) of the 10, 150, 300 and 500 db surfaces (referred to 1000 db), 7-20 Septebmer, 1973. Open circles refer to time-series stations. The 100 and 500 fathom (1 fathom = 1.829m.) isobaths are also shown (from Reed and Halpern, 1976).

a northward flow over the slope region with a southward flow further west. The 150/1000 and 300/1000 db maps are nearly identical while the 500/1000 db map shows a considerably reduced flow. From Reed and Halpern's estimates of the volume transports of the 150/1000 db layer off Vancouver Island, Mysak (1977) has estimated the maximum speed of the undercurrent in this region to be of the order of 15-20 cm s^{-1}.

The mean flow over the slope region off Washington and Vancouver Island can thus be described (at least to a first approximation) as a weak southward flow of order 5 cm s^{-1} in the upper 200m (decreasing slowly to the west) with a stronger narrow poleward jet with speed of order 10 cm s^{-1} in the approximate depth range of 200-600m. Beneath this depth, the flow is assumed to be relatively quiescent and in our model we shall take the mean flow to be identically zero at such depths.

Mysak (1977) has noted that the low frequency eddy-like motions discussed above are likely due to an instability of the mean flow itself to quasi-geostrophic perturbations at the observed length and time scales. Since, in the upper layer, the mean currents are small and the density stratification strong (see figure 3.4), Mysak assumed that this layer acts effectively as a rigid lid on the flow below and modelled the undercurrent by the two layer system shown in figure 3.3. The results of his analysis do indeed indicate the possibility that the undercurrent is baroclinically unstable. However, as Mysak noted, the vertical shear in this upper layer could be significant and thus the neglect of this surface current could be a serious omission. We are thus led to consider a three-layer model. Mysak has also noted the possible errors in introducing an artificial outer vertical wall and neglecting lateral shear in the mean currents. I shall show that both of these approximations are justified if the

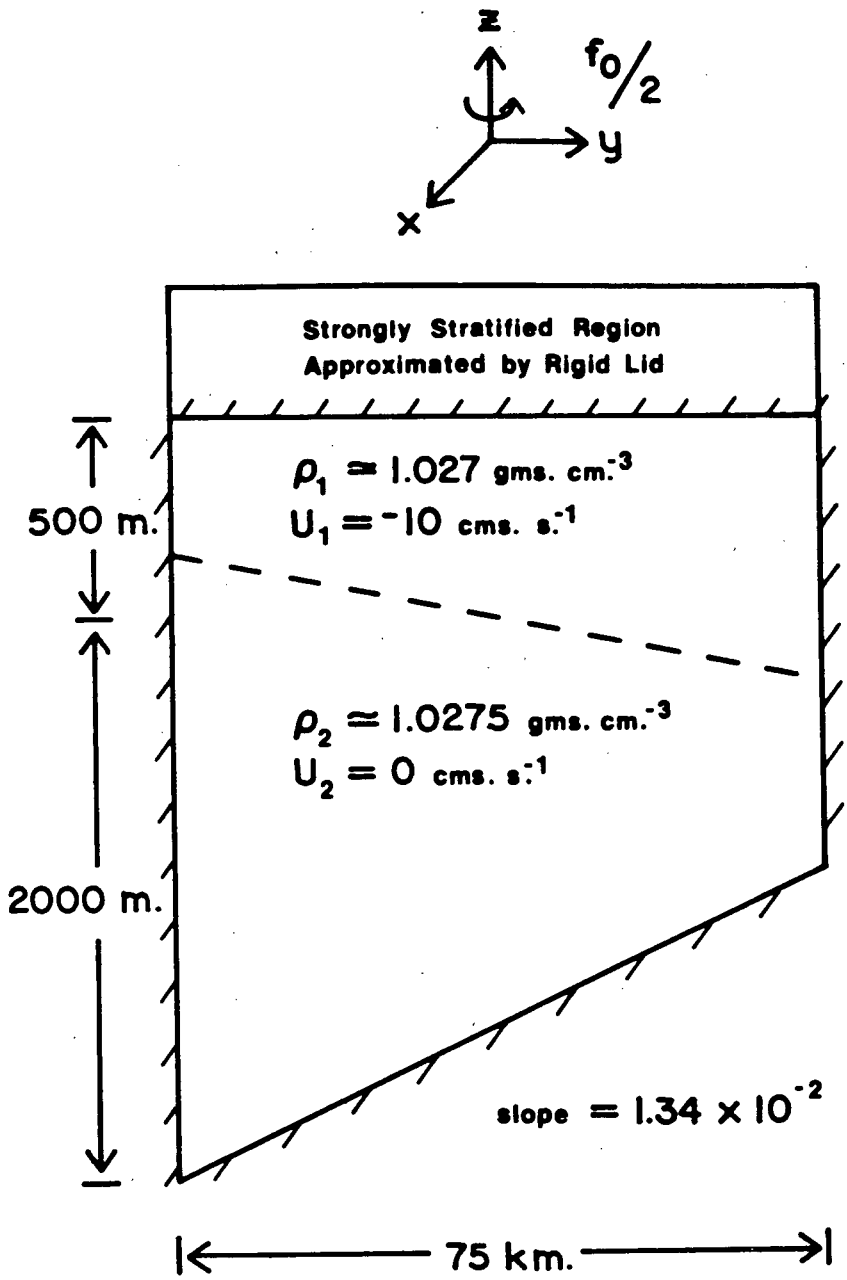

Figure 3.3: The two-layer model studied by Mysak (1977).

position of the outer wall is chosen correctly.

In figure 3.4 a typical set of temperature, salinity and σ_t profile in the slope region off Vancouver Island is shown. Clearly the three-layer model of the density stratification considered in chapters II and III of this thesis is not appropriate and we are led to consider the approximation indicated by the dashed line in figure 3.4. Following the method described in chapter II we find that the linearized equations expressing the conservation of potential vorticity in the three-layer model corresponding to this system are:

$$(U_{1o}-c)[\xi_{1oyy}-k^2\xi_{1o}+8F_1(\xi_2-\xi_{1o})/3] + \xi_{1ox}[\beta-U_{1oyy}-8F_1(U_2-U_{1o})/3] = 0$$

$$(U_2-c)[\xi_{2yy} - k^2\xi_2+8F_2(\xi_{1o}-\xi_2)/3 + F_2R(\xi_3-\xi_2)] + \xi_{2x}[\beta-U_{2yy}-8F_2(U_{1o}-U_2)/3 + F_2R(U_2-U_3)] = 0$$

$$(U_3-c)[(\frac{H_3-bh}{H_3})(\xi_{3yy}-k^2\xi_3)-RF_3(\xi_3-\xi_2)] + \xi_{3x}[(\frac{H_3-bh}{H_3})(\beta-U_{3yy})+F_3R(U_3-U_2) + \frac{b}{R_oH_3}hy] = 0 \qquad (3.1)$$

with all definitions and non-dimensionalizations exactly as in Chapter II, section 2. R is defined by:

$$R = (\rho_2-\rho_1)/(\rho_3-\rho_2) \qquad (3.2)$$

and $U_{1o} = (9U_1-U_2)/8$. ξ_1 is the (non-dimensional) perturbation stream function in the i^{th} layer and the subscript o indicates that the quantity is evaluated at the middle of

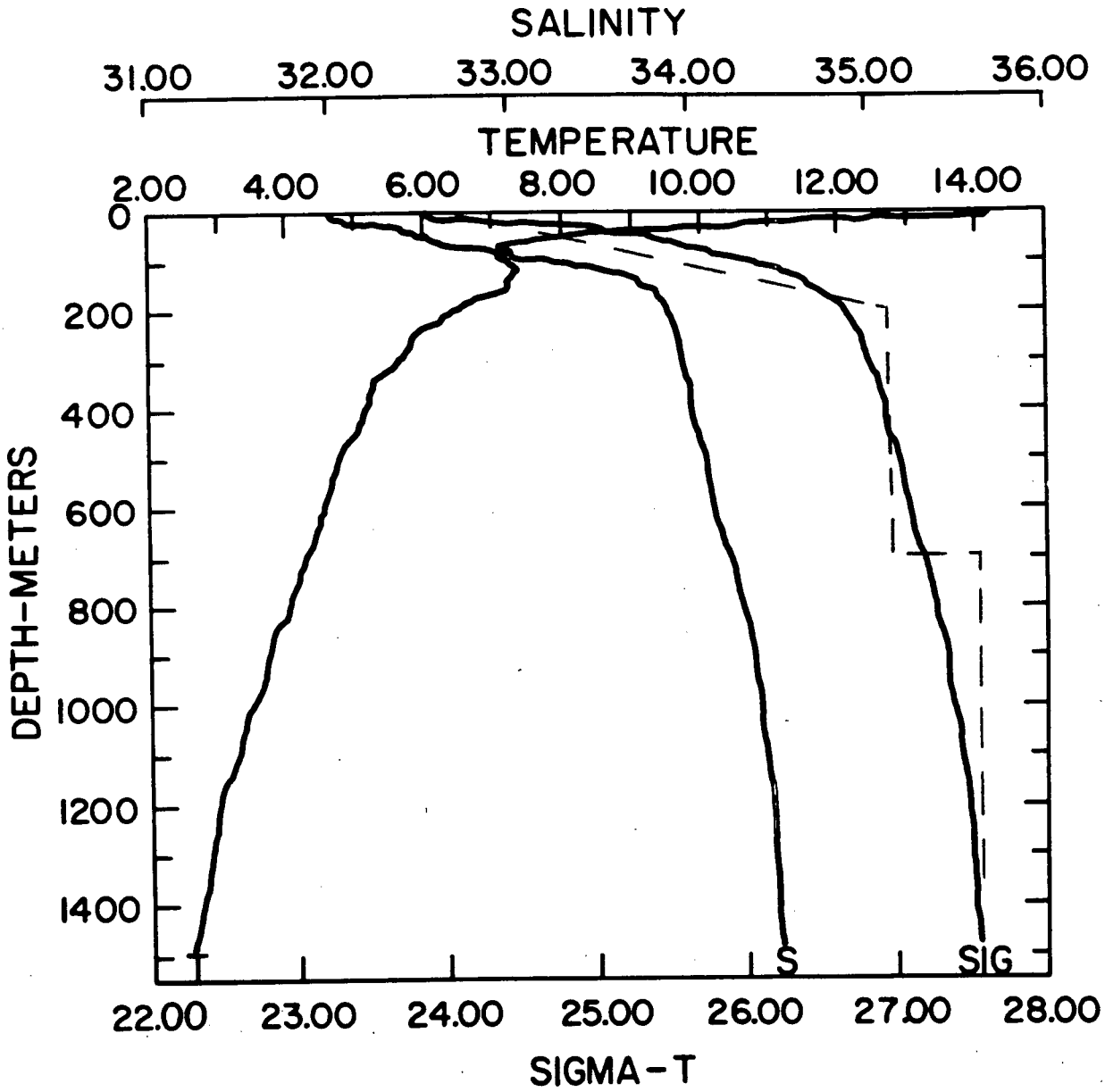

Figure 3.4: Temperature, salinity and σ_t profiles, 10 September, 1973, at 49°N, 127° 19'W (right-hand open circle in top line of time series stations shown in Fig. 3.2). (from Holbrook, 1975)

the layer.

Note that the three-layer model described by 3.1 is equivalent to the three-layer model of Davey (1977) with the density difference between the upper layers given by 3/8 of the density difference between the top and bottom of the upper layer in figure 3.7 and U_1 replaced by U_{1o}.

We must now make an appropriate choice for the bottom topography. Figure 3.5 shows isobaths off Vancouver Island and figure 3.6 shows topographic cross-sections corresponding to lines A - E in figure 3.5. Since the undercurrent lies below the shelf break, Mysak (1977) has assumed that the motion on the shelf has little influence on the stability of the undercurrent and hence models the steeply sloping region near the shelf-break by a vertical wall. Further, he has estimated that the more gently sloping region has a mean slope of approximately 0.0134. We shall follow Mysak in both these choices. Finally, Mysak considers uniform flow in each layer and considers a channel of width 75 km with constant sloping bottom. We shall consider this model (extended to include the effects of the upper layer) as well as the model including the effects of horizontal shear and a flat ocean floor of the same width as the sloping bottom. The three-layer models studied here are shown in figures 3.7 and 3.8. To compare our three-layer model with the two-layer model of Mysak (1977) we begin by considering the system depicted in figure 3.7, with bh (bottom topography) neglected with respect to H_3. For this system the cross-channel modes decouple and a simple analytic solution is possible (see chapter II). The dispersion curves corresponding to the first two cross-channel modes are shown in figure 3.9. The regions of instability corresponding to those studied by Mysak are marked as such. These waves are easily identified as they extract most of their

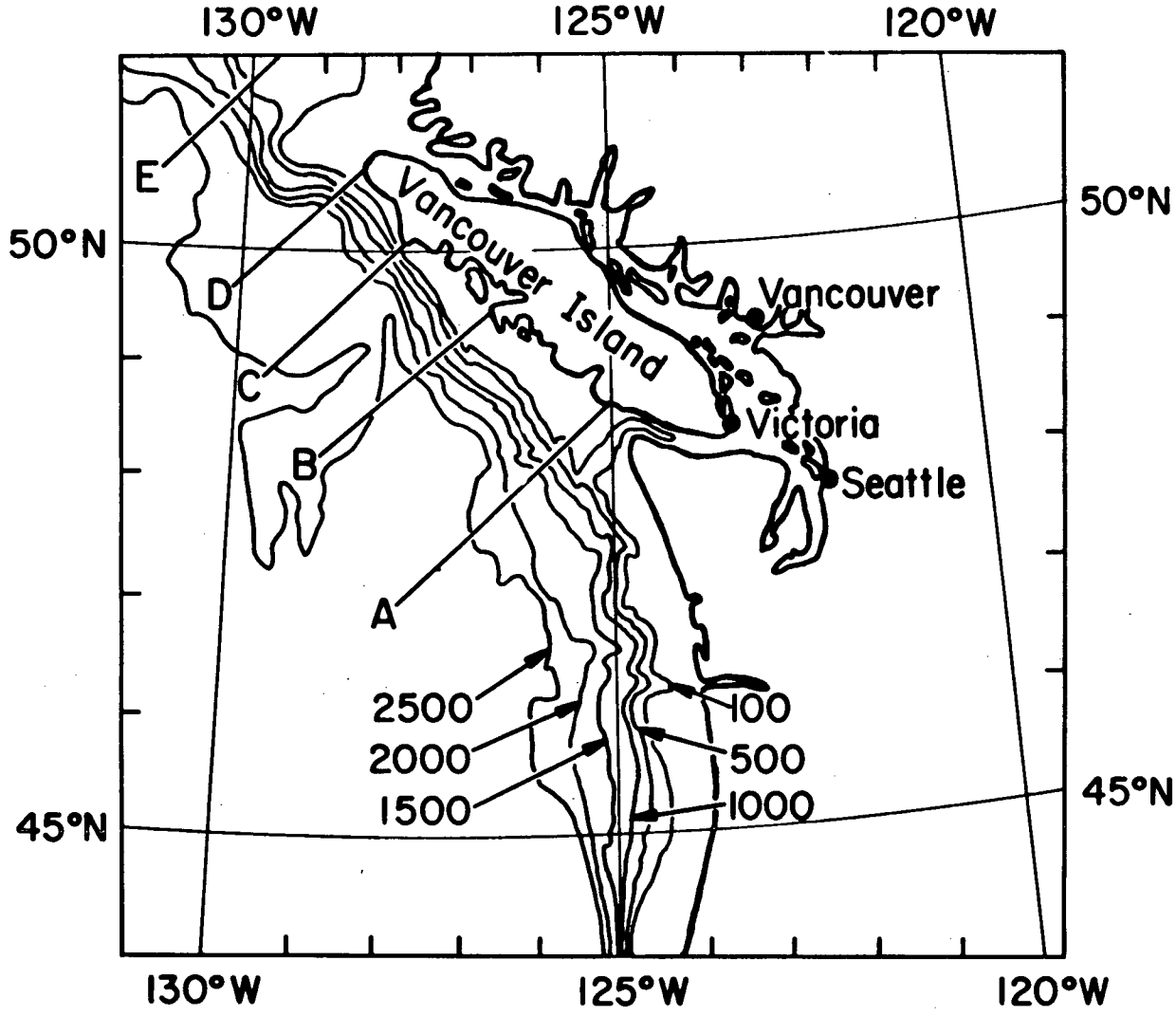

Figure 3.5: Isobaths (m) off Vancouver Island and Washington. Topographic cross-sections at lines A - E are plotted in figure 3.6. (from Mysak, 1977)

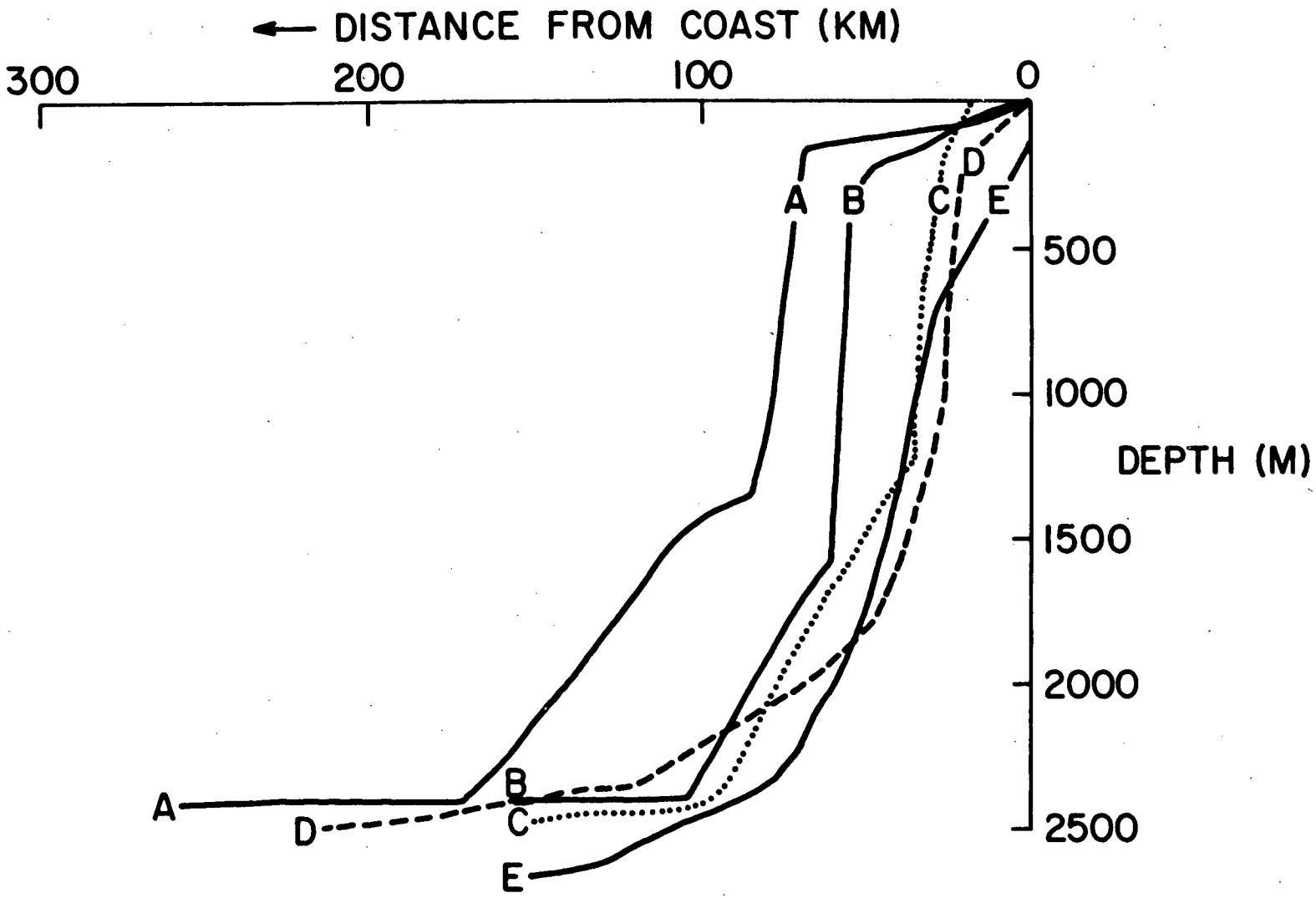

Figure 3.6: Topographic cross-sections at lines A- E shown in figure 3.5. (from Mysak, 1977).

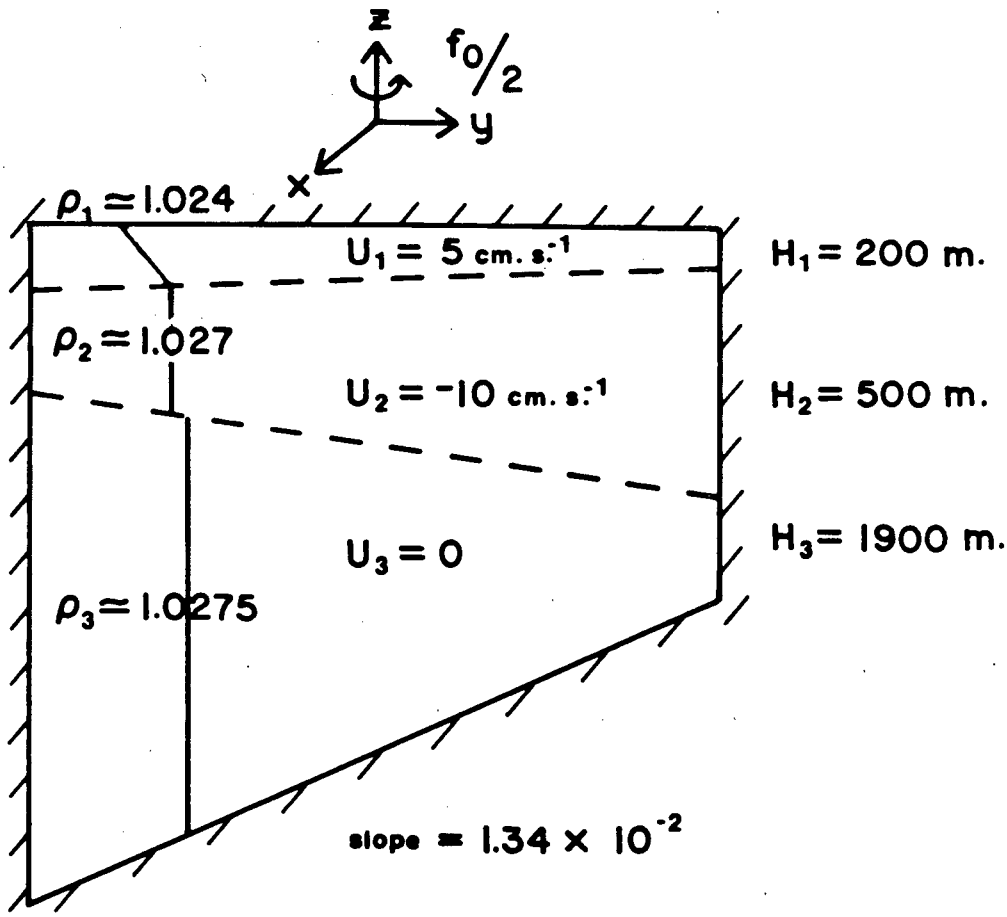

Figure 3.7: The three-layer, channel model analogous to the two-layer model of Mysak, 1977).

Table 3.1: Comparison of the instabilities found by Mysak (1977) and the corresponding instabilities found using the analogous 3-layer model. δ_1 and δ_3 are the phases of the wave in the upper and lower layers with respect to the middle layer. (A positive value of c or c_g corresponds to a southward velocity.)

Model	U_1, U_2, U_3 (x 10 cm sec^{-1})	Period (days)	Wavelength (km)	e-folding time (days)	Phase velocity (km day^{-1})	Group velocity (km day^{-1})	$\left\|\frac{\phi_1}{\phi_2}\right\|$, $\left\|\frac{\phi_2}{\phi_2}\right\|$	δ_1, δ_3 (degrees)
figure 3.3	-, -1.0, 0.0	9.2	65	13.1	-7.0	-3.3	-, 0.9	-, 78
figure 3.7	0.5, -1.0, 0.0	11.3	54	13.0	-4.7	-3.3	0.4, 0.6	0, 80

Table 3.2: Properties of the most unstable wave corresponding to the system shown in figure 3.7. δ_1 and δ_3 are the phases of the wave in the upper and lower layers relative to the middle layer. (A positive value of c or c_g corresponds to a southward velocity.)

Model	U_1, U_2, U_3 (x 10 cm sec^{-1})	Period (days)	Wavelength (km)	e-folding time (days)	Phase velocity (km day^{-1})	Group velocity (km day^{-1})	$\left\|\frac{\phi_1}{\phi_2}\right\|$, $\left\|\frac{\phi_3}{\phi_2}\right\|$	δ_1, δ_3 (degrees)
figure 3.7	0.5, -1.0, 0.0	55.7	107	6.9	-1.9	-1.0	1.7, 0.06	63, 114

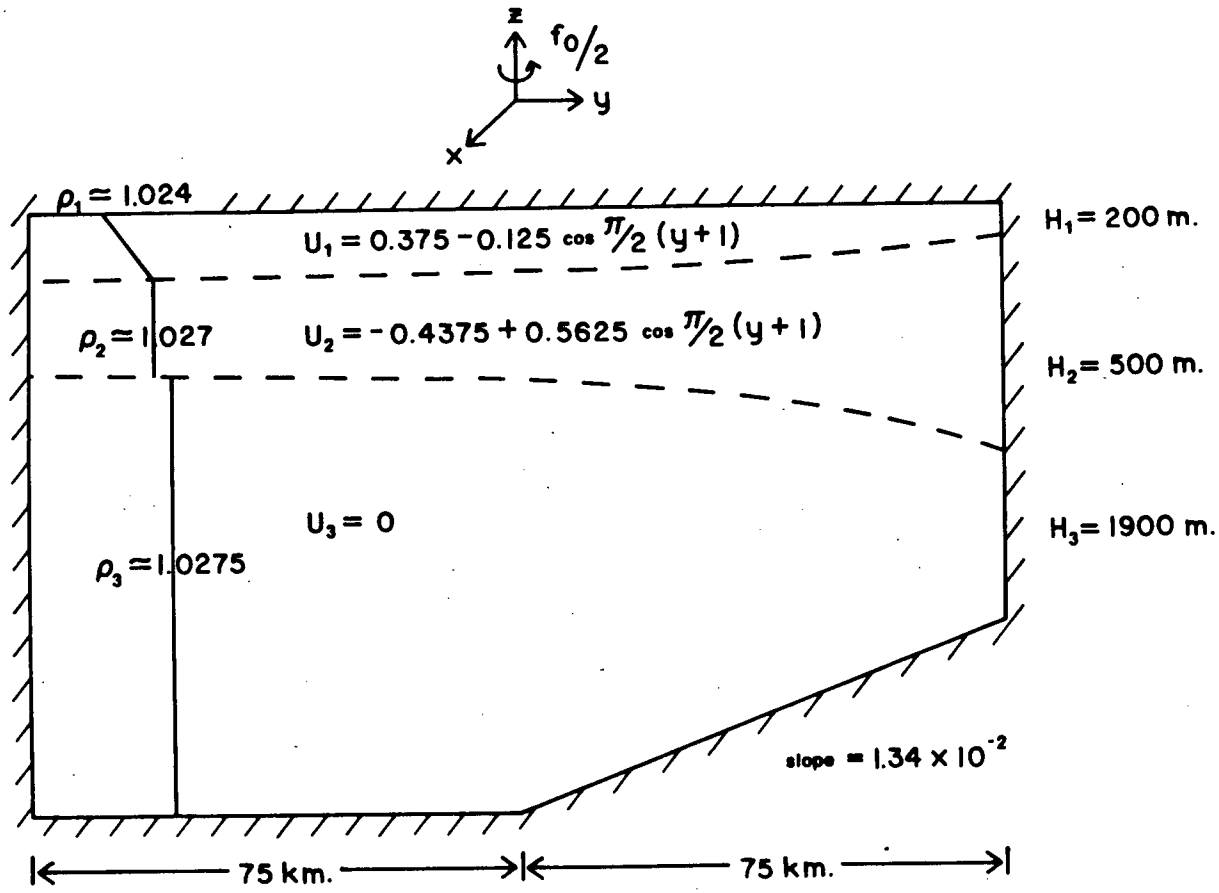

Figure 3.8: The extension of the channel model to include effects of horizontal shear and reduce the influence of the artificially imposed western boundary.

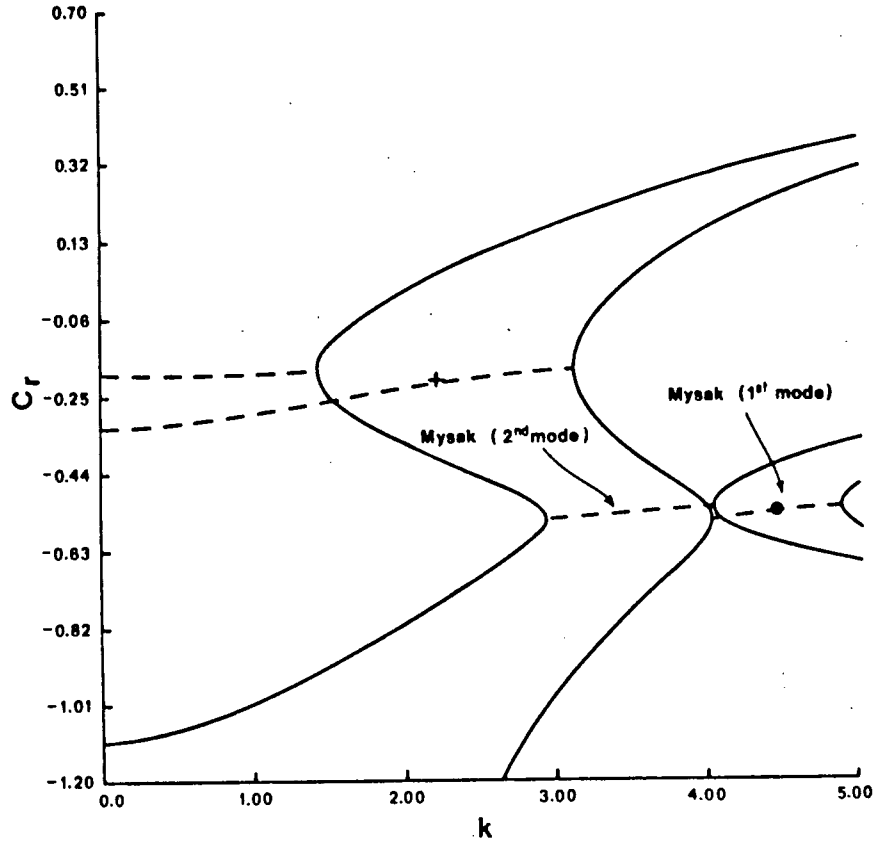

Figure 3.9: Graph of c_r (non-dimensional phase speed) in the wave-number range $k = 0 - 5$ (wavelength = ∞ - 47.1 km) for the first two cross-channel modes. The unstable regions corresponding to those studied by Mysak (1977) are labelled as such. Regions of instability are indicated by dashed lines and the position at which the largest growth rate is found is indicated by a plus sign.

energy from the tilt of the lower interface (this is the only energy source in Mysak's model). The transfer of available potential energy corresponding to the most unstable wave of this type is shown in figure 3.10 and the properties of this wave are given in table 3.1 together with the properties of the corresponding wave discussed by Mysak (1977). The results of the two models are clearly in quite good agreement. We note however that the wavelength of these instabilities is only about half of that observed (Mysak has considered other cases which show better agreement with observations but the parameter values used in these studies do not appear to be as reasonable as those used in the above model).

This class of instabilities (those extracting their energy from the tilt of the lower interface) does not however have the largest growth rates found in studying the above three-layer model. The most unstable waves found extract energy principally from the upper interface (see figure 3.11). Table 3.2 gives the properties of the most unstable waves found in the study of the model depicted in figure 3.7. The properties of this wave are significantly different from those of the corresponding wave at shorter wavelengths (compare tables 3.1 and 3.2). In particular we note that this wave is strongly intensified in the upper layers and has an along-channel wavelength approximately double that of the previously discussed instability (this wavelength is in good agreement with the observed wavelength of about 100 km.). The e-folding time, phase and group velocities are also significantly reduced which, with the surface intensification, makes this the more likely wave to be observed. Thus the predictions of the three-layer model suggest that although Mysak's

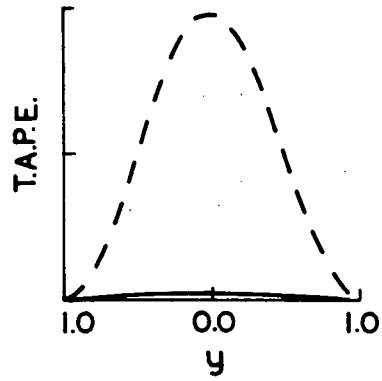

Figure 3.10: Transfer of available potential energy (in arbitrary units) corresponding to the most unstable 1st mode instability analogous to that considered by Mysak (1977). The position of this wave in figure 3.9 is marked by a circle. (The solid line corresponds to the transfer of energy due to the shear between the upper layers and the dashed line to that due to the shear between the lower layers)

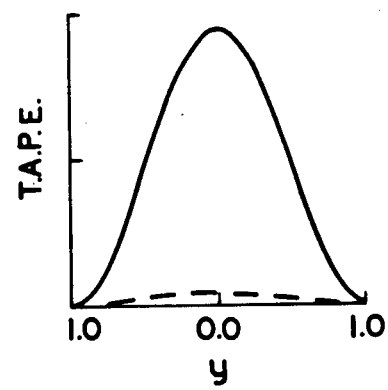

Figure 3.11: Transfer of available potential energy corresponding to the most unstable wave found using the three-layer model (plus sign in Fig. 3.9) (The solid line corresponds to the energy transfer due to the shear between the upper layers and the dashed line to that due to the shear between the lower layers.)

two-layer model gives reasonable results for one type of instability, it does not exhibit the instability which is most likely observed. The other values of the mean velocities considered by Mysak have also been considered in the above fashion (results are not reproduced here). In each case the results are similar to those for the case discussed above, i.e. the two-layer model of Mysak (1977) reveals the instability which extracts energy from the lower interface (which in some cases gives reasonable agreement with observations) but the most unstable wave is due to the shear between the upper layers. The model considered above gives the smallest growth rates of the cases considered and is believed to give a conservative estimate of the instabilities present in the region of the California Undercurrent. Hence from the above work it is clear that this current system is very unstable to quasi-geostrophic perturbations at the observed length and time scales.

We now consider the effects of the artifically introduced wall at the western boundary of the undercurrent. To do this we consider the more realistic system depicted in figure 3.8. When the western boundary is moved further out, horizontal shear must be included. The choice considered here is shown in figure 3.12(a), but the form of the mean currents can be varied considerably without significantly changing the results. The potential vorticity gradients in the three layers are given in figure 3.12b. Clearly there are two possible types of baroclinic instability in this system; one due to the change in sign of q_y between the first and second layers and the other due to the change in sign between the second and third layers. In each case the sign change occurs in the region of large vertical shear and we expect the amplitude of the unstable wave to be largest there. This is indeed

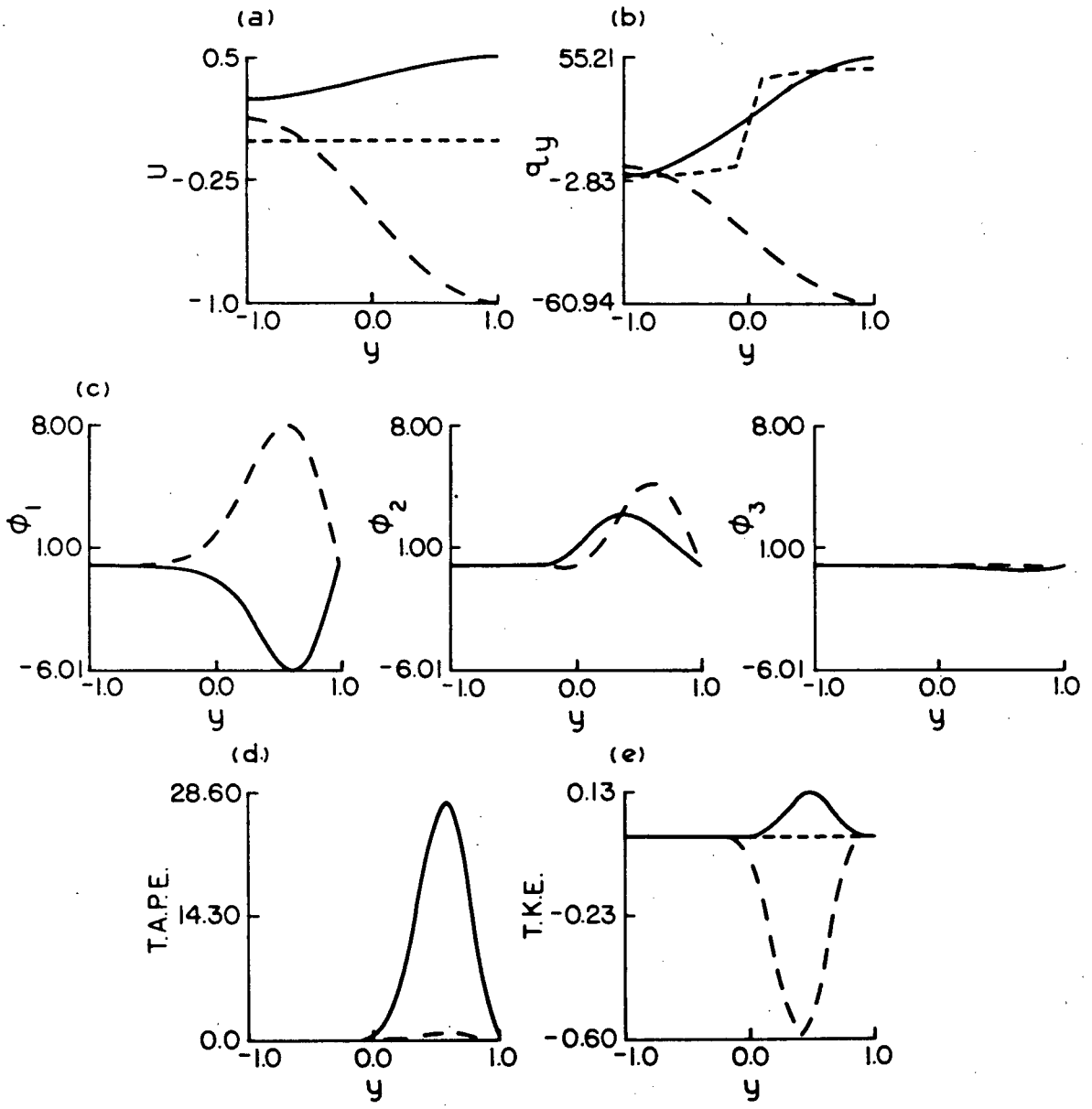

Figure 3.12: (a) Approximation to the mean currents used to model the California undercurrent off Vancouver Island (see figure 3.8); (b) The mean potential vorticity gradients corresponding to the three layers of our model: upper layer-solid line, middle layer-long dashes, lower layer-short dashes; (c) The Eigenfunctions corresponding to the most unstable wave in our model; (d) the transfer of available potential energy corresponding to the above wave; (e) The transfer of kinetic energy in the three layers. (see figure 2.7 for the meaning of the different lines in (d) and (e).)

Table 3.3: Properties of the most unstable wave corresponding to the system shown in figure 3.8. This wave is illustrated in figure 3.12. δ_1 and δ_3 are the approximate phases of the wave in the upper and lower layers relative to the middle layer in the region where the perturbations are largest. (A positive value of c or c_g corresponds to a southward velocity.)

Model	U_1, U_2, U_3 (x 10 cm sec^{-1})	Period (days)	Wavelength (km)	e-folding time (days)	Phase velocity (km day^{-1})	Group velocity (km day^{-1})	$\left\|\frac{\phi_1}{\phi_2}\right\|$,	$\left\|\frac{\phi_3}{\phi_2}\right\|$	δ_1, δ_3 (degrees)
figure 3.8	figure 3.12a	57.3	100	8.3	-1.7	-0.3	~2,	~0.03	~60, ~115

verified in figure 3.12(c). The instability due to the change in sign of q_y between the middle and bottom layers corresponds to the wave studied by Mysak (1977). Its properties are very similar to those of the corresponding wave for the system illustrated in figure 3.7 and are not further discussed. Finally we note that the energy source for the unstable perturbations which owe their existence to the change in sign of q_y between the upper two layers is almost purely potential energy from the tilt of the upper interface, and the transfer of energy occurs in the region of large vertical shear (figure 3.12(c)). The properties of the most unstable wave existing in this system (illustrated in figure 3.12(b)) are given in Table 3.3. Clearly the properties of this wave are very similar to the corresponding wave for the system illustrated in figure 3.7 (see table 3.2). The period, wavelength, e-folding time, phase velocity, vertical distribution of energy and phase shifts between the layers all show good agreement. The group velocity is considerably smaller, however both values are quite small and the difference may not be significant.

A final three-layer model was considered in which the topography in figure 3.8 was neglected but everything else was kept the same. The results were very similar to those corresponding to figure 3.8 and will not be presented here. The insensitivity of this class of instability (extracting energy from the upper interface) to topography is expected from the work done in chapter II.

Finally we note that just as Mysak (1977) studied the class of instabilities which extract energy from the lower interface it may be possible to use a two-layer model to study the class of instabilities which extract potential energy from the tilt of the upper interface.

The agreement between the results for the most unstable waves corresponding to figures (3.7) and (3.8) suggest that a simple channel model analogous to that shown in figure 3.7 should suffice to investigate this possibility. Since our study of the three-layer model shows that the wave which extracts its energy from the upper interface extracts very little energy from the lower interface, it is probably reasonable to assume that the tilt of the lower interface acts in a manner similar to a sloping bottom. The effect will, of course, not be as strong as if the lower interface were replaced by a solid bottom and hence we consider two different two-layer models. The first has zero bottom slope while the second has a bottom slope equal to the slope of the lower interface due to the vertical shear of the mean currents. It is to be expected that the true situation would be best modelled by something between these cases. Since the mean state is in hydrostatics and geostrophic balance it is easily found that the mean position of the lower interface in the three-layer channel model depicted in figure 3.7 is given by

$$\eta_3^* = \frac{f_o}{g(\rho_3^*-\rho_2^*)} (\rho_2^* U_2^* - \rho_3^* U_3^*) y^* \tag{3.3}$$

and hence:

$$\eta_{3y}^*/H_2 = \frac{f_o}{g(\rho_3^*-\rho_2^*)} (\rho_2^* U_2^* - \rho_3^* U_3^*) L/H_2 \quad . \tag{3.4}$$

We thus consider the two-layer models analogous to figure 3.7 with no lower layer and bottom topography given by

$$\left.\begin{aligned} bh_y/H_2 &= \frac{f_o}{g(\rho_3^*-\rho_2^*)}\,(\rho_2^*U_2^* - \rho_3^*U_3^*)\,L/H_2 \\ \text{or} \qquad bh_y/H_2 &= 0 \end{aligned}\right\} \qquad (3.5)$$

The properties of the most unstable waves in these two models are given in Table 3.4 together with the average of these two cases. The average is clearly in good agreement with the predictions made using the three-layer model (except for the group velocity, which although still quite small, is increased significantly) corresponding to figure 3.7, however, the strong variation of these statistics with changing bottom topography indicates the difficulties in attempting to use such a two-layer model. It appears that at least three layers are required to study a system such as the California Current system. Further, using more than three-layers would probably create unnecessary confusion as the data-base does not permit the mean currents to be sufficiently well defined to warrant the investigation of more complex models. My investigations with a three-layer model do certainly support the conjecture of Mysak (1977) that the eddies observed over the continental slope in figure 3.1 may be due to the inherent instability of the current system to perturbations at the observed length and time scales. Unlike Mysak, however, we find that the fastest growing waves in this system probably extract their energy principally from the tilt of the upper interface.

Table 3.4: Properties of the most unstable waves found using two-layer models to study the stability of the upper layers of the California current system. δ_1 is the phase of the wave in the upper layer relative to the lower layer. (A positive value of c or c_g corresponds to a southward velocity.)

Model	U_1, U_2 (x 10 cm sec^{-1})	Period (days)	Wavelength (km)	e-folding time (days)	Phase velocity (km day^{-1})	Group velocity (km day^{-1})	$\left\|\frac{\phi_1}{\phi_2}\right\|$	δ_1 (degrees)
0 bottom slope	0.5, -1.0	14.4	124.0	5.92	-0.73	-3.3	1.4	56
constant bottom slope	0.5, -1.0	111.1	91.2	5.86	-3.6	-3.0	1.0	75
Average of above cases	0.5, -1.0	62.8	102.6	5.89	-2.2	-3.2	1.2	66

4. Conclusions

Three-layer models have been used to study the stability of the current systems in Juan de Fuca Strait and the Calfiornia Undercurrent off Vancouver Island to quasi-geostrophic wave perturbations. The model developed in chapter II is applied to Juan de Fuca Strait and it is found that the most unstable wave has properties consistent with observations made by Fissel (1976). The lack of coherence between stations separated by as little as four kilometers is not expected from the predictions of our model and it is suggested that it may be due to several processes occurring at the same time at similar length and time scales. It should also be noted that the data analysed by Fissel (1976) only contains about three periods at the time scales under consideration and are not sufficient to make firm conclusions.

The observations off Vancouver Island allow us to determine an approximate wave length (~ 100km) for the eddies and show that the eddies are surface intensified. The results of the three-layer model applied to this area (a modification of that developed in chapter II) are in good agreement with the limited observations available. Further, the model predicts an e-folding time of about 8 days with a group velocity of about 0.3 km day^{-1} (to the north) making it very likely that these waves are significantly amplified before propagating out of the undercurrent region which extends all the way from California to Vancouver Island. Note however that this large growth rate applied to the initial growth of the perturbation and is significantly reduced as the eddies reach finite amplitude (Pedlosky (1970). Since the magnitudes of the mean currents used are conservative estimates it appears very likely that the undercurrent

system is highly unstable to perturbations at the observed length and time scales.

Both a simple channel flow with constant bottom slope and no horizontal shear, and a more realistic model including a flat ocean floor and horizontal shear are considered in the study of the California Undercurrent. The agreement between the two models is excellent. This agreement is, of course, strongly dependent on choosing the correct channel width in the channel model. This width must be chosen to include the region in which the majority of the energy is released to the perturbations but must not be much wider. A channel which is much to wide will predict a perturbation which is also too wide and too narrow a channel will predict too narrow an eddy as well as not including the full energy source for the perturbations. If the channel width is chosen correctly though the agreement is good. For the models considered here it appears that the choice may be made simply by considering only the region in which the vertical shear is largest but such a choice may not always be valid. An example of such a case would be furnished by any situation in which the transfer of kinetic energy due to barotropic instability is significant.

Finally a two-layer model is used to study the stability of the upper two layers of the three-layer model. It is found that the system is very sensitive to the choice of bottom slope but with a correct choice, results are in good agreement with those of the corresponding instability in the three-layer model. Due to the sensitivity of the instabilities to the bottom slope in such a model, it appears that to model a current system such as that considered here at least three layers must be used.

CHAPTER V

CONCLUDING DISCUSSION

Concluding Discussion

This study was initially undertaken in an attempt to determine whether or not baroclinic instability could make a significant contribution to the low-frequency motions observed by Fissel (1977) in Juan de Fuca Strait. Since the transition of density from its value near the surface ($\sigma_t \simeq 24.7$) to its value at depth ($\sigma_t \simeq 26.7$) occurred gradually over a depth of more than 80 m (nearly half the depth of the strait; see figure 2.3, chapter IV), the usual layered models did not appear appropriate. Although Davey's three-layer model (with each layer of constant density; Davey (1977)) could have been applied to this situation with appropriate reduction of density differences between the layers, it is not clear exactly how much these differences should be reduced. Therefore, it was decided to derive a three-layer model which would overcome (or at least minimize) this problem. This was done by modelling the observed continuous density stratification by a simpler continuous model (figure 2.3, chapter IV) and then finding an approximate solution to the new problem with three degrees of freedom in the vertical. The resulting equations are very similar in form to those derived by Davey(1977) but the differences are also significant.

DAVEY'S EQUATIONS (extended to include horizontal shear, variable layer depths and weak bottom slopes; the density difference between successive layers is equal):

$$\left(\frac{\partial}{\partial t} + U_1 \frac{\partial}{\partial x}\right)\left[\nabla^2\xi_1 + 2F_1\,(\xi_2-\xi_1)\right] + \frac{\partial \xi_1}{\partial x}\left[\beta - U_{1yy} + 2F_1(U_1-U_2)\right] = 0$$

$$\left(\frac{\partial}{\partial t} + U_2 \frac{\partial}{\partial x}\right)\left[\nabla^2\xi_2 + 2F_2(\xi_1-2\xi_2+\xi_3)\right] + \frac{\partial \xi_2}{\partial x}\left[\beta - U_{2yy} + 2F_1(U_1-U_2)\right] = 0$$

$$\left(\frac{\partial}{\partial t} + U_3 \frac{\partial}{\partial x}\right)\left[\nabla^2\xi_3 + 2F_3(\xi_2-\xi_3)\right] + \frac{\partial \xi_3}{\partial x}\left[\beta - U_{3yy} + 2F_3(U_3-U_2) + \frac{b}{R_o H_3} h_y\right] = 0$$

(1.1)

(Davey's equations have been rewritten in our notation for convenience). These equations are to be compared with equations 3.2, Chapter II (with $bh \ll H_3$):

$$\left(\frac{\partial}{\partial t} + U_1 \frac{\partial}{\partial x}\right)\left[\nabla^2\xi_1 - F_1(3\xi_1-4\xi_2+\xi_3)\right] + \frac{\partial \xi_1}{\partial x}\left[\beta - U_{1yy} + F_1(3U_1-4U_{2o}+U_3)\right] = 0$$

$$\left(\frac{\partial}{\partial t} + U_{2o} \frac{\partial}{\partial x}\right)\left[\nabla^2\xi_2 + 4F_2(\xi_1-2\xi_2+\xi_3)\right] + \frac{\partial \xi_2}{\partial x}\left[\beta - U_{2oyy} - 4F_2(U_1-2U_{2o}+U_3)\right] = 0$$

$$\left(\frac{\partial}{\partial t} + U_3 \frac{\partial}{\partial x}\right)\left[\nabla^2\xi_3 - F_3(\xi_1-4\xi_2+3\xi_3)\right] + \frac{\partial \xi_3}{\partial x}\left[\beta - U_{3yy} + F_3(U_1-4U_{2o}+3U_3) + \frac{b}{R_o H_3} h_y\right] = 0$$

(1.2)

The first thing to note is that these two sets of equations can <u>not</u> be made equivalent by any choice of density difference between the layers in Davey's model. This is due to the presence of ξ_3 (and U_3) in the first equation and ξ_1 (and U_1) in the third equation of (1.2). The modelling of vortex stretching is different; in the model developed here, the upper and lower layers feel each others influence much more strongly (and directly) than in Davey's model. One expects this kind of difference since the model

developed here takes account of the fact that the vortex tubes are continuous whereas the usual layered models do not. The second major difference is seen by considering the second layer only. Where we have $4F_2$, Davey has $2F_2$. Decreasing the density difference between the layers by a factor of two in Davey's model will eliminate this difference (note, however that the equations for the upper and lower layers are still not in agreement). This explains why, for a given density difference between the layers, the extent of the unstable range (plotted against K_m^2/F_2) is only about half as wide for Davey's model as it is for ours in the presence of large vertical curvature. Finally there is the difference between U_{2o} (the value of U at the middle of the second layer) and U_2 (the vertical mean value of U in the second layer) in the two models. Although this difference is relatively small for $S_1 \simeq S_2$, in the presence of large vertical curvature, it is significant.

It is important to notice here that both Davey's model and the one developed here are essentially finite difference approximations to the equations for a continuously stratified fluid. This is implicit in Davey's model and is introduced <u>a priori</u> by considering three layers of uniform density. The model developed here introduces the finite difference approximation rather more explicitely through a truncated power series expansion about the middle of the second layer. Such an expansion is, after all, the basis of finite difference models. By introducing the finite difference approximation in this manner, the model is automatically "fitted" to the actual density stratification and mean currents. Of course, if many layers are to be used, the two models will be essentially equivalent. However, the difference appears very significant if as few as three layers are being employed.

Due to the unusual form of our finite difference equations in the upper and lower layers, we now give a brief derivation of our equation which makes their finite difference nature more explicitely revealed.

We begin with equations (2.10)-(2.12), Chapter II. As in the previous chapters, a subscript o will be used to indicate a quantity evaluated at the middle of a given layer, and we will use a Δ to indicate the finite difference approximation of a given quantity. Thus $\Delta p_{2zz}\Big|_{z=z_m}$ is the finite difference approximation to p_{2zz} at $z=z_m$ $(=-(H_1+\frac{H_2}{H})/H)$. We will need the following expressions:

$$\begin{aligned}\Delta p_{2z}^{(0)}\Big|_{z=z_m} &= (H/H_2)(p_1^{(0)}-p_3^{(0)}) \\ \Delta p_{2zz}^{(0)}\Big|_{z=z_m} &= 4(H/H_2)^2(p_1^{(0)}-2p_{2o}^{(0)}+p_3^{(0)})\end{aligned} \tag{1.3}$$

Using the second of these in (2.11), Chapter II, we get (2.15b), Chapter II, immediately, and no further discussion of this equation is needed. The corresponding equations for the upper and lower layers are equally as simply derived. In (2.10) we use:

$$\begin{aligned}\Delta p_{2z}^{(0)}\Big|_{z=-\frac{H_1}{H}} &= \Delta p_{2z}^{(0)}\Big|_{z=z_m} + \Delta p_{2zz}^{(0)}\Big|_{z=z_m}\ (H_2/2H) + O((H_2/2H)^2) \\ &= (H/H_2)(p_1^{(0)}-p_3^{(0)}) + 2(H/H_2)(p_1^{(0)}-2p_2^{(0)}-p_3^{(0)}) + O((H_2/2H)^2) \\ &= (H/H_2)(3p_1^{(0)}-4p_{2o}^{(0)}+p_3^{(0)}) + O((H_2/2H)^2)\end{aligned}$$

and in (2.11) we use:

$$\Delta p_{2z}^{(0)}\Big|_{z=-\frac{H_1}{H}} = \Delta p_{2z}^{(0)}\Big|_{z=z_m} + \Delta p_{2zz}^{(0)}\Big|_{z=z_m}(-H_2/2H) + O((H_2/2H)^2)$$

$$= (H/H_2)(p_1^{(0)}-p_3^{(0)})-2(H/H_2)(p_1^{(0)}-2p_{2o}^{(0)}+p_3^{(0)}) + O((H_2/2H)^2)$$

$$= (H/H_2)(p_1^{(0)}-4p_{2o}^{(0)}+3p_3^{(0)}) + O((H_2/2H)^2)$$

where we have used (1.3) in each case. Substituting these expressions in (2.10) and (2.12) we get (2.15a,c).

This alternative derivation of our equations not only demonstrates the finite difference nature of our equations, but it shows the ease with which they can be derived (although this method of derivation was not obvious at the outset). The important thing to notice is that, although both this model and Davey's are essentially finite difference approximations, by introducing step discontinuities in the density profile a priori, Davey's model has altered the dynamics of the flow more than is necessary and it is not clear exactly how the model should be "fitted" to the actual situation. We suggest that if a finite difference approximation is to be used, it must be introduced in a consistent manner. The method employed in this thesis to find such an approximation is to first approximate the actual density profile by a simpler profile which closely resembles that observed and then find the appropriate finite difference equations corresponding to this approximate model. By finding the equations appropriate to a density profile which closely approximates the real situation this method results in a set of equations which can be used to model realistic oceanic circumstances more accurately than the conventional three-layer model without introducing more layers (and thus greater complexity). There will,

of course, still be an error introduced in making the finite difference approximation and the study of the precise nature of this error is indeed a worthy topic for future research.

It must be mentioned here that Davey's model does have some advantages over the one developed here. The main advantage is that in the hands of an experienced modeller (who chooses the density differences between the layers correctly, uses the correct values for U_1, U_2, and U_3 [this includes replacing U_2 by U_{2_o} when the vertical curvature of the mean currents is significant] and interprets results carefully), Davey's model may be immediately applied to a large variety of cases without re-deriving the governing equations. Although it is believed the model derived here will yield more accurate results, different density and velocity profiles will require a re-derivation of the appropriate equations. Because of this fact our method will be slightly less convenient, especially if one only desire a crude approximation before going on to do a more detailed analysis. Finally we mention that the two models may be combined as was done in chapter IV, section 3 to study the California Undercurrent system. In this manner, the region in which the large density transition occurs may be modelled quite accurately using the methods described in this thesis, and more degrees of freedom in the vertical may be added with a minimal effort. Such a model would be useful in many situations. In particular, it might be useful in studies of the open ocean where a linear density variation would model the thermocline quite well.

In chaper II, I have mentioned that a two-layer model is probably most useful when the vertical curvature of the mean currents and the region of density transition are small. I now wish to stress a point made in chapter III involving the study of pure barotropic instability in which a "one-layer" model is employed. If over some depth of the fluid, the horizontal length scale over which the mean currents vary is sufficiently strong

that $(L/r_{int})^2 \ll 1$ in this region, then barotropic instability may occur over this depth with little effect from the fluid above and below. Thus, for such a case, averaging the mean currents over the depth of the fluid results in a rather poor approximation. This will significantly reduce and may even eliminate any instabilities present. A better approach would be to consider the region in which $(L/r_{int})^2 \ll 1$ separately.

Another interesting result found in chapter III was the presence of a "barotropic" instability which can draw energy from the potential energy of tilting isopycnals due to the mean flow. This wave is filtered out under the assumption of a horizontally uniform mean flow, but even for $(L/r_i)^2$ moderately large it can have a significant growth rate and may, in some cases, be important. Thus, even for $(L/r_i)^2 \gg 1$ it may not be justified to consider the case of no horizontal shear. (Note, however, that such a study is valid for the study of baroclinic instabilities).

An interesting discussion of momentum transports for the case of mixed baroclinic-barotropic instability has been presented by Held (1975). Of particular insterest is his proof that in an arbitrary zonal flow, linear theory predicts that unstable waves cause a net transport of momentum out of the region of fluid in which the generalized Rayleigh criterion for instability (the change in sign of $\partial q/\partial y$; see Pedlosky, 1964a) is satisfied locally. Although the author was unaware of this paper until after the writing of this thesis was completed, it would certainly be enlightening to re-examing the results of chapter III in the light of Held's work. Work in this direction has now begun but will be reported elsewhere.

In each of the case studies (Juan de Fuca Strait and the California Undercurrent) made in Chapter IV it was found that the significant instabilities

are basically baroclinic instabilities extracting their energy from the interface between the upper layers. The role of the horizontal shear was simply to limit the region in which baroclinic instability was possible. The isolation of these instabilities from the bottom made the influence of topography relatively weak. This result will probably be true for many oceanic flows where the large vertical shear occurs near the surface. However, one must remember that bottom intensified waves may also exist due to bottom slopes (Rhines, 1970), so if one chooses to neglect bottom topography on the grounds that only surface intensified motions are being studied, it must be borne in mind that these waves are filtered out.

Finally we mention that many effects have not been considered in the model presented here. Some of these have been mentioned in Chaper IV, section 2 in the study of Juan de Fuca Strait. Of these effects the author finds the modifications of these low-frequency waves due to the tides to be a largely overlooked problem. The inclusion of this effect as well as the effects due to motions on the continental shelf off Washington and Vancouver Island seem to be necessary before any definite conclusions can be made about the low-frequency motions in Juan de Fuca Strait. For now, we can only say that the predictions of our model are consistent with observations.

The model of the California Undercurrent appears to be consistent with the very limited observations off Washington and Vancouver Island, however the extremely sparse observations again make definite conclusions difficult. It would be convenient to make detailed measurements here, but the relatively small width of the undercurrent in this region and the extremely long periods predicted by our model (which, by the way, make our assumption of a non-diffusive fluid rather questionable), make it unlikely that an

adequate study will be made in the near future. Perhaps a more feasible approach would be to apply the model developed here to the region off California where much more detailed observations have been made. If the model predictions in this region show good agreement with observations, one could be more certain that the same would be true further north.

REFERENCES CITED

Bernstein, R.L., Breaker, L., and R. Whritner, 1977. California Current Eddy Formation: Ship, Air and Satellite Results. Science, 353-359.

Bretherton, F.P., 1966a: Critical layer instability in baroclinic flows. Quart. J.R. Met. Soc., 92, 325-334.

Bretherton, F.P., 1966b: Baroclinic instability and the short wavelength cut-off in terms of potential vorticity. Quart. J.R. Met. Soc., 92, 335-345.

Brown, J.A., 1969a,b: A numerical investigation of hydrodynamic instability and energy conversions in the quasi-geostrophic atmosphere: Part I and II. J. Atmos. Sci., 26 352-375.

Brown, R.A., 1972: On the physical mechanism of the inflection point instability. J. Atmos. Sci., 29, 984-986.

Cannon, G.A., and N.P. Laird, 1978: Circulation in the Strait of Juan de Fuca, 1976-1977. PMEL, ERL, NOAA Technical Report, (in preparation).

Charney, G.A., and N.P. Laird, 1978: Circulation in the Strait of Juan de Fuca, 1976-1977. PMEL, ERL, NOAA Technical Report, (in preparation).

Charney, J.G., 1947: The dynamics of long waves in a baroclinic westerly current. J. Meteorol., 4, 135-162.

Charney, J.G., 1971: Geostrophic Turbulence. J. Atmos. Sci., 28, 1087-1095.

Davey, M.K., 1977: Baroclinic instability in a fluid with three layers. J. Atmos. Sci., 34, 1224-1234.

Dodimead, A.J., Favorite, F., and T. Hirano, 1963: Review of oceanography of the subartic Pacific region. Bull. Int. N. Pacific Fish Comm., 13, 195 pp.

Drazin, P.G. and L.N. Howard, 1966: Hydrodynamic stability of parallel flow of inviscid fluid. Advances in Applied Mechanics, 9, 1-89.

Eady, E.T., 1949: Long waves and cyclone waves. Tellus, 1, 33-52.

Fissel, D.E., 1976: Pressure differences as a measure of currents in Juan de Fuca Strait. Pacific Marine Science Report 76-17, 63pp. Institute of Ocean Sciences, Patricia Bay, Victoria, B.C. (Unpublished manuscript).

Fissel, D.E. and W.S. Huggett, 1976: Observations of currents, bottom pressures and densities through a cross-section of Juan de Fuca Strait. Pacific Marine Science Report 76-6, 68pp. Institute of Ocean Sciences, Patricia Bay, Victoria, B.C. (Unpublished manuscript).

Fjørtoft, R., 1951: Stability properties of large-scale atmospheric disturbances. In: Compendium of Meteorology, American Meteorology Society, Boston (Reprinted in: Theory of Thermal Convection, ed. by B. Saltzman, Dover Publications, New York, 1962).

Gent, P.R., 1974: Baroclinic instability of a slowly varying zonal flow. J. Atmos. Sci., 31, 1983-1994.

Gent, P.R., 1975: Baroclinic instability of a slowly varying zonal flow, Part II. J. Atmos. Sci., 32, 2094-2102.

Gill, A.E., Green, J.S.A. and A.J. Simmons, 1973: Energy partition in the large scale ocean circulation and the production of mid-ocean eddies. Deep Sea Research, 21, 499-528.

Green, J.S.A., 1960: A problem in baroclinic instability. Quart. J.R. Met. Soc., 86, 237-251.

Halpern, D., Reed, R.K. and R. L. Smith, 1977: On the California Undercurrent over the continental slope off Oregon. J. Geophys. Res., 83, 1366-1372.

Helbig, J.A. and L.A. Mysak, 1976: Strait of Georgia oscillations. Low-frequency currents and topographic planetary waves. J. Fish. Res. Can., 33, 2329-2339.

Held, I.M., 1975: Momentum Transport by Quasi-Geostrophic Eddies. J. Atmos Sci., 32, 1494-1497.

Hide, R. and P.J. Mason, 1975: Sloping Convection in a rotating fluid: a review. Advances in Physics, 34, 47-100.

Holbrook, J.R. and D. Halpern, 1978: Variability of near-surface currents and winds in the western Strait of Juan de Fuca. PMEL, ERL, NOAA Technical Report, (in preparation).

Holmboe, J., 1968: Instability of baroclinic three-layer models of the atmosphere. Geofysiske Publikasjoner, 28, 1-27.

Huyer, A., 1976: A comparison of upwelling efforts in two locations: Oregon and North West Africa. J. Mar. Res., 34, 531-546.

Ingraham, W.J., 1967: The geostrophic circulation and distribution of water properties off the coasts of Vancouver Island and Washington, spring and fall, 1963. Fish Bull., 66-223-250.

Killworth, P.D., 1978: Barotropic and baroclinic instability in rotating stratified fluids, with application to geophysical systems, Dyn. Atmos. Ocean. (submitted).

Kuo, H.L., 1949: Dynamic instability of two-dimensional non-divergent flow in a barotropic atmosphere. J. Meteorol., 6, 105-122.

Kuo, H.L., 1973: Dynamics of quasigeostrophic flows and instability theory. Advances in Applied Mechanics, 13, 247-330.

LeBlond, P.H. and L.A. Mysak, 1978: Waves in the Ocean. Elsevier, Amsterdam, 602 pp.

Lin, C.C., 1945: On the stability of two-dimensional parallel flows, Parts I, II, III. Quart. Appl. Math., 3, 117-142, 218-234, 277-301.

Longuet-Higgins, M.S., 1972: Topographic Rossby waves. Memoires Société Royale des Science de Liège, 6^{e} serie, tome II, 11-16.

McIntyre, M.E., 1970: On the non-separable baroclinic parallel flow instability problem. Journal of Fluid Mechanics, 40, 273-306.

Miles, J.W., 1964a: Baroclinic instability of zonal wind. Rev. of Geophys., 2, 155-176.

Miles, J.W., 1964b,c: Baroclinic instability of the zonal wind: Parts II and III. J. Atmos. Sci., 21, 500-506, 603-609.

Mysak, L.A., 1977: On the stability of the California Undercurrent off Vancouver Island. J. Phys. Oceanogr., 7, 904-917.

Narayanan, S., 1973: Quasi-geostrophic waves in the open ocean (Ph.D. thesis), Harvard University, Cambridge, Massachusetts.

Needler, G.T. and P.H. LeBlond, 1973: On the influence of the horizontal component of the earth's rotation on long-period waves. Geophysical Fluid Dynamics, 5, 23-46.

Orlanski, I. and M.D. Cox, 1973: Baroclinic instability in ocean currents. Geophysical Fluid Dynamics, 4, 297-332.

Pedlosky, J., 1963: Baroclinic instability in two-layer systems. Tellus, 15, 22-25.

Pedlosky, J., 1964a,b: The stability of currents in the atmosphere and ocean, Parts I and II. J. Atmos. Sci., 21, 201-219, 342-353.

Pedlosky, J., 1964c: An initial value problem in the theory of baroclinic instability. Tellus, 16, 12-17.

Pedlosky, J., 1970: Finite amplitude baroclinic waves. J. Atmos. Sci., 27, 15-30.

Pedlosky, J., 1971a: Finite-amplitude baroclinic waves with small dissipation. J. Atmos. Sci., 28, 587-597.

Pedlosky, J., 1971b: Geophysical Fluid Dynamics. Mathematical Problems in the Geophysical Sciences, W.H. Reid (editor), V. 13, American Mathematical Society, Providence, Rhode Island, pp. 1-60.

Pedlosky, J., 1972: Finite-amplitude baroclinic wave packets, J. Atmos. Sci., 29, 680-686.

Pedlosky, J., 1974: Long shore currents, upwelling and bottom topography. J. Phys. Oceanogr., 4, 214-226.

Pedlosky, J., 1975: On secondary baroclinic instability and the meridional scale of motion in the ocean. J. Phys. Oceanogr., 5, 603-607.

Pedlosky, J., 1976: Finite-amplitude baroclinic disturbances in downstream varying currents. Journal of Physical Oceanography, 6, 335-344.

Phillips, N.A., 1951: A simple three-dimensional model for the study of large scale extra tropical flow patterns. J. Meteorol., 8, 381-394.

Phillips, O.M., 1966: The Dynamics of the Upper Ocean. Cambridge University Press, 261 pp.

Pond, S. and G.L. Pickard, 1978: Introductory Dynamic Oceanography, Pergamon Press, 241 pp.

Rao, D.B. and T.J. Simons, 1969: Stability of a sloping interface in a rotating two-fluid system. Atmospheric Science Paper No. 151, Colorado State Univ., Fort Collins, Colo., 32 pp.

Reed, R.K. and D. Halpern, 1976: Observations of the California Undercurrent of Washington and Vancouver Island. Limnol. Oceanogr., 21, 389-398.

Rhines, P.B., 1970: Edge-, bottom-, and Rossby waves in a rotating stratified fluid. Geophysical Fluid Dynamics, 1, 273-302.

Rossby, C.G., 1949: On a mechanism for the release of potential energy in the atmosphere. J. Meteorol., 6, 163-180.

Simmons, A.J., 1974: The meridional scale of baroclinic waves. J. Atmos. Sci., 31, 1515-1525.

Stone, P.H., 1969: The meridional structure of baroclinic waves. J. Atmos. Sci., 26, 376-389.

Tabata, S., 1975: The general circulation of the Pacific Ocean and a brief account of the oceanographic structure of the North Pacific Ocean. Atmosphere, 13, 133-168.

Turner, J.S., 1973: Bouyancy Effects in Fluids, Cambridge University Press. 367 pp.

Wickham, J.B., 1975: Observations of the California counter current, J. Mar. Res., 33, 325-340.

Wooster, W.S., and J.H. Jones, 1970: California Undercurrent off northern Baja California, J. Mar. Res., 28, 235-250.

Appendix

Glossary of symbols[†]

b - amplitude of topographic variations

c^*, c - phase speed

$C = c - U_{2o}$ - doppler shifted phase speed

f - coriolis parameter

f_0 - local value of the coriolis parameter

$F_i = f_o^2 L^2 / g' H_i$ - the Burger number for the ith layer

g - acceleration due to gravity

g' - reduced gravity

h - cross-channel structure of topographic variations (bh gives the height of the bottom above $z^* = -H_T$)

H_i - thickness of the i^{th} layer

$H_T = H_1 + H_2 + H_3$

H - vertical length scale

k^*, k - long-channel wavenumber

L - horizontal length scale

p_i^* - dimensional pressure in the i^{th} layer

p_i - non-dimensional perturbation pressure in the i^{th} layer

q_i - potential vorticity in the i^{th} layer (non-dimensional)

r_i - internal deformation radius for the i^{th} layer

$R_o = U/f_o L$ - the Rossby number

$T = \frac{b}{R_o H_3} h_y$ - the topographic parameter

[†]When a variable appears both with and without a star on its shoulder, the starred variable is dimensional and the other is non-dimensional.

$\hat{T} = T/F_2$

u_i^*, u_i - eastward component of the velocity in the i^{th} layer

U_i^*, U_i - mean value of the velocity in the i^{th} layer.

U_{io}^*, U_{io} - mean value of the velocity evaluated at the middle of the i^{th} layer

v_i^*, v_i - northward component of the velocity in the i^{th} layer.

w_i^*, w_i - vertical component of the velocity in the i^{th} layer.

x^*, x - coordinate measured positive eastwards

y^*, y - coordinate measured positive northwards

z^*, z - coordinate measured positive vertically

β^* - the variation of the coriolis parameter with latitude ($f = f_0 + \beta^* y^*$)

$\beta = \beta^* L^2/U$

$\hat{\beta} = \beta/F_2$

$\delta = (\rho_3^* - \rho_1^*)/\rho_3^*$ - relative density difference between the upper and lower layers

δ_1, δ_3 - the phases of the upper and lower layers with respect to the middle layer.

η_i^*, η_i - elevation of the surface of the i^{th} layer

μ_i - amplitude factor for the mean stream function for the i^{th} layer

ρ_i^* - density of the i^{th} layer

ω - radian frequency

ψ_i - vertically averaged stream for the i^{th} layer

$\bar{\psi}_i$ - time average of ψ_i (i.e. ψ_i in the absence of perturbations)

ξ_i - perturbation of ψ_i

ϕ_i - complex amplitude of ξ_i